AD-A238 789

MENTATION PAGE

Form Approved
OMB No. 0704-0188

estimated to average 1 hour per response, including the time for reviewing instructions, searching existing data sources, g and reviewing the collection of information. Send comments regarding this burden estimate or any other aspect of this g this burden, to Washington Headquarters Services, Directorate for Information Operations and Reports, 1215 Jefferson to the Office of Management and Budget, Paperwork Reduction Project (0704-0188), Washington, DC 20503.

REPORT DATE 25 Jun 9189

3. REPORT TYPE AND DATES COVERED Final Report/1 May 87-30 Apr 91

4. TITLE AND SUBTITLE
A Measurement of Charged & Neutral Elementary Particles Emitted From Antiproton Annihilation at Rest in Heavy Nuclei

5. FUNDING NUMBERS
61102F/2301/B2

6. AUTHOR(S)
Gerald A. Smith

7. PERFORMING ORGANIZATION NAME(S) AND ADDRESS(ES)
Penn State Univ
303 Osmond Laboratory
University Park PA 16802

8. PERFORMING ORGANIZATION REPORT NUMBER
AFOSR-TR- 91 0641

9. SPONSORING/MONITORING AGENCY NAME(S) AND ADDRESS(ES)
AFOSR/NP Bld 410
Bolling AFB DC 20332-6448

10. SPONSORING/MONITORING AGENCY REPORT NUMBER
AFOSR-87-0246

11. SUPPLEMENTARY NOTES

12a. DISTRIBUTION/AVAILABILITY STATEMENT
Approved for public release; distribution is unlimited.

12b. DISTRIBUTION CODE

13. ABSTRACT *(Maximum 200 words)*

The first complete spectrum of neutrons from antiproton induced fission of Uranium has been obtained. Features of the spectrum are explained by three processes: emission of prompt ejectiles driven from the nucleus by pions in the intranuclear cascade, evaporation of neutrons from the excited nucleus before fission, and de-excitation of fission fragments. The temperature of the fission neutrons is about 67% higher than normal fission, indicating large residual energy deposited in the fission fragments. Hence, the fission process serves as a window into the excitation process itself. Results have also been obtained on gamma-rays associated with de-excitation of fission fragments after neutron emission. With respect to normal fission, the relative yield of gamma-rays to neutrons is suppressed, but the temperature of the gamma-rays is higher. Energy transfer by pi-zeros in the intranuclear cascade initiated by antiproton annihilation at rest in carbon and uranium has been measured. The prospects for initiating multifragmentation and disintegration of heavy nuclei appear good.

14. SUBJECT TERMS

15. NUMBER OF PAGES 76

16. PRICE CODE

17. SECURITY CLASSIFICATION OF REPORT	18. SECURITY CLASSIFICATION OF THIS PAGE	19. SECURITY CLASSIFICATION OF ABSTRACT	20. LIMITATION OF ABSTRACT
UNCLASSIFIED	UNCLASSIFIED	UNCLASSIFIED	UL SAR

NSN 7540-01-280-5500

Standard Form 298 (Rev. 2-89)
Prescribed by ANSI Std. Z39-18

PSU LEPS/91-06

FINAL TECHNICAL REPORT

AFOSR GRANT 87-0246
May 1, 1987 - April 30, 1991
Gerald A. Smith
Principal Investigator
June 15, 1991

A-1

91-05936

Date: June 15, 1991

To: Dr. Ralph Kelley (AFOSR)

From: Gerald A. Smith, Principal Investigator, AFOSR 87-0246

Re: Final Technical Report, May 1, 1987 - April 30, 1991

SUMMARY

Yields and energy spectra of nuclear fragments and mesons emitted from antiproton annihilation at rest in carbon, bismuth and uranium targets have been measured in experiments PS183 and PS177 carried out at the Low Energy Antiproton Ring (LEAR), located at CERN in Geneva, Switzerland. Initial studies of PS183 data concentrated on the spectrum of neutrons and nuclear gamma-rays emitted from antiproton annihilation at rest in uranium. This led to the discovery of antiproton-induced fission. We have successfully completed a measurement of the energy transfer by charged mesons to the nucleus. Combined with our previous measurement for neutral mesons, the values are 119±59 MeV and 455±50 MeV for carbon and uranium, respectively. Both measurements result from experiment PS183.

This energy is manifest in two forms, namely energy carried away by nuclear ejectiles and excitation energy which is dissipated by neutrons and gamma-ray emission. We have successfully developed software required to analyze fission fragment and neutron data from experiment PS177. This will lead to a better understanding of the division of energy between ejectiles and excitation.

RESEARCH OBJECTIVES

Excellent progress has been made toward characterization of the yields and energy spectra of charged and neutral elementary particles emitted from antiproton annihilation at rest in nuclei (carbon and uranium). These particles include (charged) pions, kaons, protons, light nuclear fragments, and fission fragments, as well as (neutral) gamma-rays and neutrons. The purpose of this research is to as accurately as possible enumerate the sources and amounts of energy released in nuclei due to the annihilation process. These facts could have an important bearing on the design parameters of an antimatter propulsion system.

RESULTS OF RESEARCH

The data used in this analysis were taken by experiments PS183 and PS177 at the Low Energy Antiproton Ring (LEAR) at CERN in Geneva, Switzerland in 1986 (PS183) and 1988 (PS177).

Initial studies of PS183 data concentrated on the spectrum of neutrons and nuclear gamma-rays emitted from antiproton annihilation at rest in uranium. This lead to the discovery of antiproton-induced fission [1,2].

More recent studies have been directed toward a thorough understanding of the energy transfer to the nucleus and the degree of excitation of the compound nucleus indicated by fission fragments (in the case of uranium) emitted during the breakup of the nucleus. We have published results [3] on the energy transfer by neutral mesons (π^0,η^0,ω^0) in the intranuclear cascade which follows the annihilation of the antiproton. We found the neutral energy transfer to be 28±43 MeV and 232±33 MeV in carbon and uranium, respectively. We have also published results on the energy transfer due to charged mesons [4]. Mr. Ellsworth Minor completed his Ph.D. thesis on this subject (Appendix V). We find the energy transfer due to all mesons (neutral and charged) to be 119±59 MeV and 455±50 MeV in carbon and uranium, respectively. Theoretical estimates of the energy transfer in uranium are 380 [5] and 480 MeV [6], which bracket our value.

Experiment PS177 also recorded data on the yield of charged fission fragments, as well as neutrons and gamma-rays which result from the decay of the fragments, for bismuth and uranium targets. The emphasis is to try to understand the mass and energy distributions of the fragments, which contain information on the excitation of the fissioning nucleus. In addition, the energy and angular distributions of decay neutrons give insight into the angular momentum involved in the process. We have (1) identified and reconstructed fission fragments using a microchannel plate, parallel-plate avalanche detector arrangement; (2) measured very precisely fragment masses with a silicon telescope detector; and (3) measured neutrons in scintillation counters. With these technologies and related software successfully demonstrated, we find the yield of neutrons to be large (13.3 on average) and the angular distributions to be characterized by significant structure, suggesting large angular momentum and high excitation of the decaying fission fragment. A paper on this subject is presently in preparation [7]. This work constitutes the Ph.D. thesis of graduate student Bin Chen.

As a result of the discovery of fission with emission of large numbers of neutrons, as well as charged pions and gamma-rays which are also capable of inducing secondary fissions, we have been motivated to investigate systems utilizing this new physics with potential applications to space propulsion. This work has been sponsored since 1988 under a contract with the Jet Propulsion Laboratory, Pasadena, California. The method under study is called antiproton-boosted microfission, wherein antiprotons are used to ignite extremely small (less than one gram) pellets of fissionable material. If the pellet is infused with hydrogen, or other materials which can result in fusion, it is possible for the fission burn to ignite fusion, resulting in a potentially large gain for the system.

These computational investigations led us to propose to the 1991 AFOSR Spring Initiatives Meeting a program of research at the Phillips Laboratory, Kirtland AFB, using the SHIVA Star liner implosion facility. The proposal was approved on March 28 for funding in FY92 and 93. The role of the Penn State group is to provide a detailed program of measurements, to design and construct a radiofrequency quadrupole for injection of antiprotons into the compressed target, and to design and construct neutron detectors. Prof. G.A. Smith was awarded a Summer Research Award, which he will use in residence at Kirtland AFB, July 22-Sept. 27, 1991.

[1] A. Angelopoulos et al, Phys. Lett. 205B, 590 (1988) (Appendix I).
[2] T.A. Armstrong et al, Z. Phys. A331, 519 (1988) (Appendix II).
[3] T.A. Armstrong et al, Z. Phys. A332, 467 (1989) (Appendix III).

[4] E.D. Minor et al, Z. Phys. A336, 461 (1990) (Appendix IV).
[5] P. Jasselette et al, Nucl. Phys. A484, 542 (1988).
[6] E. Hernandez and E. Oset, Nucl. Phys. A455, 584 (1986) and private communication.
[7] T.A. Armstrong et al, "Yields and Angular Distributions of Neutrons Produced with Fission Fragments by Antiproton Annihilation at Rest in Uranium," to be submitted to Z. Phys. A.

PUBLICATIONS

1. Search for Unusual Behavior in Neutral and Charged Particle Emission from Antiproton–Nucleus Annihilation at Rest, G. Bueche, R.A. Lewis and G.A. Smith, Physics at LEAR with Low Energy Antiprotons, Eds. C. Amsler, G. Backenstoss, R. Klapisch, C. LeLuc, D. Simon and L. Tauscher, Nuclear Science Research Conference Series Vol. 14, Harwood Academic Publishers, Switzerland, 1988, p. 689.

2. Strangeness Content in Antiproton–Nucleus Annihilation at Rest, R.A. Lewis and G.A. Smith, Physics at LEAR with Low Energy Antiprotons, Eds. C. Amsler, G. Backenstoss, R. Klapisch, C. LeLuc, D. Simon and L. Tauscher, Nuclear Science Research Conference Series Vol. 14, Harwood Academic Publishers, Switzerland, 1988, p. 693.

3. Neutron Emission from Antiproton Annihilation at Rest in Uranium, A. Angelopoulos et al, Phys. Lett. 205B, 590 (1988).

4. Antiproton Annihilation Spectra, G.A. Smith, Hyperfine Interactions 44, 43 (1988).

5. Antiproton Annihilation in Nuclei, G.A. Smith, Proc. of the RAND Workshop on Antiproton Science and Technology, ed. B.W. Augenstein, B.E. Bonner, F.E. Mills and M.M. Nieto, World Scientific, Singapore, 1988, p. 283.

6. Particle Emission from Antiproton Annihilation at Rest in Uranium, G.A. Smith, Proc. of the RAND Workshop on Antiproton Science and Technology, ed. B.W. Augenstein, B.E. Bonner, F.E. Mills and M.M. Nieto, World Scientific, Singapore, 1988, p. 296.

7. A Measurement of the S– and P–Wave Content of Antiproton Annihilation at Rest Into Two Pions in Liquid Deuterium, A. Angelopoulos et al, Phys. Lett. 212B, 129 (1988).

8. Nuclear Gamma–Ray Emission from Antiproton Annihilation at Rest in Uranium, T.A. Armstrong et al, Z. Phys. A331, 519 (1988).

9. Pion (and Muon) Production by Antiprotons on Light and Heavy Nuclei, R.A. Lewis et al, Muon–Catalyzed Fusion, ed. S.E. Jones, J. Rafelski and H.J. Monkdorst, AIP Conf. Proc. No. 181, New York, 1989, p. 415.

10. Energy Transfer by Intranuclear Cascade of Pi–Zeros Produced in Antiproton Annihilation at Rest in Nuclear Targets, T.A. Armstrong et al, Z. Phys. A332, 467 (1989).

11. Antiproton Physics Up to 120 GeV, G.A. Smith, Proc. of the Workshop on Physics at the Main Injector, Fermilab, Batavia, IL, ed. S.D. Holmes and B.D. Winstein, 1989, p. 73.

12. Charged Pion Spectra and Energy Transfer Following Antiproton Annihilation at Rest in Carbon and Uranium, E.D. Minor et al, Z. Phys. A336, 461 (1990).

13. The LEAR PS177 Low Energy K-Plus Detector, T.A. Armstrong et al, Nucl. Instrum. and Methods A289, 109 (1990) (Appendix VI).

14. Antiproton Accumulator Physics, P.A. Rapidis and G.A. Smith, Physics at Fermilab in the 1990's, ed. D. Green and H. Lubatti, World Scientific, Singapore, 1990, p. 474.

PARTICIPATING PROFESSIONALS

T.A. Armstrong, Ph.D., 1977, "Total Cross-Sections for Photoproduction of Hadrons"

R. Bishop (graduate student) M.S., 1989 (Appendix VII), "Gamma Radiation Shielding for Antiproton Annihilation Engines" (presently at the ANSER Corp., Arlington, VA)

Bin Chen (graduate student), Ph.D. expected 1992

R.A. Lewis, Ph.D., 1966, "Pion Photoproduction Angular Distributions"

E.D. Minor (graduate student) Ph.D., 1990, "Charged Pion Spectra and Energy Transfer Following Antiproton Annihilation at Rest in Carbon and Uranium" (presently postdoctoral research associate, Penn State University)

G.A. Smith, Ph.D., 1961, "Proton-Proton Interactions at 2.85 BeV"

COUPLING ACTIVITIES

a) Colloquia, Lectures and Seminars

1. G.A. Smith, invited paper, Muon Catalyzed Fusion Workshop, Sanibel Island, FL, 1988.

2. G.A. Smith, invited papers, IX European Symposium on Proton-Antiproton Interactions and Fundamental Symmetries, Mainz, FRG, 1988.

3. G.A. Smith, seminar, Department of Nuclear Engineering, Penn State University, 1989.

4. G.A. Smith, colloquium, Department of Physics, Northwestern University, 1988.

5. G.A. Smith, seminar, Jet Propulsion Laboratory, Pasadena, CA, 1989.

6. G.A. Smith, contributed paper, Antiproton Technology Workshop, Brookhaven National Laboratory, Upton, NY, 1989.

7. E.D. Minor, contributed paper, Antiproton Technology Workshop, Brookhaven National Laboratory, Upton, NY, 1989.

8. E.D. Minor, contributed paper, American Physical Society Meeting, Baltimore, MD, 1989.

9. R.A. Lewis, contributed paper, American Physical Society Meeting, Baltimore, MD, 1989.

10. G.A. Smith, lecture, IV LEAR Workshop, Villars-sur-Ollon, Switzerland, 1987, Search for Unusual Behavior in Neutral and Charged Particle Emission from Antiproton-Nucleus Annihilation at Rest, PHYSICS AT LEAR WITH LOW ENERGY ANTIPROTONS, eds. C. Amsler, G. Backenstoss, R. Klapisch, C. Leluc, D. Simon and L. Tauscher, Nuclear Science Research Conference Series Vol. 14, Harwood Academic Publishers, Switzerland, 1988, p. 689.

11. G.A. Smith, lecture, IV LEAR Workshop, Villars-sur-Ollon, Switzerland, 1987, Strangeness Content in Antiproton-Nucleus Annihilation at Rest, PHYSICS AT LEAR WITH LOW ENERGY ANTIPROTONS, eds. C. Amsler, G. Backenstoss, R. Klapisch, C. Leluc, D. Simon and L. Tauscher, Nuclear Science Research Conference Series Vol. 14, Harwood Academic Publishers, Switzerland, 1988, p. 693.

12. G.A. Smith, lecture, Proc. of the RAND Workshop on Antiproton Science and Technology, RAND Corporation, Santa Monica, CA, 1987, Antiproton Annihilation in Nuclei, p. 283.

13. G.A. Smith, lecture, Proc. of the RAND Workshop on Antiproton Science and Technology, RAND Corporation, Santa Monica, CA, 1987, Particle Emission from Antiproton Annihilation at Rest in Uranium, p. 296.

14. G.A. Smith, lecture, Antimatter 87, Kernforschungszentrum, Karlsruhe, FRG, 1987, Antiproton Annihilation Spectra, to appear in HYPERFINE INTERACTIONS.

15. G.A. Smith, colloquium, Dept. of Physics, Univ. of Arizona, February, 1988, Antiproton Annihilation in Nuclei.

16. G.A. Smith, colloquium, Physics and Theoretical Divisions, Los Alamos National Laboratory, February, 1988, Antiproton Annihilation in Nuclei.

17. G.A. Smith, colloquium, Dept. of Physics, Univ. of New Mexico, February, 1988, Antiproton Annihilation in Nuclei.

18. G.A. Smith, invited paper, "Antiproton Physics Up to 120 GeV," Main Injector Workshop, Fermilab, IL, 1989.

19. G.A. Smith, summary talk, "Antiproton Accumulator Physics," Physics at Fermilab in the 1990's, Breckenridge, CO, 1989.

20. G.A. Smith, invited paper, "An Antiproton Driver for Inertial Confinement Fusion Propulsion," NASA Symposium on Advanced Propulsion, Washington, D.C., 1989.

21. G.A. Smith, seminar, "An Antiproton Driver for Inertial Confinement Fusion Propulsion," Air Force Astronautics Laboratory, Edwards AFB, CA, 1989.

22. G.A. Smith, presentation, "An Antiproton Driver for Inertial Confinement Fusion Propulsion," NASA Center for Space Propulsion Engineering, Penn State University, 1990.

23. R.A. Lewis, invited paper, "An Antiproton Catalyst for Inertial Confinement Fusion Propulsion, AIAA/SAE/ASME/ASEE 26th Joint Propulsion Conference, Orlando, FL, 1990.

24. G.A. Smith, invited paper, "An Antiproton Driver for Inertial Confinement Fusion Propulsion," NASA Symposium on Advanced Propulsion, Jet Propulsion Laboratory, Pasadena, CA, 1990.

25. G.A. Smith, presentation, "Nuclear and Plasma Physics with Antiprotons," Dr. Robert Selden, Chief Scientist of the Air Force, The Pentagon, March 19, 1991.

26. G.A. Smith, presentation, "Nuclear and Plasma Physics with Antiprotons, AFOSR Spring Initiatives Meeting, Bolling AFB, Washington, D.C., March 27, 1991.

27. G.A. Smith, presentation, "Nuclear and Plasma Physics with Antiprotons," Dr. Joseph Janni, Chief Scientist of the Phillips Laboratory, Kirtland AFB, Albuquerque, NM, March 1, 1991.

b) Consulting

1. Air Force Studies Board meeting, Jet Propulsion Laboratory, Pasadena, CA, June 1988, contact – B. Augenstein (RAND Corporations).

2. Air Force Scientific Advisory Board, Washington, D.C., November 1988, – contact Maj. G. Nordley.

3. The RAND Corporation, antimatter propulsion, RAND Workshop on Antiproton Science and Technology, Santa Monica, CA, October 1987, contact – Dr. B. Augenstein.

4. The RAND Corporation, antimatter propulsion, Air Force Studies Board meeting, Jet Propulsion Laboratory, Pasadena, CA, June 1988, contact – Dr. B. Augenstein.

5. The RAND Corporation, "Antiproton Research – Science and Technology Applications: Relevance to DOD," B.W. Augenstein, J.C. Solem, G.A. Smith and S.J. Lukasik, 1990 (see Appendix VIII).

APPENDIX I

NEUTRON EMISSION FROM ANTIPROTON ANNIHILATION AT REST IN URANIUM

Athens–Irvine–Karlsruhe–New Mexico–Pennsylvania State

A. ANGELOPOULOS [a], A. APOSTOLAKIS [a], T.A. ARMSTRONG [b], B. BASSALLECK [c], G. BUECHE [d], M. FERO [e], M. GEE [e], N. GRAF [e], H. KOCH [d], R.A. LEWIS [b], M. MANDELKERN [c], P. PAPAELIAS [a], H. POTH [d], H. ROZAKI [a], L. SAKELLIOU [a], J. SCHULTZ [e], J. SCHWERTEL [d], G.A. SMITH [b], T. USHER [e] and D.M. WOLFE [c]

[a] *Nuclear Physics Laboratory, University of Athens, GR 15771 Athens 144, Greece* [1]
[b] *Department of Physics, Pennsylvania State University, University Park, PA 16802, USA* [2]
[c] *Department of Physics, University of New Mexico, Albuquerque, NM 87131, USA* [3]
[d] *Institut für Kernphysik, Kernforschungszentrum Karlsruhe, D-7500 Karlsruhe, Fed. Rep. Germany* [4] *and Institut für Experimentelle Kernphysik, Universität Karlsruhe, D-7500 Karlsruhe, Fed. Rep. Germany* [4]
[e] *Department of Physics, University of California, Irvine, CA 92717, USA* [3]

Received 4 February 1988

We have observed a large yield (5.77 ± 0.16/ann.) of neutrons from antiproton annihilation at rest in a thin uranium target. Significant components of fission, evaporation and direct neutrons comprise this total. The large fission yield (2.50 ± 0.10/ann.), as well as the high temperature (94 ± 10 MeV) of the direct component, have not been anticipated in the intranuclear cascade model.

We have performed an experiment at the low energy antiproton ring (LEAR) at CERN to measure the spectra of charged and neutral particles emitted from antiproton annihilation at rest in a uranium target. The purpose of the experiment was to explore in detail features of the intranuclear cascade (INC) initiated by the antiproton annihilation and the subsequent burst of pions within the nucleus. In INC models the antiproton captures in a high atomic state ($n=10, \ell=9$ or $n=9, \ell=8$), cascading down to lower levels where it annihilates on the fringes of the nuclear surface. Some of the annihilation pions penetrate the nucleus, producing high energy nucleons by πN scattering, and lower energy nucleons by evaporation from the heated nucleus [1–4]. In this paper we present first results on neutron spectra in the range 1–120 MeV kinetic energy. An unexpected result has been the observation of a large fission component and a high temperature, direct knock-out process. Results on charged spectra will be presented at a later time.

The detector (fig. 1) has been described in detail in previous papers [5]. For this experiment a cylindrical proportional chamber (CWC) with a solid angle of ~95% of 4π steradians was installed around the target to aid in the measurement of the multiplicity and direction of charged particles. In addition, four NE110 plastic neutron counters (N1–N4) were placed behind the N drift chambers (NDC), and a piece of natural uranium replaced the liquid hydrogen/deuterium target near the intersection of the beamline and magnet centerline. The LEAR beam was degraded from 350 to 250 MeV/c before striking the target, which was a disk 2 mm thick and 35 mm in diameter. The target was rotated 45° around a vertical axis, and based on vertex profiles from the drift chambers and CWC stopped ~35% of the beam.

The present analysis includes only neutron events

[1] Work supported in part by the Greek Ministry of Research and Technology.
[2] Work supported in part by the US Air Force and National Science Foundation.
[3] Work supported in part by the US Department of Energy.
[4] Work supported in part by the Federal Ministry for Research and Technology, Fed. Rep. Germany.

0370-2693/88/$ 03.50 © Elsevier Science Publishers B.V. (North-Holland Physics Publishing Division)

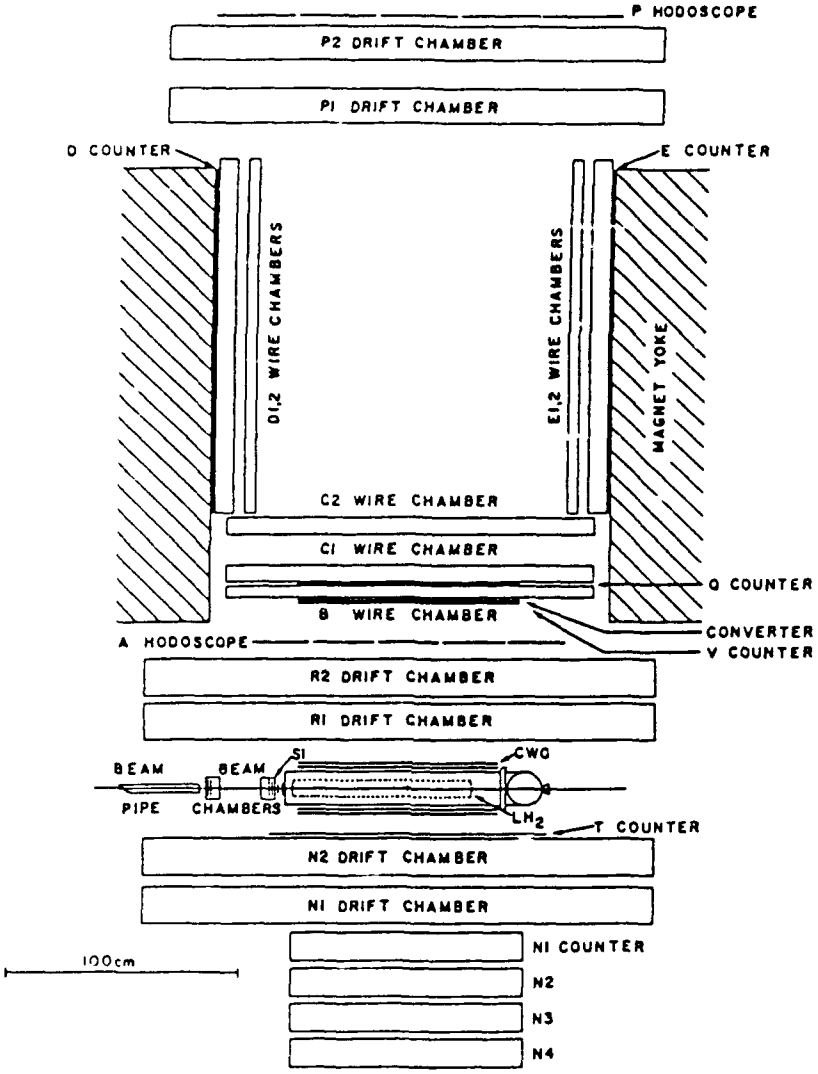

Fig. 1. PS183 spectrometer at LEAR. For this experiment the LH_2 target was replaced with a thin uranium target (see text) near the intersection of the beamline and magnet centerline.

accompanied by a charged particle which penetrated the full spectrometer, intercepting the P drift chambers (P-tracks). Event read-out was triggered on a single P-track, the rate for which was $\sim 10^3\ s^{-1}$ at an incident antiproton rate of $\sim 10^5\ s^{-1}$. The neutron counters were each 100 cm long × 20 cm high × 10 cm deep, placed 79, 93, 107 and 121 cm respectively from the target. Each counter was read out with two RCA 5-inch Quantacon photomultiplier tubes. The discriminator thresholds were calibrated at 400 keV electron equivalent ($\sim$1.3 MeV proton equivalent) energy with a Co^{60} source. Pulse heights and timing resolution (1.5 ns FWHM) were calibrated using monoenergetic pions from $\bar{p}p \to \pi^+\pi^-$ events produced in the hydrogen target. The maximum time delay was 62 ns, corresponding to a minimum energy neutron detected in (N1) of $\sim$0.9 MeV kinetic energy.

Neutrons were required to fire at least one counter after a delay of 1.5 ns relative to the expected arrival time of a $\beta = 1$ particle. Gamma-rays were identified by a prompt signal (< 1.5 ns) in or or more sequential counters. Charged tracks were rejected by a hit in the T counter and a reconstructed track in the NDC.

The individual N1–N3 TOF spectra are shown in fig. 2. The figure shows only events in which a single neutron counter was hit. Prompt gamma-ray peaks are seen, followed by a broader distribution of neutrons. Because of the requirement that only a single counter was hit, the gamma-ray peaks include only low energy ($\lesssim$20 MeV) Compton or pair-production events. The falloff in the neutron yield from N1 to N3 is due to scattering and geometrical effects. As N4 was closest to a nearby shield wall which could produce back-scattering, we have rejected any event in which a neutron appeared in N4.

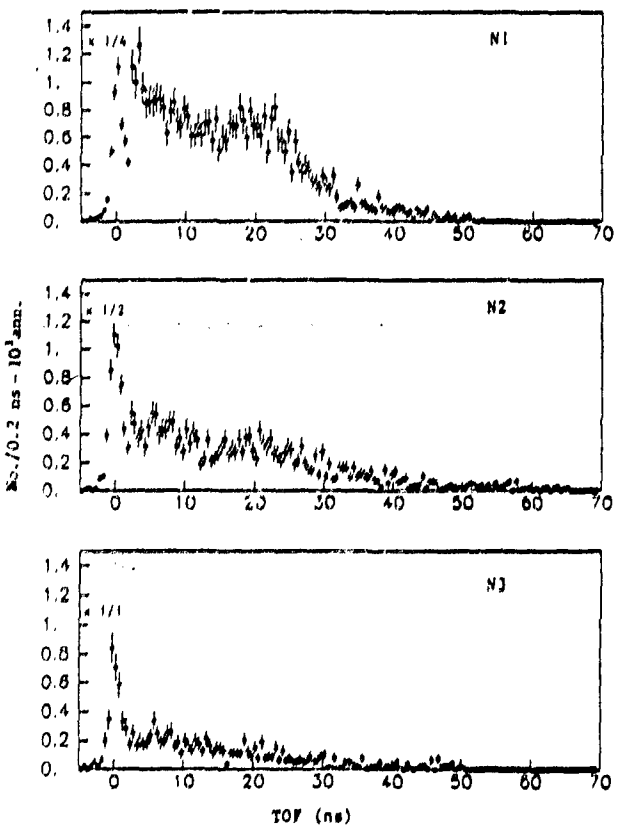

Fig. 2. Neutron TOF spectra for individual counters N1–N3. Only events with one hit have been plotted, and no corrections have been made for background. The solid points in the prompt gamma-ray peak have been multiplied by the indicated fraction.

We have investigated two possible sources of background in these spectra. First, neutrons may be produced by charged particles hitting the apparatus surrounding the target. This has been confirmed by observing neutrons from the hydrogen target, since antiprotons annihilating at rest in hydrogen are unable to produce neutrons. The TOF spectra from hydrogen exhibit neutron yields per annihilation which, on the average, are ~20% of those from the uranium target. Using reconstructed trajectories of charged particles from the drift chambers and CWC, we find that 88% of the neutrons from hydrogen are associated with charged particles which hit the NDC support frames. The remaining 12% come from the RDC and CWC frames, floor, etc. Background from the hydrogen target itself is negligible. The final neutron spectra from uranium have been corrected for this background by subtracting, bin-by-bin, hydrogen spectra normalized to the same number of annihilations.

This procedure has been verified by correcting in an identical manner the spectrum of neutrons observed with the deuterium target. We find this spectrum to be in good agreement, both in shape and magnitude, with a published neutron spectrum from $\bar{p}d$ interactions at rest [6]. We have also fit this spectrum to the deuteron spectator wave function [7] plus a Maxwell–Boltzmann (MB) term to account for the high momentum tail of the spectrum, including in this fit the neutron counter efficiency based on an established code [8]. A good fit is obtained with the yield of neutrons corrected for solid angle equal to 0.49 ± 0.04/ann., in good agreement with the expectation of the naive spectator model (0.5).

We have also considered a second form of background due to neutrons from the uranium target which scatter into the neutron detector from nearby materials. Such neutrons can also produce gamma-rays which simulate a neutron signal since they are somewhat delayed relative to prompt gamma-rays coming directly from the target. Using elastic and inelastic neutron (and proton) scattering data [9], we have simulated this process with a Monte Carlo program. The results show that this background is 15% in magnitude and similar in shape compared to the observed spectrum. Correspondingly, a downward correction of 15% has been made to all final neutron yields quoted in this paper.

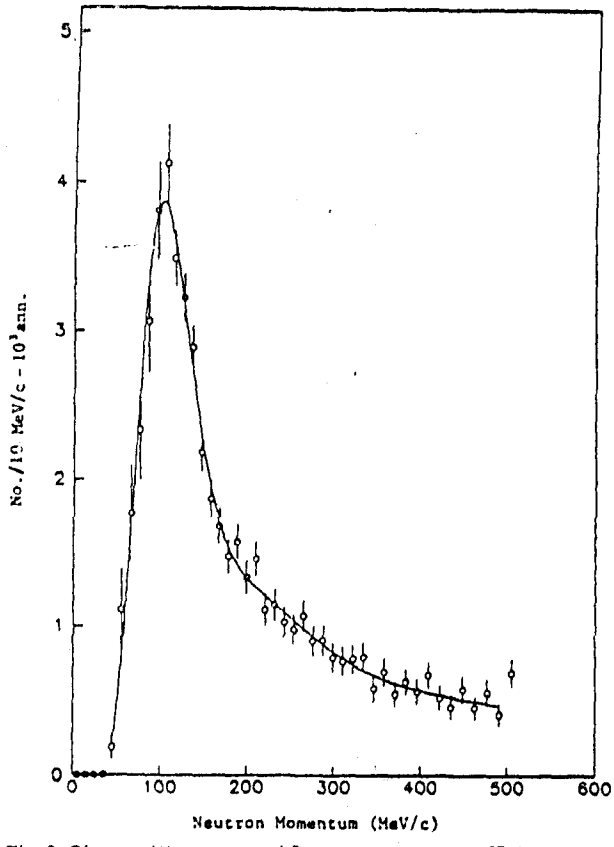

Fig. 3. Observed (uncorrected for neutron counter efficiency and solid angle) neutron momentum spectrum with charged particle induced background removed. The curve is a fit to eq. (1).

We show in fig. 3 the observed (uncorrected for neutron counter efficiency and solid angle) neutron momentum spectrum with charged particle induced background removed, as described above. We have fitted the corresponding kinetic energy spectrum with a two component (MB) function, each with a characteristic temperature, plus a third term which accounts for fission [10]. The three components are designated as (1) direct (D), (2) evaporation (EV), and (3) fission (F). The function which describes the observed kinetic energy spectrum is given by

$$Y(E)=\left(\sum_{i=1}^{2} a_i \sqrt{E}\exp(-E/T_i) + a_F \sinh(2\sqrt{E_F E}/T_F)\, E^{-E/T_F}\right) \times \epsilon_n(E)\,(\Delta\Omega/4\pi)\,, \qquad (1)$$

Table 1
Results of fits to eq. (1) with the P-track trigger. All intensities quoted here have been corrected for neutron counter efficiency and solid angle [see eq. (1)], as well as background (see text), and result from integrating the fit functions from zero to infinite energy.

a_D (no./ann)	2.00 ± 0.11
T_D (MeV)	93.8 ± 10.2
a_{EV} (no./ann)	1.27 ± 0.07
T_{EV} (MeV)	15.9 ± 1.6
a_F (no./ann)	2.50 ± 0.10
T_F (MeV)	2.50 ± 0.27
E_F (MeV)	0.74 ± 0.10
χ^2/DF	23/33

where a_i, a_F are intensities, T_i, T_F are temperatures, E_F is the mean fission fragment energy per nucleon, and $\epsilon_n(E)$ and $(\Delta\Omega/4\pi)$ are the efficiency and fractional solid angle of the neutron counter. Starting values for the parameters T_D, T_{EV}, T_F and E_F were chosen to be 100, 12.8, 2.80 and 0.63 MeV respectively. During the fit each parameter was allowed to increase or decrease by up to a factor of two from its starting value. A good fit was obtained, the result of which is shown as the curve in fig. 3, with numerical values listed in table 1.

We now turn to a discussion in our results. Of the 5.77 ± 0.16 neutrons observed per annihilation, the single largest component (2.50 ± 0.10) is due to fission. Two other stopped antiproton experiments [11,12] in uranium have reported evidence for fission. However, to the best of our knowledge this is the first reported measurement of absolute yields of fission neutrons per annihilation.

We also observe that our fission neutron yields are larger for proton than pion triggers. The distinction is based on a time-of-flight separation of P-tracks which has been described elsewhere [13]. The yields for proton (pion) triggers are 3.37 ± 0.22 (2.34 ± 0.15 for π^+, 2.29 ± 0.12 for π^-) per annihilation. The mean momenta for the trigger proton (pion) are 578 (397) MeV/c, the difference being due at least in part to the low momentum acceptance cutoff of the spectrometer. The difference in fission neutron yields may be related to this fact.

The number of fission neutrons per annihilation (2.50 ± 0.10) and mean fission fragment energy per

nucleon (0.74 ± 0.10) which we measure are consistent with values [10] for fission induced by low energy neutrons [~ 2.4 MeV, ~ 0.5 MeV respectively]. Our fission temperature (2.50 ± 0.27 MeV) is somewhat larger than values measured with low energy neutrons (~ 1.5 MeV), but appears to be consistent with the trend of values with increasing neutron energy [10]. We therefore conclude that our data are consistent with stopped antiprotons producing fission ~ 100% of the time in uranium.

The second largest component (2.00 ± 0.11/ann.) is associated with direct neutrons which are knocked out of the nucleus by annihilation pions. It is important to note that our temperature (94 ± 10 MeV) is larger than that observed for protons emitted after annihilation of 180 MeV antiprotons in bismuth (69 ± 7 MeV) [14] and uranium (77 ± 4 MeV) [15]. This difference (~ 20 MeV) appears to have been unanticipated in previous INC model calculations [1–4].

References

[1] M.R. Clover et al., Phys. Rev. C 26 (1982) 2138.
[2] A.S. Iljinov et al., Nucl. Phys. A 382 (1982) 378.
[3] M. Cahay et al., Nucl. Phys. A 393 (1983) 237.
[4] J. Cugnon and J. Vandermeulen, Nucl. Phys. A 445 (1985) 717.
[5] A. Angelopoulos et al., Phys. Lett. B 159 (1985) 210; B 178 (1986) 441.
[6] C. Amsler et al., Phys. Rev. Lett. 44 (1980) 853.
[7] L. Hulthén and M. Sugawara, Handbuch der Physik, Vol. 39 (Springer, Berlin, 1957) p. 141.
[8] R.A. Cecil et al., Nucl. Instrum. Methods 161 (1979) 439.
[9] W. Walt et al., Phys. Rev. 98 (1955) 677;
J.D. Anderson et al., Phys. Rev. 111 (1958) 572;
S. Fernbach, Rev. Mod. Phys. 30 (1958) 414;
A. Johanson et al., Ark. Fys. 19 (1961) 541;
W.T.H. van Oers et al., Phys. Rev. C 10 (1974) 307.
[10] V.M. Gorbachev et al., Nuclear reactions in heavy elements (Pergamon, New York, 1986).
[11] J.P. Bocquet et al., contributed paper IV LEAR Workshop (Villars-sur-Ollon, Switzerland, September 1987).
[12] H. Daniel et al., abstract submitted to XI Intern. Conf. on Particles and nuclei (Kyoto, Japan, April 1987); contributed paper IV LEAR Workshop (Villars-sur-Ollon, Switzerland, September 1987).
[13] A. Angelopoulos et al., AIP Conf. Proc. No. 132, ed. S. Oneda (American Institute of Physics, New York, 1985) p. 150.
[14] D. Garretta et al., Antiproton 1984 (Adam Hilger, Bristol, 1985) p. 187.
[15] P.L. McGaughey et al., Phys. Rev. Lett. 56 (1986) 2156.

APPENDIX II

Z. Phys. A – Atomic Nuclei 331, 519–520 (1988)

Zeitschrift für Physik A
Atomic Nuclei
© Springer-Verlag 1988

Short Note

Nuclear Gamma-Ray Emission from Antiproton Annihilation at Rest in Uranium*

T.A. Armstrong, R. Bishop[a], V. Harris, R.A. Lewis, E. Minor, and G.A. Smith
Laboratory for Elementary Particle Science, Department of Physics, Pennsylvania State University, University Park, PA 16802, USA

Received August 1, 1988; revised version September 1, 1988

Abstract: We have observed low energy nuclear gamma-rays, which we interpret as coming from fission fragments, from antiproton annihilation at rest in a uranium target. The high gamma-ray and previously reported fission neutron temperatures, as well as large relative neutron-to-gamma ray yields, suggest a high level of excitation of the fission fragments.

PACS: 23.2Lv; 25.85.Ge; 25.90.+k

In a recent paper we reported on the first observation of a large yield of neutrons (5.77±0.16/ann.) from antiproton annihilation at rest in a natural uranium target [1]. Included in the neutron spectrum is a significant component of low energy neutrons (2.50±0.10/ann.), which we interpreted as resulting from antiproton-induced fission (AF). An unusual feature of these fission neutrons is their temperature (2.50±0.27 MeV), which exceeds that of fission neutrons produced in low energy neutron-induced fission (LENF) by ~ 80%. This effect may be due to the high level of excitation of the target nucleus (and subsequent fission fragments) induced by the antiproton annihilation, which has been predicted to be several hundreds of MeV by Iljinov et al [2]. This calculation has successfully predicted the momentum distribution of recoiling uranium nuclei measured by Bocquet et al [3], as reconstructed from fission fragments observed in their detectors. To further explore the fission process under these extreme conditions, we have investigated the accompanying gamma-rays which were observed as a peak in our time-of-flight spectra (see Fig. 2 of ref. [1]).

The gamma-ray pulse height spectrum has been measured in the first two NE110 plastic scintillation counters (N1,2) in our apparatus at LEAR. These counters, as well as the beam, target, electronic trigger and charged-particle veto systems, were described in ref. [1]. Gamma-rays were identified by a prompt signal ($|\Delta t| < 1.2$ ns) in either N1 or N2, and no hit in the T-counter. We have estimated a fast neutron contamination of 7% by extrapolating the time-of-flight spectra into the prompt region. The resultant pulse height spectrum is shown in Figure 1 (open squares).

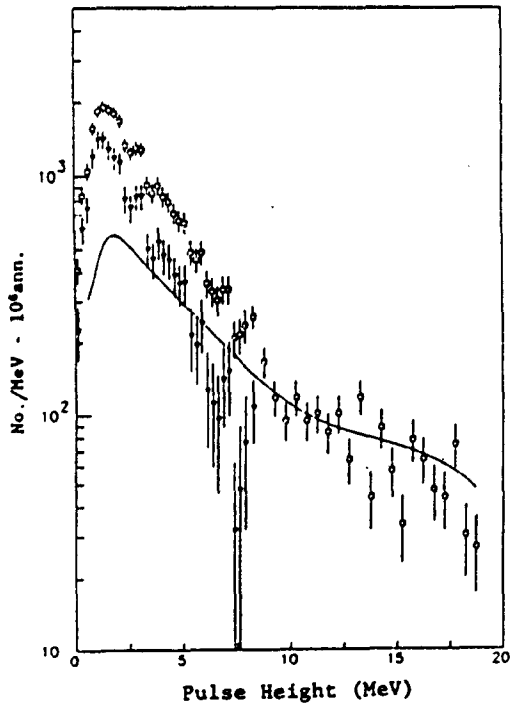

Fig. 1 - Pulse height spectra for: uranium (open squares); simulated $\pi^0 \to \gamma\gamma$ for uranium (solid curve); and the difference of the first two spectra (closed triangles).

A significant background of gamma-rays is expected from $\pi^0 \to \gamma\gamma$ decays. In order to simulate this background, we have utilized the gamma-ray spectrum taken with the liquid hydrogen target [1]. The only difference in conditions under which the uranium and hydrogen spectra were taken was the targets. The uranium target represented ~ 50% of a radiation length of material, whereas by contrast the hydrogen target was negligible (< 1%). Therefore, we have recomputed by monte

*Work supported in part by the Air Force Office of Scientific Research, Air Force Systems Command, USAF under grant AFOSR 87-0246 and the U.S. National Science Foundation.

[a] Aerospace Engineering Department, Pennsylvania State University.

carlo methods the hydrogen spectrum, including effects of Compton and pair-production absorption in the uranium target. The resultant, smoothed spectrum is shown in Fig. 1 (solid line). We see that above ~ 8 MeV the solid line and uranium spectra are in agreement, consistent with the hypothesis that gamma-rays from the uranium target above this energy come exclusively from $\pi^0 \rightarrow \gamma\gamma$ decay. However, below ~ 8 MeV we observe an excess of gamma-rays from uranium, seen in the differences spectrum (closed triangles). We attribute these gamma-rays to de-excitation of fission fragments, which we reiterate have been previously observed [1,3] with ~ 100% probability per antiproton annihilation.

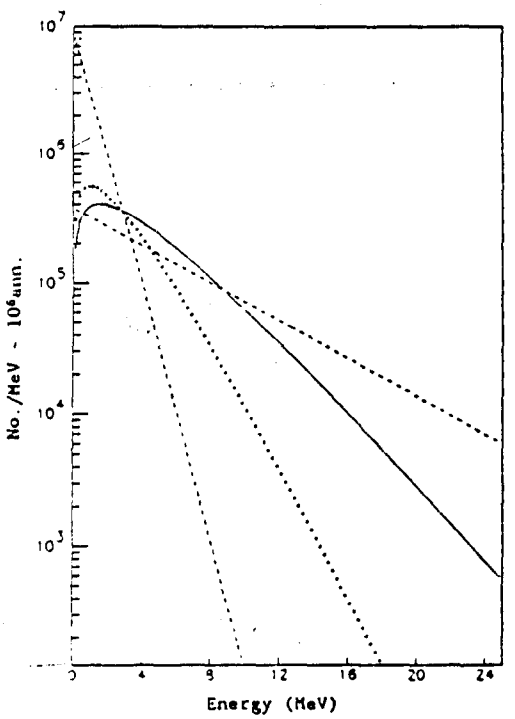

Fig. 2 - Corrected fission spectra from uranium for: AF gamma-rays (dashed curve); LENF gamma-rays (dot-dashed curve); AF neutrons (solid curve); and LENF neutrons (dotted curve).

In Figure 2 we show the final gamma-ray energy spectrum (dashed curve), corrected for target absorption, N1,2 solid angle ($\Delta\Omega/4\pi$ = 2.4%) and efficiency for the Compton process (which rises from threshold at 400 KeV electron equivalent, peaks at 55% at 1 MeV, and then falls to 25% at 8 MeV) [4], the T-counter charged-particle veto condition (veto/ann. = 0.6), and fitted to a single exponential of the form $\propto \exp[-E/T]$. The integrated yield and temperature parameter (T) are given in Table 1. For comparison, we show (dot-dashed curve) the gamma-ray spectrum for LENF [5], also fitted to a single exponential, with corresponding yield and temperature given in Table 1. One can readily see that AF produces about one-quarter as many gamma-rays, but each gamma-ray is nearly seven times more energetic, than those from LENF. Also shown in Fig. 2 is the fission neutron energy spectrum from this experiment (solid curve) [1], as well as the fission neutron spectrum (dotted curve) for LENF [5], again with yields and temperatures summarized in Table 1. As poinced out in ref. [1], one sees that AF produces comparable numbers of fission neutrons, but each neutron is nearly twice as energetic, than those from LENF.

Table 1 - Yields and temperatures of neutrons and gamma-rays from antiproton fission (AF) and low energy neutron-induced fission (LENF).

	Neutrons		Gamma-Rays	
	No./fission	T(MeV)	No./fission	T(MeV)
AF	2.50±0.10[a]	2.50±0.27[a]	2.0±0.3[c]	6.0±1.0
LENF	2.5[b]	1.4[b]	7.9[b]	0.9[b]

[a] from ref. [1]
[b] from ref. [5]
[c] Integrated from zero to infinite energy and corrected for fast neutron contamination.

The generally accepted explanation of relative neutron gamma-ray yields from LENF is based on statistical evaporation theory, modified by angular momentum considerations to explain the somewhat larger than expected gamma-ray yields [5]. For a fragment with a given angular momentum J, gamma-ray emission competes favorably with neutron emission if the excitation energy E is less than the sum of the neutron binding energy and $E_{MIN}(J)$, the so-called "yrast" energy [6]. In the case of LENF, E is apparently sufficiently close to the yrast energy to allow the yield of gamma-rays to exceed that of neutrons by over a factor of three. However, the situation for AF is reversed, namely the gamma-ray yield is slightly less than the neutron yield. This is consistent with E(J) for AF fragments being further removed from the yrast energy that for LENF, and the prediction that significant excitation is transferred to the nucleus by antiproton annihilation [2]. The higher level of excitation of the fragments is further supported by the higher temperatures we observe for AF compared to LENF.

REFERENCES

[1] A. Angelopoulos et al, Phys. Lett. B205, 590 (1988).
[2] A.S. Iljinov et al, Nucl. Phys. A393, 237 (1983).
[3] J.P. Bocquet et al, Physics at LEAR With Low Energy Antiprotons, ed. C. Amsler et al, Harwood Academic Publishers, Switzerland, p. 793.
[4] Gamma-Detection Efficiency of Organic Phosphors, K.I. Roulston and S.I.H. Naqui, Tech. Data Note 75C-8/82, Bicron Corp., Newburg, Ohio, USA.
[5] Nuclear Fission, R. Vandenbosch and J.R. Huizenga, Academic Press, New York and London, 1973; Nuclear Reactions in Heavy Elements, V.M. Gorbachev et al, Pergamon Press, New York, 1983.
[6] T. Thomas and J.R. Grover, Phys. Rev. 159, 980 (1967); J.R. Grover and J. Gilat, Phys. Rev. 157, 814 (1967).

APPENDIX III

Z. Phys. A – Atomic Nuclei 332, 467–472 (1989)

Zeitschrift für Physik A
Atomic Nuclei
© Springer-Verlag 1989

Energy Transfer by Intranuclear Cascade of Pi-Zeros Produced in Antiproton Annihilation at Rest in Nuclear Targets*

T.A. Armstrong, R. Bishop, V. Harris***, R.A. Lewis, E. Minor ****, and G.A. Smith**

Laboratory for Elementary Particle Science, Department of Physics, 303 Osmond Laboratory, Pennsylvania State University, University Park, PA, USA

Received November 11, 1988

The energy transfer by pi-zeros in the intranuclear cascade initiated by antiproton annihilation at rest in carbon and uranium has been measured to be 28 ± 43 and 232 ± 33 MeV respectively. We estimate the total energy transfer due to all pions to be 75 ± 53 and 447 ± 42 MeV respectively. The uranium value is $\sim 17\%$ larger than a recent theoretical prediction. No predictions for carbon are available. Given the expected increase in efficiency of energy transfer from antiproton beams at ~ 3 GeV/c momentum, the prospects for initiating multifragmentation and disintegration of heavy nuclei at these energies appear good.

PACS: 13.75.Cs; 21.10.Dr; 25.90.+d

1. Introduction

In recent articles it has been shown that fission fragments created in a uranium target by antiproton annihilation at rest emit unusually energetic neutrons [1] and gamma-rays [2]. Thus, through a special window provided by the fission process, there is evidence of residual energy E^* transferred to the nucleus by the intranuclear cascade (INC) generated by pions from the annihilation process. Other features of the INC have been reported, involving energy and multiplicity distributions of prompt nucleons [1, 3–5], light nuclei [5], pions and kaons [3, 6, 7], as well as heavy nuclei in the form of residual mass distributions [8]. These effects have been reviewed extensively, particularly recently theoretically by Cugnon [9] and experimentally by Guaraldo [10], and have been interpreted within the framework of several versions of the INC model.

As stressed by Golubeva et al. [11], the ability of an antiproton to annihilate in nuclear matter, thereby releasing as much as $2m_N$ of energy into the nucleus, could possibly lead to the production of nuclei with residual energy E^* comparable to their total binding energy. Under these conditions, it is suggested that multifragmentation and the ultimate disintegration of the hot residual nucleus may occur. Botvina et al. [12] have calculated that for a heavy nucleus ($A \approx 200$) with excitation of ~ 3 MeV/nucleon, one should expect a breakdown of the nucleus into two fragments with approximately equal masses ("quasi-fission") with one or two additional light clusters. However, at ~ 5 MeV/nucleon excitation the "quasi-fission" peak should melt down into a distribution which monotonically falls off with A. This suggests that a phase transition could be observed if ~ 600–1000 MeV of energy were deposited within the nucleus, well within the upper bound of $2m_N$ allowed by antiproton annihilation. In this context, anticipated results of measurements of residual mass yields from targets with $A \approx 200$ from recent LEAR experiments will be extremely useful.

* Work supported in part by the Air Force Office of Scientific Research, Air Force Systems Command, USAF under grant AFOSR 87-0246 and the U.S. National Science Foundation

** Aerospace Engineering Department, Pennsylvania State University

*** NSF Research Experiences for Undergraduates (REU) Awardee

**** NASA Graduate Trainee, Pennsylvania State University

The question of exactly how much energy is transferred by antiproton annihilation is essential to these considerations. In the case of antiprotons at rest, the annihilation takes place on the nuclear surface, resulting in a geometrical efficiency of $\sim 28\%$ for pions to transfer energy to a uranium nucleus [13]. The geometrical efficiency for in-flight annihilation is expected to approach unity with increasing antiproton energy due to penetration of the nucleus before annihilation. A recent prediction [9] for molybdenum shows that a factor of ~ 5 increase in E^* is expected at ~ 3 GeV/c antiproton momentum compared to at rest.

The measurement of the energy transfer can be accomplished in two fundamental ways. First, one may chose to sum up the measured energies of all final state particles, apart from pions. This is difficult, due to the fact that no one experiment has measured full energy spectra and yields for all participants (nucleons, light nuclei and heavy residual nuclei) in a single nucleus, and attempts to sum over several different experiments would lead to significant systematic errors. We have, instead, chosen to measure the degraded energy spectrum of gamma-rays (and hence pi-zeros, neglecting the $2.7 \pm 0.4\%$ [14] and $2.7 \pm 0.9\%$ [15] contributions from $\eta \to \gamma\gamma$ and $\omega^0 \to \pi^0 \gamma$ respectively), which when subtracted from the spectrum of undegraded gamma-rays from a hydrogen target used in the same experiment gives the pi-zero energy transfer directly.

2. Experimental Details

The experiment was performed with a magnetic pair spectrometer at LEAR. Results on gamma-ray spectra from a liquid hydrogen target over the range 50–800 MeV have been published previously [16]. Hence, the spectrometer and other detectors external to the target will not be discussed here. However, the target region was modified considerably [1, 2]. Two targets, carbon and uranium, were each exposed to $\sim 10^9$ antiprotons, which were decelerated in a thin carbon degrader from 350 to ~ 200 MeV/c before striking the target. The uranium target was disk-shaped, 2 mm thick and 35 mm in diameter, and was rotated $\sim 45°$ around a vertical axis to expose the thin dimension to the spectrometer. The carbon target was rectangular, 5 mm thick by 20 mm wide by 50 mm long, and again was positioned to expose the thin dimension to the spectrometer. The liquid hydrogen target, which was filled at this time with deuterium, was moved downstream along the beam direction (X) as far as possible, permitting the nuclear target to be positioned close ($X = -11$ cm) to the magnet center

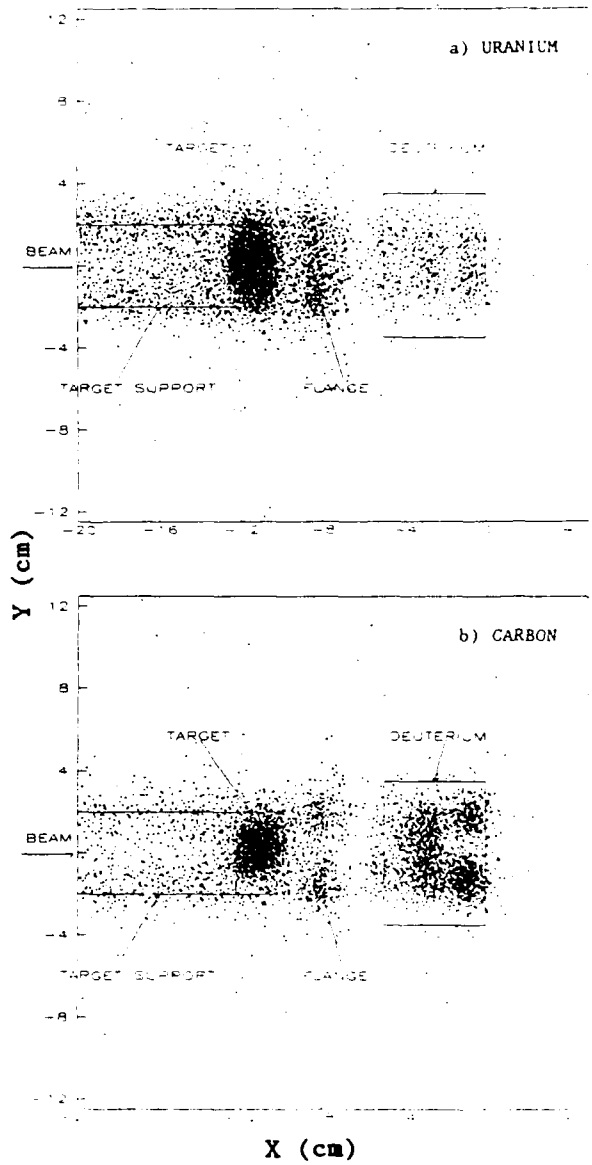

Fig. 1a and b. Elevation (XY) profiles of annihilation vertices for **a** uranium and **b** carbon. Only events with $\Delta Z = \pm 2$ cm around the nominal beam position are shown. Features of the targets and their support structures, as well as the liquid deuterium target (flange, deuterium) are outlined. Beam counters $S1, 2$ at $X = -42$ cm are not shown

line ($X = 0$). Monte Carlo calculations were made to determine the gamma-ray acceptance for a source displaced from the symmetry axis of the magnet.

Charged particles reconstructed in the drift chambers [16] around the target were used to survey the target and structures surrounding it. In Fig. 1 we show the elevation (XY) projection for annihilation vertices reconstructed to be ± 2 cm in Z around the nominal beam position for the (a) uranium and (b)

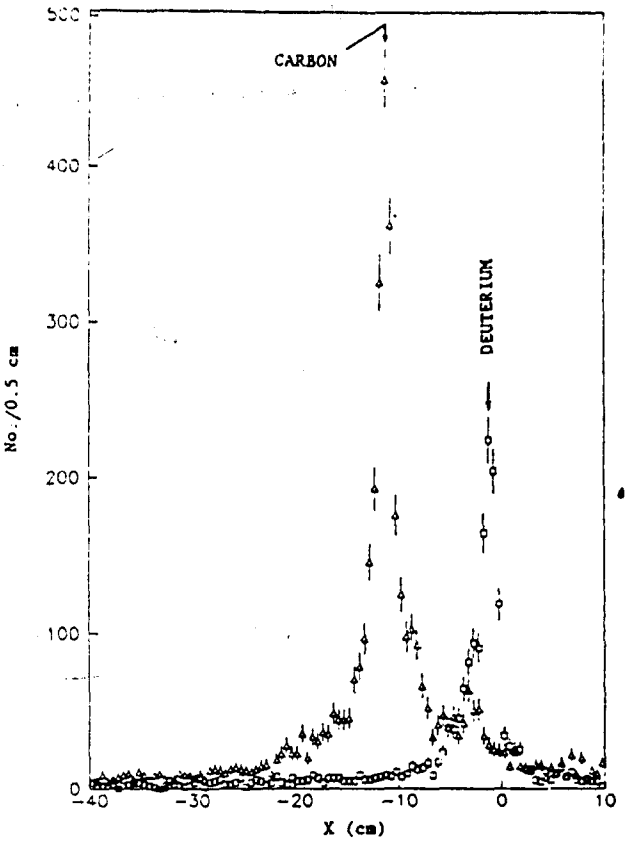

Fig. 2. Beam direction (X) vertex profiles of the carbon target arrangement selected by time-of-flight from beam counters $S1$, 2 to the Q-counter behind the radiator. Events from carbon (△) and deuterium (□) are indicated

carbon targets. One clearly sees annihilations in the uranium and carbon targets (and the thin cylindrical support structures which were coaxial with the beam upstream of the targets). In addition, interactions are seen in the flange on the upstream end of the vacuum vessel which contained the deuterium-filled flask, as well as in the deuterium itself. Interactions in the flange and the deuterium resulted from antiprotons which failed to hit the nuclear target due to scattering in two beam counters $S1, 2$ (each 2 mm thick) located upstream at $X = -42$ cm (not shown in Fig. 1). The two structures at $X = -1$ cm and -3 cm in the deuterium are due to antiprotons which were degraded in one or both of $S1, 2$.

We have used signals from $S1$, 2 and the Q-counter behind the lead converter in the spectrometer to reconstruct by time-of-flight the X-coordinate of the annihilation vertex. As an example, the profile of reconstructed vertices for the carbon target is shown in Fig. 2. The carbon peak seen at $-12.2 \leqq X \leqq -10.2$ cm, resulting from a cut $\Delta t = 7.5 \pm 0.6$ ns, is cleanly separated from the deuterium peak at $-5 \leqq X \leqq 0$ cm ($\Delta t = 9.2 \pm 0.6$ ns). Only a hint of the flange is seen at $X = -9$ cm. Similar results were obtained for the uranium target.

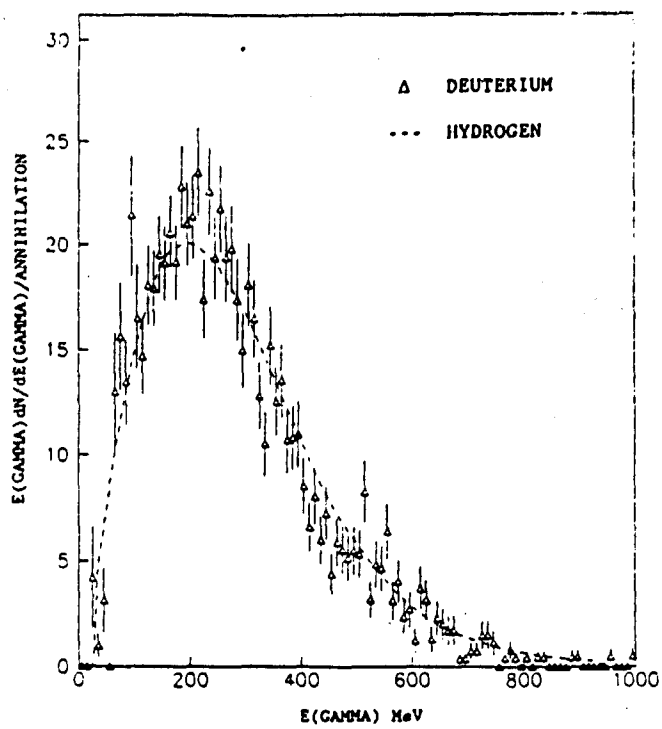

Fig. 3. Energy-weighted spectra of gamma-rays from liquid deuterium (this expt. – △) and liquid hydrogen (Ref. 17 ---)

In order to cancel systematic errors when taking differences of uranium-hydrogen and carbon-hydrogen spectra, we have chosen to use as a basis for comparison deuterium data taken during the carbon runs, In addition, our previous work [16] did not include very low energy ($\lesssim 50$ MeV) gamma-rays, whereas they are included in the present analysis. We show in Fig. 3 the reconstructed energy-weighted spectrum of gamma-rays from deuterium. The dashed curve is taken from Adiels et al. [17], who have measured the gamma-ray spectrum from liquid hydrogen in another experiment at LEAR. Each spectrum is normalized to 3.8 gamma-rays per event as reported in [17]. The agreement of the shapes of the two spectra, as well as their mean values $\langle E(\mathrm{GAMMA})\rangle$ shown in Table 1, is good and confirms our reconstruction of gamma-rays for the new target configuration. For reasons of statistical accuracy, we hereafter use the spectrum of [17] for comparisons with our nuclear target spectra.

3. Results

We show in Fig. 4 the energy-weighted spectra for carbon and uranium from this experiment, as well as hydrogen from [17]. One sees a systematic trend for the uranium data to fall below the hydrogen data by ~30% on the average. The carbon data are very

Table 1. Summary of values of average number of gamma-rays per annihilation (col. 1), average energy per gamma-ray (col. 2), average total energy of gamma-rays (col. 3) and energy transfer from pi-zeros (col. 4) for liquid deuterium, liquid hydrogen, carbon and uranium targets. Unless otherwise indicated, all values are from this experiment

	$\langle M(\text{GAMMA})\rangle$	$\langle E(\text{GAMMA})\rangle$ MeV	$\langle E(\text{TOTAL})\rangle^0$ MeV	$\langle E(\text{TRANSFER})\rangle^0$ MeV
Deuterium	3.8	198 ± 1	752 ± 4	–
Hydrogen [17]	3.8	194	737	–
Carbon	3.62 ± 0.22	196 ± 1	709 ± 43	28 ± 43
Uranium	2.73 ± 0.18	185 ± 1	505 ± 33	232 ± 33

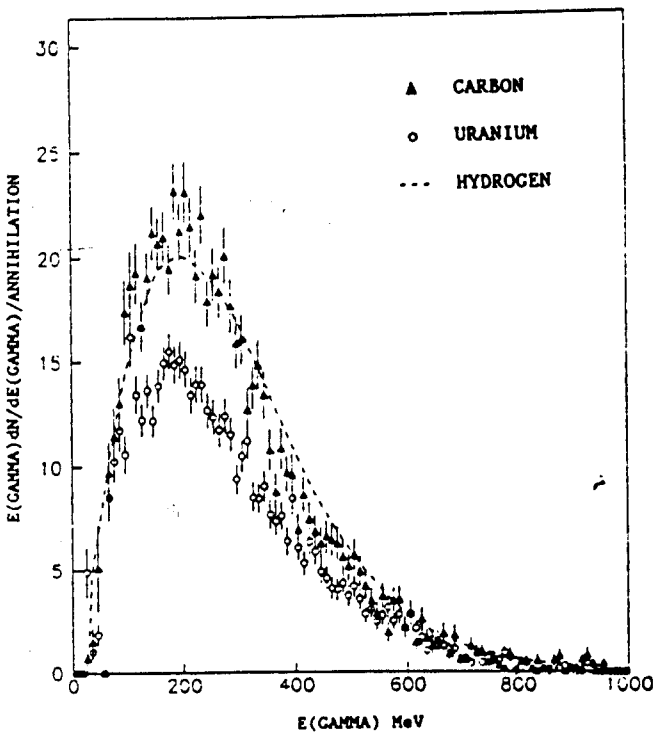

Fig. 4. Energy-weighted spectra of gamma-rays from carbon (this expt. – ▲), uranium (this expt. – o) and liquid hydrogen (Ref. 17 ---)

nearly the same as hydrogen. The spectra of Fig. 4 are summarized in Table 1. The quantity $\langle E(\text{TRANSFER})\rangle^0$ is defined as $\langle E(\text{TOTAL})\rangle^0_H - \langle E(\text{TOTAL})\rangle^0_A$, where $\langle E(\text{TOTAL})\rangle^0 = \langle M(\text{GAMMA})\rangle * \langle E(\text{GAMMA})\rangle$.

The absolute yield of gamma-rays, $\langle M(\text{GAMMA})\rangle$, was determined from measured yields of charged particles, $Y_i(p)$, identified in the spectrometer by time-of-flight [18], as well as the differential multiplicity of these particles, $\mathrm{d}M_i/\mathrm{d}p$, which when integrated over the particle's momentum p and species ($i=e^\pm, \pi^\pm, K^\pm, p$ and d) is the multiplicity, M, measured in the cylindrical wire chamber (CWC) [1] surrounding the target. These quantities are related as follows:

$$Y_i(p) = N(\bar{p}) * \mathrm{d}M_i/\mathrm{d}p * Acc_i(p), \tag{1}$$

where $N(\bar{p})$ is the number of antiprotons which annihilate in the target and $Acc_i(p)$ is the calculated acceptance of the spectrometer. The average value of M is constrained by the relationship

$$\langle M\rangle = \sum_i \langle M_i\rangle, \tag{2}$$

where $\langle M\rangle$ is an experimental observable. Equation (1), eight in number for each species, and (2) are then solved for nine unknowns, including $N(\bar{p})$ and $\langle M_i\rangle$. The values of $\langle M(\text{GAMMA})\rangle$ for carbon and uranium shown in Table 1 have been determined by dividing the number of observed gamma-rays for each target, corrected for acceptance and absorption in the target, by $N(\bar{p})$. This absorption was calculated to be 2–3% (15–25%) in the carbon (uranium) targets, averaged over all angles. We note that $\langle E(\text{TRANSFER})\rangle^0$ for uranium is slightly more than eight times larger than that for carbon.

Table 2. Summary of average numbers of pions per annihilation for carbon and uranium targets from this experiment

	$\langle M(\pi^+)\rangle$	$\langle M(\pi^-)\rangle$	$\langle M(\pi^0)\rangle$ [a]
Carbon	1.25 ± 0.06	1.61 ± 0.05	1.81 ± 0.11
Uranium	1.05 ± 0.05	1.52 ± 0.05	1.36 ± 0.09

[a] One-half of $\langle M(\text{GAMMA})\rangle$ values from Table 1

4. Discussion

In order to compare our results with predictions from INC calculations, we have estimated $\langle E(\text{TRANSFER})\rangle^{\pm,0}$ from all pions by using values of $\langle M_i\rangle$ for $\pi^{\pm,0}$ determined in this experiment (see Table 2), assuming that the ratio $\langle E(\pi^\pm)\rangle/\langle E(\pi^0)\rangle$ is the same in the nuclear targets as in hydrogen. The analysis of charged pion spectra will be published at a future date, at which time this assumption will be checked in detail. We note that our carbon values of $\langle M(\pi^+)\rangle = 1.25\pm0.06$ and $\langle M(\pi^-)\rangle = 1.61\pm0.05$ are in excellent agreement with previously published values of Agnew et al. [19] (1.35 ± 0.12, 1.50 ± 0.10), Bugg et al. [20] (1.22 ± 0.02, 1.57 ± 0.02) and Wade

et al. [21] (1.19 ± 0.06, 1.53 ± 0.07). Our value of $\langle M(\pi^0)\rangle = 1.81 \pm 0.11$ is ~ 2 standard deviations larger than that from [19] (1.15 ± 0.30). The nearest comparable measurement for uranium ($\langle M(\pi^+)\rangle = 1.05 \pm 0.05$, $\langle M(\pi^-)\rangle = 1.52 \pm 0.05$) is for lead from [19] (0.95 ± 0.02, 1.49 ± 0.03).

By definition,

$$\langle E(\mathrm{TRANSFER})\rangle^{\pm,0} = 1876.6\ \mathrm{MeV} - \langle E(\mathrm{TOTAL})\rangle_A^{\pm,0}, \quad (3)$$

where

$$\langle E(\mathrm{TOTAL})\rangle^{\pm,0} = 2\langle M(\pi^0)\rangle\langle E(\mathrm{GAMMA})\rangle + \langle M(\pi^\pm)\rangle\langle E(\pi^\pm)\rangle, \quad (4)$$

$$\langle E(\pi^\pm)\rangle_A = \frac{\langle E(\mathrm{GAMMA})\rangle_A}{\langle E(\mathrm{GAMMA})\rangle_H} * \langle E(\pi^\pm)\rangle_H, \quad (5)$$

and $\langle E(\pi^\pm)\rangle_H = 378$ MeV [22]. Substituting from Tables 1 and 2, we find $\langle E(\mathrm{TRANSFER})\rangle^{\pm,0} = 75 \pm 53$ MeV, 447 ± 42 MeV for carbon and uranium respectively.

We have compared our uranium measurement with the prediction of Jasselette et al. [13], who predict $\langle E(\mathrm{TRANSFER})\rangle^{\pm,0}$ to be ~ 380 MeV, in approximate agreement with our value of 447 ± 42 MeV. We note that the prediction can be made compatible with the measured value if the solid angle of the nucleus as seen by the antiproton at annihilation is increased by approximately 36%. This suggests that the atomic physics portion of the calculation may not be completely understood. We are unaware of any predictions for carbon, but note that the prediction for the nearby nucleus oxygen from [13] of ~ 260 MeV is much larger than our measured value of 75 ± 53 MeV for carbon. Using the results of [19] for carbon, we calculate $\langle E(\mathrm{TRANSFER})\rangle^{\pm,0}$ to be 430 ± 206 MeV. Unfortunately, the error on this value makes it compatible with both our measurement for carbon and the prediction for oxygen.

5. Conclusions

We have measured the energy transfer by pi-zeros in the INC by antiproton annihilation at rest in carbon and uranium. Extrapolating to all pions, we estimate $\langle E(\mathrm{TRANSFER})\rangle^{\pm,0}$ to be $\sim 17\%$ larger than the prediction of [13] for uranium. A similar estimate for carbon is in disagreement with a prediction for oxygen [13]. Unfortunately, to the best of our knowledge no predictions for carbon are available in the literature.

These results indicate that one may expect substantially increased energy transfer at higher antiproton momenta involving heavy nuclei. Using estimates for E^* by Iljinov et al. [23] and Cugnon et al. [24] of ~ 180 MeV for lead, and scaling E^* by a factor of five to 3 GeV/c antiproton momentum according to the estimate of [9] for molybdenum, one may expect E^* to reach a value of ~ 900 MeV, or $E^*/A \sim 4$–5 MeV. Therefore, the prospects for observing multifragmentation and disintegration of heavy nuclei under these conditions seem good.

References

1. Angelopoulos, A., Apostolakis, A., Armstrong, T.A., Bassalleck, B., Bueche, G., Fero, M., Gee, M., Graf, N., Koch, H., Lewis, R.A., Mandelkern, M., Papaelias, P., Poth, H., Rozaki, H., Sakellioui, L., Schultz, J., Schwertel, J., Smith, G.A., Usher, T., Wolfe, D.M.: Phys. Lett. **205** B, 590 (1988)
2. Armstrong, T.A., Bishop, R., Harris, V., Lewis, R.A., Minor, E., Smith, G.A.: Z. Phys. A – Atomic Nuclei **331**, 519 (1988)
3. McGaughey, P.L., Bol, K.D., Clover, M.R., DeVries, R.M., DiGiacomo, N.J., Kapustinsky, J.S., Sondheim, W.E., Smith, G.R., Sunier, J.W., Yariv, Y.: Phys. Rev. Lett. **56**, 2156 (1986)
4. Garreta, D., Birien, P., Bruge, G., Chaumeaux, A., Drake, D.M., Janouin, S., Legrand, D., Lemaire, M.C., Mayer, B., Pain, J., Peng, J.C., Berrada, M., Bocquet, J.P., Monnand, E., Mougey, J., Perrin, P., Aslanides, E., Bing, O., Erell, A., Lichtenstadt, J., Yavin, A.I.: Antiproton 1984. Pennington, M.R. (ed.), p. 187. Bristol: Adam Hilger 1985
5. Markiel, W., Daniel, H., v. Egidy, T., Hartmann, F.J., Hofmann, P., Kanert, W., Plendl, H.S., Ziock, K., Marshall, R., Machner, H., Riepe, G., Reidy, J.J.: Nucl. Phys. A **485**, 445 (1988)
6. Balestra, F., Bossolasco, S., Bussa, M.P., Busso, L., Ferrero, L., Grasso, A., Panzieri, D., Piragino, G., Tosello, T., Bendiscioli, G., Filippini, V., Fumagalli, G., Marciano, C., Rotondi, A., Zenoni, A., Guaraldo, C., Maggiora, A., Batusov, Yu.A., Falomkin, I.V., Pontecorvo, G.B., Sapozhnikov, M.G., Vascon, M., Zanella, G., Lodi Rizzini, E.: Nucl. Phys. A **452**, 573 (1986)
7. Balestra, F., Bossolasco, S., Bussa, M.P., Busso, L., Ferrero, L., Panzieri, D., Piragino, G., Tosello, T., Barbieri, R., Bendiscioli, G., Rotondi, A., Salvini, P., Zenoni, A., Batusov, Yu.A., Falomkin, I.V., Pontecorvo, G.B., Sapozhnikov, M.G., Tretyak, V.I., Guaraldo, C., Maggiora, A., Lodi Rizzini, E., Haatuft, A., Halsteinslid, A., Myklebost, K., Olsen, J.M., Breivik, F.O., Jacobsen, T., Sorensen, S.O.: CERN preprint EP/88-68 (June 1988), Nucl. Phys. A (submitted)
8. Moser, E.F., Daniel, H., v. Egidy, T., Hartmann, F.J., Kanert, W., Schmidt, G., Nicholas, M., Reidy, J.J.: Phys. Lett. **179** B, 25 (1986)
9. Cugnon, J.: Proceedings of the IV European Symposium on Antiproton-Proton Interactions and Fundamental Symmetries, Mainz, West Germany, Sept. 5–10, 1988, Nucl. Phys. A (to appear)
10. Guaraldo, C.: Physics at LEAR with Low Energy Antiprotons. Amsler, C., Backenstoss, G., Klapisch, R., Leluc, C., Simon, D., Tauscher, L. (eds.), p. 797. Switzerland: Harwood Academic 1988; Proceedings of the IV European Symposium on Antiproton-Proton Interactions and Fundamental Symmetries, Mainz, West Germany, Sept. 5–10, 1988, Nucl. Phys. A (to appear)
11. Golubeva, Ye.S., Iljinov, A.S., Botvina, A.S., Sobolevsky, N.M.: Nucl. Phys. A **483**, 539 (1988)

12. Botvina, A.S., Iljinov, A.S., Mishustin, I.N., Bondorf, J.P., Donangelo, R., Sneppen, K.: Nucl. Phys. A **475**, 663 (1987)
13. Jasselette, P., Cugnon, J., Vandermeulen, J.: Nucl. Phys. A **484**, 542 (1988)
14. Chiba, M., Doi, K., Fujitani, T., Iwahori, J., Kawaguti, M., Kobayashi, M., Koike, M., Kozuki, T., Kurokawa, S., Kusumoto, H., Nagano, H., Nagashima, Y., Omori, T., Sugimoto, S.M., Takasaki, M., Takeutchi, F., Tsuchiya, M., Ueda, M., Yamaguchi Y., Yoshida, H.: Physics at LEAR with Low Energy Antiprotons, Amsler, C., Backenstoss, G., Klapisch, R., Leluc, C., Simon, D., Tauscher, L. (eds.), p. 401. Switzerland: Harwood Academic 1988
15. Levman, G., Singer, R., Fields, T.: Phys. Rev. D **21**, 1 (1980)
16. Angelopoulos, A., Apostolakis, A., Armstrong, T.A., Bassalleck, B., Biard, J., Bueche, G., Denes, P., Fero, M., Graf, N., Hill, R., Koch, H., Komninos, N., Lewis, R.A., Mandelkern, M., Papaelias, P., Playfer, S.M., Ray, R., Rohrbach, W., Rozaki, H., Sakelliou, L., Schultz, D., Schultz, J., Smith, G.A., Soulliere, M.J., Spyropoulou-Stassinaki, M., Usher, T., Walther, D., Willuhn, K., Wolfe, D.M.: Phys. Lett. B **178**, 441 (1986)
17. Adiels, L., Backenstoss, G., Bergström, I., Carius, S., Charalambous, S., Cooper, M.D., Findeisen, Ch., Hatzifotiadou, D., Kerek, A., Pavlopoulos, P., Repond, J., Tauscher, L., Tröster, D., Williams, M.C.S., Zioutas, K.: Phys. Lett. **182** B, 405 (1980)
18. Smith, G.A.: The Elementary Structure of Matter, Richard, J.-M., Aslanides, E., Boccara, N. (eds.), p. 197. Springer Proceedings in Physics, No. 26. Berlin, Heidelberg, New York: Springer 1988
19. Agnew, Jr., L.E., Elioff, T., Fowler, W.B., Lander, R.L., Powell, W.M., Segrè, E., Steiner, H.M., White, H.S., Wiegand, C., Ypsilantis, T.: Phys. Rev. **118**, 137 (1960)
20. Bugg, W.M., Condo, G.T., Hart, E.L., Cohn, H.O., McCulloch, R.D.: Phys. Rev. Lett. **31**, 475 (1973)
21. Wade, M., Lind, V.G.: Phys. Rev. D **14**, 1162 (1976)
22. Roy, J.: Proceedings IV International Symposium on Nucleon-Antinucleon Interactions. Kalogeropoulos, T., Wali, K.C. (eds.), p. III.1. New York: Syracuse University 1975
23. Iljinov, A.S., Nazaruk, V.I., Chigrinov, S.E.: Nucl. Phys. A **382**, 378 (1982)
24. Cugnon, J., Jasselette, P., Vandermeulen, J.: Nucl. Phys. A **470**, 558 (1987)

T.A. Armstrong, R.A. Lewis, G.A. Smith
Department of Physics
Laboratory for Elementary
Particle Science
303 Osmond Laboratory
Pennsylvania State University
University Park, PA 16802
USA

R. Bishop
Aerospace Engineering Department
Pennsylvania State University
University Park, PA 16802
USA

V. Harris
NSF Research Experiences for
Undergraduates (REU) Awardee

E. Minor
NASA Graduate Trainee
Pennsylvania State University
University Park, PA 16802
USA

Z. Phys. A - Atomic Nuclei 336, 461–468 (1990)

APPENDIX IV

Zeitschrift für Physik A
Atomic Nuclei
© Springer-Verlag 1990

Charged pion spectra and energy transfer following antiproton annihilation at rest in carbon and uranium *

E.D. Minor **, T.A. Armstrong, R. Bishop *, V. Harris ****, R.A. Lewis, and G.A. Smith**

Laboratory for Elementary Particle Science, Department of Physics, 303 Osmond Laboratory, Pennsylvania State University, University Park, Pennsylvania, USA

Received December 13, 1989

The momentum spectra of charged pions following antiproton annihilation at rest in carbon and uranium have been measured. This information complements our previous measurement of the neutral pion spectra. The total charged pion multiplicity is 2.84 ± 0.10 and 2.47 ± 0.09 for carbon and uranium, respectively, in good agreement with recent INC model predictions of 2.96 and 2.48 for the same quantities. However, structures predicted by the model near 200 MeV/c and 300 MeV/c related to delta-resonance production are not seen in the data. The total energy transfers to the nucleus are calculated to be 119 ± 59 MeV(carbon) and 455 ± 50 MeV(uranium). The possibility of exciting multifragmentation with a $\bar{p}$ beam impinging on heavy nuclei is discussed.

PACS: 13.75.Cs; 21.10.Dr; 24.90.+d

1. Introduction

In a previous paper [1] we presented the yield and energy spectra of gamma-rays following the annihilation at rest of antiprotons in carbon and uranium. Assuming that the ratio of the average charged pion energy to the average neutral pion energy is the same in nuclear targets as in hydrogen, we were able to estimate the total energy transfer to the nucleus following annihilation. In this paper we present, for the first time, our measurements of the charged pion spectra and energy transfer without approximation.

These measurements also provide new information on annihilation at rest in heavy targets and extend similar investigations which began in the 1950's [2–7]. More recent measurements at LEAR of pion spectra and multiplicities have been performed for a variety of target nuclei, including carbon and uranium [8], helium and neon [9], and nitrogen [10]. A recent review of these results and others has been presented by Guaraldo [11]. Theoretically, the effort to understand these measurements has focussed primarily on development of the intranuclear cascade model (INC). Using this model, predictions for pion spectra have been made by Clover et al. [12], Cugnon et al. [13], Hernandez and Oset [14], and Iljinov et al. [15]. Cugnon [16] has recently reviewed theoretical developments in this regard.

As pointed out by Jasselette et al. [17], for antiproton annihilation at rest on nuclear targets, the dissipation of the residual energy E^* following the INC is characterized by competition among various processes. For example, in ^{238}U, fission is predicted to dominate and evidence demonstrating this behavior has been observed [18]. Using a statistical approach, Botvina et al. [19] predict the breakup of the nucleus into a few heavy fragments, when it acquires a residual energy, $E^*/A = 3$ MeV/nucleon. Further, they note that the peak in their residual mass distribution widens with increasing residual energy, finally evolving, at $E^*/A = 5$ MeV/nucleon, into a distribution sharply peaked at $A < 10$ and monotonically decreasing with increasing mass of the fragment. Independently, Cugnon [16], using an INC model, has predicted the onset of multifragmentation phenomena for $E^*/A > 3$ MeV/nucleon. Critical to the issue of multifragmentation, however, are the questions of how much energy is transferred to the nucleus by the intranuclear cascade and how thoroughly the energy is thermalized. These points will be explored in this paper, and the experimental conditions necessary to excite the multifragmented state will be discussed.

2. Experimental details

The experiment has been described previously in a series of publications providing details of the nuclear targets

* Work supported in part by the Air Force Office of Scientific Research, Air Force Systems Command, USAF under grant AFOSR 87-0246 and the U.S. National Science Foundation
** NASA Graduate Trainee, Pennsylvania State University
*** Aerospace Engineering Department, Pennsylvania State University
**** NSF Research Experiences for Undergraduates (REU) Awardee

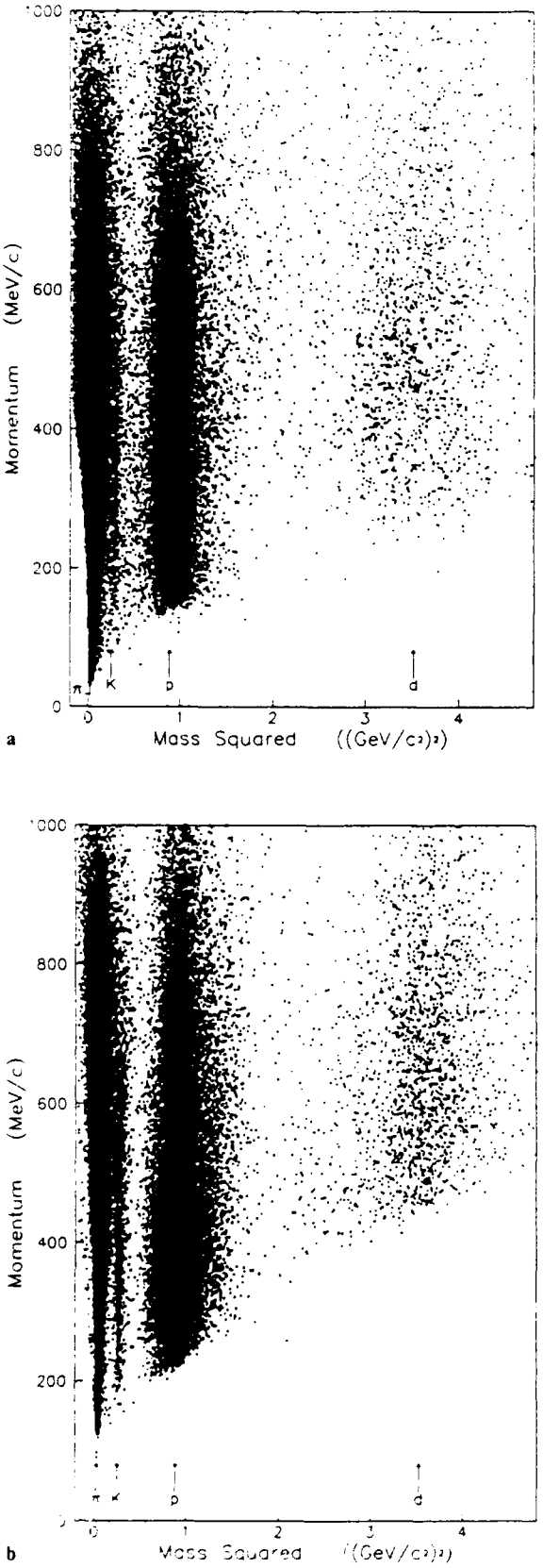

Fig. 1a, b. Momenta measured with the spectrometer vs. mass-squared for uranium target events for (**a**) T-tracks and (**b**) P-tracks

and the detector which are the subject of this paper [1, 18, 20]. The description here will consequently be brief, except for unique features relevant to the present analysis. Previously, we have shown preliminary results for charged particles having sufficiently high momentum to penetrate the entire length of the magnetic spectrometer (P-tracks) [21]. In this paper, we also include those pions incident on the magnet yoke (T-tracks) in order to lower the momentum region studied to 100 MeV/c. To illustrate the quality of these tracks, Figs. 1 and 2 show the momentum measured in the spectrometer versus the calculated m^2 for T- and P-tracks in uranium and carbon, respectively. Vertical bands corresponding to pions, kaons, protons, and deuterons are clearly seen. Pions and kaons are well separated for $P(T)$ tracks below $\approx 600(400)$ MeV/c. Contamination of kaons in the pion samples is estimated to be $\approx 0.3(0.8)\%$ above these values.

The mass of a particle is related to parameters measured in the spectrometer as

$$m^2 = p^2 \left(\frac{(t+\delta t)^2}{s^2} c^2 - 1 \right), \tag{1}$$

where t and s refer to the measured time of flight and path length between the A hodoscope and the D, E, or P counter which the particle hits. A small correction δt is calculated in order to account for the change in the particle's momentum over its path length due to dE/dx effects. The mass resolution can be explained in terms of timing resolution (400 ps rms) and momentum resolution. The latter contains a component due to spatial resolution in the wire planes (860 μm rms) and another due to Coulomb scattering.

Using these parameters, the expected resolution in m^2 at various momenta have been calculated. It is found that timing dominates the mass resolution for pions and kaons. For protons, spatial resolution (Coulomb scattering) dominates at low momenta, while spatial and timing resolution are comparable at higher momenta. Projections of the uranium m^2 distributions are shown for different momenta intervals in Fig. 3. Gaussian curves, computed using the resolutions discussed above, have been superimposed for pions and protons, and for kaons where the band is distinct. These curves explain the gross features of the data except for the tails of the measured distributions. These tails are due to the nature of Moliere scattering, for which the Gaussian approximation is valid only near the center of the distribution.

The momentum measured inside the spectrometer was extrapolated back to the annihilation point, using the Bethe-Bloch formula [22], through the various materials between the target center and the spectrometer. These materials comprised $\approx 0.18\, X_0$ for the carbon target and $\approx 0.31\, X_0$ for the uranium target, the difference being due to the target materials themselves. Once the particle was identified, its true mass and measured momentum were used to obtain a velocity for Bethe-Bloch calculations. In traversing this region, pions lost, on average, 10.8 MeV. For particles emerging on a trajectory lying within or very near the plane of the target, the

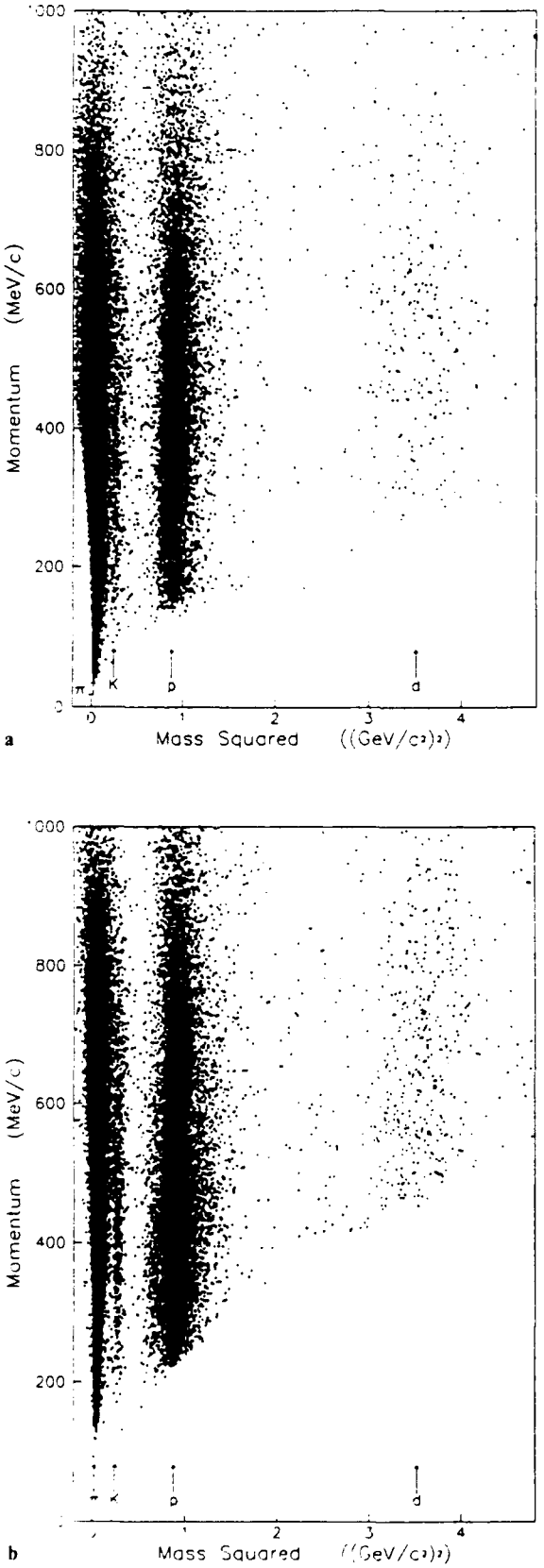

Fig. 2a, b. Momenta measured with the spectrometer vs. mass-squared for carbon target events for (**a**) *T*-tracks and (**b**) *P*-tracks

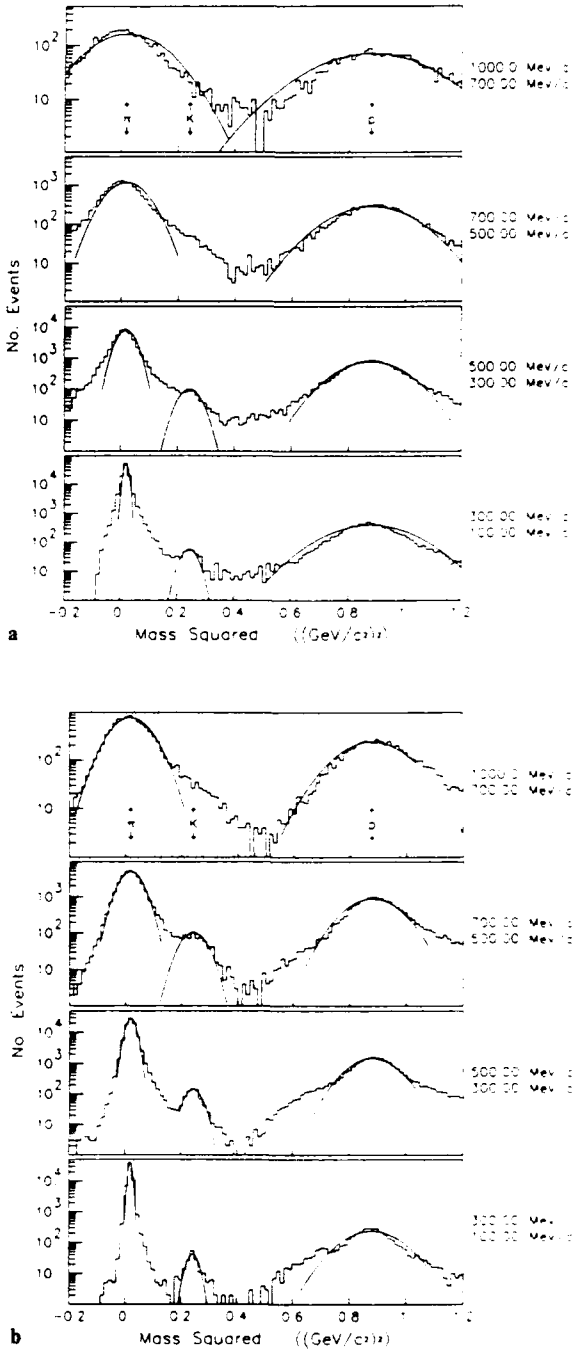

Fig. 3a, b. Mass-squared distributions for various momentum ranges for uranium (**a**) *T*-tracks and (**b**) *P*-tracks. The gaussian curves superimposed are predicted shapes based on timing and momentum resolution. The momentum ranges are specified to the right of each plot

track passed through as much as 2 cm of uranium and this correction could be very large (≈ 100 MeV). Since the annihilation point along the plane of the target was not determined, the correction could not be accurately established. Consequently, tracks which subtended an angle smaller than 5.5^0 with the plane of the target were discarded.

Only events whose vertex was located between $X = -14.5$ and $X = -10.0$ cm, where X is along the beam line, were accepted [1]. These limit assured that spurious events emanating from the nearby materials were rejected, resulting in a signal: background ratio of $\approx 20:1$ while accepting $\approx 89\%$ of the signal. The final spectra were corrected for the acceptance of the spectrometer. A Monte Carlo analysis indicated that $\approx 10\%$ of the pions decayed in flight via $\pi^{\pm} \rightarrow \mu^{\pm} \nu$ and could not be resolved in the detector, but no appreciable change to the apparent pion momentum spectra was observable in the momentum range studied (100–1000 MeV/c). The technique for normalizing yields is described in [1].

3. Results

In Table 1 we show our measured multiplicities for charged pions and photons, as well as measurements for hydrogen [23–25]. Relative to our previous determination [1], the gamma-ray multiplicity for carbon is 4.4% smaller due to an unforeseen correction for absorption in the target. For the most part, the photon multiplicity results from the decay $\pi^0 \rightarrow \gamma\gamma$, although small contributions are also present from $\eta \rightarrow \gamma\gamma$ ($2.7 \pm 0.4\%$ per annihilation) [26] and $\omega^0 \rightarrow \pi^0 \gamma$ ($2.7 \pm 0.9\%$ per annihilation) [27]. No corrections have been made for these contributions in calculating $\langle M(\pi^0) \rangle = \frac{1}{2} \langle M(\gamma) \rangle$. Hydrogen values have been included in order to demonstrate the effect of pion absorption in the nuclear environment. All multiplicities, with the one exception of π^- where the multiplicity increases slightly in going from hydrogen to carbon, are seen to decrease with increasing target mass, consistent with absorption effects within the target nuclei. The neutral/charged ratio is also constant to within 5% for all targets.

For annihilation on a proton compared to that on a neutron, the ratio

$$R_M = \frac{\langle M(\gamma) \rangle}{(\langle M(\pi^+) \rangle + \langle M(\pi^-) \rangle)} \tag{2}$$

is predicted to vary by only 5% [28]. Experimentally, one may use data for annihilation on neutrons and protons in deuterium [29] to check this prediction. If one assumes that the energy spectra of all pions are similar in shape, $R_M = 1.15 \pm 0.03$ for $\bar{p}n$ annihilations and 1.22 ± 0.02 for $\bar{p}p$ annihilations. Since nuclei are mixtures of protons and neutrons, it is expected that R_M will vary

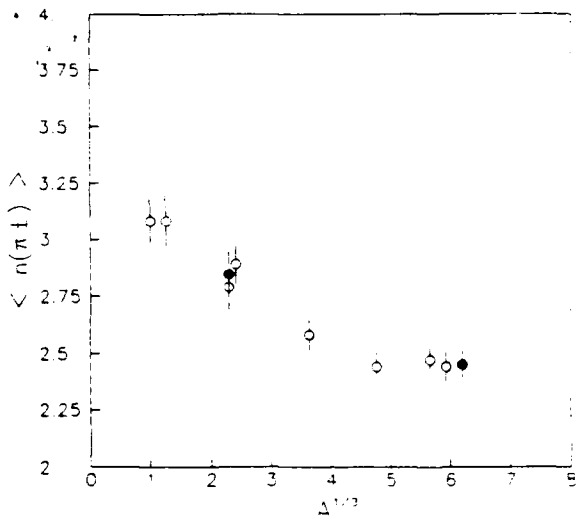

Fig. 4. Charged pion multiplicity versus the cube root of the mass number. In addition to our data, the following references are used: hydrogen [10, 23, 31], deuterium [10, 34], carbon [5, 32, 33], nitrogen [10], titanium [32], nuclear emulsion [2–4, 6, 7, 23] tantalum [32], lead [32]. Solid circles: our data; Open circles: other data

even less for such targets. We calculate, for deuterium, carbon, and uranium, respectively, $R_M = 1.19 \pm 0.02$, 1.22 ± 0.09, and 1.10 ± 0.09. These numbers agree within errors and place limits on effects due to charge exchange, as discussed in [10], and escape of excess neutral pions due to resonance formation (η, ω) [30]. The excess production of π^0's, relative to deuterium, is $0.7 \pm 2.7\%$ for carbon and $-1.6 \pm 2.8\%$ for uranium.

We compare our results to previous work in Fig. 4, where the total charged multiplicity is plotted against the cube root of the mass number of the target. Results from thirteen separate experiments [2–7, 10, 23, 31–34] are contained in this plot, some of which have been averaged into single data points. The agreement between our results and the other experiments is excellent. For neutral data, which are not shown in Fig. 4, we note that our measurement of $\langle M(\pi^0) \rangle = 1.73 \pm 0.11$ for carbon is $\approx$two standard deviations larger than that from Agnew et al. [5]: 1.15 ± 0.30. To the best of our knowledge, no comparable measurement is available for uranium.

Figure 5 shows our measured momenta spectra for π^+ and π^- for the two targets, uranium and carbon. Also plotted are π^+ spectra from McGaughey et al. [8] for the same targets, after interaction with 608 MeV/c antiprotons. The increased absorption for the inflight

Table 1. Total charged and neutral pion multiplicities. Hydrogen data are from [23–25]. Neutral data for carbon and uranium are from [1]. It is assumed that $\langle M(\pi^0) \rangle = \frac{1}{2} \langle M(\gamma) \rangle$. The first errors quoted are statistical, the second systematic

Target	$\langle M(\pi^+) \rangle$	$\langle M(\pi^-) \rangle$	$\langle M(\pi^{\pm}) \rangle$	$\langle M(\gamma) \rangle$	$\langle M(\pi^0) \rangle$	$\langle M(\pi^{\pm 0}) \rangle$
Hydrogen	1.52 ± 0.06	1.52 ± 0.06	3.04 ± 0.08	3.80 ± 0.24	1.90 ± 0.12	4.94 ± 0.14
Carbon	1.25 ± 0.01	1.59 ± 0.01	2.84 ± 0.01	3.46 ± 0.07	1.73 ± 0.04	4.57 ± 0.04
	± 0.06	± 0.08	± 0.10	± 0.21	± 0.10	± 0.15
Uranium	0.99 ± 0.01	1.48 ± 0.01	2.47 ± 0.01	2.73 ± 0.06	1.36 ± 0.03	3.84 ± 0.03
	± 0.05	± 0.08	± 0.09	± 0.18	± 0.09	± 0.13

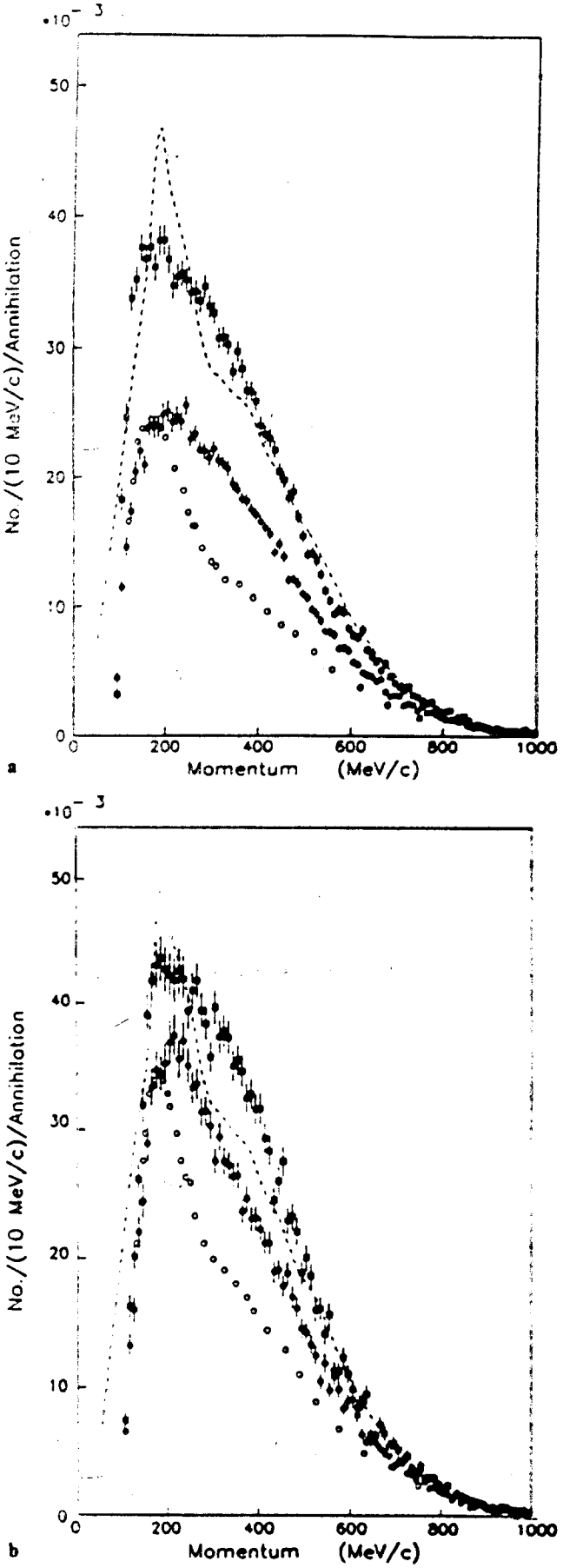

Fig. 5a, b. Charged pion yield per 10 MeV/c interval per annihilation for uranium (a) and carbon (b). Also shown are π^+ data from [8] and INC predictions for π^- from [14]. Solid squares: our π^- measurement; solid circles: our π^+ measurement; dashed line: π^- prediction from [14]; open circles: π^+ measurement from [8]

data results from the deeper penetration of the antiproton prior to annihilation and consequently greater interaction of the generated pions with the nuclear matter [17, 35]. The difference in the areas of these two sets of π^+ data is greater for the much larger uranium nucleus ($30 \pm 7\%$), but is still quite significant for the carbon target ($18 \pm 8\%$).

Also shown on Fig. 5 are the results of an INC model due to Hernandez and Oset [14]. The comparison here is for the π^- spectra only. On average, agreement between the model and the data is good. For all pions we find $\langle M(\pi^{\pm 0})\rangle = 4.57 \pm 0.16$(carbon) and 3.84 ± 0.13 (uranium), as given in Table 1. The comparable INC results are 4.64 (for carbon, where the annihilation has been assumed to occur from the $n=4$, $l=3$ state) and 3.90 (for uranium, with annihilation from the $n=9$, $l=8$ state). Prediction and measurement are in agreement to within 2%.

4. Discussion

a) The intranuclear cascade model

The excellent agreement between the measured and predicted total multiplicities does not extend to the shapes of the spectra, as seen in Fig. 5. Two regions of disagreement are apparent for either target. Near 300 MeV/c the INC model predicts a shoulder, due to delta-resonance formation leading to pion absorption [14], which is not seen in the data (π^-). Also, near 200 MeV/c, the INC predicts a sharp peak which is not seen. The population of the latter region is enhanced in the INC model by higher-momentum pions which have been degraded, either due to the afore-mentioned resonance scattering or quasi-elastic scattering. For the region above 500 MeV/c, where quasi-elastic scattering is the principle mechanism for pion interaction, there is excellent agreement between the INC and the data, suggesting that the latter mechanism is correctly implemented.

In order to check possible degradation of the spectra due to the detector's momentum resolution, we searched for the kaon decay lines:

$$K^+ \rightarrow \mu^+ \nu \qquad (236 \text{ MeV/c}) \tag{3}$$

and

$$K^+ \rightarrow \pi^+ \pi^0 \qquad (205 \text{ MeV/c}). \tag{4}$$

Events were selected for which the time of arrival of the particle at the A counter was in excess of 7 ns. For comparison, this time would be ≈ 4 ns. for a slow (400 MeV/c) proton. This cut removes most events, but not those for which a kaon comes to rest in the target or surrounding material and decays. These events are plotted in Fig. 6, which clearly shows two narrow structures due to these decays. Signals of this nature have been reported for this detector earlier [36]. The 10 MeV/c FWHM widths of these lines are much smaller than the ≈ 100 MeV/c wide structures predicted near 200 and 300 MeV/c in the INC [14]. Thus, such features in the data would not have been degraded by resolution effects.

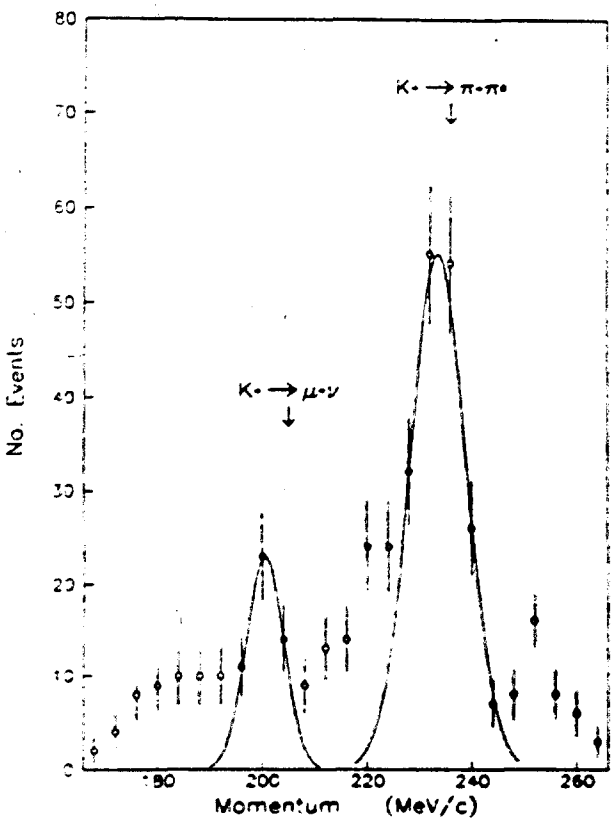

Fig. 6. Momentum spectrum of delayed positive tracks in uranium and carbon

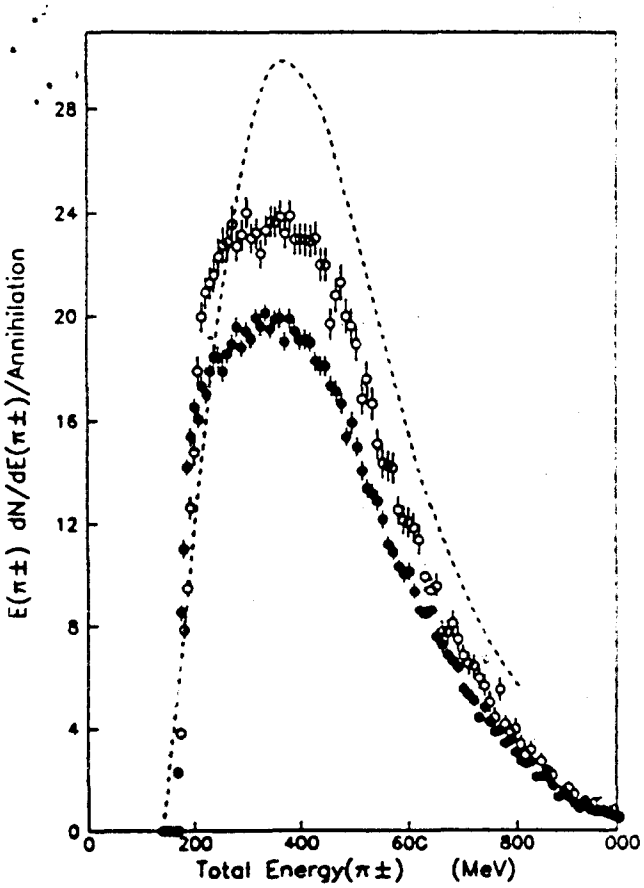

Fig. 7. Total energy yield (per 10 MeV interval) of charged pions for carbon (open circles), uranium (solid circles) and hydrogen [23, 24] (dashed line)

b) Energy transfer

The total energy released with each of the pion species is given by

$$\langle E(\mathrm{TOTAL})\rangle^{i} = \langle M(\pi^{i})\rangle\langle E(\pi^{i})\rangle,\ i=0,+,-, \tag{5}$$

where $\langle M(\gamma)\rangle\langle E(\gamma)\rangle = \langle M(\pi^{0})\rangle\langle E(\pi^{0})\rangle$. By definition,

$$\langle E(\mathrm{TRANSFER})\rangle^{\pm 0} = 1876.6 - \sum_{i}\langle E(\mathrm{TOTAL})\rangle^{i}, \tag{6}$$

where the total annihilation energy is equal to two proton masses.

The average multiplicities and energies appropriate to (5) are given in Table 2. The energy transfer represents energy released in the antiproton-nucleon annihilation which is deposited within the target nucleus through interaction with escaping pions. We calculate this quantity to be 119 ± 59 MeV for carbon. For the more extensive uranium nucleus, it is nearly three times as large, 455 ± 50 MeV. Our previous estimates, which involved approximations from scaling pion spectra using hydrogen data, were 75 ± 53 for carbon and 447 ± 42 for uranium. The effects of energy transfer from charged pions are clearly seen in Fig. 7. A similar plot for neutral pions was published previously [1]. For uranium, Jasselette et al. [17] give $\langle E(\mathrm{TRANSFER})\rangle^{\pm 0} \approx 380$ MeV, slightly smaller than our value. Hernandez and Oset [14] predict a value of 480 MeV, which expresses in a compact way the overall agreement between our data and their model. For carbon, they provide two numbers [14], depending on the atomic state from which the annihilation occurs: 271 MeV ($n=3, l=2$) and 217 MeV ($n=4, l=3$). The smaller of these numbers is nearly two standard deviations larger than our measurement.

Greater beam energy leads to greater penetration depth in the nucleus and consequently greater interaction of generated pions within the nucleus, thus resulting in a larger energy transfer. The effect is seen even as

Table 2. Mean charged pion and neutral gamma multiplicities and energies, total energy and energy transfer. Hydrogen data are from [23–25]. Neutral data for carbon and uranium are from [1]

Target	$\langle M(\gamma)\rangle$	$\langle E(\gamma)\rangle$	$\langle M(\pi^{\pm})\rangle$	$\langle E(\pi^{\pm})\rangle$	$\langle E(\mathrm{TOT})\rangle$	$\langle E(\mathrm{TRANS})\rangle$
Hydrogen	3.80 ± 0.24	194 ± 2	3.04 ± 0.08	395 ± 2	1938 ± 57	
Carbon	3.46 ± 0.22	196 ± 2	2.84 ± 0.10	380 ± 2	1758 ± 59	119 ± 59
Uranium	2.73 ± 0.19	184 ± 2	2.47 ± 0.09	372 ± 2	1422 ± 50	455 ± 50

low as 608 MeV/c. Using the data of [8] with multiplicities provided in [30], we calculate $\langle E(\text{TRANSFER})\rangle = 471 \pm 126$ MeV for carbon and 871 ± 84 MeV for uranium. In deriving these quantities, we have assumed that the ratio of neutral pions to charged pions is the same as for hydrogen to correct for the presence of π^0's. These numbers represent an increase in the energy transfer by a factor of 4.0 ± 2.2 for carbon and 1.9 ± 0.3 for uranium relative to data at rest. For either target, very significant increases in the energy transfer result from increasing the beam energy.

c) Multifragmentation

It is possible to estimate E^*, the residual energy retained by the nucleus following the fast intranuclear cascade (which terminates after $\approx 10^{-23}$ s). If the energy is thermalized, further evolution of the nucleus will depend mainly on E^*/A [16]. Our measurement of $\langle E(\text{TRANSFER})\rangle$ provides a first step toward the calculation of E^*, but lacks the correction for the energy carried off by nucleons ejected during the cascade. A number of publications have dealt with contributions to this correction. In particular, we have measured neutron spectra [18] from uranium. Markiel et al. [37] have published measurements of low-energy protons and light ions. McGaughey et al. [8] have measured protons following in-flight annihilations. Since none of these provides an inclusive mesurement, it is necessary to use an INC calculation for $W(EJ)$, the energy of nucleons ejected by the cascade process. Jasselette et al. [17] have calculated $W(EJ) = 274$ MeV for uranium. Thus, $E^* = \langle E(\text{TRANSFER})\rangle - W(EJ) \approx 181$ (MeV ≈ 0.8 MeV/nucleon, which is well below the region where multifragmentation is likely to occur.

In view of previously discussed energy transfers at 608 MeV/s [8], it is expected that E^* would increase with increasing beam momentum and consequently increasing penetration depth inside the nucleus. Cugnon [16] has used the INC model to show that E^* scales by a factor of five in ^{98}Mo as the beam kinetic energy is increased to 2 GeV. For an even heavier nucleus such as uranium, this would imply, from our measurement, E^*/A would be at least 4 MeV/nucleon, which is very near the multifragmentation regime.

Inducing multifragmentation using high-momentum antiproton beams is, however, a subject of some current debate. McGaughey et al. [38], using a different INC code [12], see no significant thermalization of the annihilation energy for 1.3 GeV antiprotons on a nucleus of atomic mass 100. They point out that primordial pions generated following such annihilations have too large an energy in order to immediately participate in Δ-resonance formation and absorption ($\pi N \to \Delta$, $\Delta N \to NN$). However, it is not clear from [38] how McGaughey et al. have treated these high-momentum πN interactions in detail. In this regard, it is worth noting that, in an article by some of the same authors [8], there is considerable disagreement between the model and the data for both pions and protons in the high momentum region, with the model underestimating the measurement by as much as a factor of five. Although different points of view exist on the question of thermalization for beam energies of 1–2 GeV, the possibility of multifragmentation following antiproton annihilation deep inside the nucleus seems nonetheless intriguing.

5. Conclusions

Our measurements, for the most part, agree with the current theoretical understanding of the problem (the INC model). The points of divergence are small, but nonetheless may be worth pursuing. It is not clear that these models suffer from technical or fundamental uncertainties, or both. Technical problems arise due to the complexity of the many-body problem. Approximations are made, for which the implications are not always clear. These include such choices as limiting the number of nucleons involved in the pion absorption process, choosing one method of integration over another, etc. Unfortunately, these technical questions are folded in with fundamental physics issues which one would like to solve. These would include elucidating the magnitude and nature of the optical potential and determining off-shell cross sections.

The possibility of exciting multifragmentation has been discussed. It would seem likely that increasing the antiproton beam energy to ≈ 2 GeV might provide us with an observation of this intriguing possibility. However, at least one reference [38] argues that the phenomenom will not occur. An appropriate experiment might thus serve two purposes: (1) assuming it were successful and the multifragmentation state were attained, it would usher in a new and exciting field of research; (2) in any case it would clearly decide the most realistic of two similar and yet somehow different INC codes, that due to Clover et al. [12] and that due to Cugnon et al. [39].

The authors are especially grateful to E. Hernandez and E. Oset, who provided unpublished calculations of multiplicities and momentum spectra for pions. Finally, we thank the staff of the CERN PS Division for their dedicated and skillful operation of LEAR during this experiment.

References

1. Armstrong, T.A., Bishop, R., Harris, V., Lewis, R.A., Minor, E.D., Smith, G.A.: Z. Phys. A – Atomic Nuclei 332, 467 (1989)
2. Barkas, W.H., Birge, R.W., Chupp, W.W., Ekspong, A.G., Goldhaber, G., Goldhaber, S., Heckman, H.H., Perkins, D.H., Sandweiss, J., Segrè, E., Smith, F.M., Stork, D.H., van Rossum, L., Amaldi, E., Baroni, G., Castagnoli, C., Franzinetti, C., Manfredini, A.: Phys. Rev. 105, 1037 (1957)
3. Amaldi, E., Baroni, G., Bellettini, G., Castagnoli, C., Ferro-Luzzi, M., Manfredini, A.: Nuovo Cimento 14, 977 (1959)
4. Chamberlain, O., Goldhaber, G., Jauneau, L., Kalogeropoulos, T., Segrè, E., Silberberg, R.: Phys. Rev. 113, 1615 (1959)
5. Agnew, L.E., Jr., Elioff, T., Fowler, W.B., Lander, R.L., Powell, W.M., Segrè, E., Steiner, H.M., White, H.S., Wiegand, C., Ypsilantis, T.: Phys. Rev. 118, 1731 (1960)
6. Berthelot, A., Choquet, C., Daudin, A., Goussu, O., Lévy, F.: Nuc. Phys. 14, 545 (1960)

7. Ekspong, A.G., Frisk, Å., Nilsson, S., Ronne, B.E.: Nucl. Phys. **22**, 353 (1961)
8. McGaughey, P.L., Bol, K.D., Clover, M.R., DeVries, R.M., DiGiacomo, N.J., Kapustinsky, J.S., Sondheim, W.E., Smith, G.R., Sunier, J.W., Yariv, Y., Buenerd, M., Chauvin, J., Lebrun, D., Martin, P., Dousse, J.C.: Phys. Rev. Lett. **56**, 2156 (1986)
9. Balestra, F., Bossolasco, S., Bussa, M.P., Busso, L., Ferrero, L., Panzieri, D., Piragino, G., Tosello, F., Barbieri, R., Bendiscioli, G., Rotondi, A., Salvini, P., Zenoni, A., Batusov, Yu.A., Falomkin, I.V., Pontecorvo, G.B., Sapozhnikov, M.G., Tretyak, V.I., Guaraldo, C., Maggiora, A., Rizzini, E.L., Haatuft, A., Halsteinslid, A., Myklebost, K., Olsen, J.M., Breivik, F.O., Jacobsen, T., Sörensen, S.O.: Nucl. Phys. A **491**, 541 (1989)
10. Riedlberger, J., Amsler, C., Doser, M., Straumann, U., Truöl, P., Bailey, D., Barlag, S., Gastaldi, U., Landua, R., Sabev, C., Duch, K.D., Heel, M., Kalinowsky, H., Kayser, F., Klempt, E., May, B., Schreiber, O., Weidenaurer, P., Ziegler, M., Dahme, W., Feld-Dahme, F., Schaefer, U., Wodrich, W.R., Ahmad, S., Bizot, J.C., Delcourt, B., Jeanjean, J., Nguyen, H., Prevot, N., Auld, E.G., Axen, D.A., Erdman, K.L., Howard, B., Howard, R., White, B.L., Comyn, M., Beer, G., Marshall, G.M., Robertson, L.P., Botlo, M., Laa, C., Vonach, H.: Preprint, Antiproton Annihilation at Rest in Nitrogen and Deuterium Gas. Phys. Rev. C **40**, 2717 (1989)
11. Guaraldo, C.: Nucl. Phys. (Proc. Suppl.) B **8**, 243 (1989); Nuovo Cimento **102** N. 4, 1137 (1989)
12. Clover, M.R., DeVries, R.M., DiGiacomo, N.J., Yariv, Y.: Phys. Rev. C **26**, 2138 (1982)
13. Cugnon, J., Deneye, P., Vandermeulen, J.: Nucl. Phys. A **500**, 701 (1989).
14. Hernandez, E., Oset, E.: Nucl. Phys. A **455**, 584 (1986); Private communication
15. Iljinov, A.S., Nazaruk, V.I., Chigrinov, S.E.: Nucl. Phys. A **382**, 378 (1982)
16. Cugnon, J.: Nucl. Phys. (Proc. Suppl.) B **8**, 255 (1989)
17. Jasselette, P., Cugnon, J., Vandermeulen, J.: Nucl. Phys. A **484**, 542 (1988)
18. Angelopoulos, A., Apostolakis, A., Armstrong, T.A., Bassalleck, B., Bueche, G., Fero, M., Gee, M., Graf, N., Koch, H., Lewis, R.A., Mandelkern, M., Papaelias, P., Poth, H., Rozaki, H., Sakelliou, L., Schultz, J., Schwertel, J., Smith, G.A., Usher, T., Wolfe, D.M.: Phys. Lett. B **205**, 590 (1988); Bocquet, J.P., Ericsson, G., Johansson, T., Konijn, J., Krogulski, T., Maurel, M., Monnand, E., Mougey, J., Nifenecker, H., Perrin, P., Polikanov, S., Rey-Campagnolle, M., Ristore, C., Tibell, G.: Physics at LEAR with Low Energy Antiprotons, Amsler, C., Backenstoss, G., Klapisch, R., Leluc, C., Simon, D., Tauscher, L. (eds.), p. 793. Chur: Harwood Academic Publishers 1988
19. Botvina, A.S., Iljinov, A.S., Mishustin, I.N., Bondorf, J.P., Donangelo, R., Sneppen, K.: Nucl. Phys. A **475**, 663 (1987)
20. Armstrong, T.A., Bishop, R., Harris, V., Lewis, R.A., Minor, E.D., Smith, G.A.: Z. Phys. A - Atomic Nuclei **331**, 519 (1988)
21. Smith, G.A.: The elementary structure of matter. Richard, J.-M., Aslanides, E., Boccara, N. (eds.) Springer Proceedings in Physics No. 26, pp. 197, 219. Berlin, Heidelberg, New York: Springer 1988
22. Fano, U., Ann. Rev. Nucl. Sci. **13**, 1 (1963)
23. Baltay, C., Franzini, P., Lütjens, G., Severiens, J.C., Tycko, D., Zanello, D.: Phys. Rev. **145**, 1103 (1966)
24. Roy, J.: p. III-1, Proceedings of the Fourth International Symposium on $N\bar{N}$ Interactions. Syracuse University, N.Y. May 2–4, 1975
25. Backenstoss, G., Hasinoff, M., Pavlopoulos, P., Repond, J., Tauscher, L., Tröster, D., Blüm, P., Guigas, R., Koch, H., Meyer, M., Poth, H., Raich, U., Richter, B., Adiels, L., Bergström, I., Fransson, K., Kerek, A., Suffert, M., Zioutas, K.: Nucl. Phys. B **228**, 424 (1983)
26. Chiba, M., Fujitani, T., Iwahori, J., Kawaguti, M., Kobayashi, M., Kurokawa, S., Nagashima, Y., Omori, T., Sugimoto, S., Takasaki, M., Takeutchi, F., Yamaguchi, Y., Yoshida, H.: Phys. Rev. D **39**, 3227 (1989)
27. Levman, G., Singer, R., Fields, T.: Phys. Rev. D **21**, 1 (1980)
28. Vandermeulen, J.: Lett. Nuovo Cimento **28**, 60 (1980)
29. Kalogeropoulos, T.E., Fillipas, T.A., Grammatikakis, G., Papadopoulou, Th., Simopoulou, E., Vayaki, A., Gray, L., Roy, J., Tzanakos, G.: Phys. Rev. Lett. **33**, 1631 (1974)
30. Cugnon, J., Deneye, P., Vandermeulen, J.: Phys. Rev. C **40**, 1822 (1989)
31. Diaz, J., Gavillet, Ph., Labrosse, G., Montanet, L., Swanson, W.P., Villemoes, P., Bloch, M., Frenkiel, P., Ghesquière, C., Lillestöol, E., Volte, A.: Nucl. Phys. B **16**, 239 (1970)
32. Bugg, W.M., Condo, G.T., Hart, E.L., Cohn, H.O., McCulloch, R.D.: Phys. Rev. Lett. **31**, 475 (1973)
33. Wade, M., Lind, V.G.: Phys. Rev. D **14**, 1182 (1976)
34. Kalogeropoulos, T., Tzanakos, G.S.: Phys. Rev. D **22**, 2585 (1980)
35. Cahay, M., Cugnon, J., Vandermeulen, J.: Nucl. Phys. A **393**, 237 (1983)
36. Angelopoulos, A., Apostolakis, A., Armstrong, T.A., Bassalleck, B., Benulis, C., Biard, J., Denes, P., Fero, M., Gee, M.Y., Graf, N., Hill, R., Komninos, N., Lewis, R.A., Mandelkern, M., McFarlane, W.K., Oh, B.Y., Papaelias, P., Playfer, S.M., Press, J.L., Ray, R., Rozaki, H., Sakelliou, L., Schultz, D., Schultz, J., Smith, G.A., Soulliere, M.J., Spyropoulou-Stassinaki, M., Usher, T., von Lintig, R.D., Whitmore, J., Wolfe, D.M.: Phys. Lett. **159** B, 210 (1985)
37. Markiel, W., Daniel, H., von Egidy, T., Hartmann, F.J., Hofmann, P., Kanert, W., Plendl, H.S., Ziock, K., Marshall R., Machner, H., Riepe, G., Reidy, J.J.: Nuc. Phys. A **485**, 445 (1988)
38. McGaughey, P.L., Clover, M.R., DiGiacomo, N.J.: Phys. Lett. **166** B, 3 (1986)
39. Cugnon, J., Kinet, D., Vandermeulen, J.: Nucl. Phys. A **379**, 553 (1982)

E.D. Minor, T.A. Armstrong, R. Bishop, V. Harris,
R.A. Lewis, G.A. Smith
The Pennsylvania State University
College of Science
Laboratory for Elementary Part Science
303 Osmond Laboratory
University Park, PA 16802
USA

APPENDIX V

PSU LEPS 90/03

The Pennsylvania State University

The Graduate School

CHARGED PION SPECTRA AND ENERGY TRANSFER FOLLOWING ANTIPROTON ANNIHILATION AT REST IN CARBON AND URANIUM

A Thesis in

Physics

by

Ellsworth D. Minor, Jr.

Submitted in Partial Fulfillment
of the Requirements
for the Degree of

Doctor of Philosophy

May 1990

Abstract

The momentum spectra of charged pions following antiproton annihilation at rest in carbon and uranium have been measured. This information complements a previous measurement of the neutral pion spectra performed with the same detector. The spectra, as well as total charged multiplicities, are presented and compared to recent intranuclear cascade model predictions and to related experiments. The total energy transfers to the nucleus are calculated. The possiblility of exciting nuclear multifragmentation with an antiproton beam impinging on heavy nuclei is discussed.

Contents

List of Figures vi

List of Tables viii

Acknowledgements ix

Chapter 1 Introduction 1

Chapter 2 Background 3

2.1 The Antiprotonic Atom 3

2.2 The Intranuclear Cascade 10

2.3 Postcascade Processes 14

Chapter 3 Experimental Details 18

3.1 The Detector 18

3.2 Data Collection 23

Chapter 4 Data Analysis 25

4.1 Vertex Reconstructions 25

4.1.1 Beam Analysis 26

4.1.2 Lateral Beam Spread 28

4.1.3 Annihilation Vertices 28

4.2 Momentum Measurement in the Spectrometer 34

4.3 Time-of-Flight Measurement 36

4.4 The Mass Calculation 40

4.5 Particle Identification 45

4.6 Correction to Vertex Momentum 53

4.7 Track Selection 55

4.8 Correction for Acceptance 57

4.9 Multiplicity Normalization 61

4.10 Estimation of Errors 62

Chapter 5 Discussion and Results 63

5.1 Results 63

5.2 Intranuclear Cascade Model 70

5.3 Energy Transfer 71

5.4 Multifragmentation 72

Chapter 6 Summary and Conclusions 76

References 79

List of Figures

2.1 The Antiprotonic Atom 5

2.2 X-ray spectra of $\bar{p}$-$^{16}O/^{17}O/^{18}O$ 6

2.3 Annihilation Radius Distribution 9

2.4 The Intranuclear Cascade 12

2.5 INC Momentum Distribution for 300 MeV/c Antiprotons in ^{208}Pb 15

3.1 The PS183 Detector, 1986 19

4.1 Carbon Annihilation Vertices 30

4.2 Uranium Annihilation Vertices 31

4.3 Momentum Resolution for Pions 37

4.4 Time Residuals 39

4.5 Momentum vs. Mass-Squared for Carbon T-Tracks 41

4.6 Momentum vs. Mass-Squared for Carbon P-Tracks 42

4.7 Momentum vs. Mass-Squared for Uranium T-Tracks 43

4.8 Momentum vs. Mass-Squared for Uranium P-Tracks 44

4.9 Calculated RMS Widths of Mass-Squared Bands for Uranium T-Tracks 46

4.10 Calculated RMS Widths of Mass-Squared Bands for Uranium P-Tracks. 47

4.11 Mass-Squared Distributions for Various Momentum Ranges for Uranium T-tracks 48

4.12 Mass-squared Distributions for Various Momentum Ranges for Uranium P-tracks 49

4.13 Mass-Squared Distributions for Uranium T-Tracks (Fine Resolution) 50

4.14 Mass-Squared Distributions for Uranium P-Tracks (Fine Resolution) 51

4.15 Delayed Events 56

4.16 Spectrum of Charged Pions Decaying into Muons 59

4.17 The Acceptance Function in Uranium 60

5.1 Charged Pion Multiplicity Versus the Cube Root of the Mass Number 67

5.2 Charged Pion Yield for Carbon 68

5.3 Charged Pion Yield for Uranium 69

5.4 Total Energy Yield for Charged Pions 73

List of Tables

3.1 Drift Chambers 21

3.2 Scintillation Counters 22

3.3 Multiwire Proportional Chambers in the Spectrometer 22

4.1 Momentum Components and Ranges of the Antiproton Beam 27

4.2 Event Center Locations for the Heavy Targets 32

4.3 Summary of Event Locations for the Heavy Target Data . . . 34

4.4 Materials Traversed by Tracks Entering the Spectrometer . . 54

4.5 Errors on Multiplicities 62

5.1 Total Charged Pion Multiplicities 64

5.2 Total Neutral Pion and Combined Multiplicities 64

5.3 Average Energy per Photon and Charged Pion and Energy Transfer 72

Acknowledgements

The author wishes to express his gratitude to Dr. Gerald A. Smith for his purposeful and efficient direction in the completion of this work, and to Dr. Raymond A. Lewis for innumerable hours of enlightening discussions. The author is also grateful to E. Hernandez and E. Oset, who generously provided unpublished theoretical calculations, to the staff of the CERN PS Division for their dedicated operation of LEAR during this experiment, and to the members of the PS183 collaboration for their skillful design, construction, and operation of the experiment discussed in this thesis. Financial support provided to the author by the Penn State NASA Center for Space Propulsion Engineering and the Air Force Office of Scientific Research, Air Force Systems Command, USAF, under grant AFOSR 87-0246 is gratefully acknowledged. Finally, the author is especially appreciative of his wife and daughter, who gave unselfishly of their own time that this work might be accomplished, and of his parents for the encouragement which began several decades ago and has never waned.

Chapter 1 Introduction

The interaction of matter with antimatter has intrigued physicists for over fifty years. Study of this interaction has provided profound insights into the fundamental forces of nature and the structure of matter at its most basic level. Important discoveries ($\omega^0, Z^0, W^\pm$, etc.) made with antiproton beams at high energy laboratories around the world attests to the fruitfulness of this approach. It is notable that development of antiproton facilities has continued unabated, in spite of the difficulty of obtaining high-intensity antiproton beams. The most clearly attractive feature of an antiproton annihilation on a neutron or proton is the release of at least $2 \times 938 = 1876$ MeV in a region of space as small as ~ 8 fm^3. in volume. Furthermore, this concentrated energy release occurs even for annihilation at rest, thus permitting the study of systems with no net forward motion.

In a nuclear environment, where the binding energy is ~ 8 MeV per nucleon, such a large deposit of energy could conceivably lead to a number of exotic effects. Speculations in the past have pointed out the possibility of formation of a quark-gluon plasma, which has not yet proven to be realistic. Somewhat more likely, perhaps, is the possible formation of the multifragmented state, in which the nucleus is almost completely dissociated into constituent nucleons. This, for instance, would occur in a uranium nucleus, where the total binding energy is very nearly equal to the total annihilation energy, if all of the energy were absorbed by the nucleus.

Investigations of antiproton annihilation in nuclei began in the 1950s[1-6]. The commissioning of the Low Energy Antiproton Ring (LEAR) at CERN in 1983, however, made an intense low-momentum source available, permitting a thousand-fold increase in statistics. Recent measurements of charged pion momentum spectra have been performed at that laboratory for various target nuclei, including carbon and uranium in flight(608 MeV/c)[7], neon[8], and nitrogen[9]. A recent review of these results and others has been provided by Guaraldo[10]. This thesis will extend these results by providing similar spectra for antiproton annihilation at rest in carbon and uranium nuclei.

Theoretically, the effort to understand these results has centered primarily on development of the intranuclear cascade model(INC). Using this model, predictions for pion spectra have been made by Clover *et al.*[11], Cugnon *et al.*[12], Hernandez and Oset[13], and Iljinov *et al.*[14]. Cugnon [15] has recently reviewed theoretical developments in this regard.

The model is discussed in Chapter 2, along with discussion of the annihilation state which precedes the cascade and the excited nucleus which remains following the cascade. Chapter 3 describes the detector in detail, while Chapter 4 outlines the analysis techniques applied to the data. Results are presented and discussed in Chapter 5 and conclusions are drawn in Chapter 6.

Chapter 2 Background

Three stages characterize antiproton annihilation at rest in nuclei. Initially, following the capture of a slow antiproton in a Coulombic orbit, there is a preannihilation stage, with the $\bar{p}$ cascading down through successively lower energy levels. This continues for $\sim 10^{-10}$ sec.[16], with the lifetime of the final (capture) state being $\sim 10^{-18}$ sec. Annihilation terminates this process as the antiproton nears the nucleus, producing a shower of pions and kaons distributed isotropically. Some of these pass into the nucleus, thus interacting with constituent nucleons. This stage, the intranuclear cascade, is over in $< 10^{-22}$ sec. Subsequent to the escape or absorption of the annihilation pions and the ejection of hard-scattered nucleons, the residual nucleus remains in some excited state. It evolves toward a ground state through photon emission, nucleon evaporation, fission, and/or multifragmentation. These processes end after $\sim 10^{-17}$ sec., although delayed fission times are observed up to $\sim$0.2 ns.[17] and radioactive residual nuclei may require very long times to decay. This Chapter will elaborate on these stages.

2.1 The Antiprotonic Atom

An antiproton (p$\simeq$200 MeV/c) impinging on a dense target loses energy through ionization according to the Bethe-Bloch equation[18],

$$\frac{dE}{dx} = D\left(\frac{Z\rho}{A}\right)_{MED}\frac{1}{\beta^2}\left[\ln\left(\frac{2m_e\gamma^2\beta^2c^2}{I}\right) - \beta^2 - \frac{C(\beta)}{Z_{MED}}\right], \qquad (2.1)$$

where D=0.3071 MeV cm^2 g^{-1} and I = the ionization potential of the medium. $C(\beta)$ refers to a correction for the effect of unfilled shells in the medium and is important at low velocities. Since antiprotons are negatively charged, they enter an atomic orbit once their energy is sufficiently low. For a hydrogenic atom,

$$E = -\frac{\alpha^2 Z^2}{2n^2}\mu, \qquad (2.2)$$

where α is the fine structure constant. The antiproton displaces an electron in the outermost shell of the atom. See Fig. 2.1. Since energy is conserved in the process, the principal quantum number of the $\bar{p}$ following capture is determined by the change in the reduced mass of the system. Therefore n is $\sim \sqrt{m_{\bar{p}}/m_e} = 43$ times larger than that of the displaced electron. Similarly, conservation of angular momentum leads to large values of l. For a typical impact parameter of 0.5Å on an uranium atom, l=170 ($L = l\hbar$). Following capture the antiproton cascades down through the numerous levels available, initially through the emission of Auger electrons, later by emission of X-rays. Evidence of this behavior has been collected for a number of different nuclei, of which one example is shown in Fig. 2.2[19]. Lines shown here are due to transitions between levels for isotopes of oxygen. The transitions (for which Δn=1, Δl=1) quickly lead to a state characterized by l=n-1, which is very nearly circular. The circularity of the orbit precludes early annihilation through contact of the antiproton with the nucleus.

At some point during the cascade, the antiproton has approached sufficiently close to the nucleus and begins to feel the effect of the strong force, permitting annihilation to occur. For annihilations occurring outside of the nuclear half-density radius, where at-rest events are believed to occur[20],

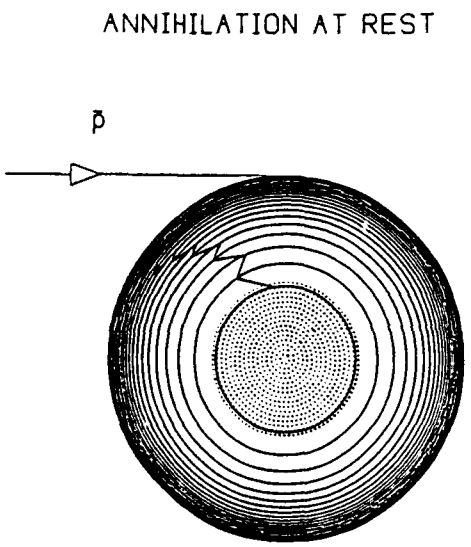

Figure 2.1: The Antiprotonic Atom. The orbits (solid lines) in this figure are spaced proportional to energy levels in ^{238}U. The nucleus is represented by the dot-filled central region. The antiproton cascade begins at the top of the figure and proceeds through a series of Δn=1, Δl=1 transitions until annihilation occurs in the vicinity of the nuclear surface.

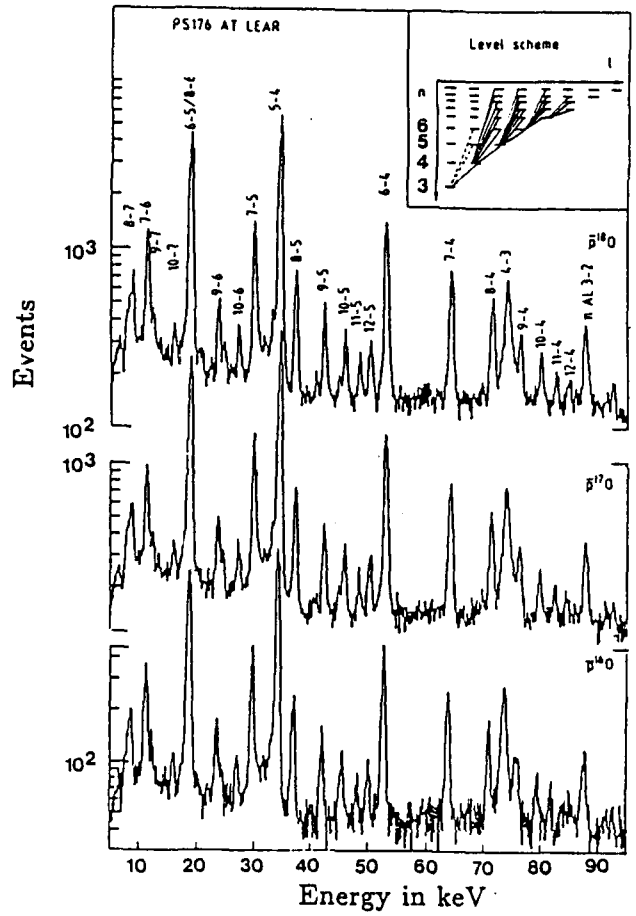

Figure 2.2: X-ray spectra of $\bar{p}$-^{16}O/^{17}O/^{18}O. The level scheme is shown in the upper right-hand corner [19].

the nucleus appears (to generated pions) as a gray disk subtending some solid angle. The magnitude of that solid angle, inversely proportional to the square of the distance from the annihilation to the center of the nucleus, determines the fraction of pions which interact with the nucleus. Thus, uncertainty in the annihilation radius contributes to uncertainty in the degree of pion interaction. Since the cross section for annihilation at rest is infinite, the use of measured cross sections to directly estimate an average annihilation radius is precluded. Instead, an optical potential approach, containing an imaginary component which leads to annihilation, is used. This approach has also been used for simulations of annihilations in flight[11].

The parameters of the potential model may be determined from observations of the capture state in nuclei whose transition lines have been measured. The $\bar{p}$-atom has been observed to be hydrogen-like with the relativistic Bohr formula approximating the energy levels. Strong interactions between the antiproton and the nucleus lead to an additional shift (ϵ) and to a width(Γ) of the capture state energy. This effect is orders of magnitude smaller for the higher states since the highly circular orbits do not permit strong interaction with the nucleus from these states. The values of ϵ and Γ have been measured for many nuclei [19,21–26] In the simplest approximation, one can determine the imaginary component of the potential from

$$\Gamma = 2\pi \int d^3r \int d^3r' \, V_{ann}(\mathbf{r}-\mathbf{r}') \mid \psi_{nl}(r) \mid^2 \rho(r') \tag{2.3}$$

$$= 8\pi^2 \int_0^\infty dr \, r^2 \mid R_{nl}(r) \mid^2 \{V_{ann}^{\bar{p}p}\rho_p(r) + V_{ann}^{\bar{p}n}\rho_n(r)\}, \tag{2.4}$$

where ψ_{nl} is the capture state wavefunction for the antiproton and ρ is the nuclear density. The second equation has been derived assuming a spherical

nucleus and a zero-range potential. The integrand is the probability distribution for the distance r between the annihilation site and the center of the nucleus and is shown in Fig. 2.3 for several nuclei[20]. For nuclei whose transitions have not been reported, the annihilation state is uncertain and the annihilation radius distribution for two possible values of the state are plotted. Arrows indicate the most probable annihilation radii for the plotted states.

In the optical model, one relates the potential to the complex average $\bar{p}N$ scattering length $\bar{a}$ and the density of protons and neutrons $\rho(r)$[27]:

$$\bar{V} = -\frac{2\pi}{\mu}\left(1 + \frac{m_{\bar{p}}}{m_N}\right)\bar{a}\rho(r) = V_{real}(r) + iV_{ann}(r) \tag{2.5}$$

where μ is the $\bar{p}$-nucleus reduced mass and m_N the nucleon mass. Optical potentials of 25 MeV (real part) and 61 MeV (imaginary part) at the nuclear surface have been shown to be consistent with antiproton scattering data[28]. The strength of the annihilation potential relative to the real part clearly suppresses bound orbits in the strong force. The complex scattering length has been experimentally determined and is found to be

$$\bar{a} = (1.53 \pm 0.27) + i(2.50 \pm 0.25) \text{ fm} \tag{2.6}$$

for ^{16}O and ^{19}F [29]. For ^{92}Mo [25] it is

$$\bar{a} = (0.25 \pm 0.30) + i(3.05 \pm 0.25) \text{ fm}. \tag{2.7}$$

The difference between these values has not been accounted for satisfactorily. A number of possibilities have been suggested[30]: (1) The approximation with the optical potential is not adequate; (2) the nuclear charge density

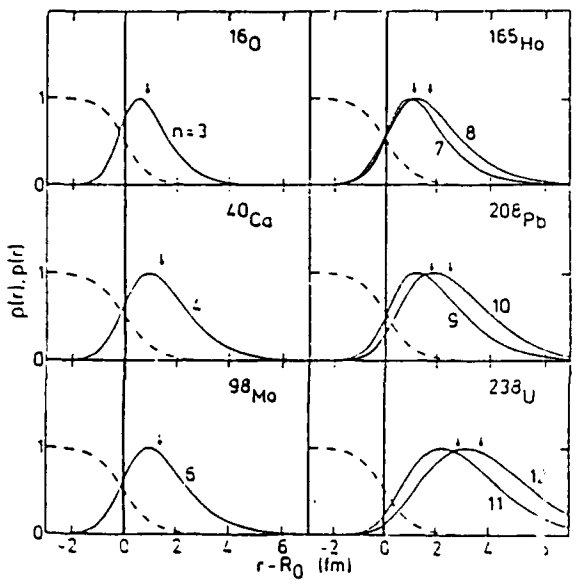

Figure 2.3: Annihilation Radius Distribution. The distribution p(r) of the annihilation site is calculated from eq. (2.4), for various targets (solid lines). The density profile of the nucleus is given by the dashed curve. R_0 is the half-density radius. The numbers labeling the solid curves indicate the principal quantum numbers of the annihilation state, while arrows denote the average value of the annihilation radius. All curves are normalized to the same maximum[20].

distribution used does not describe the density correctly at the surface; (3) $\bar{a}$ depends on the mass number A; or, (4) a spin-orbit term has to be added to the potential. The spin-orbit term plays an essential role in the shell model of the nucleus and it has been questioned whether it should also be introduced in the antiproton-nucleus potential:

$$\overline{V} = V_{real}(r) + iV_{ann}(r) + \mathbf{l}\cdot\mathbf{s}\left[V^{SO}_{real}(r) + iV^{SO}_{ann}(r)\right]. \tag{2.8}$$

Testing this final conjecture is not possible at the current time since polarized antiproton facilities do not exist. As a consequence of these uncertainties, it is clear that the radii indicated in Fig. 2.3 are first-order approximations only. Thus, a theory modeling pion interaction in nuclei following antiproton annihilation at rest must make an important approximation regarding the radius of annihilation.

2.2 The Intranuclear Cascade

The antiproton annihilates on a single nucleon ~90-97% of the time[16]. This rate has been deduced from measurements of the reaction $\bar{p}d \rightarrow \pi^- p$ for antiproton annihilations at rest in deuterium[31,32]. The stable final state mesons produced are π and K. In annihilation at rest, kaons are produced in only 5% of all events. By contrast, pions are more numerous with the average number of annihilation (primordial) pions, $< M_\pi >$, being 4.94±0.14 per event [33–35].

The momentum spectrum of pions produced in the annihilation is simulated in some realistic way. For instance, Iljinov *et al.*[14] use a Maxwell-Boltzmann shape,

$$(E_\pi + m_\pi)\frac{d^3\sigma}{dp_\pi^3} = [1 - \frac{m_\pi^2}{(E_\pi + m_\pi)^2}]e^{-(E_\pi + m_\pi)/T}, \tag{2.9}$$

where p_π is the pion momentum, E_π the pion kinetic energy, and $T = 135$ MeV, the slope (or temperature) of the curve. This distribution has been shown in practice to be an accurate representation of the measured distribution from $\bar{p}p$ annihilation at rest. By contrast, Hernandez and Oset[13] use a method based on known recursive formulae for populating phase space.

The primordial pions generated in the low-density margin of the nucleus scatter isotropically away from the "fireball" site. A majority of these escape without further interaction with the nucleus. Those which do impinge on the nucleus take part in the intranuclear cascade.

Models of the intranuclear cascade following annihilation at rest[13,14,20, 36] vary in details and produce different, but similar results. The scattering process is pictured as stochastic. Those pions whose trajectories carry them through the nucleus interact in ways consistent with our current understanding. The following scatters are implemented in most of the models:

$$NN \rightleftharpoons NN, \qquad \pi NN \rightleftharpoons NN, \tag{2.10}$$

$$\pi N \rightleftharpoons \Delta, \qquad N\Delta \rightleftharpoons NN, \tag{2.11}$$

$$NN\Delta \rightleftharpoons NNN, \quad \pi N \rightleftharpoons \pi\pi N, \tag{2.12}$$

$$\pi N \rightleftharpoons \pi N. \tag{2.13}$$

The most significant of these processes are depicted in Fig. 2.4. These interactions may be included in the model directly by applying measured scattering cross sections for on-mass-shell particles in the simulation. Alternatively, a more fundamental approach based on the Δh model (where a Δ resonance is created in a pion-nucleon interaction, leaving a "hole" in the gas of nucleons

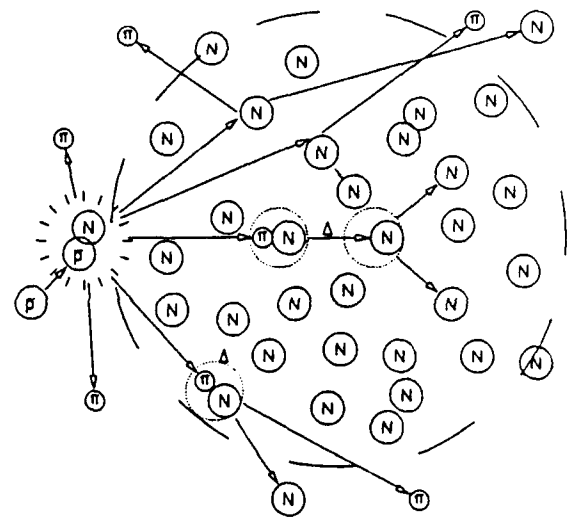

Figure 2.4: The Intranuclear Cascade. The most significant processes of the intranuclear cascade are depicted here, including quasielastic scattering, resonance formation, and pion absorption. Although the isospin degrees of freedom are not specified in this figure, any of these processes may be accompanied by charge exchange.

forming the nucleus) may be implemented[11,13]. The latter approach calculates the effect of interactions from many-body Feynman diagrams (thus, including effects due to interactions on two, three, or more nucleons) and can, in principle, avoid the difficulty inherent in applying measurements for on-mass-shell nucleons to bound nucleons.

In order to facilitate application to nuclei of widely varying mass number, the models cited above simulate the nucleus as a degenerate Fermi gas. Low-momentum-transfer interactions are greatly suppressed by Pauli blocking, just as in the nuclear shell model. The complexity and number of possible interactions require approximations and the neglect of effects which are relatively small (isospin degrees of freedom, for instance). These approximations vary among models. The most significant adjustments to the primordial spectrum are due to pion absorption (a two-step process involving reactions 2.11 and 2.12(a)) and quasi-elastic pion-nucleon scattering (either with or without intermediate resonance formation).

For the average production of five pions, the typical total energy per primordial pion is 375 MeV. For such a pion interacting with a nucleon at rest, $\sqrt{s}$ = 1266 MeV. The Δ mass is 1232±115 MeV. Thus, Δ formation is very likely to occur. It is, also, the primary mechanism for pion absorption, thus is a large contributor to energy absorption by the nucleus. The other mechanism for pion absorption, reaction 2.10(b), is significant only at very low momenta and has a small cross section even there. Consequently, correct implementation of Δ scattering is of paramount importance in the construction of a model.

The effects of pion absorption and quasi-elastic scattering (for which the number and masses of the final state particles are the same as those of the initial state particles) are seen in Fig. 2.5[13]. These results are for 300 MeV/c antiprotons, which penetrate deeper into the nucleus than do annihilations at rest and consequently have greater interaction with it. The target nucleus is ^{208}Pb. The smooth curve represents the spectrum of generated pions following annihilation. The crosses illustrate the model's prediction when pion absorption is the only mechanism operating. One sees a band of absorption between ~160 and ~500 MeV/c, with a shoulder at ~360 MeV/c . Turning on quasi-elastic scattering as well (diamonds) degrades pion momenta, leading to a well-defined peak at ~200 MeV/c and removing the shoulder.

Available data from pion and nucleon scattering are not totally inclusive for all nuclei and all momenta in the range of interest (0-1000 MeV/c). Thus, any general model must extrapolate into unmeasured regions. As has been seen, the interactions included in the model, and their strengths, will adjust the shapes of the final spectra, thus providing information to test the model.

2.3 Postcascade Processes

Subsequent to the intranuclear cascade, the nucleus remains in some excited state. A significant fraction of the annihilation energy has been carried off with primordial, scattered, and secondary pions and with ejected nucleons. A measurement of the residual energy at this stage, E*, is one of the ultimate goals of this line of research. Previously, speculations have been advanced regarding the possibility of formation of a quark-gluon plasma, hot

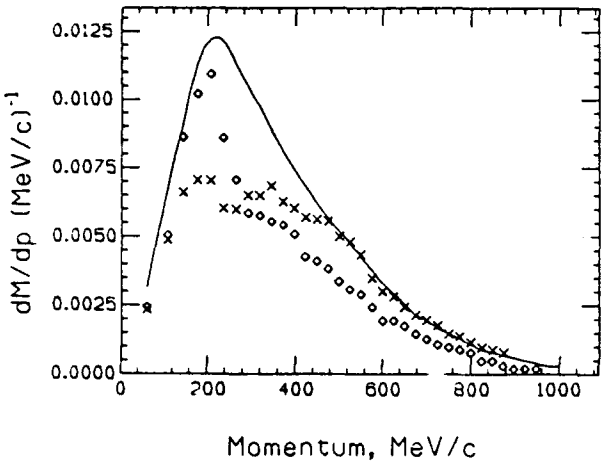

Figure 2.5: INC Momentum Distribution for 300 MeV/c Antiprotons in ^{208}Pb. The smooth curve is the free distribution. The crosses include only the pion absorption mechanism. The diamonds include absorption as well as quasi-elastic scattering[13].

spots, hot nuclear gas, and multifragmentation. These phenomena depend critically on the magnitude and concentration of E*. To date, no evidence has been presented confirming the occurrence of these phenomena following antiproton annihilation on nuclei. There may exist, however, a possibility of exciting at least one of these states (multifragmentation) following annihilation in flight.

The nucleus may de-excite through a number of well known processes. These include photon emission, nucleon evaporation, and (quasi)fission. Photon emission occurs for very light nuclei and heavier nuclei which are very near the ground state. Nucleon evaporation carries off greater amounts of energy. This is primarily neutron evaporation since these uncharged particles are not sensitive to the Coulomb repulsion, which is seen by protons inside the nucleus as well as outside. This follows from the necessity that the highest occupied energy level must be very nearly the same for either nucleon type to prevent $\beta^{\pm}$ decay. A previous result from this experiment[37] measured average evaporation neutron energy to be 15.9±1.6 MeV per nucleon.

For higher energy processes following antiproton annihilation in heavy nuclei, as pointed out by Jasselette *et al.*[20], the dissipation of E* following the INC is characterized by competition among various processes. For example, in ^{238}U, fission is predicted to dominate and evidence demonstrating this behavior has been observed[37,38]. Using a statistical approach, Botvina *et al.*[39] predict the breakup of the nucleus into a few heavy fragments, when it acquires a residual energy, E*/A = 3 MeV/nucleon. Further, they note that the peak in their residual mass distribution widens with increasing residual energy, finally evolving, at E*/A = 5 MeV per nucleon, into a distribution

sharply peaked at A<10 and monotonically decreasing with increasing mass of the fragment. Independently, Cugnon[15], using an INC model, has predicted the onset of multifragmentation phenomena for $E^*/A > 3$ MeV per nucleon. Critical to the issue of multifragmentation, however, are the questions of how much energy is transferred to the nucleus by the intranuclear cascade and how thoroughly the energy is thermalized. These points will be explored in this thesis, and the experimental conditions necessary to excite the multifragmented state will be discussed.

Chapter 3 Experimental Details

Results presented in this thesis are from data collected by CERN experiment PS183 at LEAR (Low Energy Antiproton Ring) in 1986. LEAR is a unique accelerator capable of delivering $\sim 5\times 10^6$ antiprotons per second at 350 MeV/c with momentum resolution $\delta p/p = 10^{-3}$. Details regarding the detector and data collection process are described in this Chapter.

3.1 The Detector

Fig. 3.1 provides a schematic plan of the PS183 detector. The antiproton beam entered at the lower left. Prior to impinging on the target, it traversed thin sheets of carbon and aluminum (which degraded the momentum), two multiwire proportional chambers(1-mm. wire spacing), and two scintillation counters (S1, S2). The target was a uranium disk (2-mm. thick and 35 mm. in diameter) or a carbon sheet (5-mm. thick by 20-mm. wide by 50-mm. long). In addition, for ~20% of the carbon data, a cubic target 1 cm.^{3} was used. All heavy targets were located at $X \simeq -11.5$ cm. (where X is parallel to the beam axis). The uranium disk and carbon sheet targets were rotated $\sim 45^0$ around a vertical axis so that the broad faces of the targets were exposed to both the spectrometer entrance and the beam. Located downstream (beginning at $X \simeq -8.5$ cm.) from the heavy target was a liquid deuterium target, used in previous runs, which had been displaced from its normal operating position for the nuclear target experiments. The

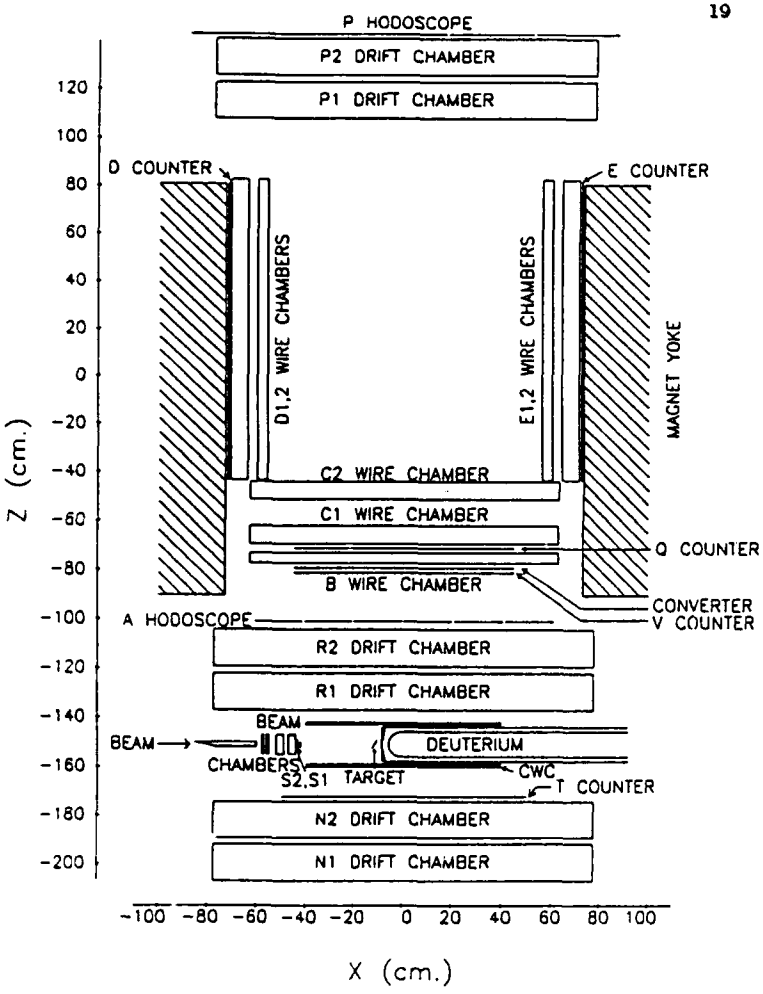

Figure 3.1: The PS183 Detector, 1986.

upstream end of the deuterium vessel contained a 2 cm. thick flange, made of resofil (a resin-impregnated cellulose product).

The target was surrounded by a cylindrical wire chamber (CWC) 75 cm. in length and 7 cm. in radius with 3-mm. wire spacing. This chamber, which counted the charged particle multiplicity for each annihilation, subtended 97.5% of a 4π solid angle about the target.

A pair of identical drift chambers, R1,2 and N1,2, stood on either side of the target region. A third, identical chamber, P1,2, was located beyond the aperture of the magnet. Each chamber consisted of six layers with two layers each oriented at -30^0, 0^0, and $+30^0$ to the vertical. The layers were grouped in triplets in order to facilitate construction. Details regarding drift chamber design and location may be found in Table 3.1 and in Ref. 40. Reconstruction of charged tracks passing through R1,2 and N1,2 provided vertex location, thus permitting the selection of events originating in the target rather than nearby materials. The rms resolution of the planes was found to be 450μm [40].

The 120 ton MEP-21-2 electromagnet produced a field of 3.5 kG centered at $X = 0$ cm. and $Z = 0$ cm., where Z is perpendicular to the beam line and in the plane of Fig. 3.1. The aperture of the magnet was $154\times50\times176$ cm.^{3} In order to reduce multiple scattering, helium filled the region of the aperture not occupied by counters or chambers. The field was normal to the plane of Fig. 3.1 and was directed down ($B_Y > 0$) and up ($B_Y < 0$) for different portions of the data. The field possessed some focusing characteri ics and thus was not perfectly uniform; however, the region in and around the aperture was accurately mapped in three dimensions prior to the experiment.

Table 3.1: Drift Chambers. All drift chambers consisted of six layers of drift cells oriented at -30^0, 0^0, and +30^0 to the vertical and arranged in triplets. Each layer contained 39 cells of width 4.064 cm. The instrumented regions in each triplet measured 130.05×53.35×12.86 cm.^{3} All drift chambers were oriented normal to the Z-axis. Figure 3.1 shows the mid-plane locations and orientations of these chambers.

Chamber	Triplet	Location
N1,2	N1	Z = -195.58 cm.
	N2	Z = -177.70 cm.
R1,2	R1	Z = -124.32 cm.
	R2	Z = -108.93 cm.
P1,2	P1	Z = +123.16 cm.
	P2	Z = +141.10 cm.

All particles entering the spectrometer and satisfying the trigger requirements passed through the A scintillation hodoscope(Table 3.2), the multiwire proportional chambers B, C1,2 (Table 3.3), and the scintillation counters V and Q (Table 3.2). In addition to forming part of the trigger, these elements provided tracking and timing information used to reconstruct the event for analysis[41]. In addition, pulse height (dE/dx) measurements in the counters were useful for confirming the identity of particles. A photon converter (0.56 mm. Pb, ~10% of a conversion length) was located at Z=-80 cm. Pair production ($\gamma \rightarrow e^+e^-$) in this converter followed by detection of the electron-positron pair in the spectrometer provided a measurement of high energy photon production in the target [42–44].

Particles exited the spectrometer on the P-counter (P-tracks, where P is for *P*enetrating through the spectrometer) or the side counters(T-tracks,

Table 3.2: Scintillation Counters. Counters had photomultiplier tubes (PMTs) at both ends where the geometry of the detector permitted. Figure 3.1 shows the locations and orientations of these counters.

Counter	No. of Elements	Element Size,cm.^{2}	Thickness cm.	Location	PMTs per element
S1	1	2.0×2.0	0.2	X=-43.5	1
S2	1	1.0×1.0	0.2	X=-43.0	1
T	1	80.0×14.0	0.5	Z=-173.0	2
A	6	21.7×40.0	0.5	Z=-99.7	2
V	1	80.0×14.0	0.5	Z=-79.0	2
Q	1	80.0×14.0	0.5	Z=-73.0	2
P	5	32.0×60.0	0.5	Z=+154.0	2
D	2	140.5×15.0	0.5	X=-73.0	1
E	2	140.5×15.0	0.5	X=+73.0	1

Table 3.3: Multiwire Proportional Chambers in the Spectrometer. All multiwire proportional chambers in the spectrometer had inner dimensions of 125.7 × 26.7 cm.^{2} with instrumented areas of 124.5 × 26.7 cm.^{2} All anode wire spacings were 0.29996 cm. (σ_{rms} = 866 μm.[41]) Figure 3.1 shows the locations and orientations of these chambers.

PWC	Thickness	Location	Planes
B	ΔZ=4.1 cm.	Z = -77.0 cm.	Vertical
C1	ΔZ=7.3 cm.	Z = -69.1 cm.	Vertical, Horizontal, 45^0
C2	ΔZ=7.3 cm.	Z = -51.2 cm.	Vertical, Horizontal, 45^0
D1	ΔX=4.1 cm.	X = -59.8 cm.	Vertical
D2	ΔX=7.3 cm.	X = -71.0 cm.	Vertical, Horizontal, 45^0
E1	ΔX=4.1 cm.	X = +59.8 cm.	Vertical
E2	ΔX=7.3 cm.	X = +71.0 cm.	Vertical, Horizontal, 45^0

where T is for *T*rapped in the spectrometer), depending on their angle of incidence and momentum. Tracking and timing information for P-tracks was provided by the P1,2 drift chambers and P hodoscope. Similar information for T-tracks was provided by D1 and D2 multiwire proportional chambers and the D counter, or by the complements of these on the E side of the spectrometer.

3.2 Data Collection

To provide efficient and reliable data collection for the experiment, an interconnected multiprocessor complex was constructed, centered around the Le Croy 4800-series CAB microprocessors[45]. The CAB is a fast (200 ns. microinstruction execution time), on-board CAMAC computer which accesses the immediate CAMAC dataway or parallel branch highway. The front-end CAB's were complimented with a PDP-11/60, for writing tapes and performing off-line analysis, and with an HP9826. The HP9826 was used as a graphic device during off-line analysis and as a system supervisor while the experiment was taking data.

The trigger was formed in a straightforward way: the coincidence of an S and a Q counter hit and of a hit in any of the other counters generated a pretrigger which served to clock a two-stage programmable logic unit system. The first stage encoded hodoscope multiplicity; the second stage determined whether the pattern formed a valid trigger, and if so, issued a trigger and encoded event topology number. The programmable logic units were downloaded by the HP9826 whenever a new trigger configuration was desired.

Several CAMAC crates housed the analog-to-digital converters (ADCs), time-to-digital converters (TDCs), scalers, etc., which were attached to elements of the detector. Data from these modules were routed through the CAB's for DMA transfer to the PDP-11/60 and onto tape. The transfers required minimal CPU time, thus leaving the processor free to produce diagnostic histograms. Interconnection with the HP9826 permitted that processor to produce diagnostic event "snapshots" and to provide remote beam chamber and scaler information for use in beam magnet control.

This implementation permitted the examination of 2000 events/sec. and recording of as many as 300 events/sec.

Chapter 4 Data Analysis

Techniques for converting measurements from the detector instrumentation into particle characteristics (momentum and mass) and, ultimately, into normalized momentum spectra and multiplicities will now be presented.

Initially, wire hit information is translated into locations in the coordinate system of Fig. 3.1, thus determining the particle trajectory. The momentum inside the spectrometer is constructed for the track from its curvature through the magnetic field. Timing information from the scintillation counters is converted to time elapsed following the arrival of the antiproton at a beam counter. To identify the particle, a mass is calculated from the trajectory length, time of flight, and momentum. The momentum at the annihilation vertex is derived from the spectrometer momentum by integrating the energy lost by the particle while traversing the target and the entrance to the spectrometer. Various parameters of the track are tested for evidence of irregularities (such as a discontinuity or an annihilation vertex not in the intended target.) Finally, a second pass analysis corrects for the acceptance of the spectrometer, which is much less than unity, and normalizes the resulting spectra into differential multiplicities (dM/dp) per antiproton annihilation.

4.1 Vertex Reconstructions

In Fig. 3.1, it is apparent that considerable material in addition to the target resides near the beam, including a cap sealing the end of the beam

pipe, the momentum degrader, the beam chambers and counters, and the vessel containing the deuterium target. In addition, there is a target holder, a cylindrical tube made of 1 mm. thick resofil and coaxial with the beam line, which is not shown in Fig. 3.1. These items affect the experiment in three ways: (1) Those substances located in the beam path reduce the momentum of the beam through ionization energy loss. Furthermore, fluctuations in the energy loss introduce an additional spread in the beam momentum. (2) The lateral spread in the beam size is increased due to multiple scattering effects. And, (3) annihilation of antiprotons may occur in any of the materials, possibly yielding a spurious track in the spectrometer.

4.1.1 Beam Analysis

The degradation of the $\bar{p}$ momentum (350 MeV/c) as it passed through materials in the beam is readily calculated from Eq. 2.1. An additional complication is introduced by the beam counters S1 and S2, which had different areas (2×2 cm.^{2} and 1×1 cm.^{2}). Since the trigger required a signal in only one of these, an antiproton could have either of two momenta when arriving at the target, depending on whether it passed through one or both of the counters. The $\bar{p}$ momentum for any particular annihilation is determined by checking for signals in each of the beam counters. Furthermore, the data are divided into runs which varied according to which of the counters was required to initiate a trigger. Those runs for which the small counter was used for the trigger clearly had only a single component in the beam. A knowledge of the beam particle momentum permits a determination of the

annihilation depth (range) in the target. Using the annihilation depth, an accurate correction can be made for the energy given up by a track as it traverses the target. Vertices seen in the deuterium target due to antiprotons which missed the heavy carbon and uranium targets have a measurable range which may be compared to the expected range calculated using Refs. 46 and 47, thus testing the beam momentum determination.

Momenta at the targets are given in Table 4.1, along with the expected ranges in the various target materials. Momentum degradation is slightly greater for that fraction of the beam impinging on the deuterium target since it must pass through an additional thin mylar window in order to enter the vessel. All heavy target ranges are within the physical thicknesses of the targets, implying that annihilations in the deuterium target downstream resulted from antiprotons circumventing the heavy targets.

Table 4.1: Momentum Components and Ranges of the Antiproton Beam. The momentum (MeV/c) of the beam arriving at the specified target is given followed by the range (cm.) in that target (in parentheses).

Target	Component One	Component Two
Carbon	196.7±2.7 (0.276±0.014)	229.9±2.2 (0.484±0.18)
Uranium	196.7±2.7 (0.064±0.003)	229.9±2.2 (0.108±0.004)
Deuterium	190.4±2.8 (2.209±0.123)	225.7±2.3 (4.098±0.162)

4.1.2 Lateral Beam Spread

The lateral spread of the beam due to Coulomb scattering can be quite significant at low velocities, since [18]

$$\theta_0 = \frac{14.1\ \mathrm{MeV/c}}{p\beta}\sqrt{L/L_R}, \tag{4.1}$$

where θ_0 is the rms scattering angle in radians and L/L_R is the material thickness in radiation lengths. Although scattering effects are largest in the momentum degrader, beam particles scattered at large angles there do not hit a beam counter and, therefore, fail to satisfy the trigger requirements. Thus, such events are not included in the data. For those events satisfying the trigger, lateral scattering is predominantly due to the beam counters for which $\theta_0 \simeq 0.049$ rad. At the heavy target, this projects to $\Delta Z_{targ} \simeq 3.2$ cm. which is approximately the width observed in those targets, as is seen in the following section. Were it not for the scattering introduced by these materials, the width would be 0.3 cm., which is the value for the beam provided by LEAR.

4.1.3 Annihilation Vertices

Determination of the annihilation vertex location is essential to selecting events which originated in the intended target. The drift chambers adjacent to the beam line, R1,2 and N1,2, have been included in the detector for this purpose. The six wire planes comprising either of these chambers overconstrain the problem of determining the intercept and slope of any charged

track passing through them. The drift chambers lie in a region of negligible magnetic field (no consistent track curvature is detectable), thus projection of the straight-line reconstructions from the chambers to the beam region is straightforward.

For ~5% of all events satisfying the charged trigger, particles traversed both R1,2 and N1,2, and the intersection of their tracks provides the location of the annihilation vertex. Figs. 4.1 and 4.2 show the vertices for two-track events for carbon and uranium, respectively.

For carbon, three scattering centers are pronounced: the target, the resofil flange, and the deuterium flask. The angle of the heavy target is clear in the horizontal projection, as is the bimodal structure in the deuterium target due to the two beam components. Events originating in the flange are more intense away from the spectrometer, indicating a slight skewing in the beam toward that side. Less dense regions are also evident, notably the events originating in the target holder surrounding the beam line and other, more random, events which are probably due to tracks which have scattered off of a frame, leading to an erroneous vertex projection.

The vertical projection shows additional structure in the deuterium target. Events due to the high-momentum beam component (at $X \simeq -1$) are separated into upper and lower lobes by the shadow of the heavy carbon target. Such a shadow is not present in the events resulting from the low-momentum component ($X \simeq -3$) since a large fraction of these are due to a run using the small cubic target. For that run, the small beam counter invoked the trigger, thus ensuring that all beam particles were of the low-momentum component. Table 4.2 gives the average location and rms width

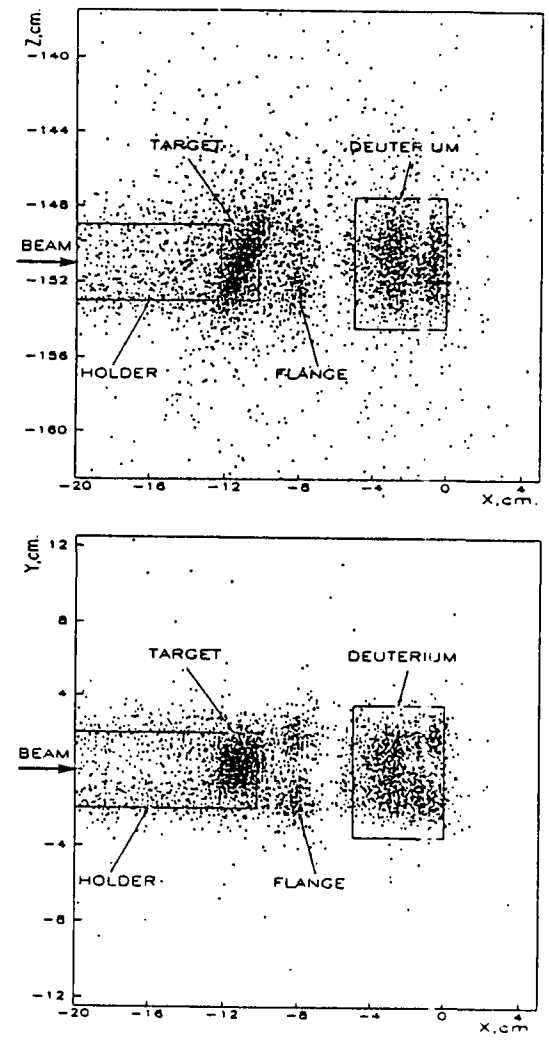

Figure 4.1: Carbon Annihilation Vertices. For these events a charged track is present in both R1,2 and N1,2. The beam enters from the left. The spectrometer is centered at X, Y, $Z = 0$ cm. (a) X-Z(horizontal) view: Events are selected for which -2 cm. $< Y < +2$ cm.; (b) X-Y(vertical) view: Events are selected for which -153 cm. $< Z < -149$ cm.

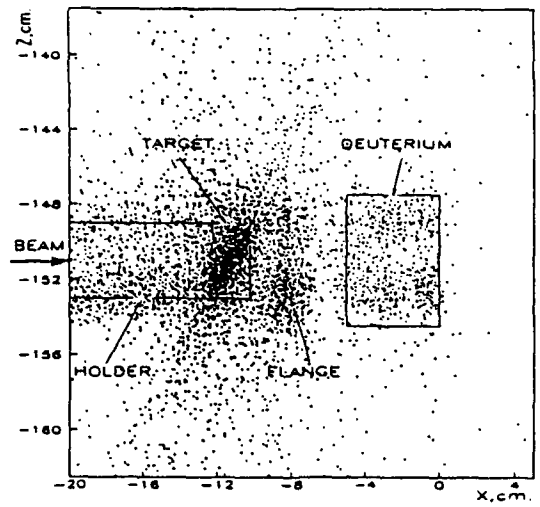

(a)

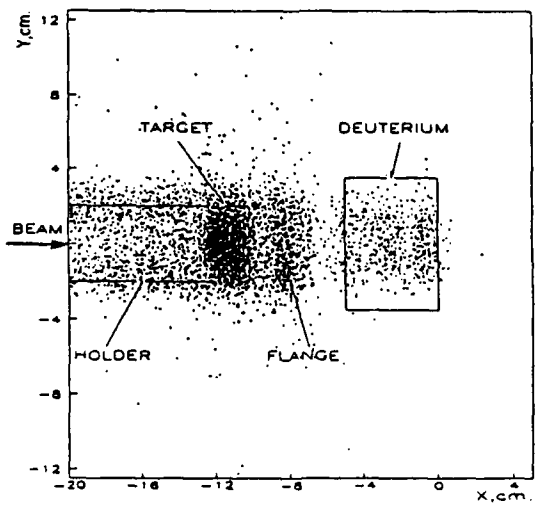

(b)

Figure 4.2: Uranium Annihilation Vertices. For these events a charged track is present in both R1,2 and N1,2. The beam enters from the left. The center of the spectrometer is at X, Y, Z= 0 cm. (a) X-Z(horizontal) view: Events are selected for which -2 cm.$<Y<+2$ cm.; (b) X-Y(vertical) view: Events are selected for which -153 cm.$<Z<-149$ cm.

of events originating in the carbon targets, as well as the mounting angle of the target. For the carbon sheet σ_Z=1.76±0.04 cm., implying a beam width of 3.52±0.06 cm., which may be compared to the estimate of ~3.2 cm. in Section 4.1.2.

Uranium target data are shown in Fig. 4.2. Features evident in the carbon plots are present here also, although there are some differences due to the slightly different geometry. Events in the deuterium target are more sparse, since the diameter of the uranium disk (35 mm.) was larger than the Y-dimension of the carbon sheet (20 mm.) Thus, fewer events were able to pass above or below the uranium target. The horizontal view shows the same two-momentum-component structure in deuterium as does carbon, however the target shadow is now evident in this view, again due to the diameter of the target disk. Such voids are not apparent in the vertical view since the rotation of the disk reduced the effective width seen by the beam, allowing antiprotons to slip past the sides of the target. See Table 4.2 for the locations of events in the uranium target.

Table 4.2: Event Center Locations for the Heavy Targets. These values represent the average locations for events occurring in the targets rather than the physical locations of the targets themselves. Coordinate values are in cm. and the mounting angle, θ, relative to the beam line is in degrees.

Target	X	Y	Z	θ
Carbon Cube	-11.64±0.33	0.36±0.78	-151.06±0.64	90
Carbon Sheet	-11.22±0.88	0.24±0.93	-151.04±1.76	65±2
Uranium	-11.45±0.62	0.52±1.47	-150.80±1.17	61±2

The spatial resolution evident in Figs. 4.1 and 4.2 can be shown to be consistent with the expected resolution of the drift chambers ($\sigma_{rms} = 450\mu$m.) For two planes ~15 cm. apart, the rms error in track angle is $\delta\phi = 0.00424$ rad. which, when projected back to the beam line and combined in quadrature with the same error for the opposite chamber, gives $\delta X_{res} = 0.20$ cm. An effect is also present due to Coulomb scattering, Eq. 4.1. The average track is a 220 MeV/c pion (see Chapter 5). Thus, $\delta X_{coul} = 0.360$ cm. Combining the two effects gives $\delta X_{proj} = 0.57$ cm., while the observed rms width for the uranium disk in Fig. 4.2 is 0.82 cm. The 60% larger width actually seen is due to approximations made in calculating the prediction: (1) The per-plane resolution is quoted for normal tracks, whereas most tracks impinge at an angle to the plane, thus degrading the resolution; (2) Many particles slower than 220 MeV/c pions are present with larger Coulomb scattering angles.

Table 4.3 lists the percentage of events for each heavy target according to location of the annihilation vertex. It is clear from this Table that only ~19-45% of all events originate in the heavy targets, making a reliable means of locating the annihilation vertex critical.

Two significant conclusions may be drawn from these studies. First, the separation of antiproton interactions in different materials near the target is good. In particular, the detector can resolve heavy target events from events originating in the nearby resofil flange. This is in spite of the fact that, for 94% of all events, a track is available in only a single drift chamber. For these events, the vertex is determined by projecting the track back to the beam line at Z=-151 cm. The possibility exists that parallax would preclude adequate separation. However, this study has determined that, using such

Table 4.3: Summary of Event Locations for the Heavy Target Data. Percentages of the total data for the specified target are listed.

Location	Carbon Cube	Carbon Sheet	Uranium
Heavy Target	19	40	45
Beam counters	2	1	2
Resofil Flange	7	6	14
Deuterium	45	22	8
Other	27	31	31

a projection, a contamination of <4% in uranium or <2% in carbon would be present from annihilations in the resofil flange, provided that events with X_{proj} >-10 cm. were excluded.

Second, the analysis of the beam is consistent with the ranging peaks seen in the deuterium target. This implies that the ranges predicted in the heavy targets are accurate, thus permitting an accurate correction to the momentum of tracks seen in the spectrometer.

4.2 Momentum Measurement in the Spectrometer

For a singly-charged particle traveling normal to a uniform magnetic field, the following relationship is well known[48, p. 29]:

$$p(\mathrm{MeV/c}) = 0.3\ B(\mathrm{kGauss})\ R(\mathrm{cm.}) \tag{4.2}$$

The non-uniformity of the PS183 field prevents direct application of this equation. However, sufficient information is available to determine the particle trajectory from the numerous wire planes in the detector in conjunction

with the magnetic field map. The drift chambers provide slopes and intercepts of charged tracks while the seven multiwire proportional chambers within the spectrometer provide position measurements. T-tracks (which terminate inside the magnet aperature) and P-tracks (which terminate on the P-hodoscope) differ in the average curvature of tracks, since their relative momentum acceptances are unequal, and in the kinds of information provided, thus the techniques used to determine the momentum differ, depending on topology.

For T-tracks, an approximate radius is first calculated from the hit locations in B, C2, and D2 or E2, giving an estimate of the momentum from Eq. 4.2. A correction factor, which is a function of the longitudinal coordinates in the chambers, is applied. This factor was obtained from simulations using the magnetic field map.

For P-tracks, which on average have smaller curvature, a method is used which has been found to give 30% more accurate results[49]. The magnetic field and the track are modeled as cubic and quintic splines. The momentum is found by improving the fit iteratively. No improvement was found using this technique for T-tracks. Consequently, the parametrization technique was retained for those tracks. Details regarding the momentum measurement techniques may be found in Refs. 41 and 50.

The detector's ability to resolve momenta is limited by the finite wire spacing of the planes and by Coulomb scattering in the detector elements and may be estimated using a uniform field approximation. Eq. 4.2 is readily shown to be equivalent to

$$p = \frac{0.3BC}{2\sin(\theta/2)}, \tag{4.3}$$

where C is the chord length between hits in the wire planes near either end of the track, and θ is the bend angle of the trajectory. Thus, errors in the momentum are a direct result of errors in the chord length measurement and in the angles of the track as it exits or enters the chambers. The chord length error can be shown to be negligible for this detector, whereas the angular error receives contributions from the effects noted above. Using average chord lengths for T- and P-tracks, the momentum resolution for pions has been estimated and is plotted in Fig. 4.3. $\delta p/p$ is seen to be nearly flat below 200 MeV/c (where it is dominated by Coulomb scattering) and to increase with increasing momentum (due to finite wire spacing). Furthermore, resolution at any given momentum is poorer for T-tracks than for P-tracks, reflecting the smaller average bend angle for T-tracks.

4.3 Time-of-Flight Measurement

Timing information is obtained from a time-to-digital converter (TDC) attached to the photomultiplier tube(s) (PMT) mounted on each scintillation counter. In addition to adjustments which account for the travel time of electrical signals in cable and light signals through plastic scintillator, a time slew correction is calculated to compensate for the finite rise time of the signal pulse in the PMT. Time measurement in the TDC begins only after the pulse voltage has risen above the discrimination level established to prevent triggering by random noise. Larger pulses reach this level more rapidly and, thus, require smaller corrections than do smaller pulses. Since pulse height is approximately proportional to ionization loss (Eq. 2.1), very fast

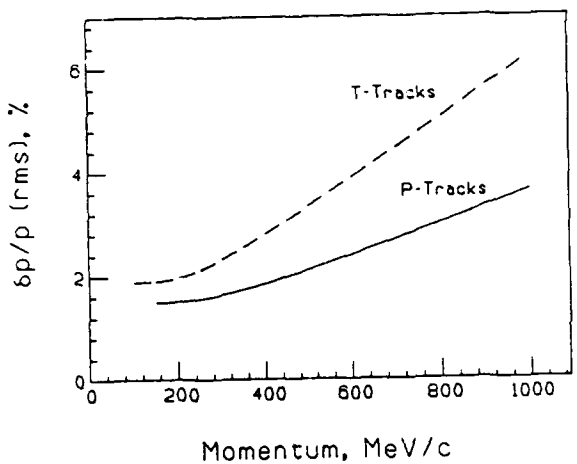

Figure 4.3: Momentum Resolution for Pions.

particles, such as pions, tend to have small pulse heights and large time slew corrections. For instance, a 280 MeV/c pion impinging on a side counter will typically require a time slew correction of 2 ns. Neglecting this correction leads to a calculated mass of 305 MeV/c^2, $\sim$ 20% larger than the known pion mass of 139.6 MeV/c^2.

In this analysis the time slew is parametrized as

$$\delta t_{slew} = A_0 + \frac{A_1}{|\mathrm{PH}|} + \frac{A_2}{|\mathrm{PH}|^2} + \frac{A_3}{|\mathrm{PH}|^3}, \tag{4.4}$$

where |PH| is the pulse height and the A_i are constants to be determined. A separate set of constants is found for each counter using regression analysis. This approach is feasible due to the large number of pions and protons in the data sample.

Timing resolution is determined from the average time residual for all tracks. The time residual, t_{res}, is defined as

$$t_{res} = t_{meas} - t_{part}, \tag{4.5}$$

where t_{part} is the predicted travel time for the track (of measured momentum and trajectory length), assuming it to have the mass of a particular particle (pion or proton), and t_{meas} is the measured time. Fig. 4.4 shows the time residuals for pions (a) and protons (b). In (a), the sharp pion peak centered at $t_{res} = 0$ clearly demonstrates the apparent timing resolution of the detector. Protons appear in this plot at later times (centered around +7 ns.) and are much wider in distribution since the difference between the pion and proton times is dependent on the trajectory and momentum. In (b) the residual of the proton time has been plotted, thus shifting the proton band to

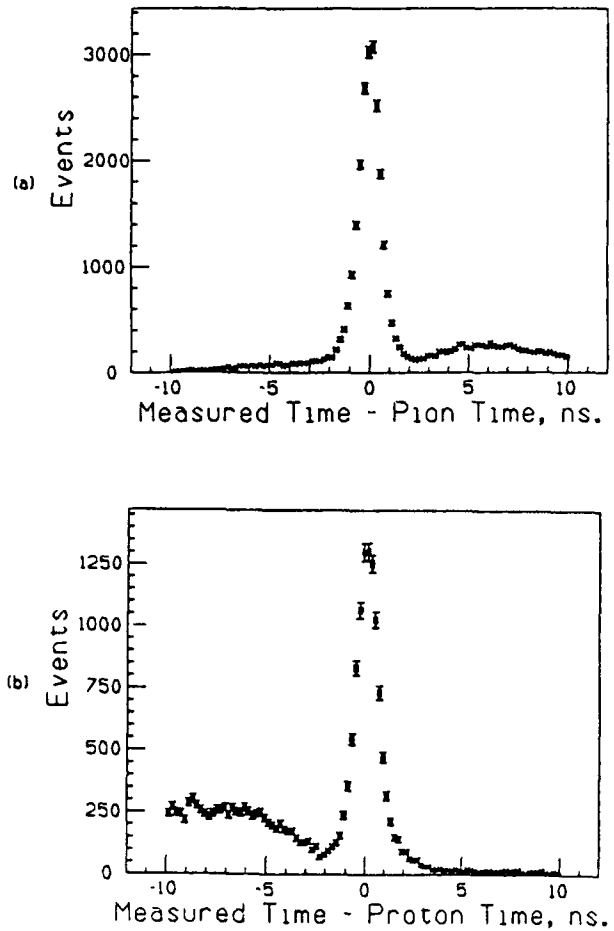

Figure 4.4: Time Residuals. (a) Pions and (b) Protons.

$t_{res} = 0$ and sharpening it while spreading the pion events over earlier times. The apparent time resolution (rms width) for T-tracks is seen to be 0.5 ns. This value contains a contribution due to momentum resolution which, when subtracted, leaves a true resolution of 0.4 ns.

4.4 The Mass Calculation

From the relativistic momentum equation,

$$p = m\beta\gamma, \tag{4.6}$$

it is straightforward to derive

$$m^2 = p^2\left(\frac{t^2}{s^2}c^2 - 1\right), \tag{4.7}$$

where s is the length of a particle's trajectory and t is the time required to traverse s. In order to minimize the variation in momentum along the trajectory due to dE/dx losses, s is chosen to include only that portion of the track between the A hodoscope and and a terminating counter (D, E, or P). A small correction is subtracted from t to compensate for the change in the particle's velocity resulting from passage through the chambers, counters, and converter following the A hodoscope. This correction was found to alter the mass-squared calculation by <5% for the worst-case particles.

Figs. 4.5-4.6 and 4.7-4.8 show the momentum measured in the spectrometer vs. mass-squared for T- and P-tracks in carbon and uranium, respectively.

Vertical bands corresponding to pions, kaons, protons, and deuterons are clearly seen. Pions and kaons are well separated for T(P)-tracks below

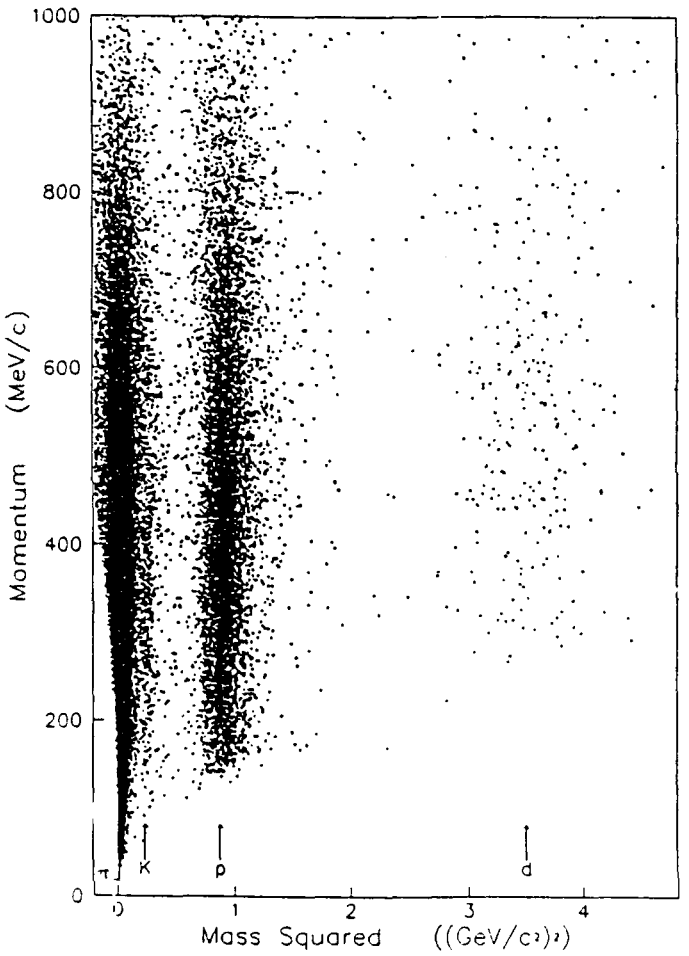

Figure 4.5: Momentum vs. Mass-Squared for Carbon T-Tracks.

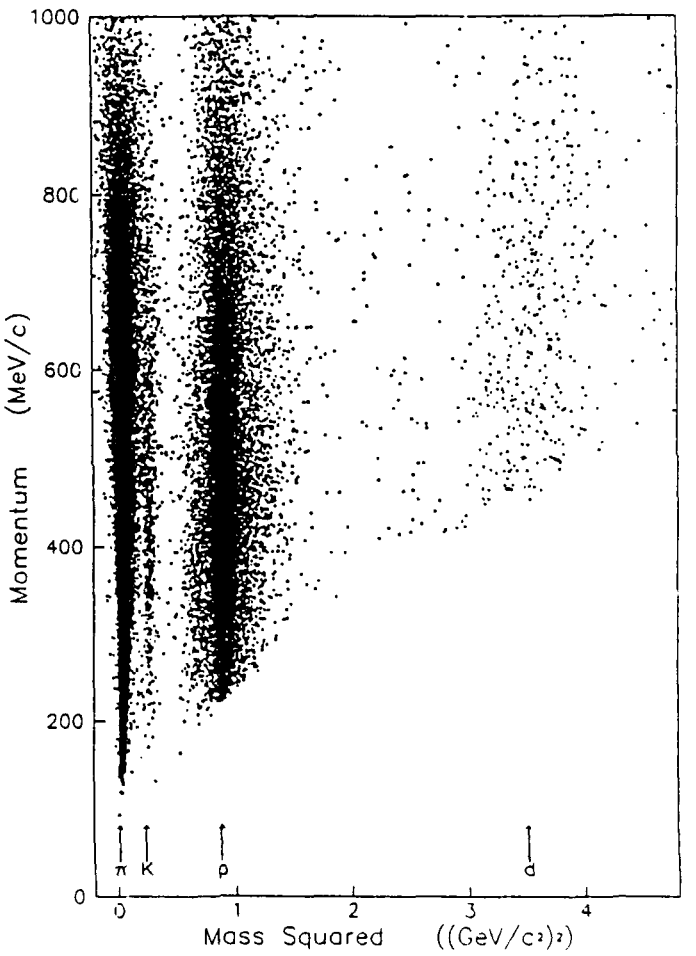

Figure 4.6: Momentum v . Mass-Squared for Carbon P-Tracks.

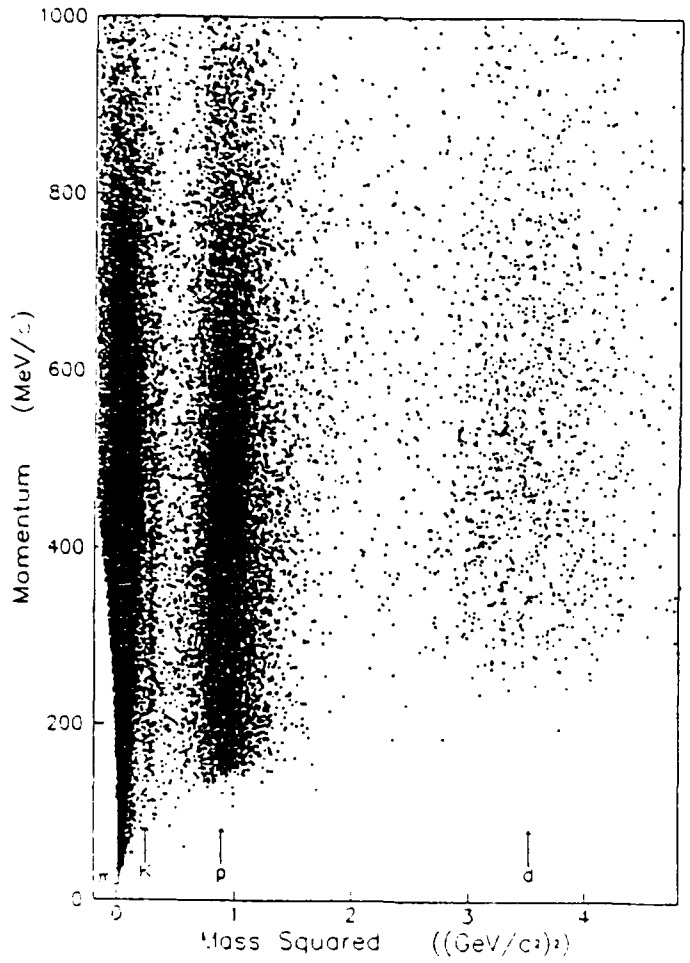

Figure 4.7: Momentum vs. Mass-Squared for Uranium T-Tracks.

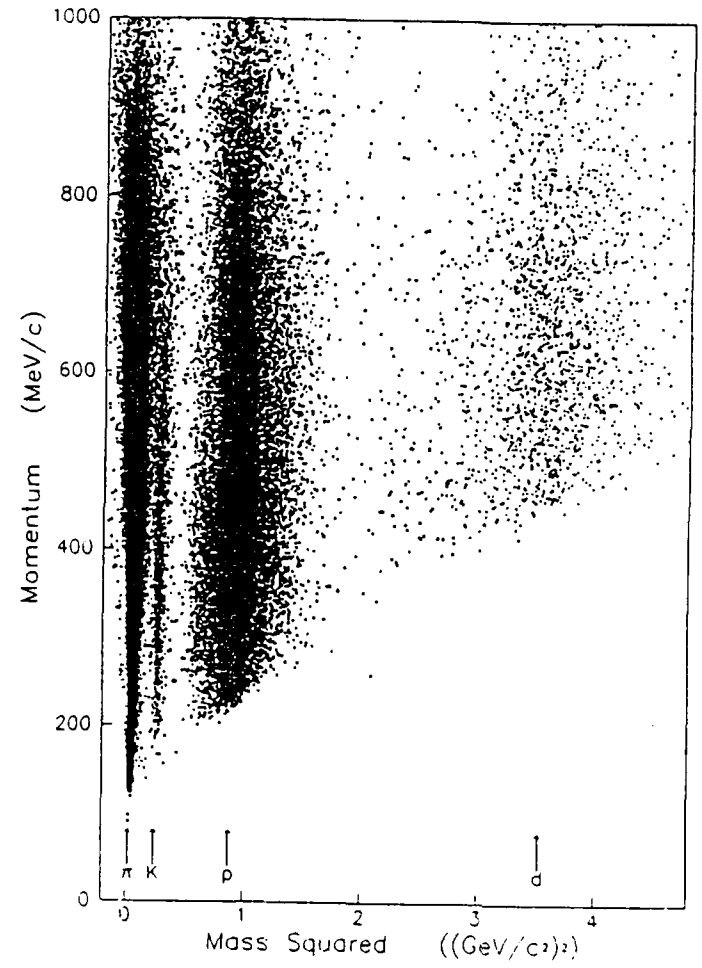

Figure 4.8: Momentum vs. Mass-Squared for Uranium P-Tracks.

~400(600) MeV/c. Contamination of kaons in the pion samples is estimated to be ~0.8(0.3)% above these values.

The widths of the bands are due to the finite timing and momentum resolutions discussed in previous sections. The contributions from these components have been calculated and are displayed in Figs. 4.9 and 4.10 for the uranium target. These results show that timing dominates the mass-squared resolution for pions. Projections of the uranium mass-squared distributions are shown for different momentum intervals in Figs. 4.11 (T-tracks) and 4.12 (P-tracks). Gaussian curves, computed using the resolutions cited above, have been superimposed for pions and protons, and for kaons where the band is distinct. These curves explain the gross features of the data except for the tails of the measured distributions. These tails are due to the nature of Moliere scattering, for which the Gaussian approximation is valid only near the center of the distribution.

4.5 Particle Identification

Pion identification is based on mass-squared cuts. It is evident from Figs. 4.5–4.8 that an upper limit of $m^2 < +0.20(\mathrm{GeV}/c^2)^2$ excludes kaons and heavier particles. Similarly, a lower limit of $m^2 > -0.30\ (\mathrm{GeV}/c^2)^2$ includes all of the pion band. However, examination of Figs. 4.11 and 4.12 in greater detail below 300 MeV/c (see Figs. 4.13 and 4.14) demonstrates the presence of electrons and positrons, as well as muons, below ~200 MeV/c.

The $e^\pm$ and $\mu^\pm$ are treated differently in the analysis for fundamental reasons. Muons result from the decay of charged pions ($\pi^\pm \rightarrow \mu^\pm\nu$) and, thus,

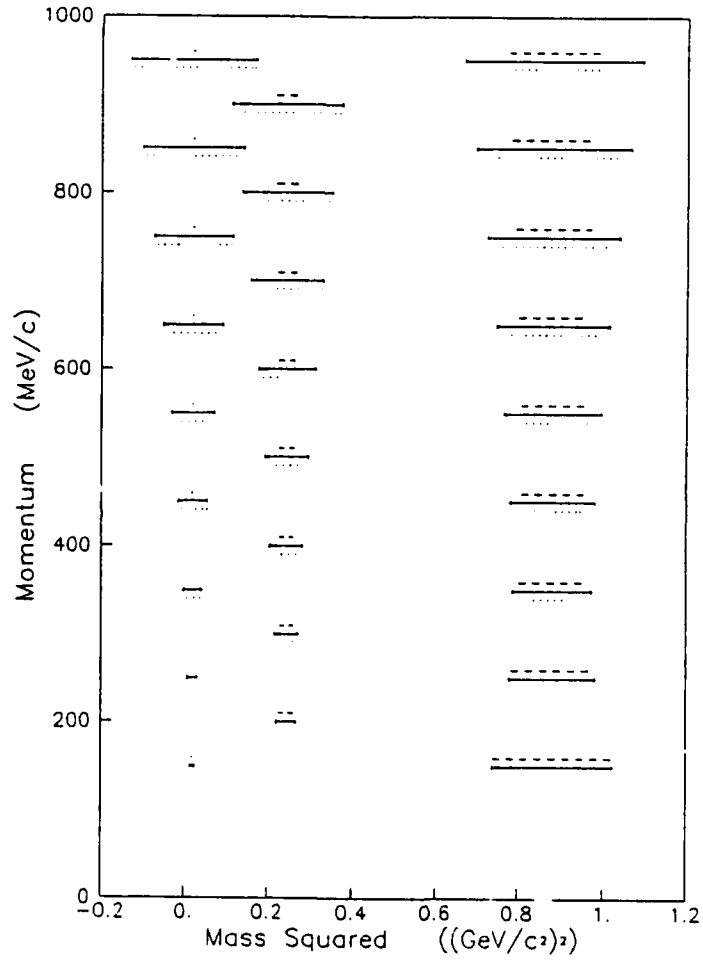

Figure 4.9: Calculated RMS Widths of Mass-Squared Bands for Uranium T-Tracks. The solid lines give the total predicted widths for pions, kaons, and protons. The dotted lines give the contribution due to time resolution, while the dashed lines give the contribution from momentum resolution.

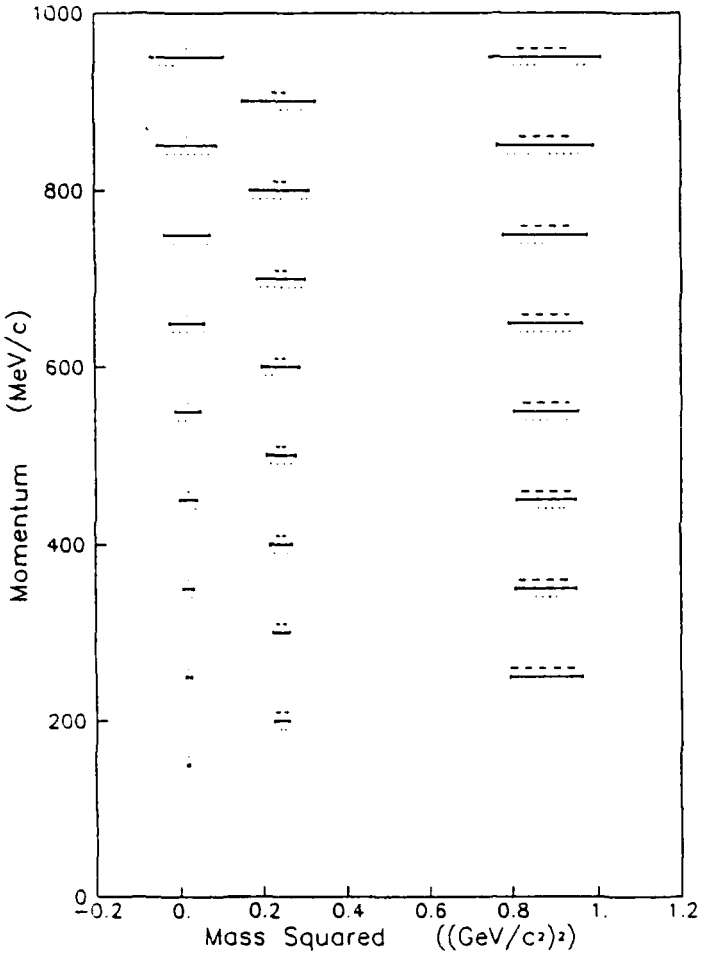

Figure 4.10: Calculated RMS Widths of Mass-Squared Bands for Uranium P-Tracks. The solid lines give the total predicted widths for pions, kaons, and protons. The dotted lines give the contribution due to time resolution, while the dashed lines give the contribution from momentum resolution.

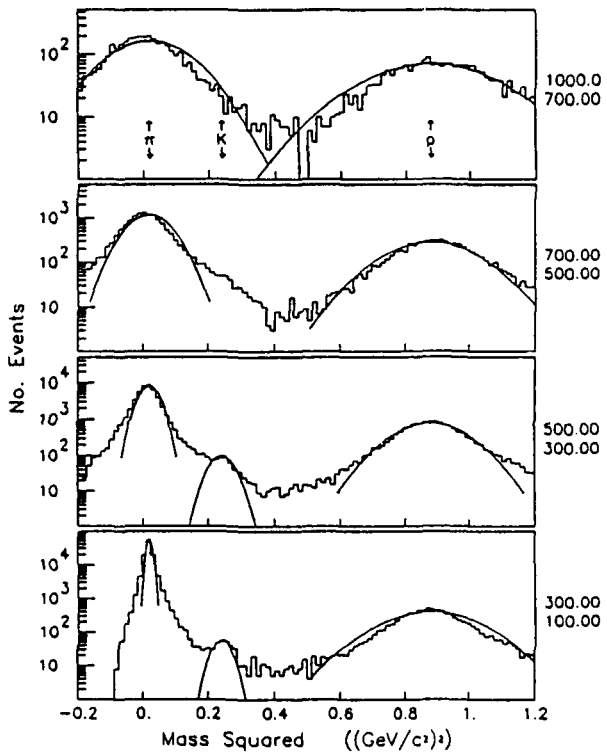

Figure 4.11: Mass-Squared Distributions for Various Momentum Ranges for Uranium T-Tracks. The Gaussian curves superimposed are predicted shapes based on timing and momentum resolution. The momentum ranges in MeV/c are specified to the right of each plot.

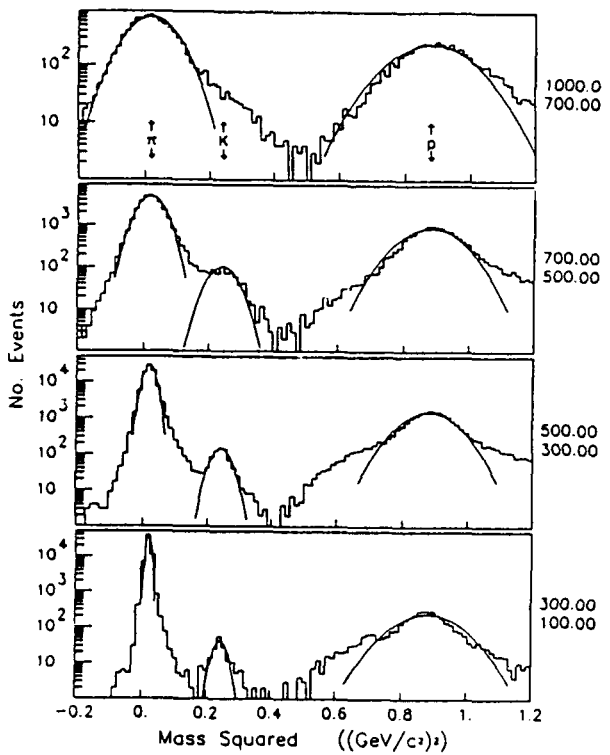

Figure 4.12: Mass-Squared Distributions for Various Momentum Ranges for Uranium P-Tracks. The Gaussian curves superimposed are predicted shapes based on timing and momentum resolution. The momentum ranges in MeV/c are specified to the right of each plot.

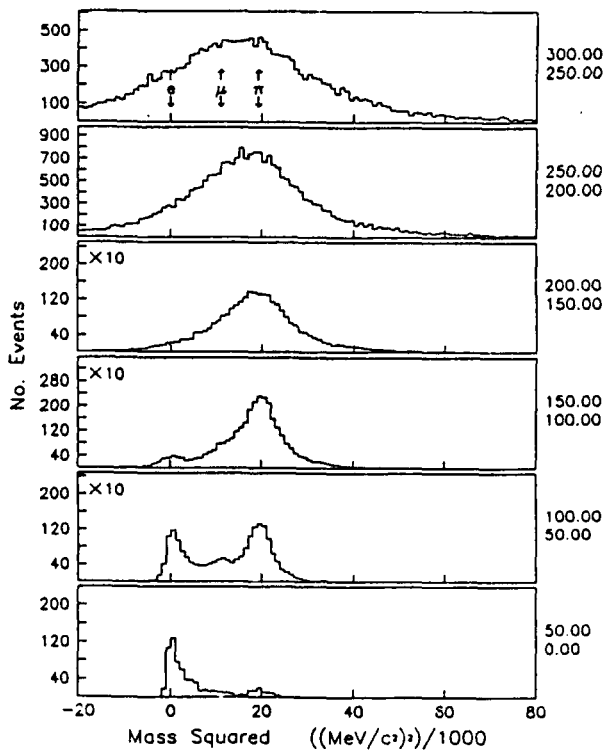

Figure 4.13: Mass-Squared Distributions for Uranium T-Tracks (Fine Resolution). The momentum ranges in MeV/c are indicated to the right of each plot.

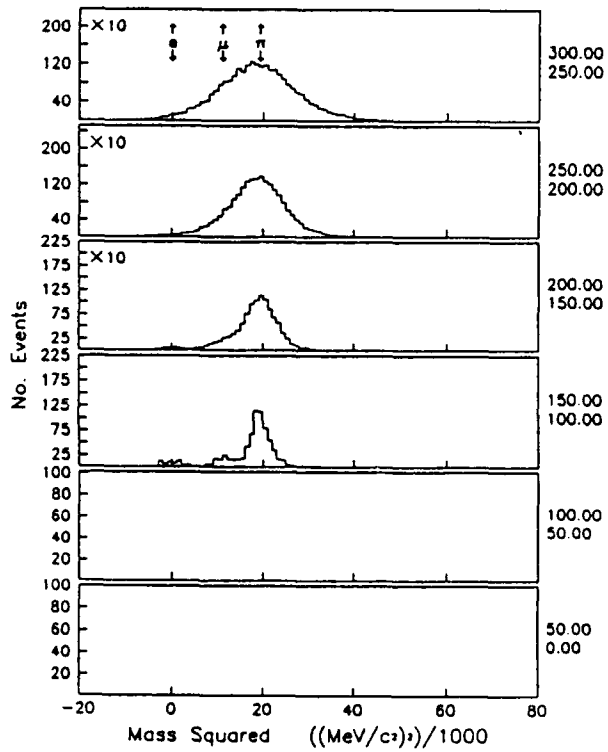

Figure 4.14: Mass-Squared Distributions for Uranium P-Tracks (Fine Resolution). The momentum ranges in MeV/c are indicated to the right of each plot.

are included in the measurement. The construction of the pion momentum spectrum, however, will be distorted by these decays for two reasons. First, the decay process yields, on average, a secondary particle whose momentum is different from that of the parent particle. Second, if the decay occurs inside the spectrometer, an undetectable discontinuity results in the track, and an erroneous momentum is reconstructed. Monte Carlo studies have shown that ~10% of the charged pions decayed in flight and could not be resolved in the detector. The net result of both effects is an average measured momentum degraded by ~30 MeV/c for the decayed particles. A correction applied to the spectra to adjust these distortion will be discussed in Sec. 4.8.

Electrons and positrons, however, result from neutral pion decay and pair production in the target and these events should be excluded from the sample of charged pions. The $e^{\pm}$ spectrum is generated by the two-step process:

$$\pi^0 \rightarrow \gamma\gamma, \tag{4.8}$$

and

$$\gamma \rightarrow e^+e^-. \tag{4.9}$$

This two-step process, with the momentum of the decay products being reduced by 50% (on average) from that of the parent particle at each step, suggests that the average $e^{\pm}$ momentum is greatly reduced from that of the parent neutral pions. Figs. 4.13 and 4.14 exhibit $e^{\pm}$ multiplicities decreasing rapidly with increasing momentum, thus confirming this supposition. While T-tracks (Fig. 4.13) exhibit comparable numbers of $e^{\pm}$ and $\pi^{\pm}$ between 50 and 100 MeV/c, P-tracks (Fig. 4.14) show that the $e^{\pm}$ peak between 150 and 200 MeV/c contains only ~4% of the area of the pion peak. These data

show that reasonable separation among e, μ, and π can be made for T-tracks (P-tracks) below 150 (250) MeV/c. The 4% $e^{\pm}$ seen in P-tracks between 150 and 200 MeV/c indicates, first, that the misidentification in that region is no more than ~2% for both topologies combined and, second, that the $e^{\pm}$ population is falling off rapidly with increasing momentum and is negligible for higher momenta.

Consequently, a variable lower mass-squared limit has been established which depends on topology and momentum. For T-tracks (P-tracks) the lower limit is set at +0.013 $(\mathrm{GeV}/c^2)^2$ at $p \leq 75$ (125) MeV/c and widens smoothly, reaching -0.30 $(\mathrm{GeV}/c^2)^2$ at 400 MeV/c.

4.6 *Correction to Vertex Momentum*

Once the track is identified, its true mass is used to calculate a velocity which is used in Eq. 2.1 to integrate the energy lost by the particle in the target and the entrance to the spectrometer. Thus, the momentum of the particle just outside the annihilation nucleus is determined. Table 4.4 lists the substances traversed by the particle. These materials comprised ~0.18 radiation lengths for the carbon target; the greater density of uranium increased this number to ~0.31 radiation lengths for that target. An average pion lost 10.8 MeV in the target and spectrometer entrance.

Using the vertex momentum, an experimental verification of the momentum resolution of the detector is available using the kaon decay lines:

$$K^+ \rightarrow \mu^+\nu \qquad (236\ \mathrm{MeV}/c), \qquad (4.10)$$

Table 4.4: Materials Traversed by Tracks Entering the Spectrometer. The values provided for the heavy targets are for the low-momentum (high-momentum) beam component. Gas used in drift chambers was argon-ethane (proportion 70-30); "magic" gas was used for the multiwire proportional chambers (argon-isobutane-freon in the proportion 70-29.6-0.4).

Detector Element	Material	Thickness (cm.)
Target	Carbon Sheet	0.48(0.83)
	Uranium	0.11(0.19)
CWC	Resofil	2×0.1
	Gas	4.0
R1,2	Mylar	4×0.0076
	Gas	25.7
A counter	Scintillator	0.50
	Al foil	0.0051
	Plastic sheet	0.056
V counter	Scintillator	0.50
	Al foil	0.0051
	Plastic sheet	0.056
B chamber	Mylar	2×0.0076
	Gas	4.1
Photon Converter	Lead	0.056
Q counter	Scintillator	0.50
	Al foil	0.0051
	Plastic sheet	0.056
C1 chamber	Mylar	2×0.0076
	Gas	7.3
C2 chamber	Mylar	2×0.0076
	Gas	7.3

and

$$K^+ \rightarrow \pi^+\pi^0 \qquad (205\ \mathrm{MeV/c}). \qquad (4.11)$$

These lines were identified in events for which the arrival time of the particle at the A hodoscope exceeded 7 ns. For comparison, this time would be ~4 ns. for a slow (400 MeV/c) proton. This cut removes most events, but not those for which a kaon (τ = 12 ns.) comes to rest in the target or surrounding material and decays. These events are plotted in Fig. 4.15, which clearly shows two narrow structures at 200±4 and 236±5 MeV/c.

4.7 Track Selection

Tests are applied to ensure that only valid tracks are included in the data sample. The determination of the annihilation vertex (Section 4.1) leads to one such test. Only events whose vertex was located between X=-14.5 and X=-10.0 cm. are accepted. These limits assure that events originating other than in the heavy targets are rejected, resulting in a signal:background ratio of ~20:1 while accepting ~89% of the signal. In addition, each track is tested for continuity and for realistic slopes at the chambers to exclude particles scattered off of frames and decaying in flight with large opening angles. Finally, for particles emerging on a trajectory lying within or very near the plane of the target, the track passed through as much as 4 cm. of uranium (or 5 cm. of carbon) and the dE/dx correction could be very large (~100 MeV). Since the annihilation point along the plane of the target is not determined for single-track events, the correction cannot be accurately established. Consequently, tracks are discarded if they subtended an angle smaller than 5.5° with the plane of the target.

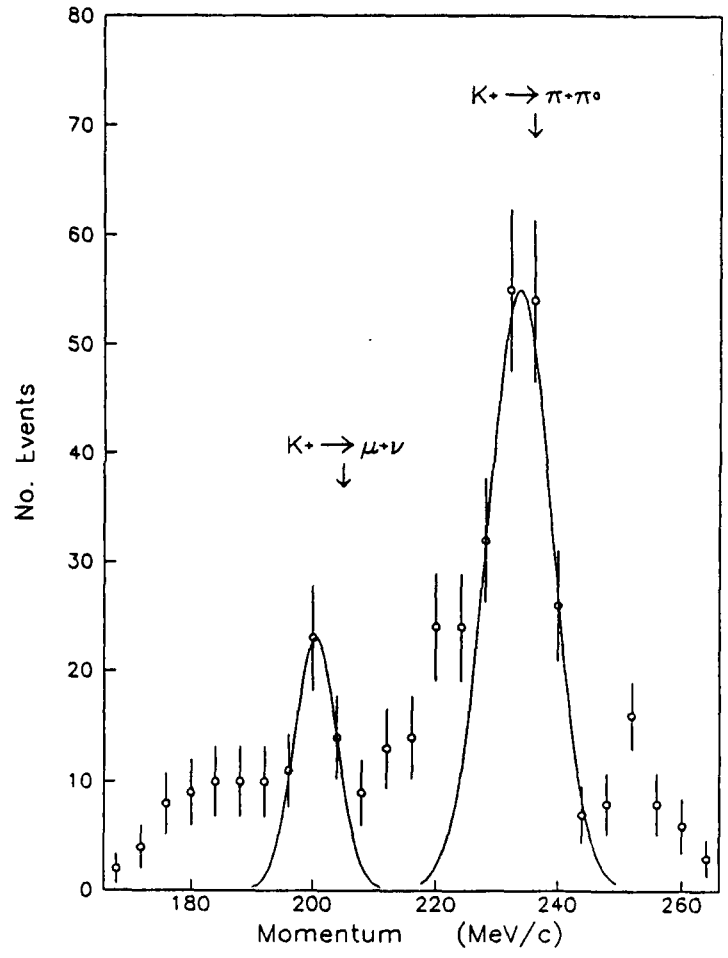

Figure 4.15: Delayed Events. Events plotted here arrived at the A hodoscope in excess of 7 ns. after the trigger began.

4.8 Correction for Acceptance

The small solid angle of the detector about the target (~1% of 4π steradians) necessitates a correction to the measurement in order to normalize the results to those which would have been seen by a detector fully enclosing the target. Furthermore, the magnetic field introduces a momentum dependence into the detector's acceptance. Both of these characteristics are described by an acceptance function, defined as

$$A(p) = \frac{Y_{meas}(p, \delta p)}{Y_{true}(p, \delta p)}, \tag{4.12}$$

where $Y_{meas}(p, \delta p)$ and $Y_{true}(p, \delta p)$ refer to the measured and true yields in a small interval δp around momentum p. A Monte Carlo calculation provides the acceptance function. In the calculation, the geometry of the detector is simulated and an integrating routine tracks a large number of particles, generated with random momentum and direction, from their origin in the target to a terminating counter (for accepted events) or to infinity (for misses). The acceptance function is found from

$$A(p) = \frac{N_{accepted}(p, \delta p)}{N_{generated}(p, \delta p)}, \tag{4.13}$$

where N designates the numbers of events accepted and generated in the calculation.

The accuracy of the acceptance function is assured by simulating the detector, physically realistic particle behavior, and algorithms similar to those used for data analysis. For example, the effects of finite wire spacing in the chambers, multiple scattering in the counters and photon converter, and

the algorithm used to determine momentum all contribute to ensure that the momentum resolution of the simulation is comparable to that of the detector. Ionization losses are calculated twice for each event. Initially, the generated particle loses energy as it escapes the target and enters the spectrometer. Once the momentum in the spectrometer is determined, the vertex momentum is reconstructed by integrating the energy loss with the same technique as the analysis program. Thus, any approximations in the correction to vertex momentum which are present in analysis are reproduced in the acceptance calculation. With the same objective, any cuts affecting track selection (Section 4.7) are included in order to create a realistic event sample.

Finally, pion decay into muons is simulated in order to evaluate possible distortions introduced into the charged-pion spectrum through that mechanism. The calculation estimates that fraction of pions which decay, noting their momentum prior to decay and determining the value of momentum which would be measured by the spectrometer following decay. Fig. 4.16 shows the parent and daughter spectra for these events based on the measured pion spectra. Significant distortions resulting from the different acceptances of T- and P-tracks are only observed near 150 MeV/c as bumps in the measured spectra.

Fig. 4.17 shows the acceptance function for charged pions for the uranium target. The acceptance is zero below ~100 MeV/c and rises rapidly with increasing momentum, leveling off above 250 MeV/c. Acceptance between 100 and 200 MeV/c is due primarily to side tracks, which are responsible for the shoulder near ~150 MeV/c. It is clear that for high-momentum

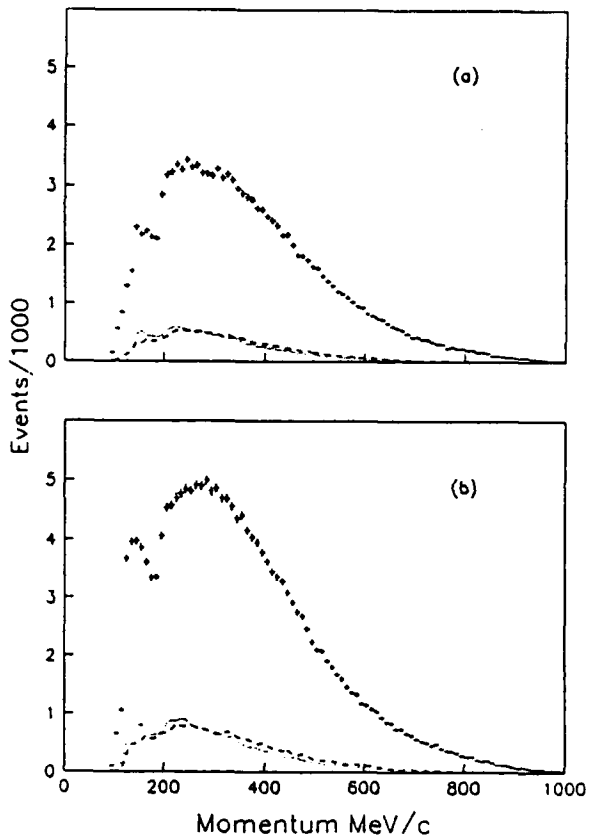

Figure 4.16: Spectrum of Charged Pions Decaying into Muons. The points with error bars represent all charged pions measured in the spectrometer. A monte carlo calculation predicts that a fraction of those pions will decay into muons. The dashed line shows the momentum distribution of such pions prior to decay, while the dotted line represents the distribution of the resulting daughter muons when measured in the spectrometer. (a) π^+; (b) π^-.

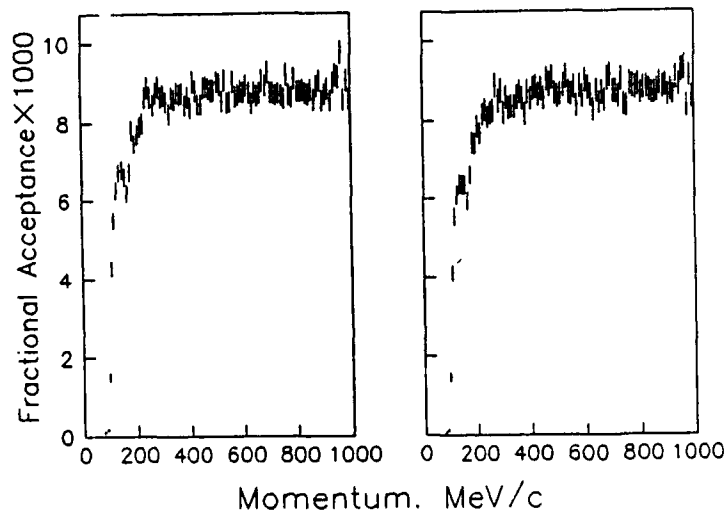

Figure 4.17: The Acceptance Function in Uranium. (a) π^+; (b) π^-.

tracks (which have small curvature) the acceptance is dominated by the solid angles of the detector elements about the target and, thus, is approximately constant. Lower limits of the acceptance are due to magnetic field curvature and dE/dx losses.

4.9 Multiplicity Normalization

Normalization of the measured yields to multiplicity per antiproton annihilation is facilitated by the CWC surrounding the target which counted the charged multiplicity for each event. The measured yield $Y_i(p)$, where i denotes the particle species ($i = e^{\pm}$, $\pi^{\pm}$, $K^{\pm}$, p, and d), are related to the absolute differential multiplicities by

$$\frac{dY_i(p)}{dp} = N_{\bar{p}}\, A_i(p)\, \frac{dM_i(p)}{dp}, \tag{4.14}$$

where $N_{\bar{p}}$ is the number of antiprotons which annihilate in the target, $A_i(p)$ is the acceptance function for the individual particle species, and $M_i(p)$ is the multiplicity per annihilation for the particle. These equations are constrained by

$$< M >= \sum M_i, \tag{4.15}$$

where $< M >$ is an experimental observable, the average charged multiplicity per event, determined by the cylindrical wire chamber. These equations, nine in number, are solved for the nine unknowns, $N_{\bar{p}}$ and $< M_i >$.

In practice, the number of equations is reduced by subtracting the raw multiplicities for $e^{\pm}$, $K^{\pm}$, and d (seen in Figs. 4.5-4.8, 4.13, and 4.14) from $< M >$. The analysis of protons has been completed to a level where changes in the proton multiplicity will change the pion results by only the systematic errors described in the following section.

4.10 Estimation of Errors

Errors relating to individual portions of the spectra have been noted where appropriate. These include possible kaon and electron contaminations in the pion spectra (Sections 4.4 and 4.5).

Systematic errors on the integrated multiplicities arise from a number of sources, of which two have been found to be significant. An uncertainty regarding the number of protons which enter the CWC (and are counted in the mean charged multiplicity), but are not sufficiently energetic to enter the detector, has been estimated using the Monte Carlo technique. They are found to be 2.3% for carbon target events and 2.5% for uranium target events. In addition, an uncertainty due to the measurements by different topologies (T-tracks and P-tracks) has been found to be 4.0%(4.7%) for π^+ (π^-) in carbon and 4.1% (4.9%) in uranium. In addition, statistical errors which are an order of magnitude smaller are included. Table 4.5 summarizes the errors for the particles and targets.

Table 4.5: Errors on Multiplicities. Systematic and statistical errors are quoted as percentage of total multiplicity.

Target	Particle	Systematic Error, %	Statistical Error, %
Carbon	π^+	4.6	0.6
	π^-	5.3	0.6
Uranium	π^+	4.8	0.5
	π^-	5.5	0.4

Chapter 5 Discussion and Results

5.1 Results

The measured multiplicities for charged pions following antiproton annihilation in hydrogen [33,35], carbon, and uranium are shown in Table 5.1. Results for photons [34,42–44,51] are given in Table 5.2, along with the combined pion multiplicity. For the most part, the photon multiplicity results from the decay $\pi^0 \rightarrow \gamma\gamma$, although small contributions are also present from $\eta \rightarrow \gamma\gamma$(2.7±0.4% per annihilation)[52] and $\omega^0 \rightarrow \pi^0\gamma$ (2.7±0.9% per annihilation)[53]. No corrections have been made for these contributions in calculating $< M(\pi^0) >= \frac{1}{2} < M(\gamma) >$. Hydrogen values have been included in order to demonstrate the effect of pion absorption in the nuclear environment. All multiplicities, with the one exception of π^- where the multiplicity increases slightly in going from hydrogen to carbon, are seen to decrease with increasing target mass, consistent with absorption effects within the target nuclei. The neutral/charged ratio is also constant to within 5% for all targets.

For annihilation on a proton compared to that on a neutron, the ratio

$$R_M = \frac{< M(\gamma) >}{(< M(\pi^+) > + < M(\pi^-) >)} \tag{5.1}$$

is predicted to vary by only 5%[54]. Experimentally, one may use data for annihilation on neutrons and protons in deuterium[55] to check this prediction. If one assumes that the energy spectra of all pions are similar in shape,

Table 5.1: Total Charged Pion Multiplicities. Hydrogen data are from Refs. 33 and 35. The first errors quoted are statistical the second systematic, except for hydrogen where the errors are combined.

TARGET	$< M(\pi^+) >$	$< M(\pi^-) >$	$< M(\pi^\pm) >$
Hydrogen	1.52±.06	1.52±.06	3.04±.08
Carbon	1.25±.01 ±.06	1.59±.01 ±.08	2.84±.01 ±.10
Uranium	0.99±.01 ±.05	1.48±.01 ±.08	2.47±.01 ±.09

Table 5.2: Total Neutral Pion and Combined Multiplicities. Hydrogen data are from Refs. 33–35. Neutral data for carbon and uranium are from Refs. 42–44 and 51. It is assumed that $< M(\pi^0) >= \frac{1}{2} < M(\gamma) >$. The first errors quoted are statistical, the second systematic, except for hydrogen, where the errors are combined.

TARGET	$< M(\gamma) >$	$< M(\pi^0) >$	$< M(\pi^{\pm 0}) >$
Hydrogen	3.80±.24	1.90±.12	4.94±.14
Carbon	3.46±.07 ±.21	1.73±.04 ±.10	4.57±.04 ±.15
Uranium	2.73±.06 ±.18	1.36±.03 ±.09	3.84±.03 ±.13

R_M = 1.15±0.03 fo $\bar{p}n$ annihilations and 1.22±0.02 for $\bar{p}p$ annihilations. Since nuclei are mixtures of protons and neutrons, it is expected that R_M will vary even less for such targets. One calculates, for deuterium, carbon, and uranium, respectively, R_M = 1.19±0.02, 1.22±0.09, and 1.10±0.09. These numbers agree within errors and place limits on effects due to charge exchange, as discussed in Riedlberger *et al.*[9], and escape of excess neutral pions due to resonance formation (η,ω) discussed by J. Cugnon [56]. The excess production of π^0's, relative to deuterium, $\Delta_D(M(\pi^0)/M(\pi^{\pm 0}))$, is 0.7±2.7% for carbon and -1.6±2.8% for uranium.

Riedlberger *et al.*[9] argue that charge exchange effects will favor conversion of neutral pions into charged pions. The net $\pi^0 \rightarrow \pi^{\pm}$ conversion probability is parametrized as f_{CE}, a constant, estimated to be 1.8±0.6%[9]. For a typical event, they show that $M(\pi^0)$ is expected to increase by $\sim\frac{3}{7}Zf_{CE}M(\pi^+)$ $+\frac{3}{7}(Z-1)f_{CE}M(\pi^-)$ for $Z = N$ nuclei. Ignoring second order effects, this gives, for carbon, $\Delta_D(M(\pi^0)/M(\pi^{\pm 0}) = -3.1 \pm 1.0\%$, within 1.4 standard deviations of our measurement. However, for uranium, ignoring the excess of N over Z, this quantity is -57±19%, in total disagreement with the measurement.

Cugnon [56] shows that production of η and ω, which may be expressed as a number of "equivalent pions", augments the overall multiplicity escaping the nucleus due to a lower interaction probability of the resonances with constituent nucleons. Both resonances preferentially decay into photons or π^0's (η: 87% photons, 13% $\pi^{\pm}$; ω: 53% photons, 47% $\pi^{\pm}$). Thus, the mechanism implies a disproportionate increase in the neutral multiplicity relative to charged multiplicity. The relevant estimates have not been included in

Ref. 56. Since the calculation requires an INC code, only the above limits are given here.

Results from PS183's measurement are compared to previous work in Fig. 5.1, where the total charged multiplicity is plotted against the cube root of the mass number of the target. Results from thirteen separate experiments [1–6,9,33,57–60] are contained in this plot, some of which have been averaged into single data points. The agreement between PS183's results and the other experiments is excellent.

Figs. 5.2 and 5.3 show the measured momenta spectra for π^+ and π^- for the two targets, carbon and uranium. Also plotted are π^+ spectra from McGaughey *et al.*[7] for the same targets, after interaction with 608 MeV/c antiprotons. The increased absorption for the in-flight data results from the deeper penetration of the antiproton prior to annihilation and consequently greater interaction of the generated pions with the nuclear matter [20,61]. The difference in the areas of these two sets of π^+ data is greater for the much larger uranium nucleus(30±7%), but is still quite significant for the carbon target(18±8%).

Also shown on Figs. 5.2 and 5.3 are the results of an INC model due to Hernandez and Oset[13]. The comparison here is for the π^- spectra only. On average, agreement between the model and the data is good. For all pions one finds that $< M(\pi^{\pm 0}) > = 4.57 \pm 0.16$ (carbon) and 3.84±0.13 (uranium), as given in Table 5.2. The comparable INC results are 4.64 (for carbon, where the annihilation has been assumed to occur from the n=4, l=3 state) and 3.90 (for uranium, with annihilation from the n=9, l=8 state). Prediction and measurement are in agreement to within 2%.

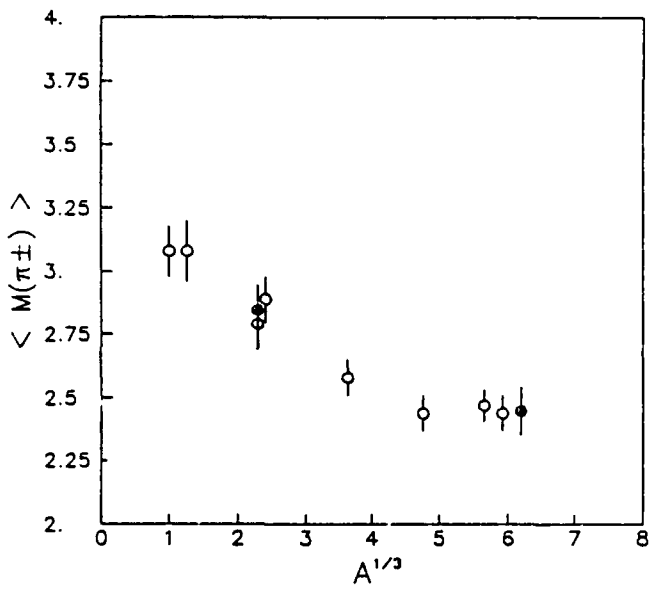

Figure 5.1: Charged Pion Multiplicity Versus the Cube Root of the Mass Number. In addition to data from PS183, the following references are used: hydrogen[9,33,57], deuterium[9,58],carbon[4,59,60], nitrogen[9], titanium [59], nuclear emulsion[1–3,5,6,33], tantalum[59], lead[59]. Solid circles: PS183 data; Open circles: other data.

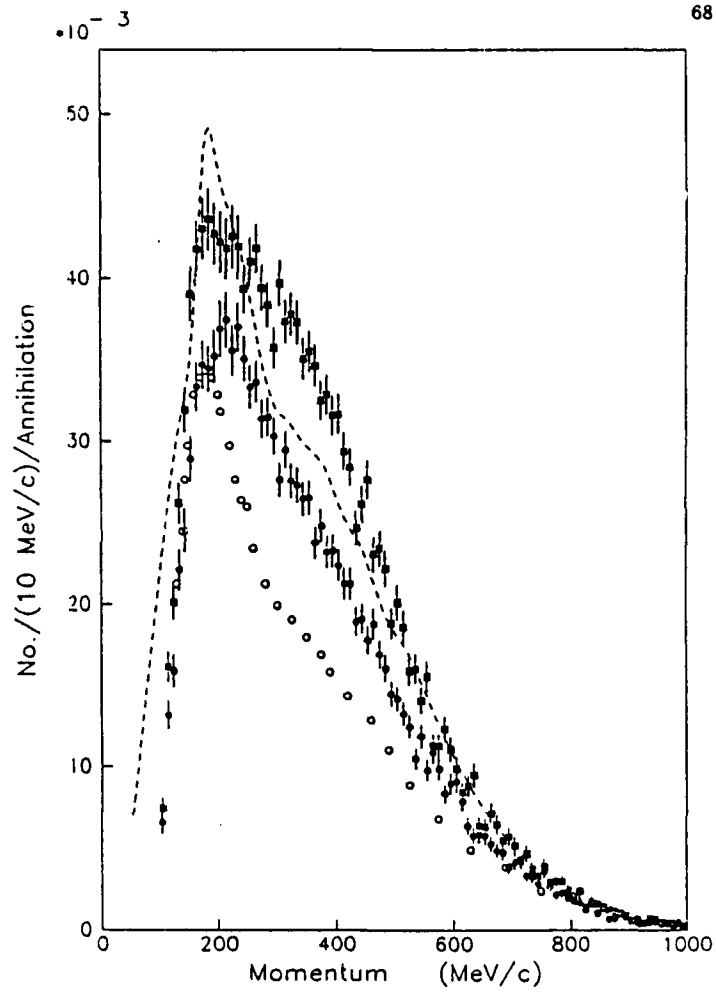

Figure 5.2: Charged Pion Yield for Carbon. Results are given per 10 MeV/c interval per annihilation. Also shown are π^+ data from Ref. 7 and INC predictions for π^- from Ref. 13. Solid squares: PS183's π^- measurement; solid circles: PS183's π^+ measurement; dashed line: π^- prediction [13]; open circles: π^+ measurement [7].

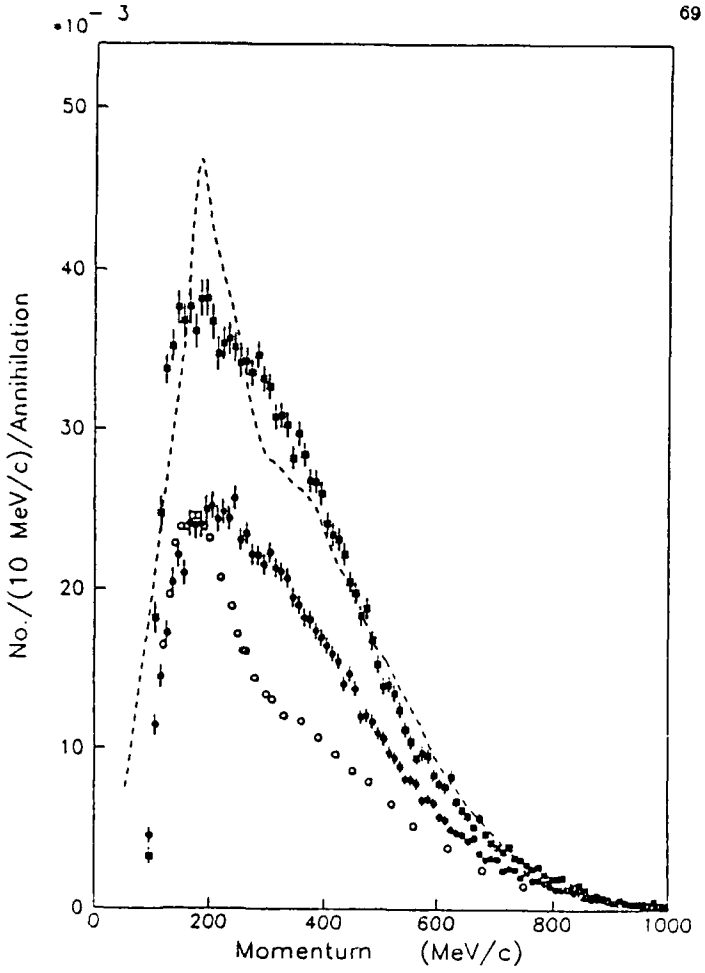

Figure 5.3: Charged Pion Yield for Uranium. Results are given per 10 MeV/c interval per annihilation. Also shown are π^+ data from Ref. 7 and INC predictions for π^- from Ref. 13. Solid squares: PS183's π^- measurement; solid circles: PS183's π^+ measurement; dashed line: π^- prediction [13]; open circles: π^+ measurement [7].

5.2 Intranuclear Cascade Model

The excellent agreement between the measured and predicted integrated multiplicities does not extend to the shapes of the spectra, as seen in Figs. 5.2 and 5.3. Two regions of disagreement are apparent for either target. Near 300 MeV/c the INC model predicts a shoulder, due to delta-resonance formation leading to pion absorption[13], which is not seen in the data(π^-). Also, near 200 MeV/c, the INC predicts a sharp peak which is not seen. The population of the latter region is enhanced in the INC model by higher-momentum pions which have been degraded, either due to the aforementioned resonance scattering or quasi-elastic scattering. For the region above 500 MeV/c, where quasi-elastic scattering is the principle mechanism for pion interaction, there is good agreement between the INC and the data (particularly for carbon), suggesting that the latter mechanism is correctly implemented.

The momentum resolution of the detector in the vicinity of the disagreements is demonstrated by the observation of kaon decay lines (Fig. 4.15), which clearly show FWHM widths much smaller than the ~100 MeV/c wide structures predicted near 200 and 300 MeV/c in the INC[13]. Thus, such features in the data would not have been degraded by resolution effects.

The disagreement between the shapes of the curves near 300 MeV/c suggests that the $\Delta N\pi$ coupling strength, f^*, in Ref. 13 may be too large. Reducing the magnitude of this quantity may remove the predicted shoulder and simultaneously decrease the peak near 200 MeV/c. Furthermore, the annihilation radius might be adjusted slightly to maintain good overall agreement in the integrated multiplicities.

5.3 Energy Transfer

The total energy released with each of the pion species is given by

$$< E(TOTAL) >^{i} = < M(\pi^{i}) >< E(\pi^{i}) >, \; i = 0, +, - \quad , \tag{5.2}$$

where $< M(\gamma) >< E(\gamma) > = < M(\pi^0) >< E(\pi^0) >$. By definition,

$$< E(TRANSFER) >^{\pm 0} = 1876.6 - \sum_{i} < E(TOTAL) >^{i} \quad , \tag{5.3}$$

where the total annihilation energy is equal to two proton masses for annihilation at rest.

The average multiplicities and energies appropriate to Eq. 5.2 are given in Tables 5.1–5.3. The energy transfer represents energy released in the antiproton-nucleon annihilation which is deposited within the target nucleus and with ejected nucleons through interaction with escaping pions. This quantity is calculated to be 119±59 MeV for carbon. For the more extensive uranium nucleus, it is nearly three times as large, 455±50 MeV. The effects of energy transfer from charged pions are clearly seen in Fig. 5.4. For uranium, Jasselette *et al.*[20] gives $< E(TRANSFER) >^{\pm 0} \simeq$ 380 MeV, slightly smaller than the measured value. Hernandez and Oset[13] predict a value of 480 MeV, which expresses in a compact way the overall agreement between the data and their model. For carbon, they provide two numbers, depending on the atomic state from which the annihilation occurs: 271 MeV(n=3, l=2) and 217 MeV(n=4, l=3). The smaller of these numbers is nearly two standard deviations larger than the measurement.

Greater beam energy leads to greater penetration depth in the nucleus and consequently greater interaction of generated pions within the nucleus,

Table 5.3: Average Energy per Photon and Charged Pion and Energy Transfer. $< E(TOT) > = \sum_i < E(TOTAL) >^i$. Hydrogen data are from Refs. 33–35. Neutral data for carbon and uranium are from Refs. 42–44 and 51.

TARGET	$< E(\gamma) >$	$< E(\pi^{\pm}) >$	$< E(TOT) >$	$< E(TRANS) >$
Hydrogen	194±2	395±2	1938±57	
Carbon	196±2	380±2	1758±59	119±59
Uranium	184±2	372±2	1422±50	455±50

thus resulting in a larger energy transfer. The effect is seen even as low as 608 MeV/c. Using the data of Ref. 7 with multiplicities provided in Ref. 56, one calculates $< E(TRANSFER) >$=471±126 MeV for carbon and 871±84 MeV for uranium. In deriving these quantities, it is assumed that the ratio of neutral pions to charged pions is the same as for hydrogen to correct for the presence of π^0's. These numbers represent an increase in the energy transfer by a factor of 4.0±2.2 for carbon and 1.9±0.3 for uranium relative to data at rest. For either target, very significant increases in the energy transfer result from increasing the beam energy.

5.4 Multifragmentation

It is possible to estimate E*, the residual energy retained by the nucleus following the fast intranuclear cascade (which terminates after $\sim 10^{-22}$ sec.) If the energy is thermalized, further evolution of the nucleus will depend mainly on E*/A[15]. This experiment's measurement of $< E(TRANSFER) >$ provides a first step toward the calculation of E*, but lacks the correction for

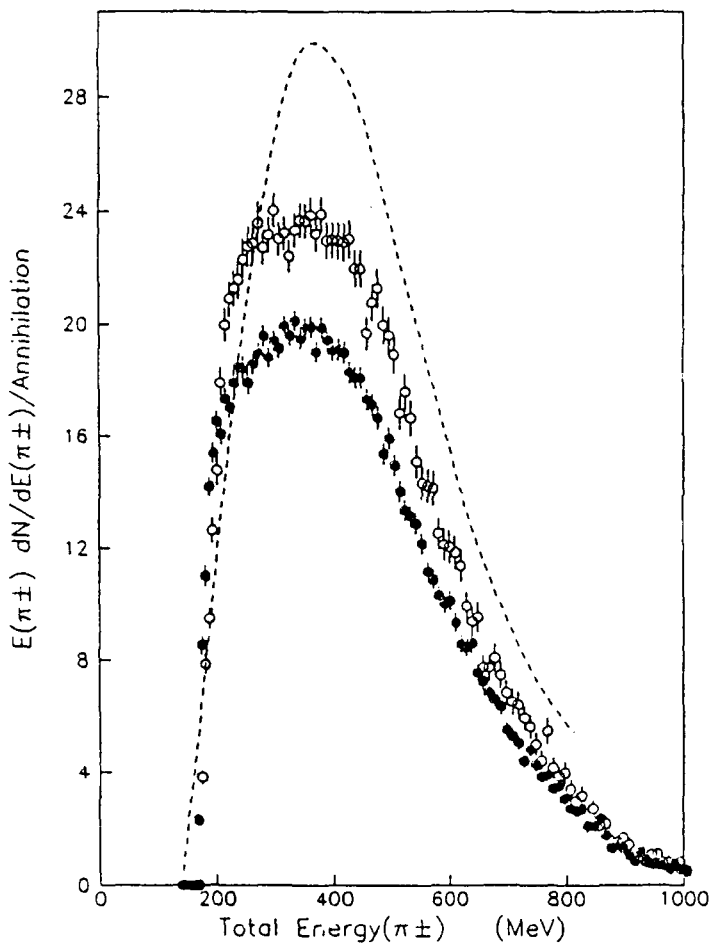

Figure 5.4: Total Energy Yield for Charged Pions. Results are given per 10 MeV interval for carbon(open circles), uranium(solid circles) and hydrogen[31,33] (dashed line).

the energy carried off by nucleons ejected during the cascade. A number of publications have dealt with contributions to this correction. In particular, Angelopoulos *et al.*[62] have measured neutron spectra from uranium. Markiel *et al.*[63] have published measurements of low-energy protons and light ions. McGaughey *et al.*[7] have measured protons following in-flight annihilations. Since none of these provides an inclusive measurement, it is necessary to use an INC calculation for W_{eject}, the energy of nucleons ejected by the cascade process. Jasselette *et al.*[20] have calculated W_{eject}=274 MeV for uranium. Thus, $E^* = < E(TRANSFER) > - W_{eject} \simeq 181$ MeV $\simeq 0.8$ MeV/nucleon, which is well below the region where multifragmentation is likely to occur.

In view of previously discussed energy transfers at 608 MeV/c, it is expected that E^* would increase with increasing beam momentum. Greater beam momentum increases the penetration depth of the antiproton into the nucleus thus permitting greater interaction of annihilation pions with nuclear matter. Cugnon[15] has used the INC model to show that E^* scales by a factor of five in ^{98}Mo as the beam kinetic energy is increased to 2 GeV. For an even heavier nucleus such as uranium, this would imply, from the measurement, that E^*/A would be at least 4 MeV/nucleon, which is within the multifragmentation regime.

Inducing multifragmentation using high-momentum antiproton beams is, however, a subject of some current debate. McGaughey *et al.*[64], using a different INC code[11], see no significant thermalization of the annihilation energy for 1.3 GeV antiprotons on a nucleus of atomic mass 100. They point out that primordial pions generated following such annihilations have too

large an energy in order to immediately participate in Δ-resonance formation and absorption ($\pi N \rightarrow \Delta$, $\Delta N \rightarrow NN$). (The Δ resonance dominates others. The next resonance, at $p_\pi \simeq 1.5$ GeV/c, is an order of magnitude smaller.) However, it is not clear from [64] how McGaughey *et al.* have treated these high-momentum πN interactions in detail. In this regard, it is worth noting that, in an article by some of the same authors[7], there is considerable disagreement between the model and the data for both pions and protons in the high momentum region, with the model underestimating the measurement by as much as a factor of five. Although different points of view exist on the question of thermalization for beam energies of 1-2 GeV, the possibility of multifragmentation following antiproton annihilation deep inside the nucleus seems nonetheless intriguing.

Chapter 6 Summary and Conclusions

The need to elucidate nuclear behavior following the deposit of a large concentration of energy within or near the nucleus motivated the research described here. Toward this end, the spectra of emitted pions and nucleons following antiproton annihilation at rest in carbon and uranium were measured. The charged pion component is the subject of this thesis. This work contributes to two objectives: (1) the testing of the intranuclear cascade model (INC) for multiple pion interactions in nuclei; and, (2) a measurement of the residual energy which characterizes the nucleus following the cascade and which determines its subsequent evolution.

In pursuit of these objectives, the annihilations of $\sim 10^6$ antiprotons in carbon and uranium targets were observed with a magnetic spectrometer whose momentum resolution, $\delta(p)/p$, varied from $\sim$2% at 200 MeV/c to $\sim$5% at 1000 MeV/c. Corrections are applied to the data to account for multiple scattering and energy loss in the elements of the detector, for pion decay into muons, and for the acceptance of the detector. The measured spectra are normalized per antiproton annihilation.

The charged multiplicity, $< M(\pi^\pm) >$, for carbon and uranium, respectively, is found to be 2.84±0.10 and 2.47±0.09 particles per annihilation. These values, combined with that of hydrogen (3.04±0.08)[33,35], clearly show nuclear absorption increasing as mass number increases. In addition, the ratios of photons (from $\pi^0 \rightarrow \gamma\gamma$) to charged pion multiplicity are constant within errors: 1.19±0.02, 1.22±0.09, and 1.10±0.09 for

deuterium[55], carbon, and uranium, respectively. These ratios demonstrate that excess neutral production due to charge exchange[9] or neutral resonance formation[56] is limited, with the excess production of neutral pions, relative to deuterium, being 0.7±2.7% for carbon and −1.6±2.8% for uranium.

The total pion multiplicities, $< M(\pi^{\pm 0}) >$, are found to be 4.57±0.16 (carbon) and 3.84±0.13 (uranium). These values are seen to agree well with INC predictions of 4.64 and 3.90[13]. Some disagreement exists, however, between the measured and predicted spectra, possibly resulting from excessive delta-resonance formation in the model or from a flaw in the structure of the model (such as the assumption of immediate hadronization of the released energy at the point of annihilation). It is not clear that the model suffers from technical or fundamental uncertainties, or both. Technical problems arise due to the complexity of the many-body problem. Approximations are made, for which the implications are not always clear. These include such choices as limiting the number of nucleons involved in the pion absorption process, choosing one method of integration over another, etc. Unfortunately, these technical questions are folded in with fundamental physics issues which one would like to solve. These would include elucidating the magnitude and nature of the optical potential and determining off-shell cross sections.

Less absorption occurs for antiproton annihilations at rest than for in-flight (608 MeV/c) annihilations [7]: total charged multiplicity is found to be greater for at-rest annihilations by 18±8% (30±7%) in carbon (uranium). The difference results from deeper penetration of the in-flight antiproton into the nucleus prior to annihilation and, thus, greater interaction of the annihilation pions with nuclear matter.

The energy transfers from the annihilation pions to all nucleons are found to be 119±59 and 455±50 MeV for carbon and uranium. The INC model predicts the increase with increasing mass number, but expects somewhat larger values of 217 and 480 MeV for the energy transfers.

Subtracting an INC prediction for the energy of ejected nucleons from the energy transfer gives an estimate of the residual energy E^* remaining within the nucleus following the intranuclear cascade. This is found to be 0.8 MeV/nucleon for uranium. It has been shown that energy transfer increases with increasing beam energy [7], implying an increase in the residual energy as well. It is predicted that E^* increases by a factor of five as the beam kinetic energy is increased to 2 GeV[15]. Thus, one might expect that $E^* \rightarrow 4$ MeV/nucleon for uranium. Multifragmentation of the nucleus, an unobserved but intriguing phenomenon, may occur in this energy regime. However, at least one reference[64] argues that the phenomenon will not occur. An appropriate experiment might thus serve two purposes: (1) assuming it were successful and the multifragmentation state were attained, it would usher in a new and exciting field of research; (2) in any case it would clearly help to determine the most realistic of various INC codes, including those discussed in this thesis [11-14,65].

References

[1] H. Barkas *et al.*, Phys. Rev. **105**, 1037 (1957).

[2] E. Amaldi *et al.*, Nuovo Cimento **14**, 977 (1959).

[3] O. Chamberlain *et al.*, Phys. Rev. **113**, 1615 (1959).

[4] L.E. Agnew *et al.*, Phys. Rev. **118**, 1371 (1960).

[5] A. Berthelot *et al.*, Nuc. Phys. **14**, 545 (1960).

[6] A.G. Ekspong *et al.*, Nuc. Phys. **22**, 353 (1961).

[7] P.L. McGaughey *et al.*, Phys. Rev. Lett. **56**, 2156 (1986).

[8] F. Balestra *et al.*, Nucl. Phys. **A491**, 541 (1989).

[9] J. Riedlberger *et al.*, Phys. Rev. **C40**, 2717 (1989).

[10] C. Guaraldo, Nucl. Phys. (Proc. Suppl.) **B8** (1989) 243; Nuovo Cimento **A102**, N. 4, 1137 (1989).

[11] M.R. Clover *et al.*, Phys. Rev. **C26**, 2138 (1982).

[12] J. Cugnon *et al.*, Nucl. Phys. **A500**, 701 (1989).

[13] E. Hernandez and E. Oset, Nucl. Phys. **A455**, 584 (1986), and private communication.

[14] A.S. Iljinov *et al.*, Nucl. Phys. **A382**, 378 (1982).

[15] J. Cugnon, Nucl. Phys. (Proc. Suppl.) **B8**, 255 (1989).

[16] J. Cugnon and J. Vandermeullen, Ann. Phys. Fr. **14**, 49 (1989).

[17] S. Polikanov, Nuc. Phys. **A478**, 805c (1988).

[18] U. Fano, Ann. Rev. Nucl. Sci. **13**, 1 (1963).

[19] Th. Köhler, Phys. Lett. **B176**, 327 (1986).

[20] P. Jasselette *et al.*, Nucl. Phys. **A484**, 542 (1988).

[21] H. Poth, *Proc. Int. Symp. on Medium-Energy Nucleon and Antinucleon Scattering, Bad Honnef 1985.* H.V. von Geramb(ed.) Springer Lecture Notes in Physics, Berlin, 357 (1985).

[22] T.P. Gorringe *et al.*, Phys. Lett. **162B**, 71 (1985).

[23] D. Rohmann *et al.*, Z. Phys. **A325**, 261 (1986).

[24] L.M. Simons, *Physics at LEAR with Low Energy Antiprotons*, C. Amsler *et al.*(eds.) Harwood Academic Publishers, Switzerland, 703 (1988).

[25] W. Kanert, Phys. Rev. Lett. **56**, 2368 (1986).

[26] H. Poth, Workshop on Antimatter Physics at Low Energy. Batavia, 325 (1986); CERN-EP/86-105.

[27] C.I. Batty, Nucl. Phys. **A372**, 418 and 433 (1981).

[28] D. Garetta, *et al.*, Phys. Lett. **135B**, 266 (1984); **139B**, 464 (1984).

[29] H. Poth *et al.*, *Physics with Antiprotons at LEAR in the ACOL Era*, U. Gastaldi *et al.*(eds.) Frontiéres, Gif-sur-Yvette, France, 312 (1985); Phys. Lett. **B176**, 327 (1986).

[30] T. von Egidy, Nature **328**, 773 (1987).

[31] R. Bizzarri *et al.*, Lett. Nuovo Cimento **2**, 431 (1969).

[32] G.A. Smith, *The Elementary Structure of Matter*, J.-M. Richard *et al.*(eds.) Springer Proceedings in Physics No. 26, Springer-Verlag, Germany, 197 (1988).

[33] C. Baltay *et al.*, Phys. Rev. **145**, 1103 (1966).

[34] G. Backenstoss *et al.*, Nuc. Phys. **B228**, 424 (1983).

[35] J. Roy, *Proceedings of the Fourth International Symposium on $N\bar{N}$ Interactions.* Syracuse University, N.Y., III-1 (1975).

[36] J. Cugnon and J. Vandermeullen, Phys. Rev. **C36**, 2726 (1987).

[37] A. Angelopoulos *et al.*, Phys. Lett. **B205**, 590 (1988).

[38] J.P. Bocquet *et al.*, *Physics at LEAR with Low Energy Antiprotons*, C. Amsler *et al.*(eds.) Harwood Academic Publishers, Switzerland, 793 (1988).

[39] A.S. Botvina *et al.*, Nucl. Phys. **A475**, 663 (1987).

[40] J.C. Biard, "A Study of the Operational Characteristics of the PS183 Drift Chambers," Penn. State Univ. M.S. thesis (1985) unpublished.

[41] M.J. Soulliere, "Charged Meson Production From Proton-Antiproton Annihilation at Rest," Penn. State Univ. Ph.D. thesis (1987) unpublished.

[42] T.A. Armstrong *et al.*, Phys. Lett. **B178**, 441 (1986).

[43] T.A. Armstrong *et al.*, Z. Phys. **A331**, 519 (1988).

[44] T.A. Armstrong *et al.*, Z. Phys. **A332**, 467 (1989).

[45] P. Denes, Nucl. Instrum. Meth. **A236**, 354 (1985).

[46] W.H. Barkas and M.J. Berger, "Tables of Energy Losses and Ranges of Heavy Charged Particles," NASA SP-3013, 1 (1964).

[47] D.M. Ritson, *Techniques of High Energy Physics*, Interscience Publishers,Inc., New York (1961).

[48] D.H. Perkins, *Introduction to High Energy Physics*, Addison-Weseley, Menlo Park, California (1987).

[49] D.K. Griegel, "Least Squares Momentum Reconstruction for the PS183 Spectrometer," Penn. State Univ. Undergraduate Scholars thesis (1985) unpublished.

[50] H. Wind, Nucl. Instrum. Meth. **115**, 431 (1974).

[51] E.D. Minor *et al.*, "Charged Pion Spectra and Energy Transfer Following Antiproton Annihilation at Rest in Carbon and Uranium," submitted to Z. Phys. A (1989).

[52] M. Chiba *et al.*, Phys. Rev. **D39**, 3227 (1989).

[53] G. Levman *et al.*, Phys. Rev. **D21**, 1 (1980).

[54] J. Vandermeullen, Lett. Nuovo Cimento **28**, 60 (1980), and references therein.

[55] T. Kalogeropoulos *et al.*, Phys. Rev. Lett. **33**, 1631 (1974).

[56] J. Cugnon, Phys. Rev. **C40**, 1822 (1989).

[57] J. Díaz *et al.*, Nucl. Phys. **B16**, 239 (1970).

[58] T. Kalogeropoulos and G.S. Tzanakos, Phys. Rev. **D22**, 2585 (1980).

[59] W.M. Bugg *et al.*, Phys. Rev. Lett. **31**, 475 (1973).

[60] M. Wade and V.G. Lind, Phys. Rev. **D14**, 1182 (1976).

[61] M. Cahay *et al.*, Nucl. Phys. **A393**, 237 (1983).

[62] A. Angelopoulos *et al.*, Phys. Lett. **159B**, 210 (1985).

[63] W. Markiel *et al.*, Nuc. Phys. **A485**, 445 (1988).

[64] P. McGaughey *et al.*, Phys. Lett. **166B**, 3 (1986).

[65] J. Cugnon *et al.*, Nucl. Phys. **A379**, 553 (1982).

Nuclear Instruments and Methods in Physics Research A289 (1990) 109–114
North-Holland

THE LEAR PS177 LOW ENERGY K^+ DETECTOR *

T.A. ARMSTRONG, D.M. ELIAS, R.A. LEWIS, E.D. MINOR, J. PASSANEAU and G.A. SMITH

Laboratory for Elementary Particle Science, Department of Physics, Pennsylvania State University, University Park, PA 16802, USA

Received 10 August 1989 and in revised form 16 November 1989

We have constructed and used a low energy, wide energy band, large solid angle K^+ detector in LEAR experiment PS177. In this application, the detector is used to search for hypernuclear effects in association with fission induced in a uranium target by antiproton annihilation at rest. We identify K^+ in the momentum range 250–750 MeV/c in a solid angle of 16% of 4π sr. The yield of K^+ is in good agreement with predictions based on a Monte Carlo simulation and previous measurements of inclusive antiproton annihilation in uranium.

1. Introduction

LEAR experiment PS177 has observed delayed fission due to antiprotons stopping in thin uranium [1] and bismuth [2] targets. Because the lifetime of this effect approximates that of the free Λ^0 hyperon, it has been suggested that the effect is due to a hypernuclear state which, when it decays weakly (i.e. $\Lambda N \rightarrow NN$), induces fission. If this explanation is correct, the production of this state must be accompanied by a meson of strangeness plus one to conserve overall strangeness. Thus, the observation of a K^+ in coincidence with the delayed fission would confirm the hypernuclear hypothesis. Because the rate per antiproton for this process is small ($\sim 10^{-3}$), an appropriate detector must have large acceptance in both solid angle and energy. In the following discussion we describe a detector, called the Kaon Range Telescope (KRT), which was built and used in a follow-on run of PS177, and satisfies these criteria.

2. The kaon range telescope (KRT)

The KRT was designed to make a simultaneous measurement of the direction, energy loss and lifetime of the K^+. The fundamental concepts utilized in the design of the KRT were recognized many years ago, albeit incorporated into smaller detectors with less current technologies [3]. A schematic drawing of the KRT is shown in fig. 1. It is rectangular in shape, $100 \times 100 \times 50$ cm^3 in size, and comprised of 25 towers (A, B, C, $\cdots$) each of size $20 \times 20 \times 50$ cm^3. The front face of the KRT was placed 45 cm from the target behind one of the two parallel-plate avalanche chambers (PPAC) used to detect fission fragments [1,2]. The only significant materials between the target and the KRT were the 4-mm thick aluminum backing of the PPAC and a 20-mm thick aluminum vacuum box (not shown). So positioned, the KRT subtended 16% of the full 4π sr solid angle.

A schematic drawing of a tower is shown in fig. 2. It is constructed of 36 acrylic scintillator [4] plates and 12 iron plates, which alternate every third scintillator plate.

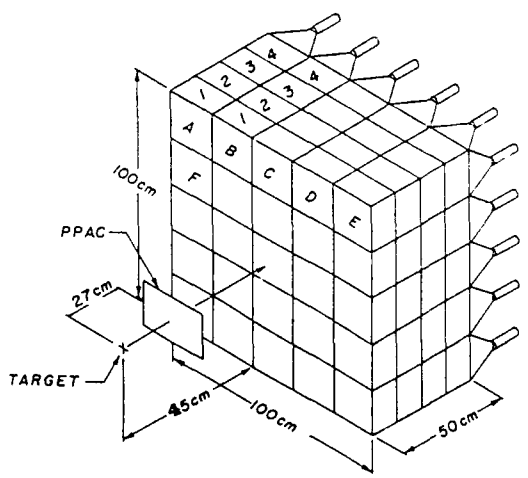

Fig. 1. Isometric view of the KRT, showing its 25 towers, each containing 4 cells. The front face of the KRT was 45 cm from the target. Also shown is one of the parallel-plate avalanche chambers (PPAC) used to detect fission fragments. Not shown is the vacuum box surrounding the target and PPAC.

* Work supported in part by the Air Force Office of Scientific Research, Air Force Systems Command, USAF under grant AFOSR 87-0246.

0168-9002/90/$03.50 © Elsevier Science Publishers B.V. (North-Holland)

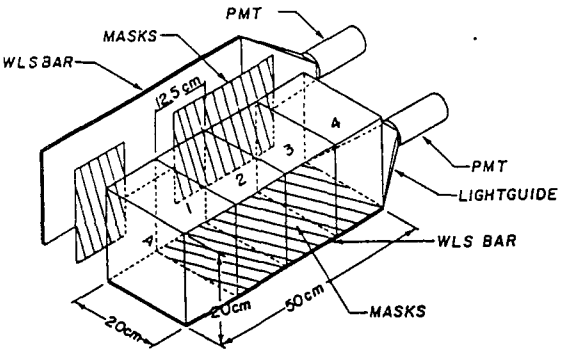

Fig. 2. Cut-away isometric view of a tower, showing two wavelength shifter bars (WLS) used for readout through lightguides to photomultiplier tubes (PMT), and masks for providing longitudinal segmentation.

Each scintillator plate is wrapped in 25-μm aluminum foil for light tightness. The scintillator is read out through wavelength shifter (WLS) bars [5] on each of the four sides of the tower (for clarity, only two bars are shown in fig. 2) to a plastic lightguide and Amperex XP2230 photomultiplier tube (PMT). Each WLS bar is mounted on a single 0.16-cm thick piece of G-10 board at the front of the tower, which also provides light tightness. Each tower is divided into four equal cells (1, 2, 3, 4) of length 12.5 cm. This is accomplished by placing 25 μm aluminum foil masks on each side of the tower so that only one quarter of the tower surface (a cell) can be read out (e.g. in fig. 2 cells A1 and A2 are read out on the bottom and back sides of the tower, respectively). In this manner longitudinal segmentation is created.

The scintillator and steel stack was compressed in a jig and wrapped in 25-μm aluminum foil, leaving an opening on each side at the appropriate cell position to match an opening on the WLS bar which was also wrapped in aluminum foil. The jig was removed, and the WLS bars were positioned and held in place with tape wrapping. Each tower was inserted into an 0.08-cm thick aluminum box, which was attached to the front plate of G-10 and at the back end of the tower to a 1.27-cm aluminum plate, through which four holes were drilled to permit access for the lightguides and PMTs. A threaded rod attached to the backplate was tightened to maintain the overall structural rigidity of the tower. The adiabatic lightguides are constructed of six strips of formed 0.64-cm thick lucite with polished edges. They are terminated on a 5-cm diameter × 0.64-cm thick lucite disk, which is glued to the PMT face with epoxy, and wrapped in aluminum foil.

In summary, the KRT is comprised of 100 cells which provide energy loss and timing information, as well as coarse tracking in three dimensions. Both the scintillator and iron serve as moderators, contributing roughly equally to energy loss. The 50-cm thickness of each tower stops kaons up to 750 MeV/c. In this application, materials between the target and the KRT render a low momentum cutoff of 250 MeV/c. A typical kaon deposits ~ 60 MeV per cell in the scintillator as it ranges. A muon (or pion) from a stopped K^+ decay ($K^+ \to \mu^+\nu$ or $\pi^+\pi^0$) deposits ~ 50 MeV per cell. On the basis of a previous measurement of 0.8 photoelectrons per MeV for a similar scintillator of half the linear dimension [6], ~ 20 photoelectrons per cell are expected. The cell size was chosen so that a muon (or pion) from a stopped K^+ decay (almost) always leaves the cell in which the K^+ stops and hence is independently recorded in adjacent cells. This provides a signature for K^+ decay, which is delayed on the average by its lifetime of 12.4 ns.

3. Monte Carlo simulation

In order to simulate the performance of the KRT, a large number of K^+ and π^+ tracks were created within the solid angle of the assuming isotropic production and

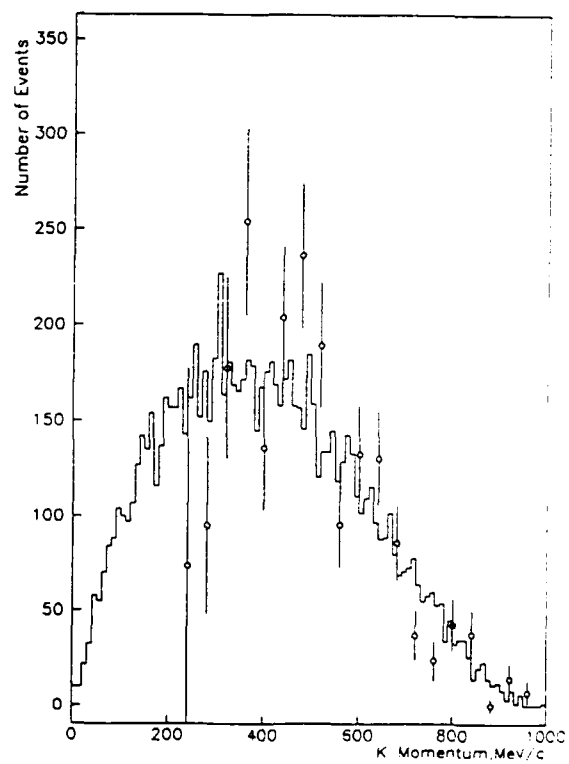

Fig. 3. Monte Carlo generated K^+ spectrum (histogram) for antiproton–nucleon annihilation at rest, compared with a measured spectrum above 250 MeV/c (circles) for antiproton–uranium annihilation at rest [8].

Table 1
Chronological history of a typical K^+ decay (Monte Carlo) in the KRT.

Cell	Time [ns]	Pulse height [MeV]	Early [MeV]	Late [MeV]
T1	4.2	51.5	x	
Y1	4.6	75.9	x	
Y2	5.1	56.0	x	
T2	9.1	43.9		x
T3	9.5	45.5		x
Pulse height sums			183.4	89.4

momentum spectra from antiproton–nucleon annihilation at rest [7]. To verify the appropriateness of using these spectra for heavy nuclear targets, a comparison was made with uranium data from LEAR experiment PS183 [8] for momenta above 250 MeV/c. Although limited by statistics in the case of K^+ (see fig. 3), the comparison was found to be good overall.

Using these tracks, an algorithm was developed for identifying stopped K^+ which decay in the KRT as well as rejecting contamination from stopped π^+ decays ($\pi^+ \to \mu^+ \nu$) which live an average of 26 ns, or subsequent $\mu^+ \to e^+ \nu \bar{\nu}$ decays which live an average of 2.2 μs. Kaon and pion tracks were swum from the target through the KRT. Energy loss was computed along the path, including the 24 mm of aluminum in the PPAC and vacuum walls of the fission fragment detector. Multiple coulomb scattering effects were not included, as the coarseness of the cell structure did not warrant it. Time and pulse height signals from each cell were recorded. A typical stopped K^+ event is shown in table 1. The K^+ arrives in the first cell at 4.2 ns, hits two additional cells at 4.6 and 5.1 ns, then decays at 9.1 ns with the decay muon subsequently hitting an additional cell at 9.5 ns before leaving the KRT.

The event identification algorithm is structured as follows. All hits are arranged in chronological order and divided into two time groups, early or late. A discontinuity in chronology of greater than 2 ns between sequential hits, called a time gap, defines the boundary between the groups. This is based on the observation in the actual data that the rms width of pulses detected from individual cells is typically 2 ns, which is due to a combination of effects, including differences in propagation time of light pulses in a detector of finite size, the intrinsic response time of the scintillator and WLS to charged particles, and statistics at the photocathode of

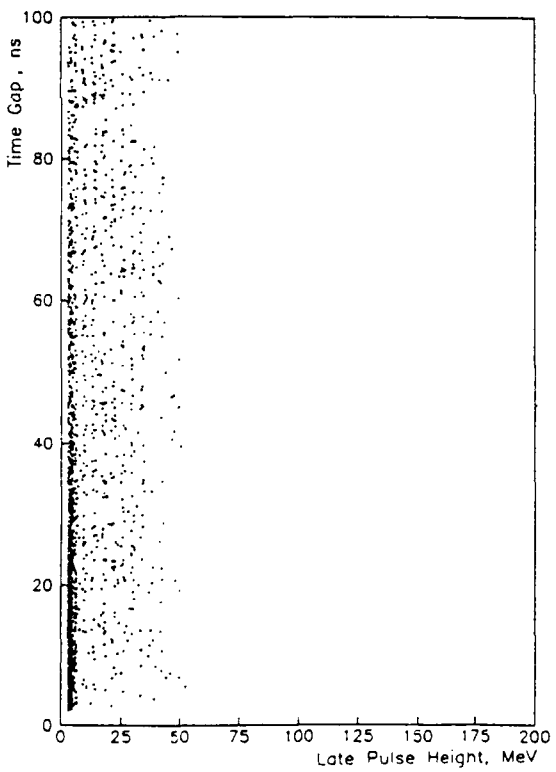

Fig. 4. Plot of the time gap versus late pulse height for Monte Carlo simulated π^+ tracks stopping in the KRT.

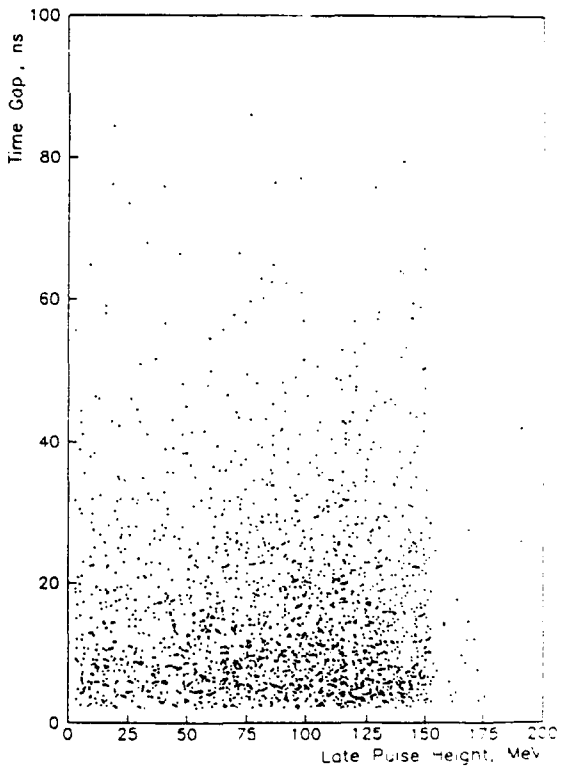

Fig. 5. Plot of the time gap versus late pulse height for Monte Carlo simulated K^+ tracks stopping in the KRT.

the PMT. For example, the event of table 1 has three early hits, two late hits, and one time gap. Pulse heights for all cells in a time group are summed to distinguish the energy of the K^+ from its decay products, as illustrated in table 1.

In figs. 4 and 5 we plot the late pulse height deposited in the KRT versus the time gap for π^+ and K^+, respectively. In fig. 4 the intense band at the left-hand border is due to μ^+ which stop in the KRT. The remaining events scattered at larger pulse heights are due to e^+ from μ^+ decay. By contrast, the decay products from K^+ decay (μ^+, π^+) in fig. 5 are scattered over a much larger area. Using this distinction to advantage, we define K^+ events as those with late pulse height > 25 MeV and 1 < time gap < 50 ns. With these criteria, we successfully identify 1999 out of the original 6375 K^+ in the range 250–750 MeV/c (31%). Of the remaining 4376, 2869 K^+ (45%) are undetectable since they decay in flight, and 1507 (24%) stop and decay in a surface boundary cell where the decay μ^+ or π^+ moves in an outward direction and is not contained. In this regard, we note that 42, 32 and 8 cells have 1, 2 and 3 exterior boundary surfaces, respectively. In addition, only 90 out of the original 188964 π^+ (0.05%) pass these criteria, resulting in a contamination of 7.5% for a 97% π^+, 3% K^+ admixture of tracks [8].

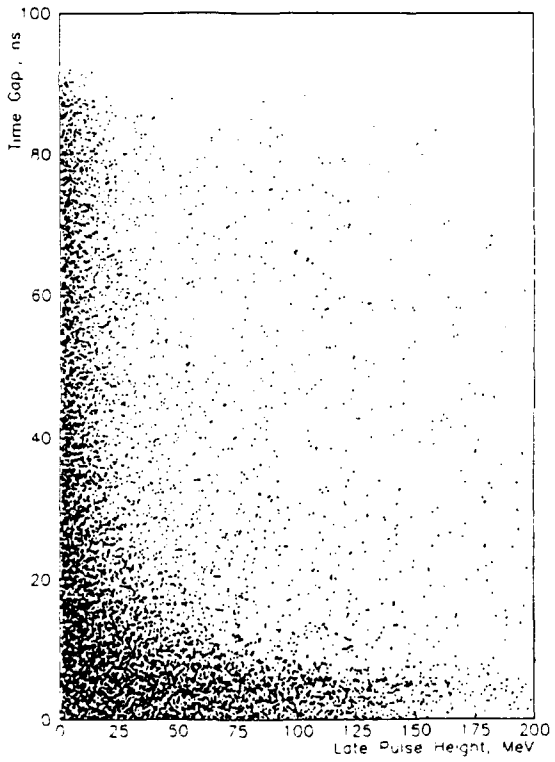

Fig. 6. Plot of the time gap versus late pulse height for the data.

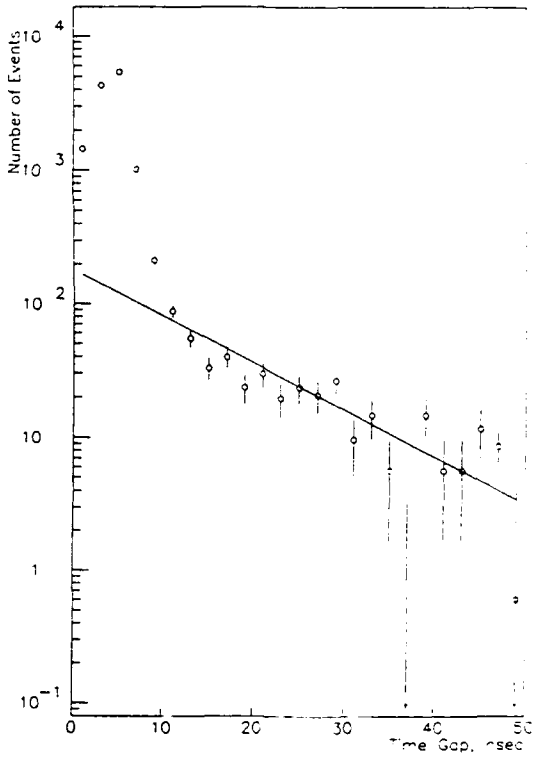

Fig. 7. Distribution of time gaps for events with late pulse height > 55 MeV. A beam time accidentals rate of 10.3 per 2 ns has been subtracted. The solid line is the expected shape of the decay curve for K^+ with an average lifetime of 12.4 ns.

4. Results

The following results were obtained during an exposure of a uranium target to stopped antiprotons at LEAR during October 1988. To prepare for these data, an approximate energy calibration for each cell was obtained with cosmic rays. The high voltage of each cell was adjusted so that the minimum ionizing peak corresponded to 25 ADC counts, providing a dynamic range of ~ 2000 MeV. Subsequently, during the run TDC offsets were periodically adjusted by locating the prompt peak in each cell for hits with > 10 MeV of energy deposited. All events were triggered in coincidence with two fission fragments detected in the PPACs [1,2].

In seeking to identify K^+ decays, all cells containing > 1 MeV of energy were arranged in time order. Cells with times earlier than 5 ns before nominal prompt times, as measured by the arrival of fast pions, were attributed to stray signals in the lightguides. Initially a scan for time gaps exceeding 4 ns was made. If one or more such gaps was found, the times and pulse height sums for each group were recorded. If no time gaps were found, a scan was made for gaps between 1 and 4

ns and data were recorded as above. An event was allowed to contain up to 2 time gaps. Two tests were imposed to eliminate events due to interactions of two consecutive beam particles (beam accidentals). First, the early time group was required to contain a hit in the first layer, corresponding to a K^+ entering the KRT from the direction of the target. Second, at least one cell in the early group and one cell in the next time group were required to be contiguous, corresponding to the decay of a K^+. To illustrate the need for these tests, at a CW beam rate of 150 kHz, the counting rate in the KRT resulting from any of ~ 12 particles (principally pions, kaons, protons, gamma rays and neutrons) into 16% of 4π sr is ~ 150 kHz. Therefore, the probability of a beam accidental event with 1 < time gap < 50 ns is ~ 0.75%, to be compared with an anticipated (Monte Carlo) K^+ probability of 0.04%.

In fig. 6 we show a plot of the time gap between the earliest and second earliest groups versus late pulse height for the data. Three prominent features are seen in the plot: (1) by comparison with fig. 5, K^+ decay candidates are observed for large time gaps and large late pulse heights; (2) by comparison with fig. 4, π^+ and μ^+ decays are observed for small late pulse heights; and (3) events on the lower boundary due to interactions of hadrons in the KRT (which were not included in the Monte Carlo simulation) are observed. For example, the probability for a pion and a slow proton from the same event to interact in the KRT giving a 1 < time gap < 4 ns and satisfying the geometry and time tests described above is ~ 1%, to be compared with the aforementioned expected K^+ probability of 0.04%.

To extract the K^+ signal, the time gap distribution for all events with late pulse height > 55 MeV has been plotted and is shown in fig. 7. This cut eliminates all π^+ and μ^+ decays as seen in fig. 4. A number of counts equal to 10.3 has been subtracted from each 2 ns bin to correct for remaining beam time accidentals, seen as an excess of events (not shown in fig. 7) for time gap $\geqslant$ 35 ns. The solid line indicates the expectation due to the K^+ decay, with a mean lifetime of 12.4 ns. A least-squares fit to the data of fig. 7 in the interval 10–50 ns gives a lifetime of 12.0 ± 1.2 ns, in good agreement with this value. Events below 10 ns are ascribed to the hadronic interaction mechanism described above. We have estimated the number of K^+ expected, based on the number of annihilations recorded, the number of K^+ per annihilation from PS183 [8,9], the solid angle of the KRT and efficiencies predicted by the Monte Carlo discussed earlier. Table 2 provides a summary of this information and estimates of the yields expected. We find that the predicted value (446 ± 49) is in good agreement with the measured value (436 ± 25), indicating we have identified the expected number of K^+.

Table 2
Predicted number of K^+ expected in this measurement.

1) Number of annihilations in coincidence with 2 fission fragments recorded	1.25×10^6
2) Number of K^+ per annihilation [a)]	0.020 ± 0.002
3) Solid angle of KRT/4π	0.16
4) Estimated efficiency of KRT (see text)	0.31 ± 0.01
5) K^+ lifetime correction for time gap cut > 10 ns	0.45 ± 0.01
6) Correction for late pulse height cut > 55 MeV	0.80 ± 0.02
7) Number of K^+ expected (product of factors 1–6)	446 ± 49

[a)] number is the product of the K^+/π^- ratio averaged over the range 250–750 MeV/c [8] (0.021 ± 0.001), the π^-/annihilation ratio [9] (1.52 ± 0.05), and the fraction of K^+ in the range 250–750 MeV/c (see fig. 3) 0.64, in uranium.

5. Conclusions

We have constructed and used a wide energy band, large solid angle detector which utilizes energy loss, timing and tracking measurements to detect K^+ decays at rest. The efficiency for identifying K^+ produced by stopped antiprotons annihilating in uranium entering the detector in the momentum range 250–750 MeV/c is found to be ~ 31%, as predicted by the Monte Carlo simulation. For other applications, where low energy K^+ identification is required, it would appear that the wide energy acceptance of the KRT would be especially attractive compared to other techniques [10].

Acknowledgements

We would like to thank our PS177 colleagues from Grenoble, Orsay, Uppsala, NIKHEF (Amsterdam), Warsaw, Saclay and GSI (Darmstadt) for their help and support in these efforts. We owe special gratitude to the LEAR staff of the CERN PS Division for their dedicated and skillful operation of LEAR during this experiment.

References

[1] J.P. Bocquet et al., Phys. Lett. B182 (1986) 146.
[2] J.P. Bocquet et al., Phys. Lett. B192 (1987) 312.
[3] D.M. Ritson, Techniques of High Energy Physics (Interscience, New York, 1961) p. 358
[4] Scintiplex III acrylic scintillator, National Diagnostics Inc., 1013–17 Kennedy Blvd., Manville, NJ 08835.
[5] BBQ wavelength shifter, National Diagnostics Inc., 1013–17 Kennedy Blvd., Manville, NJ 08835.

[6] W. Hoffmann et al., Nucl. Instr. and Meth. 195 (1982) 475.
[7] J. Roy, Proc. 4th Int. Symp. on NN Interactions, Syracuse, NY, 1975, vol. 1, p. III.2.
[8] G.A. Smith, The Elementary Structure of Matter, eds. J.-M. Richard, E. Aslanides and N. Boccara, Springer Proceedings in Physics no. 26 (Springer, Berlin, 1988) p. 219.
[9] T.A. Armstrong et al., Z. Phys. A332 (1989) 467.
[10] See, for example, K. Kleinknecht, Detectors for Particle Radiation (Cambridge University Press, Cambridge, 1987) p. 149.

APPENDIX VII

The Pennsylvania State University

The Graduate School

Department of Aerospace Engineering

GAMMA RADIATION SHIELDING FOR ANTIPROTON ANNIHILATION ENGINES

A Thesis in

Aerospace Engineering

by

Robert Bishop

Submitted in Partial Fulfillment
of the Requirements
for the Degree of

Master of Science

December 1989

ABSTRACT

The gamma radiation emanating from antiproton annihilations is examined generally, and specifically for the solid core, heat transferring engine, LIPTHANE. Shielding needs are evaluated based on the vulnerability of humans and electronics to this radiation. Antimatter propulsion and electron-photon showers are reviewed.

The Monte Carlo Code System, EGS4, is used to track photons, positrons, and electrons through an unshielded and shielded version of LIPTHANE. Values for the fluence per annihilation are recorded at various distances from the engine. Energy absorbed and particle numbers are also recorded.

The results indicate that significant, but not prohibitive, shielding will be necessary for the safe operation of LIPTHANE or any antiproton annihilation engine.

We approve the thesis of Robert Bishop.

Date of Signature

Gerald A. Smith
Director of Laboratory for Elementary
Particle Science
Professor of Physics
Thesis Adviser

Michael M. Micci
Associate Professor of Aerospace Engineering

Dennis K. McLaughlin
Department Head of Aerospace Engineering
Professor of Aerospace Engineering

I grant The Pennsylvania State University the nonexclusive right to use this work for the University's own purposes and to make single copies of the work available to the public on a not-for-profit basis if copies are not otherwise available.

Robert Bishop

TABLE OF CONTENTS

LIST OF FIGURES vi

LIST OF TABLES ix

ACKNOWLEDGMENTS x

Chapter 1. ANTIMATTER ANNIHILATION PROPULSION 1

Introduction 1
Advanced Propulsion Concepts 2

Specific Impulse and Delta V 3
Mission Requirements and Propulsion Concepts 5
Engine Designs 6

Antiproton Annihilation Engines 6
Nuclear Engines 9

Antiproton Technology 10

Production of Antiprotons 10
Handling and Storage of Antiprotons 12

The Physics of Antiproton Annihilation 13

Properties of Antiprotons 13
Interaction of Antiprotons and Protons 13
Products of Annihilation 15

Antiproton-Proton Annihilation 15
Antiproton-Nucleus Annihilation 19
Electron-Positron Annihilation 20

Chapter 2. RADIATION SHIELDING AND ELECTRON-PHOTON SHOWERS 22

The Physics of Electron-Photon Showers 23

Pair Production 24
Bremsstrahlung 25
Compton Scattering 26
Photoelectric Effect 27
Positron Annihilation 28
Møller Scattering 29
Bhabha Scattering 29
Continuous Electron Energy Loss 30
Multiple Coulomb Scattering 30
Comparison of Cross Sections for Lead 30

Human Vulnerability to Gamma Radiation 31

Electronics Vulnerability to Gamma Radiation 37

Chapter 3. EGS4: MONTE CARLO PROGRAM FOR SHOWER SIMULATION 41

Introduction 41
The EGS4 Code System 42

Structure of EGS4 42
Cross Sections Used by EGS4 44
Verification of EGS4 44
Limitations of EGS4 48

The Elwert Correction 48
The Migdal Correction 48
The Suppression Effect 49
Rayleigh Scattering 49
Secondary Modes of the Photoelectric Effect 49

General Results 49

Chapter 4. SIMULATION OF A SOLID CORE ENGINE, LIPTHANE 53

Introduction 53
Description of LIPTHANE 54
The Modeling of LIPTHANE 56
Results of the Monte Carlo Simulation 58

Incident Photons 58
Fluence 60
Energy Absorption 62
Number of Photons and Electrons 69

Chapter 5. EVALUATION AND CONCLUSIONS 71

Introduction 71
Antiproton Annihilation Gamma Radiation 71
Human Safety and LIPTHANE 72
Electronics Operation and LIPTHANE 75
Shielding 77
Future Study 78

Appendix. ADDITIONAL MONTE CARLO RESULTS 80

REFERENCES 90

LIST OF FIGURES

1.1 Comparison of Energy Release of Selected Reactions 5

1.2 Cutaway Side View of a Solid Core Engine 7

1.3 Cutaway Side View of a Plasma Core Engine 8

1.4 Cutaway Side View of a Beam Core Engine 8

1.5 Production and Applications of Antiprotons 11

1.6 Energy Spectrum of the Photons Created by Antiproton-Proton Annihilation [11] 18

1.7 Weighted Energy Spectrum of Photons Produced by Annihilation of Antiprotons with Hydrogen, Uranium, and Carbon [13] 21

1.8 Momentum Spectrum of Neutrons Emitted by Antiproton Annihilation in Uranium [14] 21

2.1 Feynman Diagram of Pair Production 25

2.2 Feynman Diagram of Bremsstrahlung 26

2.3 Feynman Diagram of Compton Scattering 27

2.4 Feynman Diagram of Positron Annihilation 29

2.5 Cross Sections for Lead for (a) Processes Involving Incident Photons and (b) Electron Processes [15] 31

3.1 Number of Photons vs. Depth [cm * 0.513] with (a) 1 MeV Minimum Energy and (b) 10 MeV Minimum Energy, per Incident 100 MeV Photon According to Messel and Crawford and EGS4 46

3.2 Number of Electrons vs. Depth [cm * 0.513] with (a) 1 MeV Minimum Energy and (b) 10 MeV Minimum Energy, per Incident 100 MeV Photon According to Messel and Crawford and EGS4 46

3.3 Comparison of the Cross Sections Used by Messel and Crawford and EGS4 for (a) Pair Production, (b) Bremsstrahlung, (c) Compton Scattering, and (d) Photoelectric Effect 47

3.4 Fraction of Energy Remaining vs. Depth [cm] for Various Materials as Determined by EGS4 51

3.5 Comparison of Fraction of Energy Remaining as a Function of Depth in Tungsten as Determined by EGS4 and Cassenti 51

4.1 A Cross Sectional View of LIPTHANE 55

4.2 Initial Gamma Radiation Spectra for (a) Unshielded and (b) Shielded Simulations. Based on a Sample of 100,000 Annihilation Photons 59

4.3 Positions of the Planes Used to Measure Fluence 61

4.4 Fluence in J/m^2 per Annihilation vs. Radius in cm at 50 cm from Vehicle End of LIPTHANE (z=-50 cm) for (a) Unshielded and (b) Shielded 63

4.5 Fluence in J/m^2 per Annihilation vs. Radius in cm at 100 cm from Vehicle End of LIPTHANE (z=-100 cm) for (a) Unshielded and (b) Shielded 63

4.6 Fluence in J/m^2 per Annihilation vs. Radius in cm at 500 cm from Vehicle End of LIPTHANE (z=-500 cm) for (a) Unshielded and (b) Shielded 64

4.7 Fluence in J/m^2 per Annihilation vs. Radius in cm at 1000 cm from Vehicle End of LIPTHANE (z=-1000 cm) for (a) Unshielded and (b) Shielded 64

4.8 Fluence in J/m^2 per Annihilation vs. Radius in cm at 10000 cm from Vehicle End of LIPTHANE (z=-10000 cm) for (a) Unshielded and (b) Shielded 65

4.9 Fluence in J/m^2 per Annihilation vs. Radius in cm at 50 cm from Space End of LIPTHANE (z=+120 cm) for (a) Unshielded and (b) Shielded 65

4.10 Fluence in J/m^2 per Annihilation vs. Radius in cm at 100 cm from Space End of LIPTHANE (z=+ 70 cm) for (a) Unshielded and (b) Shielded 66

4.11 Fluence in J/m^2 per Annihilation vs. Radius in cm at 500 cm from Space End of LIPTHANE (z=+570 cm) for (a) Unshielded and (b) Shielded 66

4.12 Fluence in J/m^2 per Annihilation vs. Radius in cm at 1000 cm from Space End of LIPTHANE (z=+1070 cm) for (a) Unshielded and (b) Shielded 67

4.13 Fluence in J/m^2 per Annihilation vs. Radius in cm at 10000 cm from Space End of LIPTHANE (z=-+10070 cm) for (a) Unshielded and (b) Shielded 67

5.1 Energy Flux vs. Distance from Annihilation Point for Several Annihilation Rates 73

5.2 Fluence vs. Exposure Time for Several Values of Energy Flux 73

A.1 Photons per MeV vs. Energy [MeV] Exiting the (a) Target, (b) Inner Cooling Region, (c) First Shell, and (d) the First Propellant Duct, from a Total of 100,000 Annihilation Photons 81

A.2 Photons per MeV vs. Energy [MeV] Exiting the (a) Shell #2, (b) Second Propellant Duct, (c) Shell #3, and (d) the Third Propellant Duct, from a Total of 100,000 Annihilation Photons 82

A.3 Photons per MeV vs. Energy [MeV] Exiting the (a) Shell #4, (b) Fourth Propellant Duct, (c) Shell #5, and (d) the Fifth Propellant Duct, from a Total of 100,000 Annihilation Photons 83

A.4 Photons per MeV vs. Energy [MeV] Exiting the (a) Shell #6, (b) Sixth Propellant Duct, (c) Shell #7, and (d) the Seventh Propellant Duct, from a Total of 100,000 Annihilation Photons 84

A.5 Photons per MeV vs. Energy [MeV] Exiting the (a) Shell #8, (b) Shield, (c) Plane at z=+120 cm, and (d) the Plane at z=-50 cm, from a Total of 100,000 Annihilation Photons 85

A.6 Energy [MeV/cm] vs. Radius [cm] for (a) z=-50 cm, No Shield, (b) z=-50 cm, Shield, (c) z=-100 cm, No Shield, and (d) z=-100 cm, Shield for 100,000 Total Annihilation Photons 86

A.7 Energy [MeV/cm] vs. Radius [cm] for (a) z=-500 cm, No Shield, (b) z=-500 cm, Shield, (c) z=-1000 cm, No Shield, and (d) z=-1000 cm, Shield for 100,000 Total Annihilation Photons 87

A.8 Energy [MeV/cm] vs. Radius [cm] for (a) z=-10,000 cm, No Shield, (b) z=-10,000 cm, Shield, (c) z=+120 cm, and (d) z=+170 cm, for 100,000 Total Annihilation Photons 88

A.9 Energy [MeV/cm] vs. Radius [cm] for (a) z=+570 cm, (b) z=+1070 cm, and (c) z=+10,070 cm for 100,000 Total Annihilation Photons 89

LIST OF TABLES

1.1 Specific Impulses and Thrust to Weight Ratios of Various Rocket Engines... 4

1.2 Properties of Elementary Particles in Antiproton Annihilation 14

1.3 Annihilation Particle History 16

2.1 Photoelectric Constants 28

2.2 Biological Effects of Acute Radiation Exposure 33

4.1 Materials, Densities, and Positions of LIPTHANE Subcomponents 57

4.2 Number of Photons per 10 MeV vs. Photon Energy for 10^5 Annihilation Photons (=2.632×10^4 Annihilations) as Adapted from Figure 1.6..... 59

4.3 Percentage of Initial Gamma Radiation Energy Absorbed by Region..... 68

4.4 Number of Photons and Electrons Emerging Per Incident Photon by Region 70

5.1 Times of Failure for Electronics of Unshielded LIPTHANE..... 76

ACKNOWLEDGMENTS

The author wishes to express gratitude to the Air Force Office of Scientific Research, Air Force Systems Command, USAF, whose support has made this research possible.

Also, special thanks to Dr. G.A. Smith and Dr. R.A. Lewis for providing encouragement and assistance.

Chapter 1
ANTIMATTER ANNIHILATION PROPULSION

Introduction

Antimatter was first predicted to exist on the basis of quantum field theory by P.A.M. Dirac in 1928 [1]. The antielectron (positron) was discovered experimentally in 1933 [2]. Subsequently, the antiproton was discovered in 1955 [3]. The quantities of antiprotons produced thus far have been miniscule compared to even a milligram of ordinary matter. Even so, antimatter has long been heralded as the fuel that would take us to the stars, in speculation by science-fiction writers and in futuristic assessments by scientists [4,5,6]. Now, that future is drawing closer. It is entirely possible that in only ten years the production of antiprotons will be high enough to support a number of space propulsion applications. Eventually, it may be possible to produce enough antimatter to propel a substantial payload to a significant fraction of the speed of light, indeed making interstellar travel practical. Barring any new radical developments in physics, antimatter provides the best available means in the Universe to traverse space.

The property of antimatter that makes it so attractive is that it annihilates with matter. In this process the rest mass of both the matter and antimatter is released as energy which may then be harnessed to propel a spacecraft. Compared to other forms of energy release used for propulsion, both actual and theoretical, antimatter annihilation has, by far, the greatest release of energy per unit mass. The advantage is so great that missions considered impossible in the past would achieve practicality with antimatter

annihilation. Fission rockets, fusion rockets and today's heavily used chemical rockets would become obsolete.

This tremendous potential for the use of antimatter as a propellant has inspired a number of research papers in the last decade, some of which have included preliminary designs of antimatter annihilation engines. There are a number of concerns special to an engine which utilizes antimatter. The handling and storage of antiprotons represents a significant problem since the particles must be isolated from all matter until annihilation is desired. Very high temperatures are usually developed, straining cooling technologies. Another problem, the one addressed in this paper, is the high energy radiation created by annihilation. This radiation is dangerous to humans and damaging to electronics, making shielding an issue in the functionality and safety of annihilation engines. Any shield will add mass to the engine, hurting its performance. Thus, analysis of the shielding needs is critical to evaluating the antimatter engine concept as a whole.

In this chapter advanced propulsion concepts, antimatter technology, and the physics of antimatter annihilation will be reviewed.

Advanced Propulsion Concepts

As more ambitious plans for exploring space have developed, the need for more efficient methods of propulsion has grown acute. With chemical rockets the amount of propellant that must be used to make these more demanding missions possible is tremendous. In addition to the gross inefficiency brought about by the propellant having to waste most of its energy simply propelling itself, such vehicles turn into engineering nightmares due to the large volume of propellant involved. Clearly,

alternatives to chemical rockets must be developed in order to make such missions as manned exploration of Mars, and many others, practical.

Fortunately, there are reactions that are more energetic than chemical reactions. They are fission, fusion, and annihilation. The technologies associated with each of these three present certain obstacles that must be overcome before they become useful, and each has a different level of potential. In this section, advanced propulsion concepts utilizing these three phenomena will be evaluated and compared to energy requirements for sample missions.

Specific Impulse and Delta V

Delta V is a useful measure of the energy required for a given mission. Neglecting gravity and assuming constant propellant exhaust velocity, an idealized situation, Δv may be related to properties of the vehicle and is equal to:

$$\Delta v = v_e \ln \frac{m_o}{m_f} \qquad (1.1)$$

where v_e= exhaust velocity of the propellant, m_o= initial vehicle mass, m_f= vehicle mass - propellant mass, and Δv= the velocity increment applied to the vehicle.

Specific impulse is directly related to the propellant exhaust velocity:

$$I_{sp} = \frac{v_e}{g_o} \qquad (1.2)$$

where I_{sp}=Specific Impulse, v_e=propellant exhaust velocity, and g_o=gravity at the Earth's surface (≈9.8m/s^2). The higher the exhaust velocity and specific impulse, the less propellant is needed to provide a given amount of thrust. It is a convenient way to compare the capabilities of various types of engines. Table 1.1 shows the specific

impulses and thrust to weight ratios of several actual and proposed engines [7]. The values for antimatter engines found within the table are taken from proposed engines or are based on theoretical calculations. They are meant to convey typical values and are not rigorously inclusive.

These are useful relations in that they show how specific impulse impacts on the design of a spacecraft. The lower the specific impulse, the more propellant must be carried and the dependence is logarithmic. It is in the more ambitious missions that require large amounts of energy (i.e. large Δv) where high specific impulses are needed. Otherwise designs become unworkable, either from an engineering standpoint or due to time considerations.

Table 1.1: Specific Impulses and Thrust to Weight Ratios of Various Rocket Engines.

Rocket Engine Type	Specific Impulse [s]	Thrust to Weight Ratio
Chemical (solid propellant)	350	.01-100
Chemical (liquid propellant)	450	.01-100
Ion Engines	5000-25000	10^{-5}-10^{-3}
Arcjets	400-2000	10^{-4}-10^{-2}
MPD	4000-15000	10^{-5}-10^{-3}
Nuclear - fission	500-1100	.01-30
Nuclear thermal - fusion	10000	.01-30
Antimatter solid core	500-1000	.5-14
Antimatter beam core	10^{7}+	10^{-8}-10^{-4}

Mission Requirements and Propulsion Concepts

There are many space missions that are of interest to mankind. With past and current technologies, manned missions to Earth orbit and the Moon and unmanned missions to most of the planets in the Solar System have been accomplished. However, it has become clear that the methods of propulsion used so far are not suitable for other desirable missions.

To solve this problem there has been extensive research into alternative sources of energy for propulsion. Among the leading candidates are nuclear fission and fusion. Also receiving attention are more efficient chemical propellants and electric engines. Antimatter annihilation has been a subject of speculation for quite some time, and as the prospects for higher production rates grow, it is being seriously considered by many as a viable option.

Figure 1.1 shows the energy available per kilogram of mass for several propulsion energy sources, actual and proposed, on a logarithmic scale. Antimatter is seen to be more energetic by two orders of magnitude over its closest competitor, fusion.

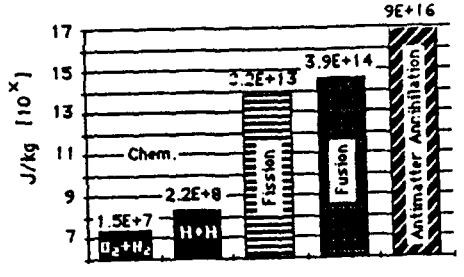

Figure 1.1: Comparison of Energy Release of Selected Reactions.

Engine Designs

All rockets work by the conservation of momentum principle, increasing vehicle velocity by expelling matter in the opposite direction to which they are traveling. Chemical rockets use chemical reactions to convert a very tiny amount of mass into thermal energy. Some of this thermal energy is converted to kinetic energy of the rocket by means of the force exerted by the resultant high pressure gas. Nuclear fission also liberates energy that may be used to heat a propellant. Nuclear fusion liberates an even larger amount of energy, and annihilation releases all of energy available. Proposed engine designs follow.

Antiproton Annihilation Engines

A number of different concepts of engines that utilize antiprotons have emerged in the last decade. These may be categorized by the way they convert the kinetic energy of the annihilation's charged particles. The categories are solid core, plasma core, and beam core. Each has its particular efficiency, thrust capability, and antiproton requirements and is examined below.

Solid Core Antiproton Annihilation Engines. In this type of engine, as seen in Figure 1.2, the annihilation area is surrounded by a dense material which absorbs the energy of the particles that move through it, converting it to heat. This heat is then, in turn, transferred to a propellant. The propellant is raised to a high temperature and is expanded through a nozzle, providing thrust.

Solid core engines produce relatively higher thrust and relatively lower specific impulse than the other two types of annihilation engines considered in this section. In addition they require fewer antiprotons than the other two, making them the most attractive option at this time.

Because the solid core engine is the more likely of the annihilation engines to be built first, its shielding needs and radiation production have been emphasized in this paper.

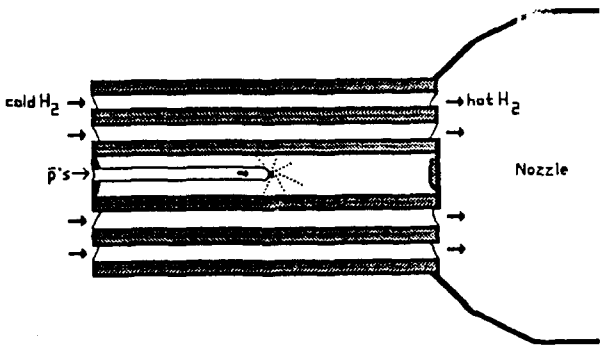

Figure 1.2: Cutaway Side View of a Solid Core Engine.

Plasma Core Antiproton Annihilation Engines. These engines use the energy from antiproton annihilations to create a plasma. Compared to the solid core engine, this type of engine would have a higher specific impulse, but lower thrust. It would be suitable for interplanetary missions and perhaps a precursor to an interstellar mission.

Annihilation occurs in the center of the engine and the charged particles created are trapped by a magnetic field, moving along a spiral trajectory. Eventually these particles will collide with gas particles filling the engine, transferring some of their energy, ionizing atoms and creating a plasma. Such an engine is shown in Figure 1.3.

The plasma is fairly transparent to the gamma radiation that is produced. Since this radiation is damaging to magnets some shielding will be necessary.

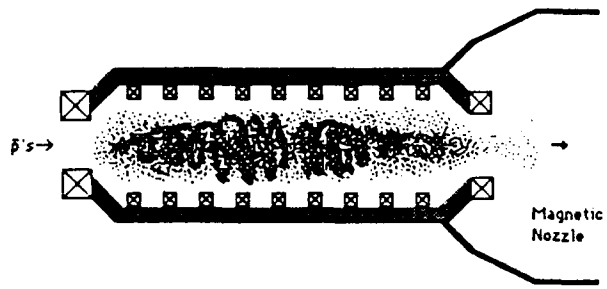

Figure 1.3: Cutaway Side View of a Plasma Core Engine.

Beam Core Antiproton Annihilation Engines. In a beam core engine (see Figure 1.4), the charged products of annihilation themselves are directed by a strong magnetic field in order to create thrust. This design is appealing in its simplicity but would create relatively low thrust and would require a great number of antiprotons. However, this design concept is the only one that has the capability of fulfilling an interstellar mission within a reasonable time frame. Significant fractions of the speed of light are possible.

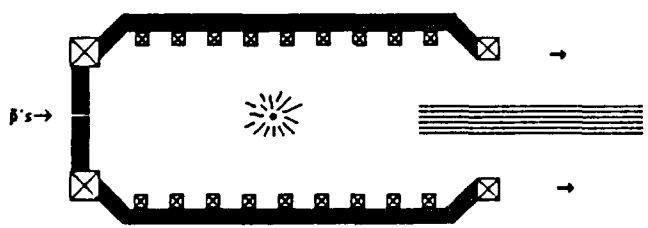

Figure 1.4: Cutaway Side View of a Beam Core Engine.

Nuclear Engines

In fission, an atom is split into two or more separate atoms, releasing energy in the process. Nuclear fission has been in use for more than four decades now, making it attractive from an experience perspective. However, its limited applicability and political disfavor due to public questions about safety present serious obstacles.

Fusion is the counterpart to fission in that it involves the joining together of atoms instead of their splitting. Fusion converts a greater amount of mass to energy than does fission and is thus more desirable. However, fusion has proved elusive, and it is the subject of intensive laboratory investigation worldwide.

There are two basic designs of nuclear engines, both similar to the annihilation engines discussed above: nuclear-thermal, and nuclear-electric.

Nuclear-Thermal Engines. In this type of engine, controlled nuclear fission or fusion creates high energy radiation consisting of neutrons, photons, and heavier particles. This radiation is absorbed in a dense material which converts the energy to heat. The heat is then imparted to a propellant, creating thrust. This engine is very similar to the solid-core antimatter annihilation engine, differing mainly in the amount of energy released.

Nuclear-Electric Engines. Once again, controlled nuclear fission or fusion creates high energy particles which are absorbed by a heavy material. The energy is then used to create a plasma which is accelerated out of the engine by magnetic fields, creating thrust.

Antiproton Technology

Although antiprotons have been created in laboratories, the technology surrounding their production, storage, handling, and usage is in a fledgling state. While strong reasons exist for swift development of these necessary technologies, it is difficult to predict the magnitude of public and government support for such efforts. In light of the antiproton's high potential for use in a number of areas, many are predicting rapid advances.

This section explores the production, handling, and storage of antiprotons.

Production of Antiprotons

Currently, antiprotons are made at only three facilities: the Center for European Nuclear Research in Switzerland (CERN), Fermi National Accelerator Laboratory near Chicago, and the Institute for High Energy Physics in the Soviet Union. The numbers of antiprotons produced per day, $\approx 10^{11}$, is well below the number needed for application in space travel. In addition, storage capabilities are only able to handle a fraction of a day's production. For example, the Low Energy Antiproton Ring (LEAR) at CERN holds $\approx 10^{10}$ antiprotons.

A recent study by Rand Corporation has examined the issue of increasing production of antimatter [8]. It is their estimation that within fifteen years, given a suitable commitment, a production capability of 0.1-1.0 grams of antiprotons per year is possible. Intermediate stages would include ≈1 nanogram per year in only three years and ≈10-500 micrograms *in less than ten years.*

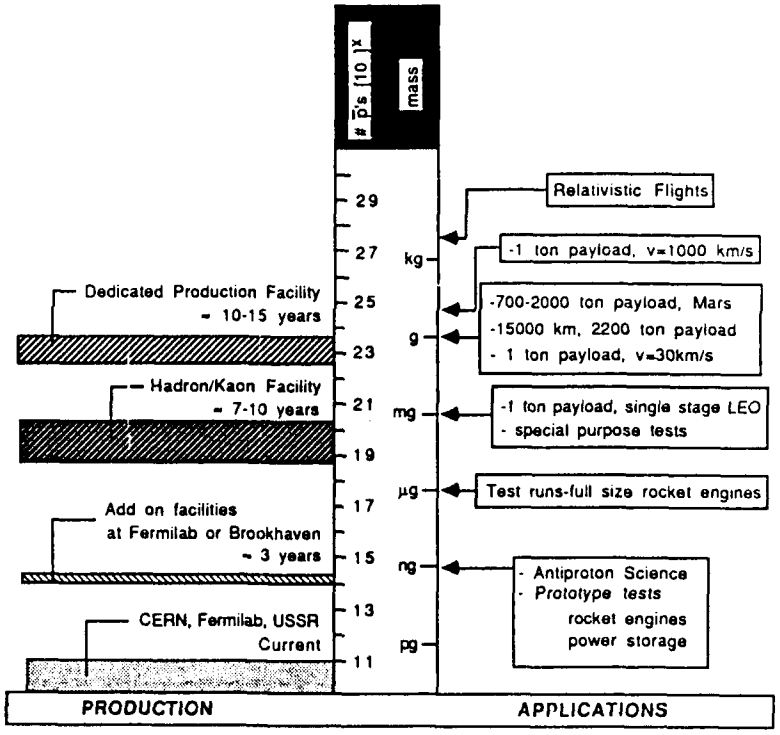

Figure 1.5: Production and Applications of Antiprotons.

Figure 1.5 summarizas the current and projected antimatter production capabilities and compares them to the amounts needed for certain applications. At the nanogram level, testing of full scale engines becomes practical. At the milligram level a number of applications become possible.

Handling and Storage of Antiprotons

Possible ways to transport antiprotons from their production sites to remote laboratories are currently being explored. While the number of antiprotons transportable would still be several orders of magnitude too low for propulsion uses, this accomplishment would be a major milestone in antiproton propulsion technology. The wide availability of antiprotons would allow a pace of research not currently possible with the antiprotons confined to their place of origin. Such research is necessary to provide preliminary results, define problems, and generally shape the future research effort.

It is thought possible that antiprotons could be transported in a smaller version of the rings in which they are presently stored. There are also other designs that, if successful, would be able to provide enough antiprotons to laboratories to enable significant research. Besides being a boon for propulsion research, basic science would receive a considerable boost from widely available antiprotons. Because they annihilate, antiprotons are a good tool to investigate the physics of elementary particles.

Concerning the long term storage of quantities of antiprotons large enough to be of interest for propulsion purposes, there are numerous ideas, but most remain speculative. In order to overcome space charge density limitations, antiprotons are envisioned in combination with positrons to form the antimatter version of hydrogen,

antihydrogen. Antihydrogen would behave exactly as hydrogen does except, of course, that it would annihilate if it came in contact with ordinary matter. It would further be desirable to have the antihydrogen in solid form, requiring extremely low temperatures. Some studies have concluded that it would be possible, even though the antihydrogen atom would be electrically neutral, to control a sphere of solid antihydrogen by using magnetic and electric fields [9]. Antihydrogen atoms would be "boiled" off the sphere by a laser and ionized so that the antiproton could be controlled by a magnetic field. The antiproton would then be maneuvered to the point or area of annihilation. An attractive feature of this scheme is that many of its principles may be tested using normal hydrogen, making research possible in the near term.

The Physics of Antiproton Annihilation

Properties of Antiprotons

Antiprotons are defined as being identically equal to protons except that they are opposite in the sign of electric charge and magnetic moment. For example, while a proton has a charge of +1, an antiproton has a charge of -1. However, in mass a proton and an antiproton are exactly alike. Table 1.2 shows the symbol, charge, spin, mass, and average lifetime of the elementary particles encountered in antiproton annihilation.

Interaction of Antiprotons and Protons

There are no stable entities that include both protons and antiprotons. There are transient states wherein a proton and antiproton form a bound state. However, these bound states lead directly to annihilation. The proton-antiproton system is named

Table 1.2: Properties of Elementary Particles in Antiproton Annihilation.

Particle Name	Symbol	Charge	Spin	Mass [MeV]	Mean Life [s]
proton	p	+1	1/2	938.3	stable
antiproton	$\bar{p}$	-1	1/2	938.3	stable
electron	e^-	-1	1/2	0.511	stable
positron	e^+	+1	1/2	0.511	stable
neutron	n	0	1/2	939.6	932
antineutron	$\bar{n}$	0	1/2	939.6	932
pion	π^+	+1	0	139.6	2.6×10^{-8}
	π^0	0	0	135.0	0.8×10^{-16}
	π^-	-1	0	139.6	2.6×10^{-8}
kaon	K^+	+1	0	493.7	1.2×10^{-8}
	K^0_S	0	0	497.7	8.8×10^{-11}
	K^0_L	0	0	497.7	5.2×10^{-8}
	K^-	-1	0	493.7	1.2×10^{-8}
muon	μ^-	-1	1/2	105.7	2.2×10^{-6}
	μ^+	+1	1/2	105.7	2.2×10^{-6}
photon	γ	0	1	0	stable
electron neutrino	ν_e	0	1/2	0	stable
	$\bar{\nu}_e$	0	1/2	0	stable
muon neutrino	ν_μ	0	1/2	0	stable
	$\bar{\nu}_\mu$	0	1/2	0	stable

protonium.

Equations giving the cross section for capture and annihilation are complex and are not presented here. It should be noted, however, that it is not difficult to entice antiprotons to annihilate with protons. The problem instead is to completely isolate the antiprotons from the protons until annihilation is desired.

Products of Annihilation

There are many possible annihilations that may occur, since any antiparticle will annihilate with any particle. The ones of interest from a propulsion standpoint are those that involve stable particles. In this section, antiproton-proton, antiproton-nucleus, and electron-positron annihilation are examined.

Antiproton-Proton Annihilation

The primary products of antiproton-proton annihilation are pions and kaons, both charged and neutral. Neither of these is stable and eventually they will decay into secondary products: photons, muons, electrons, and neutrinos. Pions occur more frequently than kaons. On average, the reaction may be summarized as follows [10]:

$$p + \bar{p} \longrightarrow 1.527\pi^+ + 1.527\pi^- + 1.96\pi^0 + 0.012K^+ + 0.012K^- + 0.013K^0 + 0.013\bar{K}^0 \tag{1.3}$$

See table 1.3 for a summary of annihilation particle history, including the particle pathlengths and lifetimes in the engine frame, decay modes, decay branching ratios, and energy distribution (by mass, kinetic energy, gamma radiation and neutrinos). There is still some uncertainty in these numbers.

The π^0's are the first particle resulting from the annihilation to decay. Although the lifetime of a π^0 is 8×10^{-17} s, relativistic effects due to the high kinetic energy of the π^0's in the engine frame will extend their lifetime to approximately 2.2×10^{-16} s.

Table 1.3: Annihilation Particle History. *Time and Length are Measured in the Engine Frame. M=Rest Mass, KE=Kinetic Energy, GE=Gamma Radiation Energy, NE=Neutrino Energy.

Length* [m]	Reaction	%	Energy [MeV]	Time* [ns]
. .	$p + \bar{p} \longrightarrow 1.527\pi^+ + 1.527\pi^- + 1.96\pi^0 + .012K^+ + .012K^- + .013K^0 + .013\bar{K}^0$	.	M=715.6 KE=1161 GE=0 NE=0	0
6.1×10^{-8}	$\pi^0 \longrightarrow 2\gamma$ $e^- + e^+ + \gamma$	98.8 1.17	M=451 KE=722.9 GE=702.7 NE=0	$<10^{-6}$
0.02	$K_S^0 \longrightarrow \pi^+ + \pi^-$ $2\pi^0 \longrightarrow 4\gamma$	68.6 31	M=445.2 KE=726.1 GE=705.3 NE=0	.11
2.98	$K^\pm \longrightarrow \mu^\pm + \nu$ $\pi^\pm + \pi^0 \longrightarrow \pi^\pm + 2\gamma$ $\pi^\pm + \pi^+ + \pi^-$ $e^\pm + \nu + \pi^0 \longrightarrow e^\pm + \nu + 2\gamma$ $\mu^\pm + \nu + \pi^0 \longrightarrow \mu^\pm + \nu + 2\gamma$ $\pi^\pm + 2\pi^0 \longrightarrow \pi^\pm + 4\gamma$	63.8 20.9 5.6 4.9 3.2 1.7	M=436.1 KE=727.8 GE=707.2 NE=5.5	16
12.21	$K_L^0 \longrightarrow \pi^\pm + e^\mp + \nu$ $\pi^\pm + \mu^\mp + \nu$ $3\pi^0 \longrightarrow 6\gamma$ $\pi^+ + \pi^- + \pi^0 \longrightarrow \pi^+ + \pi^- + 2\gamma$	38.8 26.8 21.5 12.6	M=431.6 KE=728.3 GE=709.4 NE=7.3	66
19.4+	$\pi^\pm \longrightarrow \mu^\pm + \nu$	100	M=326.4 KE=586.3 GE=709.4 NE=254.5	100
250+	$\mu^\pm \longrightarrow e^\pm + \nu + \bar{\nu}$	100	M=1.6 KE=317.9 GE=709.4 NE=847.7	7000+

Since the π^0's are produced with a range of kinetic energies, it is impossible to give an exact time for this decay. The kinetic energy of each π^0 will determine its lifetime in the engine frame.

Relativistic lengthening of particle lifetime applies to each of the particles produced by antiproton-proton annihilation. This is a result of a significant amount of the antiproton's and proton's mass being converted into the kinetic energy of the annihilation products. It is typical for an annihilation pion to be traveling at more than 0.9c, where c is the speed of light. From the results of special relativity, time dilation of a particle in the engine's frame may be expressed by:

$$t_{\text{engine frame}} = t_{\text{average particle lifetime}} \left(\frac{1}{\sqrt{1 - \frac{v^2}{c^2}}} \right) \qquad (1.4)$$

These extended lifetimes of annihilation products lead to longer paths before decay as well. This is a fortunate result, allowing extended interaction with the heavy charged particles (pions and muons) before they decay into lighter electrons. This longer interaction time improves the efficiency of almost every antimatter annihilation engine concept.

The π^0's each decay into two photons, which will have distinct energies. In the pion's rest frame, it will emit two photons of equal energy and at opposite angles. However, in the engine's rest frame, this symmetry becomes quite distorted, again due to relativistic effects caused by the pion's extremely high velocity. As a result, the photons created will have a spectrum of energy. These pions are the dominant source of photons throughout the annihilation decay process. Approximately 99% of the total gamma radiation energy produced is from π^0 decay. The photon spectrum is shown in Figure 1.6 and has been reproduced from reference [11].

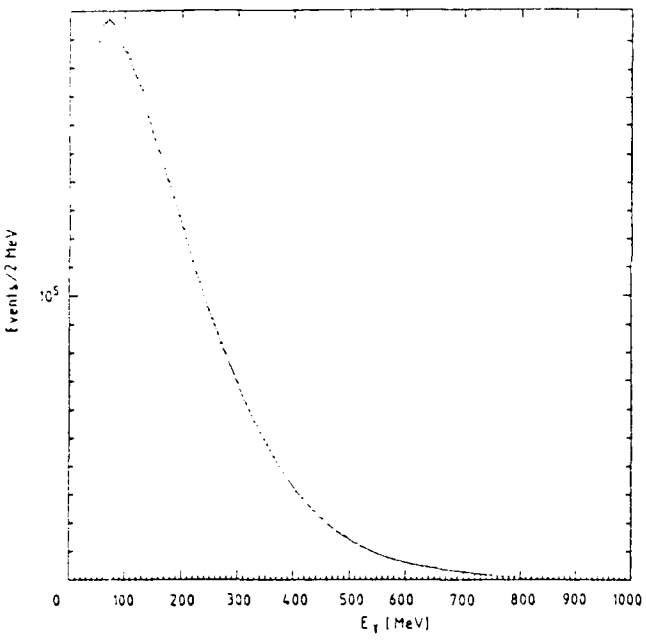

Figure 1.6 Energy Spectrum of the Photons Created by Antiproton-Proton Annihilation [11].

The kaons decay after the π^0's, but before the charged pions, and have a number of decay modes. The main products are muons, pions, neutrinos, and electrons. Neutrinos are stable particles that have virtually no interactions with matter. Thus, energy that is carried away by neutrinos may be considered lost to the system, decreasing the efficiency of the annihilation engine.

Charged pions, those produced by annihilation and those produced by kaon decay, are the next to decay. They do so almost exclusively by emitting a neutrino, leaving a muon having the same charge as the initial pion. These pions will have traveled, on average, approximately 20 meters before decaying. In comparison to reasonable engine dimensions, this is a significant length. If the pions have not been steered by a magnetic field up to this point, it is likely that they will have collided with the engine walls. This is, in fact, the exact scheme that solid core annihilation engines use, converting the kinetic energy of the pions to thermal energy.

Muons are longer lived than pions and kaons, lasting about 7 microseconds before they decay into an electron of the same charge, a neutrino, and an antineutrino. At this point, unless an effort has been made to direct the muons in the system, as a plasma or beam core engine might attempt, the muons will most likely have escaped.

The products of muon decay (electrons, positrons, and neutrinos) are all stable, bringing an end to the decay of the annihilation products.

Antiproton-Nucleus Annihilation

The annihilation of antiprotons in nuclei containing neutrons, as demonstrated by experiment, is complicated. The large amount of energy released by annihilation overwhelms the forces that glue the nucleus together, creating a shower of nuclear fragments as well photons. All of the phenomena discovered by experiment are not

fully understood. The spectra of photons emerging from antiproton-proton and antiproton-nucleus annihilation are seen, in Figure 1.7, to be similar in shape, but generally reduced in number for heavy nuclear targets, such as uranium [12,13]. While this appears to be advantageous, new effects appear such as the emission of neutrons, which present new special problems. Figure 1.8 shows the neutron emission spectrum obtained from antiproton annihilation with uranium [14]. This shower of neutrons can be as damaging to humans and electronics as photons are, creating another shielding problem. In this paper, neutrons are ignored. Unless annihilation is to occur in hydrogen, however, they will be present and warrant future serious study.

Electron-Positron Annihilation

Electrons and positrons annihilate, usually, to produce at least two photons. Reactions are possible as well that lead to the emission of only one photon or more than two photons. At relevant energies however the two photon annihilation process dominates. The photons collectively will have 1.022 MeV of energy and must conserve the original momentum of the system.

It is likely that this reaction will play only a secondary part, if any at all, in the use of antimatter for propulsion. Space charge density limits severely curtail the available energy in a positron only system. It is very possible however that positrons will be used to form antihydrogen. In such a scheme, the positrons might be used as an auxiliary power source, supplying electricity to vehicle systems. In an engine that annihilated antihydrogen with hydrogen, the electron-positron annihilations would release less than 0.1% of the total energy involved. Accordingly, it is common for positron-electron annihilation to be ignored in annihilation engine analyses.

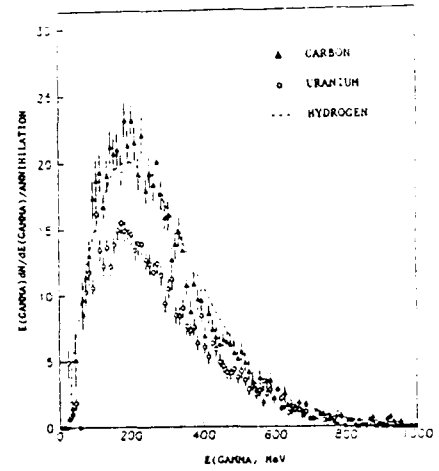

Figure 1.7: Weighted Energy Spectrum of Photons Produced by Annihilation of Antiprotons with Hydrogen, Uranium, and Carbon [13].

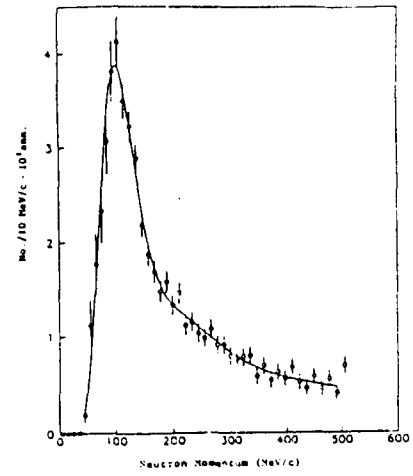

Figure 1.8: Momentum Spectrum of Neutrons Emitted by Antiproton Annihilation in Uranium [14].

Chapter 2
RADIATION SHIELDING AND ELECTRON-PHOTON SHOWERS

Introduction

In terrestrial applications radiation shielding is sometimes necessary, but hardly ever critical to the feasibility of a project. If there is any question about the safety of a device because of the radiation it creates, enough shielding is added to satisfy the safety requirements. The same cannot be said however about most propulsion engines. In the case of rockets, every kilogram added to the mass of the engine is in effect subtracted from the mass of the payload that the engine can deliver to the final orbit or destination. Radiation shielding is thus a necessary evil in space propulsion. In the worst case, the mass of shielding required for the safe and continued operation of an engine would be so high that no payload could be carried, making the engine of no use. In the best, no shielding at all would be required or so little that the capabilities of the engine are little affected. This paper explores the radiation shielding needs of antimatter engines, thus helping to determine their feasibility.

Radiation shielding is not an issue in most current rockets. Ordinary chemical reactions do not produce the kinds of radiation considered harmful to humans or electronics. Antiproton annihilation on the other hand produces dangerous high energy photons in great numbers. Each proton-antiproton annihilation produces, on average, approximately 3.8 of these photons. If these photons are then allowed to travel unobstructed into human tissue or electronic devices, damage will result. If enough

damage accumulates, the result will be death for living creatures, and the disabling of electronics.

Key issues are the physical processes behind the concept of radiation shielding and the tolerance of humans and electronics to radiation. These topics are covered in the following sections.

The Physics of Electron-Photon Showers

A photon or an electron traveling through a material has a certain probability of reacting with that material. This probability is measured by a mathematical construction called the cross section. It has the dimension of area per atom and the probability of interaction per unit length may be derived from the cross section by the following equation:

$$P_{interaction} = \frac{N_a \rho \sigma}{M} \qquad (2.1)$$

where N_a=Avogadro's Number, ρ=material density, σ=cross section, and M=molecular weight. Furthermore, an electron or photon has separate cross sections for several different possible events. In a shower, pair production, bremsstrahlung, Compton scattering, and many other processes occur with different probabilities. All of these individual cross sections add up to the total cross section, which determines the absolute probability of interaction. The individual processes comprising electron-photon showers and their cross sections will be described.

The term "electron-photon shower" arises due to the cyclical nature of events that take place. Photons may produce electrons and positrons, and electrons and positrons

may produce photons. In this manner the number of particles grows rapidly, each having a fraction of the energy of the original particle that entered the shield. The particle paths resemble a shower since most of the particles created will be traveling in a direction similar to the original particle.

Pair Production

A photon of high enough energy may, in the presence of a nucleus, spontaneously transform into a pair of oppositely charged particles. Since electrons and positrons have a rest mass equivalent to an energy of 0.511 MeV, any photon with energy above 1.022 MeV has the potential to undergo this "pair production." Any excess energy will be carried away by the electron and positron as kinetic energy. Figure 2.1 illustrates pair production. Feynman diagrams show the particles involved in a process; time is taken to increase from bottom to top. A nucleus is necessary in order to conserve momentum.

The cross section for pair production is complicated and is typically given in differential form with respect to the created positron's energy:

$$\frac{d\sigma_{pair}}{dE_+} = \frac{A_p r_0^2 \alpha Z(Z+\xi)}{k^3}\left((E_+^2+E_-^2)(\phi_1 - \frac{4}{3}\ln Z - 4f_c) + \frac{2}{3}E_+E_-(\phi_2 - \frac{4}{3}\ln Z - 4f_c)\right) \tag{2.2}$$

where E_+= positron total energy [MeV], E_-= electron total energy [MeV], k=incident photon energy [MeV], r_0=classical electron radius (2.8176×10^{-15} m), α=fine structure constant (0.0072970), Z=atomic number of the material, and:

$\phi_1 = 20.867 - 3.242\delta + 0.625\delta^2$ if $\delta <= 1$ or $= 21.12 - 4.184\ln(\delta + 0.952)$ for $\delta > 1$

$\phi_2 = 20.029 - 1.930\delta - 0.086\delta^2$ if $\delta <= 1$ or $= \phi_1$ for $\delta > 1$

$\delta = \frac{km}{2E_+E_-}$; m=mass of electron

A_p= empirical correction factor (=1 for k>50 MeV)

$\xi = \frac{\ln 1194\ Z^{-2/3}}{\ln 184.15\ Z^{-1/3} - f_c}$ for Z>4

$f_c = a^2\left((1+a^2)^{-1} + 0.20206 - 0.0369a^2 + 0.0083a^4 - 0.002a^6\right)$

= 0 if k>50 MeV

$a = \alpha Z$

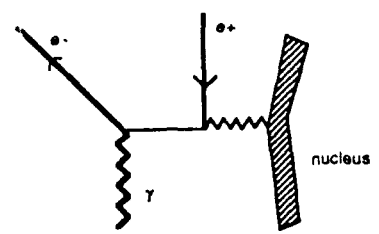

Figure 2.1: Feynman Diagram of Pair Production.

Bremsstrahlung

In the process of bremsstrahlung, an electron or positron emits a photon, losing some of its kinetic energy to create it. Figure 2.2 illustrates the process.

$$\frac{d\sigma_{brem}}{dk} = \frac{A r_0^2 \alpha Z(Z+\xi)}{k}\left((1+(\frac{E}{E_0})^2)(\phi_1 - \frac{4}{3}\ln Z - 4f_c) + \frac{2}{3}(\frac{E}{E_0})(\phi_2 - \frac{4}{3}\ln Z - 4f_c)\right) \tag{2.3}$$

where k=created photon energy [MeV], E_0=incident electron total energy [MeV], and E=post bremsstrahlung electron total energy. Again, similar to pair production, a nucleus must be present to conserve momentum. The other variables are identical to those for equation (2.2), with the following exceptions:

A=bremsstrahlung empirical correction factor (=1 for k>50 MeV)

$\delta=\frac{k}{2E_0}\frac{\eta}{E}$

$f_C=0$ if $E_0>50$ MeV.

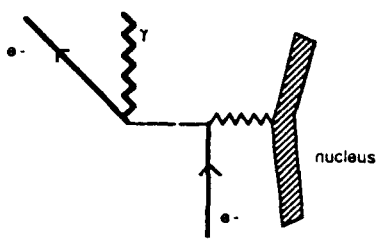

Figure 2.2: Feynman Diagram of Bremsstrahlung.

Compton Scattering

When a high energy photon collides with an atomic electron, that electron is ejected from its atom and the photon leaves the collision at a different angle and with reduced energy. In differential form with respect to the post collision photon energy, the cross section for this process is:

$$\frac{d\sigma_{comp}}{dk}=\frac{X_0 n\pi r_0^2 m}{k_0^3}\left(2m+k+\frac{m^2}{k_0}+\frac{1}{k}\left(\frac{k_0}{km^2}+k_0^2-2m^2-2mk_0\right)\right) \qquad (2.4)$$

where k_0=incident photon energy [MeV], k=scattered photon energy [MeV], m=electron rest energy [MeV], n=electron density [electrons/cm^3], X_0=radiation length [cm], and r_0=classical electron radius [cm].

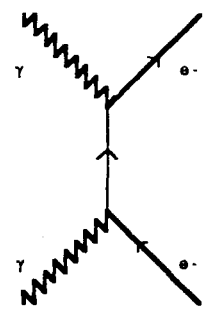

Figure 2.3: Feynman Diagram of Compton Scattering.

Photoelectric Effect

In this process a relatively low energy photon is absorbed by a bound electron. This electron is then excited enough to escape its host atom. The cross section is approximated by Messel and Crawford [15] as:

$$\phi=4\pi r_0^2 a^4 \frac{Z}{k}\frac{\rho N_0}{A}\left(b_0+b_1k^{-1}+b_2k^{-2}\right)f(a) \qquad (2.5)$$

Table 2.1 gives the values of the empirical constants. EGS4, the Monte Carlo program, takes data directly from Storm and Israel [16] for simulating this process.

Table 2.1: Photoelectric Constants.

$a=\alpha Z$	b_0	b_1	b_2	$f(a)$
0.00	1.008	1.926	2.107	
0.10	0.704	1.647	1.592	1.079
0.15	0.604	1.547	1.411	
0.20	0.523	1.460	1.258	1.092
0.25	0.455	1.392	1.114	
0.30	0.402	1.339	0.985	1.102
0.35	0.358	1.297	0.866	
0.40	0.323	1.265	0.753	1.115
0.45	0.293	1.247	0.636	
0.50	0.268	1.234	0.528	1.134
0.55	0.248	1.234	0.407	
0.60	0.232	1.243	0.278	1.162
0.65	0.218	1.263	0.134	
0.70	0.207	1.299	-0.041	1.201

Positron Annihilation

When a positron and an electron collide, annihilation occurs. Since positrons are created as part of the shower by bremsstrahlung, positron annihilation plays a role in the dynamics of the shower. While annihilations emitting only one photon and annihilations yielding three or more photons do occur, two photon annihilation dominates in the relevant energy range. The total cross section for two photon positron annihilation is given by:

$$\Phi_{pos\ annih} = \frac{X_0 \pi r_0^2 n}{\gamma + 1}\left(\frac{\gamma^2 + 4\gamma + 1}{\gamma^2 - 1}\ln\left(\gamma + \sqrt{\gamma^2 - 1}\right) - \frac{\gamma + 3}{\sqrt{\gamma^2 - 1}}\right) \qquad (2.6)$$

where $\gamma = E_0/m$, and E_0=incident positron total energy [MeV].

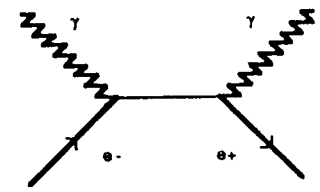

Figure 2.4: Feynman Diagram of Positron Annihilation.

Møller Scattering

In collisions between high energy electrons and atomic electrons, the atomic electron may be knocked free. This is called Møller scattering and its cross section is given by:

$$\frac{d\sigma_{Møller}}{dE} = \frac{2X_0 n \pi r_0^2 m}{\beta^2 T_0^2}\left(\left(\frac{\gamma - 1}{\gamma}\right)^2 + \frac{T_0^2}{T^2} - \frac{T_0(2\gamma - 1)}{T\gamma^2} + \frac{1}{\left(1 - \frac{T_0}{T}\right)^2} - \frac{2\gamma - 1}{\gamma^2\left(1 - \frac{T_0}{T}\right)}\right) \qquad (2.7)$$

where T_0=kinetic energy of incident electron [MeV], T=kinetic energy of scattered electron [MeV], γ=incident electron energy divided by electron rest energy, and $\beta = v/c$.

Bhabha Scattering

Bhabha scattering, or inelastic positron scattering, is similar to Møller scattering except that the incident particle is a positron instead of an electron. The result is the same in that an electron is knocked free from its atom, but the cross sections are different because charge plays a role:

$$\frac{d\sigma_b}{dE_-} = \frac{2\pi X_0 n r_0^2 n}{T_0^2}\left(\frac{T_0^2}{T_-^2\beta^2}\cdot\frac{T_0}{T_-}\left(2+\frac{1}{(\gamma+1)^2}\right)+2\cdot\frac{1}{(\gamma+1)^2}+\frac{T_-^2}{T_0^2}\left(1-\frac{2}{\gamma+1}\right)^3\cdot\frac{2T_-}{T_0}\left(1-\frac{2}{\gamma+1}\right)^2\left(1-\frac{1}{\gamma+1}\right)\right) \tag{2.8}$$

where T_0=incident positron kinetic energy [MeV], T_-=kinetic energy of secondary electron, γ=incident positron energy divided by positron rest energy, and β=v/c.

Continuous Electron Energy Loss

In the case where an electron or positron suffers a collision but an insufficient amount of energy is transferred to liberate an electron from an atom, or in the case where a very low energy photon is created by the process of bremsstrahlung, the events may be approximated as continuous energy loss of the particle. This is possible because these types of events are so numerous that they can well be described on average, and because the secondary particles that are created (if any) are low enough in energy to be insignificant compared to the particles of the shower. The low energy photons will be quickly absorbed by an atomic electron.

Multiple Coulomb Scattering

A high energy electron undergoes numerous elastic collisions in a material that do not significantly change its energy but do change its direction. No secondary particles are created.

Comparison of Cross Sections for Lead

In order to understand the dynamics of a shower, it is useful to compare the cross sections for the different physical processes. Figure 2.5 shows their comparative strengths over a wide energy range for lead [15]. Figure 2.5(a), showing the cross sections for processes involving incident photons, indicates that pair production

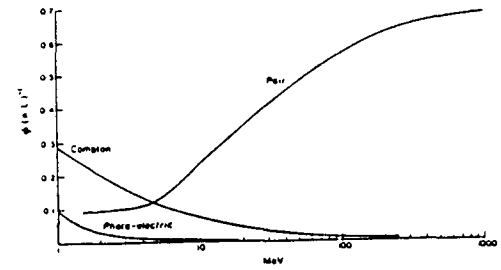

(a)

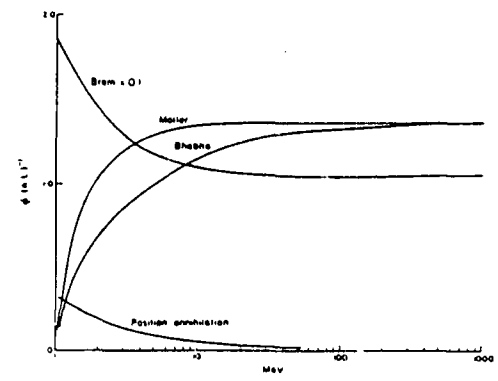

(b)

Figure 2.5: Cross Sections for Lead for (a) Processes Involving Incident Photons and (b) Electron Processes [15].

dominates at higher energies while Compton scattering dominates at the lower energies. The plot of the cross sections for electron processes, figure 2.5(b), shows that bremsstrahlung is the prevalent phenomenon at all energies. Although these graphs are for lead in particular, the relative strengths of the various processes are similar in any absorber.

Human Vulnerability to Gamma Radiation

When a high energy photon, or gamma radiation, enters living tissue it has a probability of interacting with it. The result is that some of the atoms in the living tissue are ionized, causing damage and disrupting their normal functions. Some of the effects observed in living cells are swelling, an increase in the viscosity of cell fluid, an increase in the membrane permeability, a delay or prevention of cell division, and injury to the chromosomes. The body is largely water. The ionization of water indirectly creates hydrogen gas, hydrogen peroxide, and hydroperoxyl radicals, chemically toxic products that will damage the body. If an atom of a protein molecule is ionized, a broken chain may result, causing molecule damage. Accumulation of small doses causes cancer, life shortening, and cataracts. Gene mutations also result [17].

An elusive factor in considering radiation damage to living creatures is the rate at which the body is able to repair itself. If the rate of repair exceeds the rate of damage being done then there will be few ill effects. This rate varies in individuals and in any case is generally low enough that it is ignored when considering significant fluxes of radiation. Biological effects resulting from acute dosages have been determined. Long

term radiation effects would be less, indicating that acute effects provide a conservative guideline by which to set criteria for safety. Table 2.2, reproduced from reference [17], relates acute doses and biological effects.

Table 2.2: Biological Effects of Acute Radiation Exposure.

Acute Dose [mSv]	Probable Observed Effect
50 - 750	Chromosomal aberrations and temporary depression of white blood cell levels in some individuals. No other observable effects.
750 - 2000	Vomiting in 5 to 50% of exposed individuals within a few hours, with fatigue and loss of appetite. Moderate blood changes. Recovery within a few weeks for most symptoms.
2000 - 6000	For doses of 3000 mSv or more, all exposed individuals will exhibit vomiting within 2 hours or less. Severe blood changes, with hemorrhage and increased susceptibility to infection, particularly at the higher doses. Loss of hair after 2 weeks for doses over 3000 mSv. Recovery from 1 month to a year for most individuals at the lower end of the dose range; only 20% survive at the upper end of the range.
6000 - 10000	Vomiting within 1 hour. Severe blood changes, hemorrhage, infection, and loss of hair. From 80% to 100% of exposed individuals will succumb within 2 months; those who survive will be convalescent over a long period.

The unit of absorbed dose in SI units is the Gray (Gy), and the unit of dose equivalent for biological damage, the Sievert (Sv), is directly related to it:

$$Gy = 1 \frac{J}{kg} \tag{2.9}$$

$$Sv = Q\,Gy \tag{2.10}$$

The factor Q, the quality factor, depends on the type of radiation and is meant to account for long-term risk from low-level chronic exposure. In the case of gamma radiation, Q=1. In relation to other commonly used units of absorbed dose and dose equivalent, the rad and the rem, the Gray and the Sievert differ by two orders of magnitude. One Gray equals 100 rads and 1 Sievert equals 100 rems.

These quantities concerning the amount of energy absorbed may be related simply to the flux of energy at the position in question. To do this an approximate relationship between human surface area and human mass is needed. In the process under investigation, antiproton annihilation propulsion, all the radiation is assumed to originate at a point some distance away from any crew. The surface area that is involved then is not the total surface area as would be the case for isotropic radiation, but a two dimensional projection of it. A typical person is about 1.8 meters tall and 0.55 meters wide. This yields an exposed surface area of approximately 1 square meter, a convenient number to work with. Then, taking this typical person to be about 75 kg (or approximately 165 pounds) the value obtained for mass per square meter of exposed area is 75 kg/m^2. In the analysis that follows, however, one should realize that 75 kg/m^2 is only an estimate and may vary from person to person. The energy (or alternately the number of particles) per m^2, fluence ($\mathcal{F}$), which will be generated during the entire time of operation of an antiproton engine and which is position dependent, can be related to the amount of radiation absorbed by a typical human. Let U=the dose absorbed in Sieverts:

$$U = \eta \frac{\mathcal{F}}{75 \ [\frac{kg}{m^2}]} \qquad (2.11)$$

where η is the fraction of incident energy actually absorbed. Considering a 30 cm thick human and approximating his composition as entirely water, an estimate of η can be made. The fraction of energy absorbed is a function of the energy of the incident photons. The lower the energy, the higher the percentage of absorption. Some knowledge of the incident radiation's energy is thus necessary. In this paper, photons of 0-10 MeV, especially those with energies between 0-2 MeV, are found to dominate the spectrum of photons humans might be exposed to. The Monte Carlo shower simulation program, EGS4, which is used extensively in this paper, indicates η=0.65. This is a conservative estimate. While photons with energies less than 1 MeV will, on average, surrender a somewhat greater fraction of their energy to humans (>0.7), the fraction drops for 2 MeV photons (≈0.61). For η≈0.65, a simple equation follows:

$$U \ [Sv] \approx 0.00867 \ [\frac{m^2 Sv}{J}] \ \mathcal{F} \qquad (2.12)$$

Equations for the fluence are not generally available. Instead, the fluence will be determined, in this paper, for the engine in question by EGS4, which tracks all individual particles.

The question remains as to what levels of radiation absorbed are dangerous. The United States has set the maximum permissible occupational whole body dose at 50 mSv/year. This standard is 10 times higher than the standard for the general public. In practice, for some past space applications, exposures to personnel have been greater than the rate of 50 mSv/yr. Due to the unique nature of space flight, its usually limited duration and the presence of energetic cosmic rays, a conscious decision to allow higher than standard radiation exposure levels may be made if added shielding is considered too mission constraining. As seen in Table 2.2, an exposure of up to 750 mSv or somewhat less would probably not cause irreparable harm to personnel or

interfere with their ability to perform their functions. Nevertheless, in this paper the 50 mSv/yr. standard will be adhered to, allowing the possibility of long duration manned flights to distant planets, or farther, powered by antiproton annihilation engines. Converting to seconds, the standard becomes:

$$\left(\frac{dU}{dt}\right)_{max} = 1.585 \times 10^{-9} \left[\frac{Sv}{s}\right] \qquad (2.13)$$

Since each annihilation of a proton and an antiproton releases ≈1.1.56 x 10^{-10} J (≈709 MeV) of gamma radiation energy on average, the fluence associated with unshielded annihilations is:

$$\mathcal{F} = \frac{t \times \frac{\text{annihilations}}{s} \times 1.1356 \times 10^{-10} \left[\frac{J}{ann.}\right]}{4\pi d^2} \qquad (2.14)$$

where t=time operated, and d=distance from the point of annihilation. A typical value for the fluence per unit time (energy flux) would be, assuming an annihilation rate of 1 x 10^{17} annihilations/s (a rate associated with some proposed antiproton annihilation engines):

$$\text{Flux} = \left(\frac{d\mathcal{F}}{dt}\right) = 9 \times 10^3 \left[\frac{J}{m^2 s}\right] \quad \text{for } d=10 \text{ m} \qquad (2.15)$$

$$\text{Flux} = \left(\frac{d\mathcal{F}}{dt}\right) = 90 \left[\frac{J}{m^2 s}\right] \quad \text{for } d=100 \text{ m} \qquad (2.16)$$

Then:

$$\left(\frac{dU}{dt}\right) = 0.00867 \left(\frac{d\mathcal{F}}{dt}\right) = 0.78 \left[\frac{Sv}{s}\right] \quad \text{for } d=100 \text{ m} \qquad (2.17)$$

The need for shielding is clearly seen. This value for dU/dt is 4.9x10^8 times larger the maximum U.S. standard. Even locating people as much as 100 km away from the point of annihilation does not solve the problem.

Electronics Vulnerability to Gamma Radiation

The analysis applied to humans in the previous section is directly applicable to electronics as well, the only differences being the method of damage, the level of sensitivity to radiation, and the fraction of energy absorbed.

It is expected that any payload carried by an annihilation engine and perhaps significant parts of the engine itself could be damaged by high energy radiation. The electronics aboard a probe or spacecraft, and the powerful magnets required in plasma or beam type annihilation engines are examples. The radiation shielding problem extends to providing protection for these things as well as human beings. In fact, it is likely that the first annihilation engines, should they ever be built, would not be used for manned flights, thus making any problem of human vulnerability to radiation moot.

Operation of any electronic device depends greatly on its semiconductors, and in turn these semiconductors are sensitive to small changes in their structure. The interaction of photons with semiconductors alters the electric properties of the semiconductor, and eventually may disable the semiconductor altogether. Clearly this is unacceptable. Failure of the electronic systems aboard a spacecraft would interfere with data acquisition, analysis, and communication, and could very well jeopardize the functioning of the engine itself. It remains to quantify these effects and determine a safety threshold that may be used for analysis.

The physical mechanism whereby high energy photons damage an electronic device is through ionization and the subsequent effects that its high energy electrons cause. These electrons may have enough energy to reach the conduction band, creating an electron-hole pair and increasing conductivity. The electrons may also be captured in the insulating parts of semiconductors, producing an electric field and increasing their conductivity as well, defeating their purpose. The rate of hole-electron pair creation in silicon is known [18]:

$$\text{Pair Creation} = 4.2\times10^{11}\left(\frac{\text{hole-electron pairs}}{\text{cm}^3\ \text{Gy}}\right) \qquad (2.18)$$

The effect of this rate is semiconductor dependent. Even semiconductors of the same type have a wide range of susceptibility to radiation. For instance, widely used MOS (Metal Oxide Semiconductor) devices have displayed operational difficulties as low as 10 Gy and have operated successfully up to 10^5 Gy in special cases where "hardening," or consciously designing to counter radiation problems, has been implemented [18]. Other types of semiconductors, which are utilized for their different speeds and abilities, typically have radiation failure thresholds in this range. It is improper to choose one level of radiation absorption as a standard value for safe operation of electronic devices, especially semiconductors, because of their variety. While a value such as 1 Gy would assure the continued operation of virtually all of these devices, 1 Gy is probably much too strict a standard for a specialized application such as antiproton annihilation engines. In such a specific setting, hardening could easily increase the safe exposure level by orders of magnitude, thereby reducing the need for massive shielding.

Within the range of 10^2-10^4 Gy most semiconductors will fail or will begin to have trouble. However, capitalizing on hardening techniques, electronics engineers could probably design a system that would be able to operate correctly within this range of total radiation absorption. For the purpose of evaluating radiation effects on semiconductors therefore, an absorbed dose of greater than 10^4 Gy will be considered unacceptable, while anything less than 10^2 Gy will be considered completely safe. Doses between these two values will be considered potentially troublesome but acceptable.

As for humans, a relation is needed relating exposed surface area to mass for semiconductors. Considering a small cubic portion of silicon, say 1 mm of length on all sides, the exposed surface area is 1 mm^2 and the volume is .001 cm^3. With the density of silicon being 2.33 g/cm^3, the ratio of mass to surface area in this case is:

$$\frac{\text{mass}}{\text{S.A.}} = \frac{.00233\ [g]}{1\ [mm^2]} = 2.33\times10^{-6}\left[\frac{kg}{mm^2}\right] \qquad (2.19)$$

Now, relating the dose absorbed by the semiconductor, U^*, to the fluence, $\mathcal{F}^*$ with units of J/mm^2 (simply $10^{-6}\,\mathcal{F}$, except within shielded areas less than 1 m^2):

$$U^* = \eta^* \frac{\mathcal{F}^*}{\left(2.33\times10^{-6}\left[\frac{kg}{mm^2}\right]\right)} \qquad (2.20)$$

EGS4 was used to determine η^* for a 1 mm slab of silicon exposed to low energy photons (0-10 MeV). For 0.5 MeV to 2.0 MeV photons, the most populated range of photon energy (see figure A.5(a)), η^* ranges from 0.0085 to 0.0025. A reasonable estimate, therefore, is η^*=0.003. The higher energy photons, carrying a greater

fraction of the incident energy than the low energy photons, will have a somewhat lower η^*. Once again a simple relation between the dose absorbed and the fluence is obtained:

$$U^* \, [Gy] = 1287.6 \, [\frac{mm^2 Gy}{J}] \, \mathcal{F}^* \qquad \{2.21\}$$

Unlike the case for humans, however, there is no safety standard for the rate of absorption. In both cases, it is the total amount of radiation absorbed that is significant. The rate of exposure standard for humans is a safeguard devised with the total level of absorption in mind.

The relations involving fluence developed in this chapter will be used in Chapter 5 to evaluate radiation hazards.

Chapter 3
EGS4: MONTE CARLO PROGRAM FOR SHOWER SIMULATION

Introduction

In order to determine the radiative properties of an antimatter annihilation engine, a method is needed to simulate the propagation of particles, specifically electrons, positrons, and photons which comprise the showers described in Chapter 2. Computer codes which track individual particles and simulate their interactions with matter are known as Monte Carlo codes, so named because interactions are reproduced based upon known probabilities and random number generation. These probabilities are derived from the cross sections associated with the actual physical events (see equations {2.1}-{2.8}).

General equations are inadequate for describing the radiation environment around an annihilation engine. One quickly finds, due to complicated geometries, that analyzing a specific engine of any complexity becomes unmanageable. Deprived of this more general approach, Monte Carlo codes are necessary to accurately determine the position dependent fluence outside of an annihilation engine.

Monte Carlo codes, due to their nature, are time consuming. Many original particles, as well as the multiplicity of secondary particles created by each, must be tracked in order to reasonably eliminate statistical phenomena. Due to this reality, the number of simulations that can be run is quite constrained. Of course, with the advent and availability of faster computers the number of possible simulations will continue to grow in size and scope.

In this chapter, the Monte Carlo code used for this study, EGS4, will be described and the results of an effort to verify its accuracy will be reported. General results obtained from EGS4 will be presented and compared to a previous study of annihilation shielding.

The EGS4 Code System

The Monte Carlo code that has been used extensively to produce the results presented in this paper is EGS4, which stands for Electron-Gamma Shower 4. The code was developed at the Stanford Linear Accelerator (SLAC) by Walter Nelson, Hideo Hirayama, and David Rogers [19]. In this section an overview of EGS4's capabilities will be given with particular attention paid to its structure and limitations.

Structure of EGS4

Before EGS4 can be run, a file containing all the necessary data for the materials involved must be created. This is done with the help of an auxiliary program named PEGS4. PEGS4 is capable of simulating elements, compounds, and mixtures. In all cases cross section data are produced that EGS4 will call upon while running. Its implementation is simple [19].

In order to use EGS4, the user must write a segment of code which describes the geometry, which defines the position, orientation, and energy of the incident particles, which records the desired results, and which calls the necessary subroutines (HATCH and SHOWER).

The user must restrict the movement of each particle (in the subroutine HOWFAR) so that it travels only within one material in any given step. If the particle is set to

step across a boundary, the size of the step must be changed and the new region assigned to the particle so that EGS4 will be using the correct cross section data. Distinct regions may be set up within the same material as well if the user desires. By carefully setting up various regions, the user can create a complex geometry simulating any number of devices.

The subroutine SHOWER is called each time the user wants to simulate the shower resulting from a single incident particle. Part of the information that must be made available to SHOWER is the particle's energy, initial position, type (electron, positron, or photon), and its orientation in the form of direction cosines. A particle is discarded, no longer tracked by the code, either forcibly by the user or when its energy falls below a threshold energy set by the user before the simulation begins. Subroutine SHOWER ends when all the particles created in a shower have been discarded, annihilated, or absorbed.

EGS4 calls two user written subroutines while it is running (HOWFAR and AUSGAB). The subroutines may be used to record any desired information about the particles involved in the shower. For example, the energy of the photons that cross a particular boundary may be saved, creating a histogram for later study. It is possible to keep track of many variables.

Once the main user code and the two subroutines, HOWFAR and AUSGAB, have been written, EGS4 may be successfully run. EGS4 itself consists of a number of subroutines that are designed to ascertain if any events occur, choose the energies, types and directions of any secondary particles that are created, and to transport the particles.

Cross Sections Used By EGS4

Most of the cross sections that EGS4 uses in order to determine probability of interaction are given in Chapter 2. The exceptions are the photoelectric effect cross section which EGS4 takes directly from the empirical data of Storm and Israel [16], the pair production cross section which, for energies below 50 MeV, also uses Storm and Israel data, and two for which the formulas are quite complex and not given in Chapter 2: continuous electron energy loss and multiple coulomb scattering [19].

Verification of EGS4

In order to determine the correctness of the EGS4 code, a comparison with the established work of Messel and Crawford [15] was carried out. The authors of the code claim to have extensively checked the output of EGS4 with experiment and other Monte Carlo codes. An independent check was done to verify this claim.

Messel and Crawford [15] had previously compiled a table of shower results for lead and copper, recording the numbers of photons and electrons at varying depths. They found their results using an earlier Monte Carlo code. Messel and Crawford's 'Shower Book' has been considered quite accurate in most of the physics community.

EGS4 was able to reproduce the exact same conditions that Messel and Crawford used for some of their runs. Close agreement between EGS4 and Messel and Crawford would be taken as evidence that EGS4 was accurate enough for the antiproton annihilation engine study to be conducted.

The results of this comparison between EGS4 and Messel and Crawford follow. Four series of data were recorded: the number of photons above 1 MeV as a function of depth per incident 100 MeV photon, the number of electrons above 1 MeV as a function of depth per incident 100 MeV photon, the number of photons above 10 MeV as a

function of depth per incident 100 MeV photon, and the number of electrons above 10 MeV as a function of depth per incident 100 MeV photon. All of these were done with lead as the absorber. The results appear graphically in Figures 3.1 and 3.2. In each Figure, the solid line represents an approximation to the Messel and Crawford results while the diamond shaped symbols represent data produced by EGS4.

The data from the two independent sources agree quite well except for the first case, low energy photons. In light of the study to be done it was determined that this discrepancy could be serious as there is nearly an order of magnitude difference in the number of photons at the higher depths between EGS4 and Messel and Crawford, with Messel and Crawford predicting the greater number. If Messel and Crawford were correct, then it would indicate that EGS4 might seriously underpredict the amount of shielding actually needed.

This discrepancy was investigated in order to determine its source. Messel and Crawford, being almost two decades old, was thought to perhaps be outdated in some of its cross section formulas. A reconstruction of the cross sections used in both EGS4 and Messel and Crawford was carried out to test this theory. The results are shown in Figure 3.3. The cross sections for Compton scattering and photoelectric effect are seen to be essentially identical. The cross sections for bremsstrahlung and pair production were found to be somewhat different. At low energies where the discrepancy occurs (there was basic agreement above 10 MeV) there is nearly an order of magnitude difference in the pair production cross sections and a factor of as much as two separating the bremsstrahlung cross sections. The discontinuities at 50 MeV arise due to the way that EGS4 handles its cross sections, with empirical factors used below 50 MeV and none for energies higher than that.

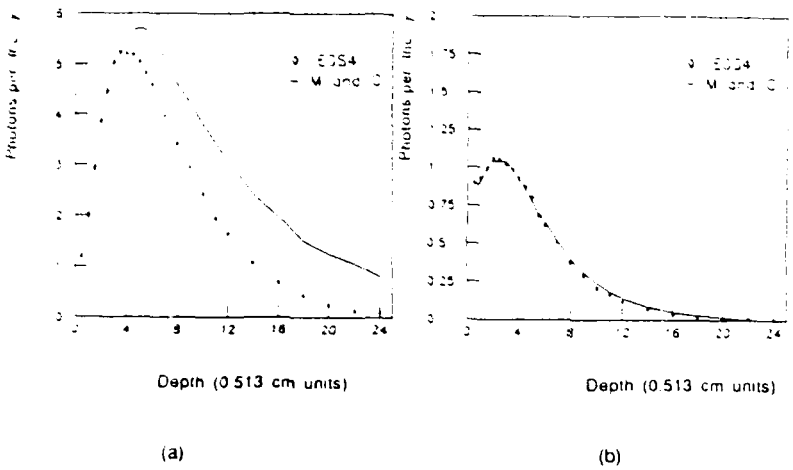

Figure 3.1: Number of Photons vs. Depth [in units of 0.513 cm] with (a) 1 MeV *Minimum Energy* and (b) 10 MeV Minimum Energy, per Incident 100 MeV Photon According to Messel and Crawford and EGS4.

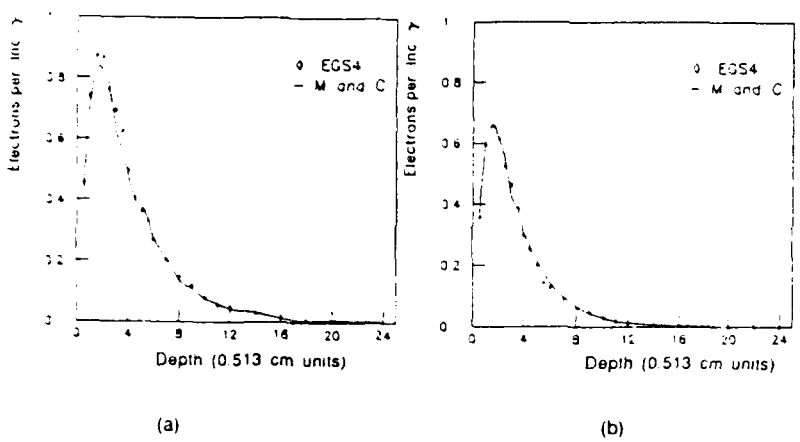

Figure 3.2: Number of Electrons vs. Depth [in units of 0.513 cm] with (a) 1 MeV Minimum Energy and (b) 10 MeV Minimum Energy, per Incident 100 MeV Photon According to Messel and Crawford and EGS4.

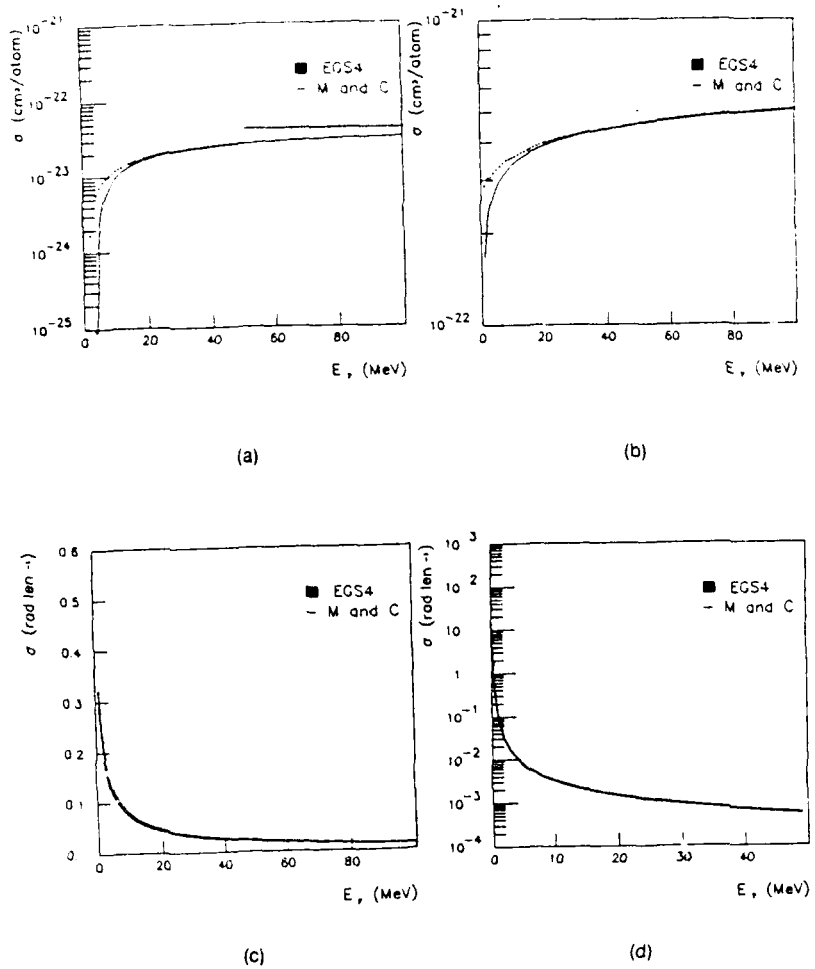

Figure 3.3: Comparison of Cross Sections Used by Messel and Crawford and EGS4 for (a) Pair Production, (b) Bremsstrahlung, (c) Compton Scattering, and (d) *Photoelectric Effect*.

For incident energies below 50 MeV, EGS4 relies directly on experimental data for values of the pair production cross section. For bremsstrahlung, EGS4 incorporates experimental results into an empirical correction factor. In addition, EGS4 is widely used and has been extensively benchmarked. All of this supports the validity of EGS4. Messel and Crawford's Monte Carlo code, based on theory and older experimental results, is more likely to contain inaccuracies. Forward biasing, ignoring backwards scattered particles, may be partly responsible for its shortcomings.

Limitations of EGS4

In many engineering problems it is unnecessary and inefficient to include every possible physical interaction into a model of a system. Accurate results can be obtained by ignoring some of the minor details. Such is the case with EGS4. There are certain phenomena that the authors have chosen to leave out. These include the Elwert correction, the Migdal correction, the Suppression effect, Rayleigh scattering in the default mode, and certain secondary modes of the photoelectric effect.

The Elwert Correction

The Elwert correction becomes significant at low electron energies, approximately when the kinetic energy of the electron is below 2 MeV. Its effect is to slightly increase the cross sections for both bremsstrahlung and pair production.

The Migdal Correction

The Migdal correction is needed due to the polarization of media, its practical effect being the cutoff of the differential bremsstrahlung cross section at a certain fraction of the incident electron energy. For example, if the Migdal correction were included a

100 MeV electron could not produce any photons below 0.012 MeV. This is a minor restriction expected to have little effect.

The Suppression Effect

The Suppression effect decreases bremsstrahlung and pair production cross sections at very high energies, such as 10^7 MeV. This is much greater than the energies encountered in this study.

Rayleigh Scattering

Rayleigh scattering is applicable to radiation whose wavelength is relatively long compared to the size of the atoms that it scatters off. A relation between the incident wavelength and the scattered wavelength is known and is dependent upon the inverse fourth power of the incident wavelength. It is reasonable to ignore Rayleigh scattering in this study since most of the photons transported are of a much higher energy (i.e. shorter wavelength).

Secondary Modes of the Photoelectric Effect

The photoelectric effect is dominated by electrons released from the innermost shell of the atom. Electrons from other shells may be released but are safely ignored in many cases.

General Results

From a shield engineering perspective, the amount of material needed to absorb a given fraction of the incident energy is the most important criteria. Although the question of how much shielding will be needed can become quite complex due to the

geometry or other characteristics of any particular engine, an answer to this question can allow good estimates.

In order to address this question, simple simulations were carried out using EGS4. Photons representative of antiproton-proton annihilations were transported, in a beamlike fashion, into a large slab of material and the energy absorbed by the material was recorded as a function of depth. This was done for a number of materials, specifically tungsten, carbon, aluminum, and lead. Figure 3.4 presents the results in graphical form. It is evident that the denser materials are the better absorbers of the radiation energy. The energy is completely absorbed by less than 20 cm of tungsten.

An earlier paper on the shielding needs of annihilation engines by Brice Cassenti [20] presented a similar analysis for tungsten. A comparison of the energy absorption predicted by his code and by EGS4 is shown in Figure 3.5. Cassenti's results indicate a higher rate of energy absorption than does EGS4.

Cassenti's study was admittedly approximate. For example,

(1) The annihilation radiation used, a monoenergetic collection of 200 MeV photons instead of the actual spectrum ranging from 10 MeV to 800 MeV, is an oversimplification. While 200 MeV is approximately the average energy of the photons created by annihilation, the cross sections of the physical processes involved in electron-photon showers are functions of energy, making this a poor approximation.

(2) Electrons created by ionization and Compton scattering were not considered. The result of this is to eliminate a source of low energy photons, which these electrons would have produced through bremsstrahlung. By doing so, energy losses are more strictly localized, resulting in a higher rate of absorption.

(3) The one-dimensional nature of the analysis further affected the rate of energy absorption (by slightly decreasing it).

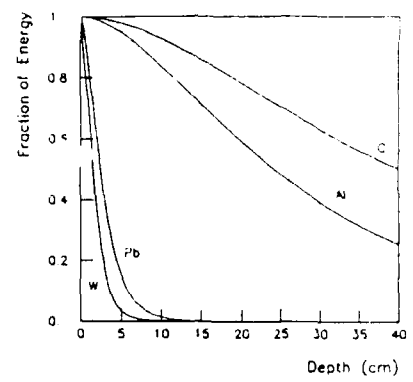

Figure 3.4: Fraction of Energy Remaining vs. Depth [cm] for Various Materials as Determined by EGS4.

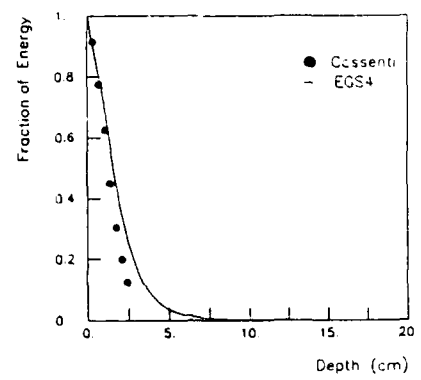

Figure 3.5: Comparison of Fraction of Energy Remaining as a Function of Depth in Tungsten as Determined by EGS4 and Cassenti.

(4) The numerical technique was approximate.

Overall, the result of these approximations was to overpredict the rate of energy absorption. Perhaps the most significant factor, however, was the overestimation of the allowable fluence. Cassenti took the range of 10^3-10^4 Gy, from an article on nuclear weapons [21], as the level of dose absorption to avoid. This corresponds to a lethal dose and exposure should actually be kept more than an order of magnitude lower than this in order to avoid ill effects. Cassenti's conclusion is that only 16 radiation lengths of tungsten (≈5.6 cm) are needed to adequately protect a crew at 100 m distance from an annihilation engine in which 4 mg of antiprotons are used (≈2.4×10^{21} annihilations). EGS4 indicates that at least 29 radiation lengths (≈10 cm) of tungsten would be required to achieve the four order of magnitude reduction in fluence needed to reduce it to a safe level.

In his paper, Cassenti calls for a Monte Carlo simulation "tracking thousands of particles" that would avoid major approximations and clarify the issue of annihilation engine shielding. This paper, using EGS4, answers that request.

Chapter 4
SIMULATION OF A SOLID CORE ENGINE, LIPTHANE

Introduction

The Monte Carlo code, EGS4, has been applied to a specific antiproton annihilation engine in order to determine that engine's radiative properties. The engine studied was designed by Giovanni Vulpetti of Telespazio in Italy [22]. It has undergone some evolution since it was first introduced in 1986, when it had equally thick concentric shells and a chamber filled with gas designed to annihilate the antiprotons. The characteristics of the current design of LIPTHANE (for Liquid Propellant THermal ANnihilation Engine) are given in the first section of this chapter [23]. The modeling of LIPTHANE is subsequently considered, after which the results will be presented. Included in the results will be the fluence by axial position and radius, the fraction of energy absorbed in each shell and other engine parts, and the number of electrons and photons that develop by region.

Two separate simulations were conducted using LIPTHANE, one without any extra shielding and the other with a 20 cm thick tungsten (5% rhenium) shield placed between the vehicle and the engine (see Figure 4.1). The two simulations were conducted in an attempt to ascertain how much shielding was needed to make the LIPTHANE environment safe for people and electronics. A shield thickness of 20 cm was chosen based on preliminary indications that most or all of the energy would be absorbed by this much tungsten (see Figure 3.4). In the notation that follows, "unshielded" refers to the LIPTHANE engine (including all of its shells) without any

additional shielding, and "shielded" refers to the LIPTHANE engine with the 20 cm tungsten-rhenium shield included (but no extra shielding in the radial direction).

Description of LIPTHANE

The premise behind an engine like LIPTHANE is simple. In order to capture the energy from annihilations, dense material is placed so that it surrounds the annihilation point or region. The high energy particles that are created, pions and photons mainly, transfer some or all of their energy as they pass through the matter. The material will increase in temperature, enabling a transfer of heat to a propellant which will, in turn, increase in temperature and pressure. Once this is accomplished, thrust can be obtained by expanding the heated propellant out a nozzle. A cross sectional view of LIPTHANE is presented in Figure 4.1.

The design does not address how the antiprotons are stored or managed. Instead, it is assumed that this aspect of the engine has been worked out and the engine's hypothetical performance is considered. In order to achieve annihilation, the antiprotons are shepherded down a vacuum tube which ends in a small target of carbon located at an axially central position. Here the antiprotons will annihilate with the protons and neutrons of the carbon, releasing their energy.

The current design of LIPTHANE uses a mixture of tungsten and rhenium for the dense concentric shells that will capture all this energy. The 5% rhenium was added to preclude the re-crystallization of the tungsten, which would damage its mechanical properties. These mainly tungsten shells, referred to as the heat conversion and transfer system (HCTS), satisfy the major requirements of high density, high melting point, and good heat conduction. The innermost and outermost shells are exceptions; they are relatively thin compared to the other shells and are meant to ease the cooling

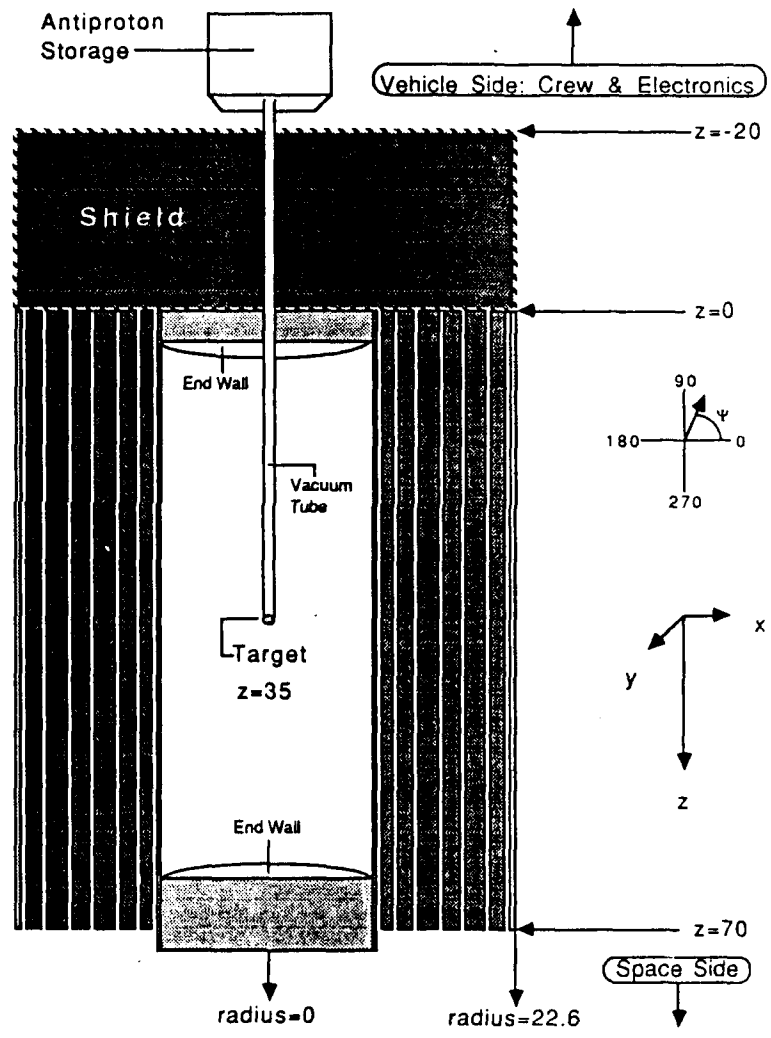

Figure 4.1: A Cross Sectional View of LIPTHANE.

requirements. They are low density, high-temperature substances. Carbon-carbon fiber was chosen for the innermost shell, but the outermost shell was left unspecified. The end walls of the interior region are 3 cm and 7 cm on the vehicle and space side respectively. Both gaseous and liquid cooling are used to keep the innermost shell and the target from melting. Table 4.1 gives the exact materials and measurements of the engine, taking into account the assumptions detailed in the section on modeling LIPTHANE. The device is smaller than a cubic meter, 70 cm in length and less than 46 cm in diameter.

Liquid hydrogen is used as the propellant and is pumped between the concentric shells of the HCTS. While it is true that the liquid hydrogen will absorb some energy directly from the annihilation products as they pass through, the overwhelming portion of the energy absorbed will be the heat transferred from the tungsten-rhenium shells.

The Modeling of LIPTHANE

In the modeling of LIPTHANE for the Monte Carlo simulation, several approximations, simplifications, and assumptions were made:

(1) The outermost shell of unspecified material was assumed to be carbon-carbon fiber, the same as the innermost shell.

(2) The vacuum tube was ignored.

(3) The interior region, the region bounded by the first shell and the engine end walls, was assumed to be entirely liquid hydrogen except for the centrally located carbon target. Thus, the cooling system was considerably simplified.

Table 4.1: Materials, Densities, and Positions of LIPTHANE Subcomponents.

Name	Material	Density [g/cm^3]	Radius [cm]	Axial(z) [cm]
Target	Carbon	2.26	.5 (sph)	35
Inner Cooling Region	Liquid Hydrogen	.0708	0-10 (cyl)	3-65
Shell #1	Carbon-Carbon Fiber	2.5	10-10.48	0-72
Between 1-2	Liquid Hydrogen	.0708	10.48-10.98	0-70
Vehicle End	Carbon-Carbon Fiber	2.5	0-10	0-3
Space End	Carbon-Carbon Fiber	2.5	0-10	65-72
Shell #2	Tungsten (5% Rhenium)	19.361	10.98-12.2	0-70
Between 2-3	Liquid Hydrogen	.0708	12.2-12.4	0-70
Shell #3	Tungsten (5% Rhenium)	19.361	12.4-13.7	0-70
Between 3-4	Liquid Hydrogen	.0708	13.7-14	0-70
Shell #4	Tungsten (5% Rhenium)	19.361	14-15.45	0-70
Between 4-5	Liquid Hydrogen	.0708	15.45-15.8	0-70
Shell #5	Tungsten (5% Rhenium)	19.361	15.8-17.51	0-70
Between 5-6	Liquid Hydrogen	.0708	17.51-17.8	0-70
Shell #6	Tungsten (5% Rhenium)	19.361	17.8-19.71	0-70
Between 6-7	Liquid Hydrogen	.0708	19.71-19.97	0-70
Shell #7	Tungsten (5% Rhenium)	19.361	19.97-21.9	0-70
Between 7-8	Liquid Hydrogen	.0708	21.9-22.2	0-70
Shell #8	Carbon-Carbon Fiber	2.5	22.2-22.6	0-70
Shield	Tungsten (5% Rhenium)	19.361	0-22.6	-20-0
Everywhere Else	Vacuum	0.0	-	-

(4) The engine end walls were assumed to be completely solid and whole. No allowance was made for an entry hole for the antiprotons. In the case of the shielded engine no allowance was made for passage of the propellant through the shield.

(5) Electrons below 1 MeV total energy and photons below 0.01 MeV were discarded. Previous results had indicated this restriction would not have a significant impact.

(6) The carbon target was assumed to be a sphere with a radius of 0.5 cm.

(7) All regions not specified were assumed to be vacuum.

While all of these assumptions will had an effect upon the results of the simulations, none was believed to have had a serious impact.

Results of the Monte Carlo Simulations

In this section, results obtained through the Monte Carlo simulation of the propagation of photons, electrons, and positrons in the LIPTHANE engine by the code EGS4 will be presented.

Incident Photons

For the photons created by the decay of the π^0's, a probability for each energy was calculated from the antiproton-proton spectrum shown in Figure 1.6. Random number generation was then used to reproduce the original spectrum. The spectra created during the two simulations, shielded and unshielded, are shown in Figure 4.2. For comparison, values from the spectrum they were intended to reproduce, adjusted to indicate number of photons per 10 MeV from a sample of 10^5 annihilation photons

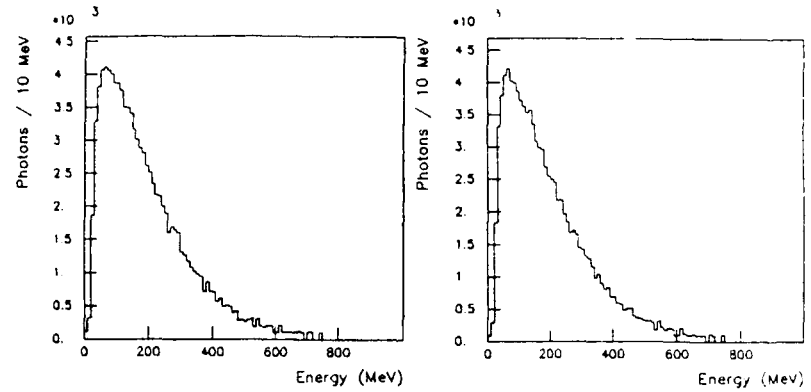

(a) (b)

Figure 4.2: Initial Gamma Radiation Spectra for (a) Unshielded and (b) Shielded Simulations. Based on a Sample of 100,000 Annihilation Photons.

Table 4.2: Number of Photons per 10 MeV vs. Photon Energy for 10^5 Annihilation Photons ($\approx 2.632 \times 10^4$ Annihilations) as Adapted from Figure 1.6.

Photon Energy [MeV]	Number of Photons [10^3]
100	3.95
200	2.60
300	1.46
400	0.63
500	0.32
600	0.13
700	0.04

(=2.632 x 10^4 annihilations), are given in table 4.2. Good agreement between the spectra is apparent.

Fluence

Fluence data, the amount of energy per unit area, were not directly available from the EGS4 runs. Instead, the energies and radii of particles crossing preselected longitudinal boundaries were recorded (see Appendix A). The data representing energy as a function of radius were transposed to give the fluence in J/m^2. This was achieved by *summing the contributions of 10^4 adjacent square centimeters, centered about the* radius in question. An average value of 3.8 photons per annihilation was used to transpose the values to fluence per annihilation. Figure 4.3 illustrates the planes used to measure fluence. Data were collected for planes at distances of 100 m, 10 m, 5 m, 1 m, and 0.5 m from both ends of LIPTHANE. Figures 4.4-4.13 give the fluence per annihilation in J/m^2 as a function of radius for both the shielded and unshielded simulations. Axial positions of the planes, in which the radii exist, were measured from either end of the engine, vehicle side or space side, as indicated. Values in parentheses are the actual axial positions in centimeters (z=35 cm is at the center of the engine, z=0 cm is the vehicle end, and z=70 cm is the space end).

There are several things to note about the fluence data:

(1) *The fluences obtained in the shielded simulation, for z<0, are approximately* three to four orders of magnitude below the fluences at the identical positions in the unshielded simulation.

(2) The reduction of fluence can be seen in the data for progressive distances away from the engine. Peak fluences fall steadily and spread out over larger ranges of radii.

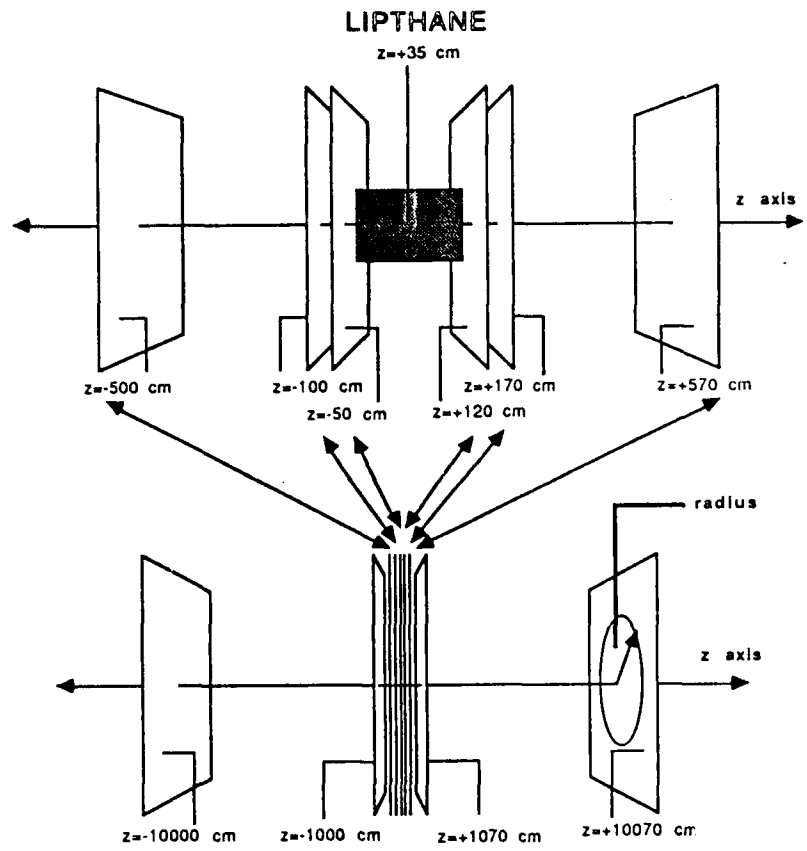

Figure 4.3: Positions of the Planes Used to Measure Fluence.

(3) For the unshielded case, within one meter from the engine, the most dangerous area is clearly within a radius of less than one meter. Five meters from the engine the most dangerous area is clearly within a radius of 2 meters.

Care must be taken when deriving the fluence in J/mm^2 from the available fluence data in J/m^2. For the shielded simulations, energy data indicate that no energy is transferred on the vehicle side within a radius of 22.6 cm (i.e. the shield blocks all of the particles incident upon it, see Figure A.6). This is not obvious from the fluence data in Figures 4.4(b) and 4.5(b) since , in those results, integration of the fluence has been done over too course an area. For fluences in J/mm^2, F^*, therefore, simply dividing the fluences in J/m^2 by 10^6 is incorrect for areas directly behind the shield.

Energy Absorption

While EGS4 is unable to determine the total amount of energy absorbed in matter as a result of annihilations because it ignores many of its products (pions, kaons, muons, etc.), it is able to determine the energy absorbed for the particles that it does track, namely photons, electrons, and positrons. Since greater than one third of the total energy released from antiproton annihilations is in the form of photons, this is of significance to the overall design of the HCTS. The results for both the unshielded and shielded simulations are given in table 4.3. "Perpendicular" indicates the particles that remained within the original axial engine coordinates ($0 < z < 70$) out to a radius of 100 m.

Note that the 20 cm tungsten-rhenium shield absorbed (or backscattered) all of the energy incident upon it. The energy that did escape on the vehicle side is a result of those particles that escaped shell #8.

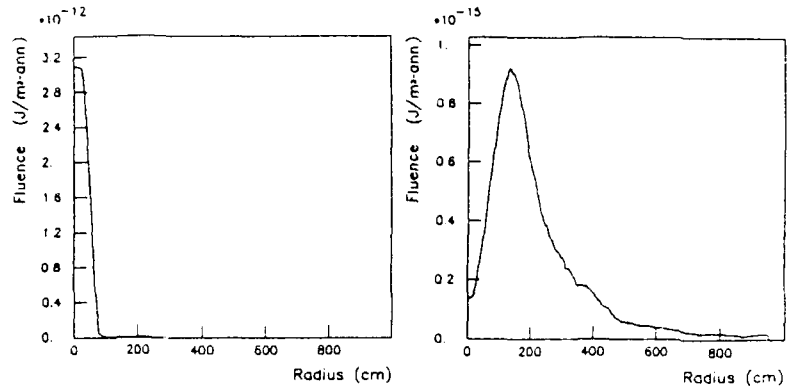

Figure 4.4: Fluence in J/m^2 per Annihilation vs. Radius in cm at 50 cm from Vehicle End of LIPTHANE (z=-50 cm) for (a) Unshielded and (b) Shielded.

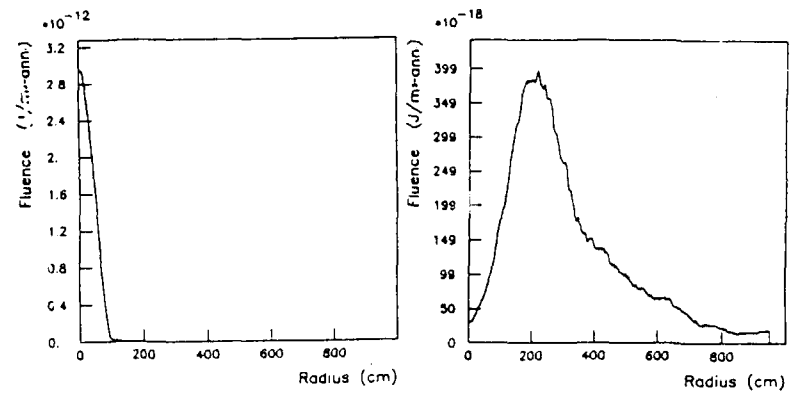

Figure 4.5: Fluence in J/m^2 per Annihilation vs. Radius in cm at 100 cm from Vehicle End of LIPTHANE (z=-100 cm) for (a) Unshielded and (b) Shielded.

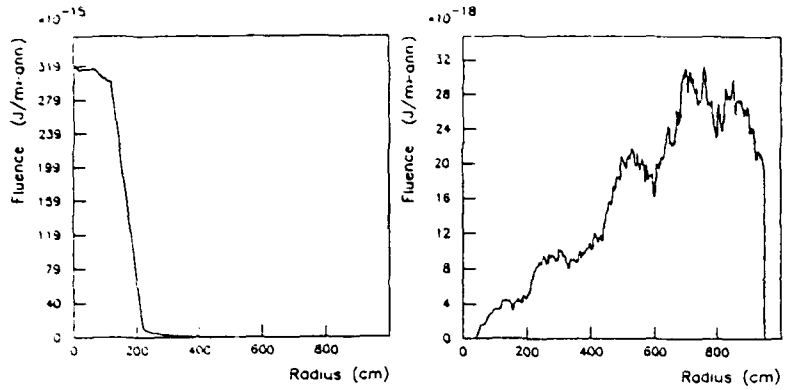

(a) (b)

Figure 4.6: Fluence in J/m^2 per Annihilation vs. Radius in cm at 500 cm from Vehicle End of LIPTHANE (z=-500 cm) for (a) Unshielded and (b) Shielded.

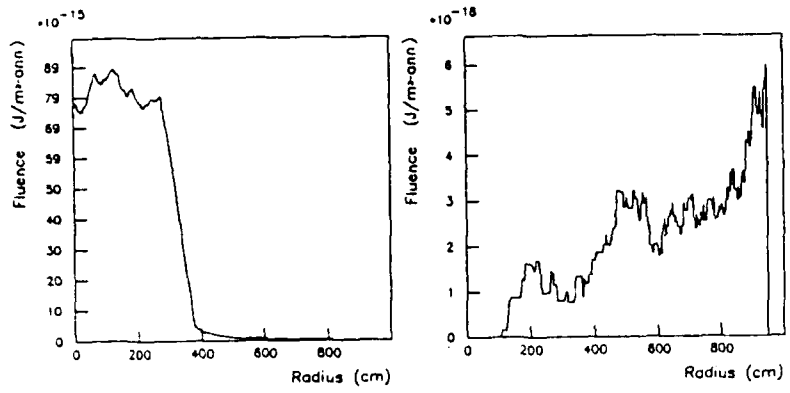

(a) (b)

Figure 4.7: Fluence in J/m^2 per Annihilation vs. Radius in cm at 1000 cm from Vehicle End of LIPTHANE (z=-1000 cm) for (a) Unshielded and (b) Shielded.

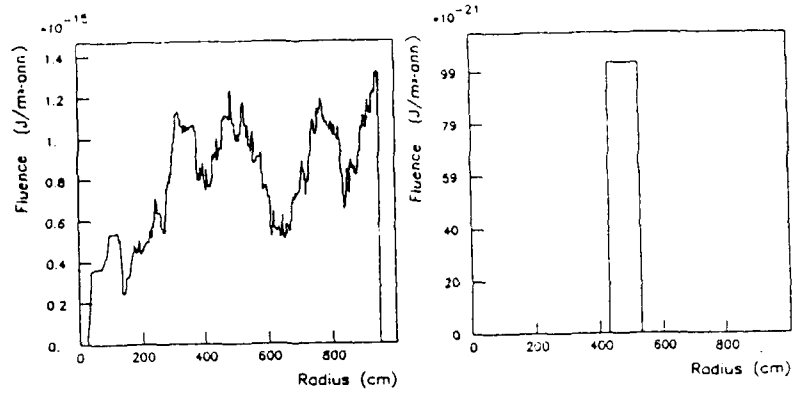

(a) (b)

Figure 4.8: Fluence in J/m^2 per Annihilation vs. Radius in cm at 10000 cm from Vehicle End of LIPTHANE (z=-10000 cm) for (a) Unshielded and (b) Shielded.

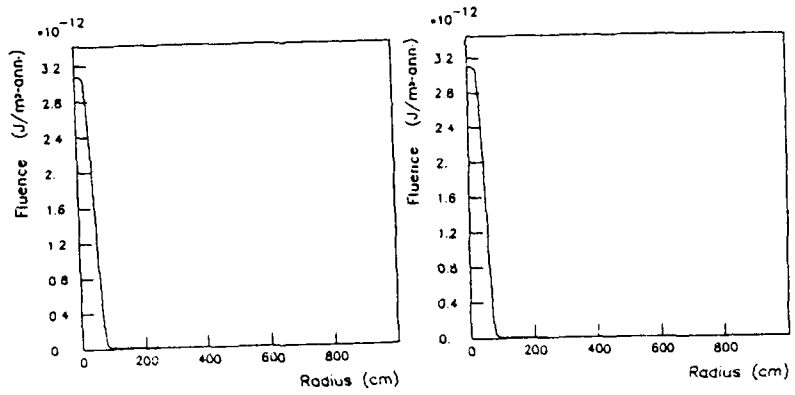

(a) (b)

Figure 4.9: Fluence in J/m^2 per Annihilation vs. Radius in cm at 50 cm from Space End of LIPTHANE (z=+120 cm) for (a) Unshielded and (b) Shielded.

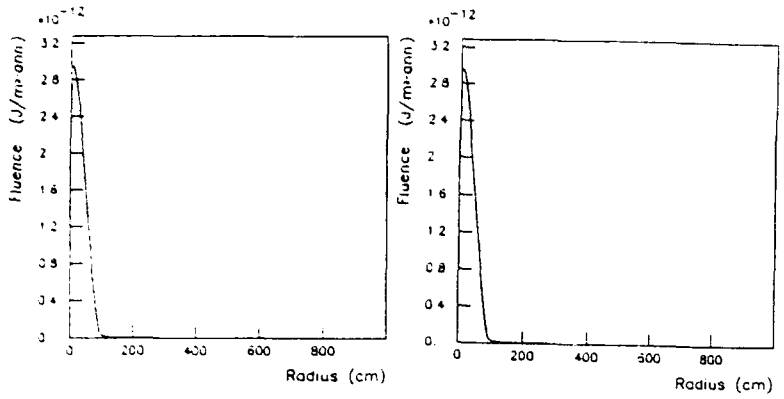

(a) (b)

Figure 4.10: Fluence in J/m^2 per Annihilation vs. Radius in cm at 100 cm from Space End of LIPTHANE (z=+170 cm) for (a) Unshielded and (b) Shielded.

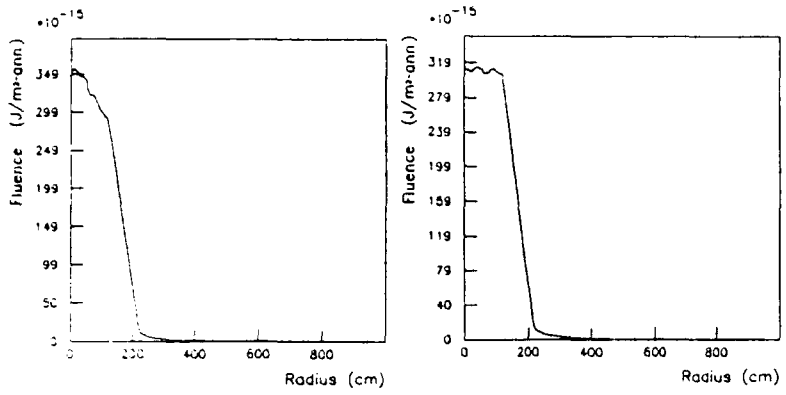

(a) (b)

Figure 4.11: Fluence in J/m^2 per Annihilation vs. Radius in cm at 500 cm from Space End of LIPTHANE (z=+570 cm) for (a) Unshielded and (b) Shielded.

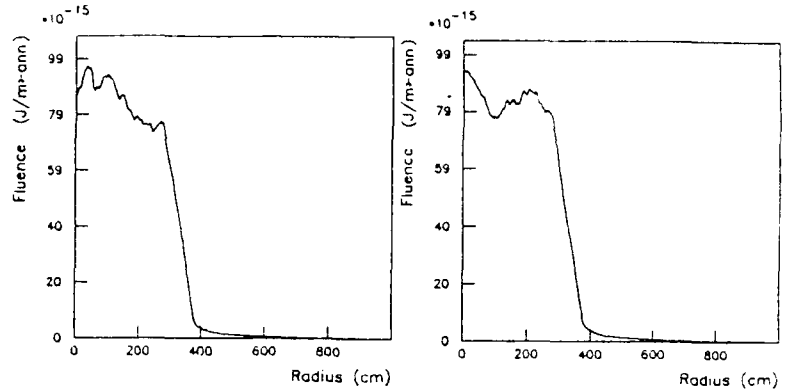

(a) (b)

Figure 4.12: Fluence in J/m^2 per Annihilation vs. Radius in cm at 1000 cm from Space End of LIPTHANE (z=+1070 cm) for (a) Unshielded and (b) Shielded.

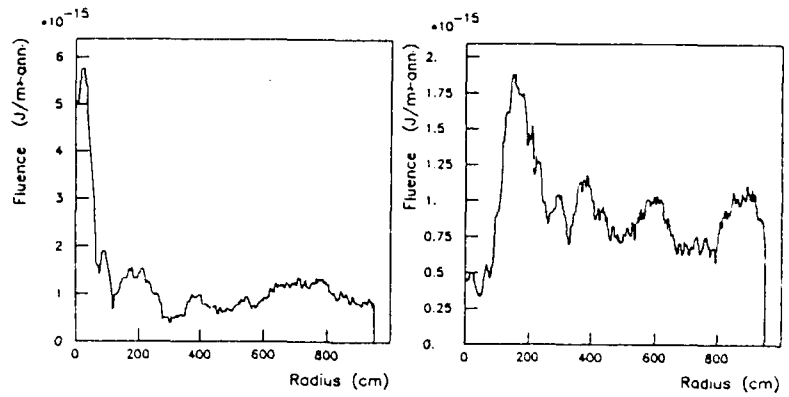

(a) (b)

Figure 4.13: Fluence in J/m^2 per Annihilation vs. Radius in cm at 10000 cm from Space End of LIPTHANE (z=+10070 cm) for (a) Unshielded and (b) Shielded.

Table 4.3: Percentage of Initial Gamma Radiation Energy Absorbed by Region.

Region	Unshielded [%]	Shielded [%]
Target (C)	.040	.037
Interior Cooling (LH)	.445	.428
Shell #1 (C)	.472	.484
Between 1-2 (LH)	.089	.089
Shell #2 (W-Rh)	44.220	44.085
Between 2-3 (LH)	.428	.431
Shell #3 (W-Rh)	31.962	32.010
Between 3-4 (LH)	.159	.160
Shell #4 (W-Rh)	11.931	11.986
Between 4-5 (LH)	.039	.040
Shell #5 (W-Rh)	3.766	3.800
Between 5-6 (LH)	.007	.007
Shell #6 (W-Rh)	.963	.974
Between 6-7 (LH)	.001	.001
Shell #7 (W-Rh)	.209	.212
Between 7-8 (LH)	.000	.001
Shell #8 (C)	.000	.000
Shield	N.A.	2.591
Escape Towards Vehicle Side ($0<\Psi<180$)	2.651	.028
Escape Towards Space Side ($180<\Psi<360$)	2.616	2.634
Escape Perpendicular ($0<z<70$, $r=100$ m)	.000	.001

Number of Photons and Electrons

As the shower develops, the number of photons and "electrons" (where "electrons" includes positrons as well) will change from region to region. These values were recorded and are valuable, in conjunction with the energy spectrum of the photons (see Appendix A), in exploring the dynamics of the shower. Table 4.4 gives the number of photons and electrons that were found to exit each region (in any direction), on average, per incident annihilation photon.

For the first few shells the creation of lower energy photons from bremsstrahlung overwhelms the absorption of the photons through ionization. At its peak, there are over 15 photons present, on average, for every photon introduced into the engine by annihilation. Of course, the sum of the energy of these photons will be less than the energy of the original photon. Evidently, as the shower develops, the incident high energy photons are converted to numerous lower energy photons and electrons. The electrons are not as numerous as the photons because they are quicker to lose their energies in collisions and bremsstrahlung. Thus, many never reach the boundaries of the regions in which they were created. They are born and die within the same region.

Since no photons were recorded exiting the shield on its $z=-20$ side, the 0.046 entry for the number of photons exiting the shield consists entirely of backscattered photons.

Table 4.4: Number of Photons and Electrons Emerging Per Incident Photon by Region.

Region	Unshielded		Shielded	
	photons	electrons	photons	electrons
Target	.988	.035	.989	.033
Interior Cooling	2.622	0.054	2.648	.052
Shell #1	4.369	.123	4.437	.125
Between 1-2	4.257	.117	4.311	.119
Shell #2	15.161	1.046	15.187	1.051
Between 2-3	15.717	1.063	15.721	1.069
Shell #3	10.569	.487	10.590	.487
Between 3-4	9.138	.317	9.164	.319
Shell #4	4.093	.131	4.120	.134
Between 4-5	3.453	.074	3.478	.076
Shell #5	1.195	.029	1.206	.030
Between 5-6	.984	.015	.995	.015
Shell #6	.289	.005	.295	.006
Between 6-7	.236	.002	.239	.003
Shell #7	.067	.001	.067	.001
Between 7-8	.054	.001	.053	.001
Shell #8	.053	.001	.053	.001
Shield	N.A	N.A.	.046	.003
Escape Towards Vehicle Side ($0<\Psi<180$)	.239	.009	.027	.000
Escape Towards Space Side ($180<\Psi<360$)	.219	.013	.229	.014
Escape Perpendicular ($0<z<70$, $r=100$ m)	.088	.002	.078	.001

Chapter 5
EVALUATION AND CONCLUSIONS

Introduction

The fluence data presented in Chapter 4 and the general results presented at the end of Chapter 3 can be used to assess the danger to humans and electronics in an antiproton annihilation environment.

This Chapter includes a section on the general characteristics of antiproton annihilation radiation and its effects, a detailed look at the radiation environment of LIPTHANE, and finally, how shielding might be used and how it would affect the performance of LIPTHANE.

Antiproton Annihilation Gamma Radiation

Independent of a specific engine configuration, certain conclusions can be drawn from the general properties of antiproton annihilation. It is known that approximately 709 MeV of the original 1877 MeV that is involved in an antiproton-proton annihilation (or 37.8%) *will escape in the form of photons (gamma radiation)*. If many annihilations occur at nearly the same position, the radiation may be considered as emanating from a point. A calculation based on the annihilation rate then yields the energy flux at any distance away from the point of annihilation, assuming the photons are traveling in a vacuum. By integrating the resulting equation with respect to time, one arrives at the position dependent fluence. Assuming a constant annihilation rate, equation (2.14) is derived.

Figure 5.1 shows energy flux as a function of distance and annihilation rate. Figure 5.2 shows fluence as a function of time and energy flux. Together these Figures can be used to find the fluence at any distance up to 500 m for reasonable annihilation rates and durations of exposure. Recall that for humans the fluence should not exceed 0.75 Sv ($<10^2$ J/m^2) and for electronics it should not exceed 10^2-10^4 Gy ($<10^4$-$<10^6$ J/m^2). For an annihilation rate of 10^{17} ann./s, humans within 500 m (and farther) will be seriously affected. Electronics within about 30 m will fail in less than 3 hours. This analysis is independent of the LIPTHANE engine and is meant to convey the general radiation properties of antiproton annihilation.

Human Safety and LIPTHANE

With the fluence per annihilation known as a function of position for both the unshielded and shielded version of the LIPTHANE engine, the safety of humans can be evaluated.

Adhering to the U.S. occupational standard of safe rate of radiation absorption, 1.585×10^{-9} Sv/s (or 50 mSv/yr., see equation (2.13)), and considering the rate of annihilation that LIPTHANE was designed to operate at, 2.6×10^{17} annihilations/s in the current configuration, the following analysis applies:

$$\left(\frac{\mathcal{F}}{\text{annihilation}}\right)_{max} = \frac{1.585 \times 10^{-9}\,[\frac{Sv}{s}]}{\left(2.6\times10^{17}\,[\frac{ann.}{s}]\right)\left(0.00867\,[\frac{m^2\,Sv}{J}]\right)} \qquad (5.1)$$

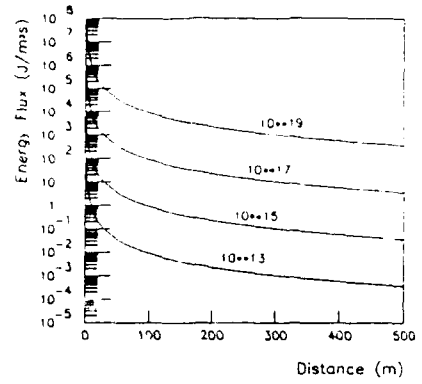

Figure 5.1: Energy Flux vs. Distance from Annihilation Point for Several Annihilation Rates.

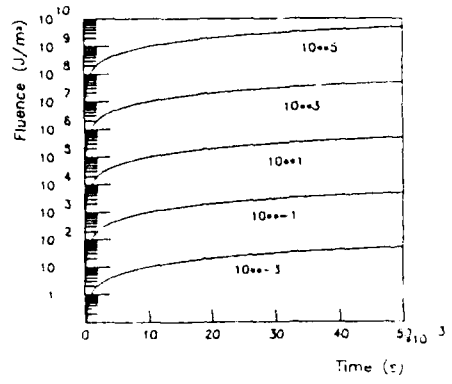

Figure 5.2: Fluence vs. Exposure Time for Several Values of Energy Flux.

$$\left(\frac{\mathcal{F}}{\text{annihilation}}\right)_{max} = 7.052 \times 10^{-25} \left[\frac{J}{m^2\ \text{ann.}}\right] \qquad (5.2)$$

Examination of the fluence per annihilation results presented in Figures 4.4-4.13 shows that both the unshielded and shielded LIPTHANE produce radiation that is well above this standard out past a distance of 10 m from the engine and even out to 100 m in the unshielded case. There is, however, a safe region directly behind the shield which grows from 45.2 cm in diameter (see Figure A.6(b)) to approximately 2 m in diameter 5 meters away (see Figure A.7(b)), and 4 m in diameter 10 meters away (see Figure A.7(d)). As seen in Figure 4.6(b), approximately three square meters of area centered along the longitudinal axis of LIPTHANE are completely protected from all radiation at a distance of 5 m.

The conclusion must be that shielding is necessary for the operation of LIPTHANE and that 20 cm of tungsten-rhenium is adequate for that purpose. In order to completely prevent any radiation from escaping on the vehicle side, all that would be needed would be to either extend the radius of the shield or add a ninth shell of tungsten-rhenium of less than 10 cm thickness.

Optimum thicknesses for the shield and the extra shell, if added, were not exactly determined in this study. Complementary runs of EGS4, however, indicate that approximately 16 or 17 cm of tungsten is sufficient to absorb all of the energy incident upon it (see Figure 3.5).

Electronics Operation and LIPTHANE

The situation regarding electronics is a bit more complicated than for humans since there are no standards dictating a maximum rate of radiation absorption. Instead, only the total amount of radiation absorbed is important and 10^2-10^4 Gy was determined to be the range for the onset of failure in Chapter 2. A maximum time for safe operation will be found, rather than determining whether a rate of exposure standard is violated.

The relation between fluence [J/mm^2] and dose absorbed by the semiconductors [Gy] was derived in Chapter 2:

$$U^{\bullet}\ [Gy] = 1287.6 \left[\frac{mm^2 Gy}{J}\right] \mathcal{F}^{\bullet} \qquad (2.21)$$

Recall that $\mathcal{F}^{\bullet}$ has the units of [J/mm^2] since a cubic millimeter of silicon is considered. The equation for the time and position dependent fluence is based on the fluence per annihilation and the annihilation rate:

$$\mathcal{F}^{\bullet} = \frac{\text{fluence}}{\text{annihilation}} \times \frac{\text{annihilations}}{s} \times \text{time operated} \qquad (5.3)$$

The fluence per annihilation data were presented in the previous chapter and for LIPTHANE the annihilation rate is 2.6×10^{17} annihilations/s. From equation (2.21) it is possible to determine the fluence that corresponds to both 10^2 and 10^4 Gy of absorbed radiation:

$$\mathcal{F}^{*}_{max,\ low} = \frac{10^2\ [Gy]}{1287.6\ [mm^2/kg]} = 7.77\times10^{-2}\ [\frac{J}{mm^2}] \qquad (5.4)$$

$$\mathcal{F}^{*}_{max:\ high} = \frac{10^4\ [Gy]}{1287.6\ [mm^2/kg]} = 7.77\ [\frac{J}{mm^2}] \qquad (5.5)$$

An equation for the safe time of operation is readily available:

$$time\ operated_{max} = \frac{\mathcal{F}^{*}_{max}}{\left(\frac{fluence}{annihilation}\right)\left(2.6\times10^{17}\ [\frac{ann}{s}]\right)} \qquad (5.6)$$

For the unshielded LIPTHANE, values for fluence per annihilation in J/mm^2 are obtained by dividing the results presented in Figures 4.4-4.13 by 10^6. Thus, the fluence per annihilation ranges from 3.0×10^{-18} J/mm^2 at 50 cm from the engine to 1.0×10^{-21} J/mm^2 at 100 m from the engine. The maximum times of safe operation are then calculatec using equation (5.6). Table 5.1 shows the results. For comparison, a mission using 1 mg of antiprotons would last 2.3×10^3 s. Clearly, some shielding is needed to protect the electronics.

Table 5.1: Times of Failure for Electronics of Unshielded LIPTHANE.

	Time Before Failure [s]	
Distance from Engine [m]	$\mathcal{F}^{*}_{max}=7.77\times10^{-2}\ [\frac{J}{mm^2}]$	$\mathcal{F}^{*}_{max}=7.77\ [\frac{J}{mm^2}]$
0.5	0.1	10.0
1.0	0.1	10.0
5.0	1.0	100.0
10.0	3.75	375
100.0	300.0	3.0×10^4

For the shielded LIPTHANE, the case is quite different. Since the 20 cm shield stops all of the radiation incident upon it, there is a cone of volume that is completely safe for electronics. Outside of that cone, the environment is still much improved over the unshielded case. Some 5 m from the engine, 1.0×10^6 s of exposure is acceptable. At 1 m, however, there is still danger (only 10^3 s of operation is safe).

Shielding

LIPTHANE is a high energy density engine. Its annihilation rate of 2.6×10^{17} annihilations/s releases a great number of high energy photons, recalling that on average 3.8 photons carry away a total of 709 MeV (1.1356×10^{-10} J) per annihilation. Over 10^7 J are released per second in the form of gamma radiation in the LIPTHANE engine. Because this energy release is so high, the shielding job is difficult.

The first simulation carried out indicated that an unshielded LIPTHANE would be lethal to humans and destructive to electronics within any reasonable distance and time of operation that would be associated with a spacecraft. The second simulation, with a 20 cm mainly tungsten shield added to the vehicle side of LIPTHANE, showed that the energy can be absorbed by a reasonable amount of material, preventing harm to humans and electronics. Although some areas still remained dangerous, shielding could easily be added to protect any sensitive regions. An additional tungsten-rhenium shell of approximately 7 cm in thickness, along with the 20 cm tungsten-rhenium shield, would make the vehicle side of the engine completely clear of radiation.

An unshielded LIPTHANE is estimated to have a mass of 2000 kg. A cylindrical tungsten-rhenium(5%) shield of 20 cm (17 cm) thickness and 22.6 cm radius would have a mass of 621 kg (528 kg), increasing the mass of LIPTHANE by about 30%

(26%). Its thrust to mass ratio would drop from 5.5 N/kg to 4.2 N/kg (4.35 N/kg). If an additional 7 cm thick shell were added to LIPTHANE, the mass would increase by another 1350 kg and the thrust to mass ratio would fall to 2.8 N/kg.

This shielding analysis and the simulation of LIPTHANE have assumed no intervening material between the vulnerable parts of the vehicle and the engine itself. In reality, of course, this will not be the case. For LIPTHANE it would be likely that a large storage tank of propellant (liquid hydrogen) would be situated directly behind the engine. The walls of the tank and the liquid hydrogen would serve to absorb and scatter some of the radiation and the distance put between the crew or electronics and the engine would help remove them from danger. Additionally, there continue to be advancements in the hardening of semiconductors and careful designs might limit their exposure to the radiation. Therefore it is possible that less shielding would be needed. It is very clear, however, that LIPTHANE cannot be analyzed separately from its radiation issues. Too much energy is produced for them to be ignored. Debate over the usefulness of solid core and other types of antimatter engines should recognize the unique shielding questions that confront their design.

Future Study

If antimatter annihilation propulsion approaches actual utilization, more detailed studies should be conducted on the question of shielding. Minimizing the mass of shielding and determining the best suited and most reliable materials should be the goal of this research. It is likely that neutrons will be created by annihilation with atomic nuclei as well. These neutrons will present an additional and significant shielding challenge and should be studied. Additionally, one can envision using powerful magnetic

and electric fields to control the electrons and positrons so that they are directed away from vulnerable people or spacecraft parts. A series of thin foils to trigger pair production coupled with these fields could possibly reduce the necessary shielding mass and create additional thrust or electricity as a by-product. This idea deserves investigation.

More generally, antiproton annihilation propulsion still has many large obstacles to overcome before it can be realized. Production levels must increase, dense storage and handling techniques must be devised, and the basic physics of antiprotons and annihilation better understood. Research into all of these areas should continue.

Appendix
ADDITIONAL MONTE CARLO RESULTS

Introduction

Raw data not presented in the main body are presented in this appendix. Original energy data are included as are the energy spectra for the photons as they transfer regions inside the engine.

Note:

(1) All of the histograms are based on a sample of 10^5 annihilation photons, the number of photons simulated in both the unshielded and shielded case.

(2) No energy with a radius less than 22.6 cm is transported beyond the shield.

(3) Low energy photons quickly dominate the spectra after the first shell.

(4) Energy distributions show how the energy concentrations gradually diminish as distance from the engine grows and how the radiation spreads from a narrow beam into a more diffuse spray.

(5) The coordinate z refers to the axial coordinate where the center of the engine lies at z=+35 cm and the shield, if used, lies from z=-20 cm to 0 cm. See figure 4.1 and table 4.1 for more details.

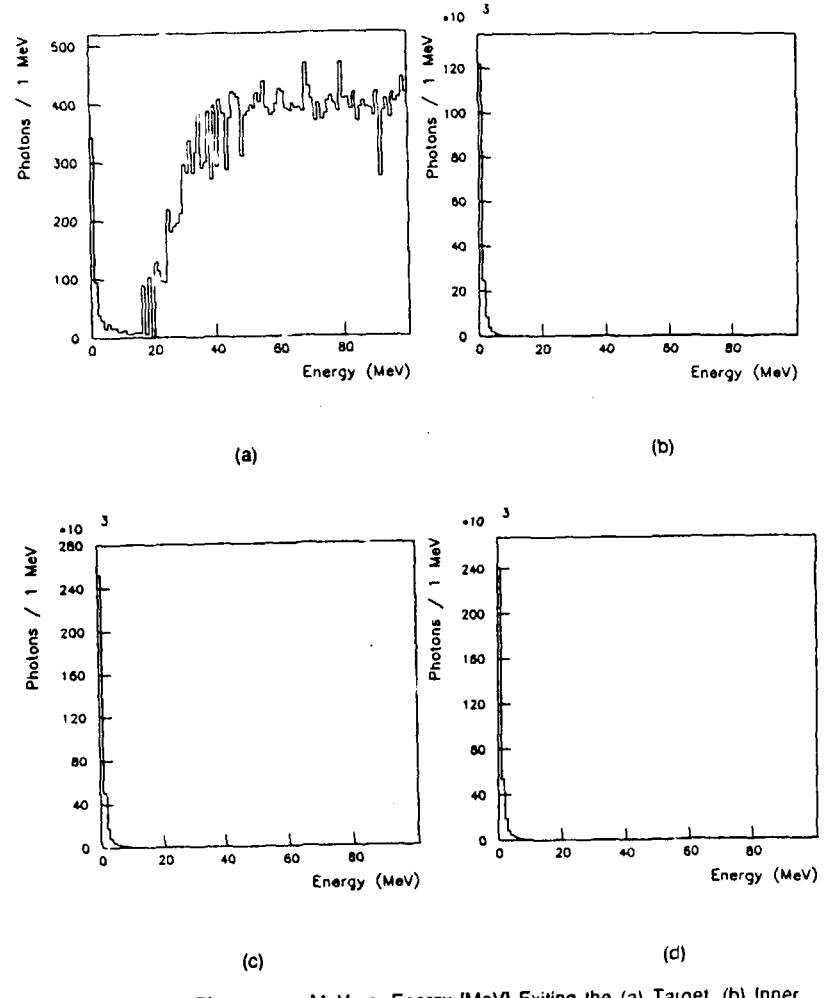

Figure A.1: Photons per MeV vs. Energy [MeV] Exiting the (a) Target, (b) Inner Cooling Region, (c) First Shell, and (d) the First Propellant Duct, from a Total of 100,000 Annihilation Photons.

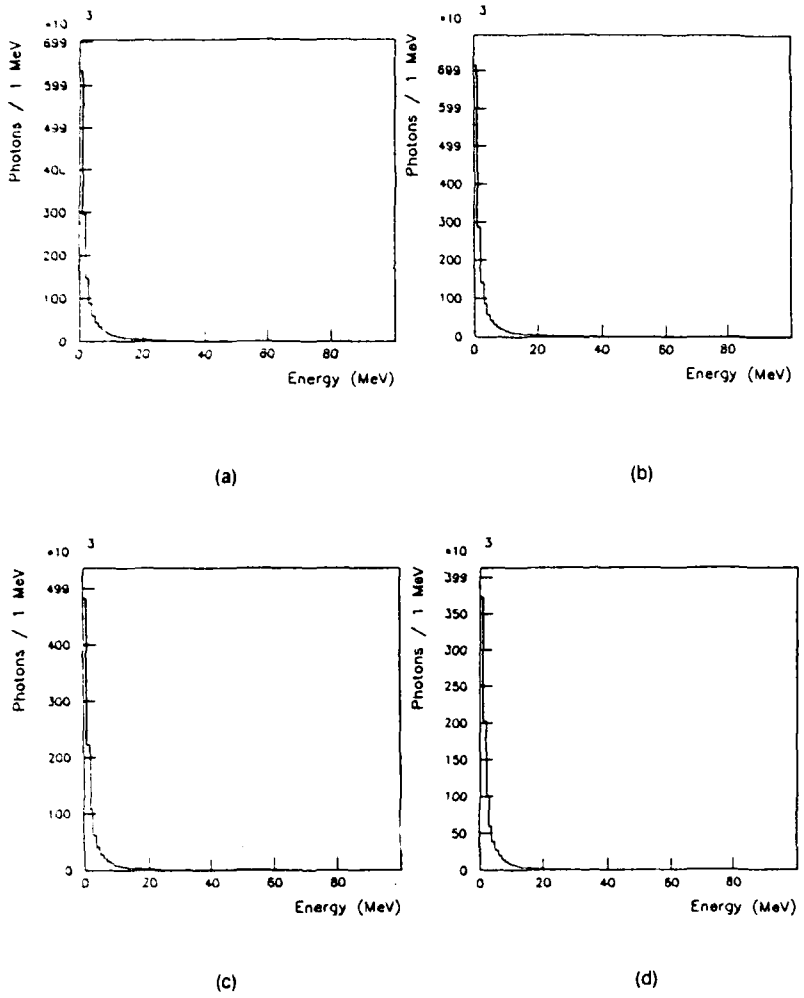

Figure A.2: Photons per MeV vs. Energy [MeV] Exiting the (a) Shell #2, (b) Second Propellant Duct, (c) Shell #3, and (d) the Third Propellant Duct, from a Total of 100,000 Annihilation Photons.

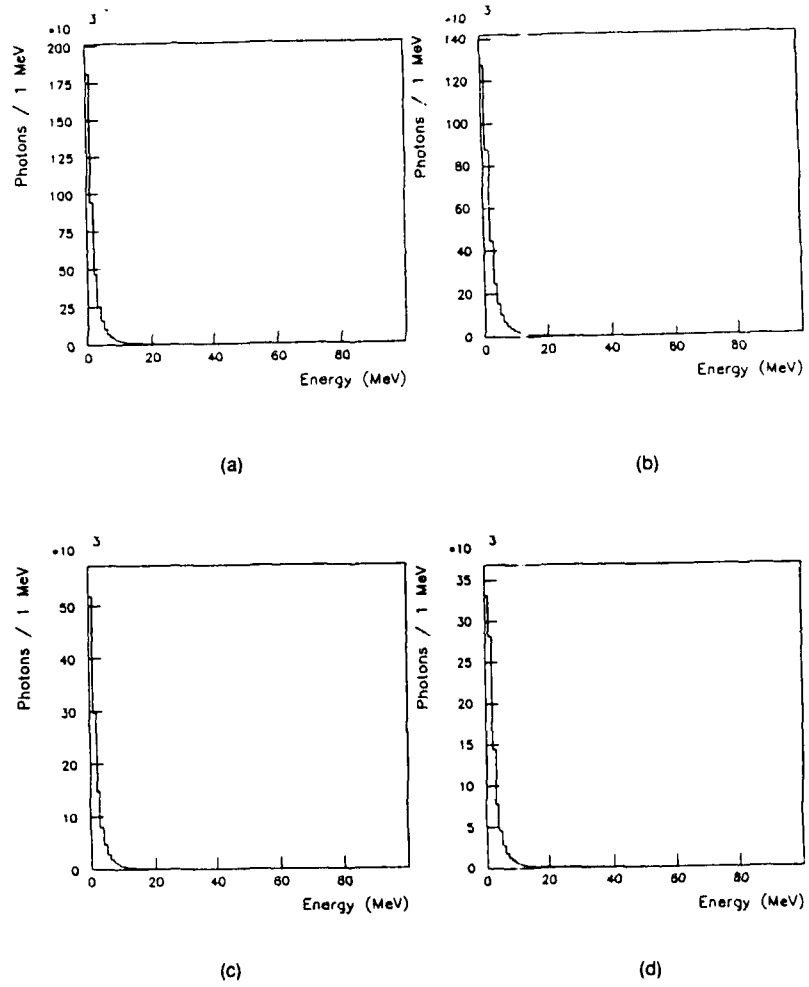

Figure A.3: Photons per MeV vs. Energy [MeV] Exiting the (a) Shell #4, (b) Fourth Propellant Duct, (c) Shell #5, and (d) the Fifth Propellant Duct, from a Total of 100,000 Annihilation Photons.

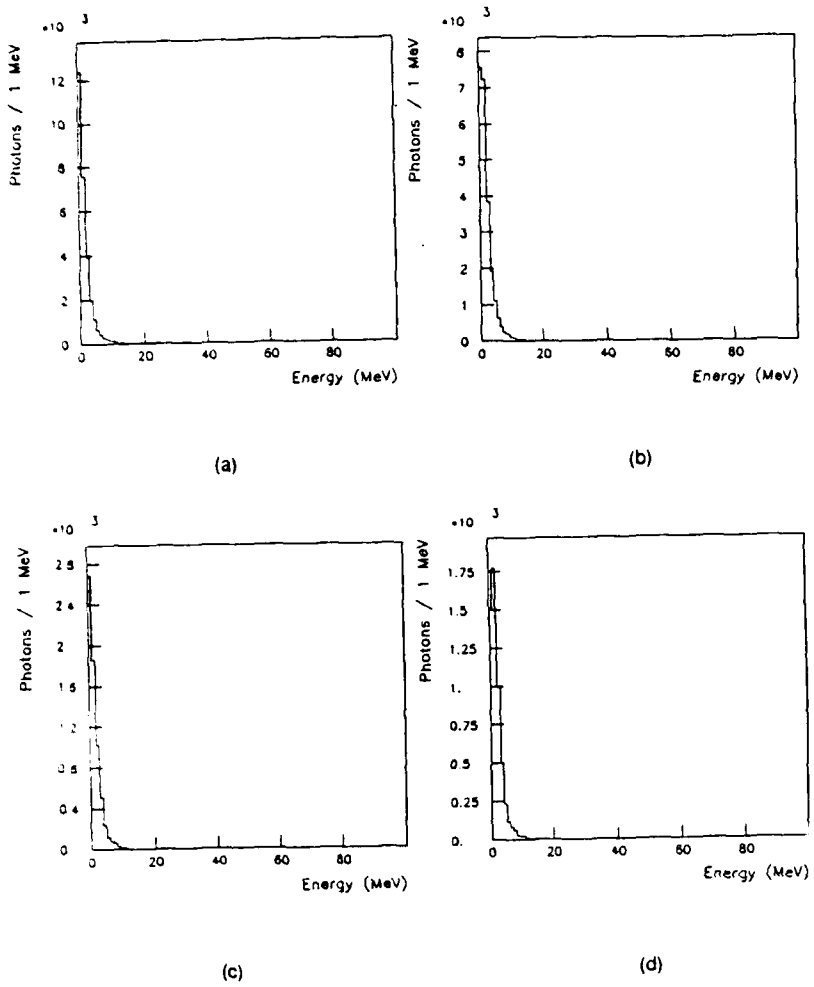

Figure A.4: Photons per MeV vs. Energy [MeV] Exiting the (a) Shell #6, (b) Sixth Propellant Duct, (c) Shell #7, and (d) the Seventh Propellant Duct, from a Total of 100,000 Annihilation Photons.

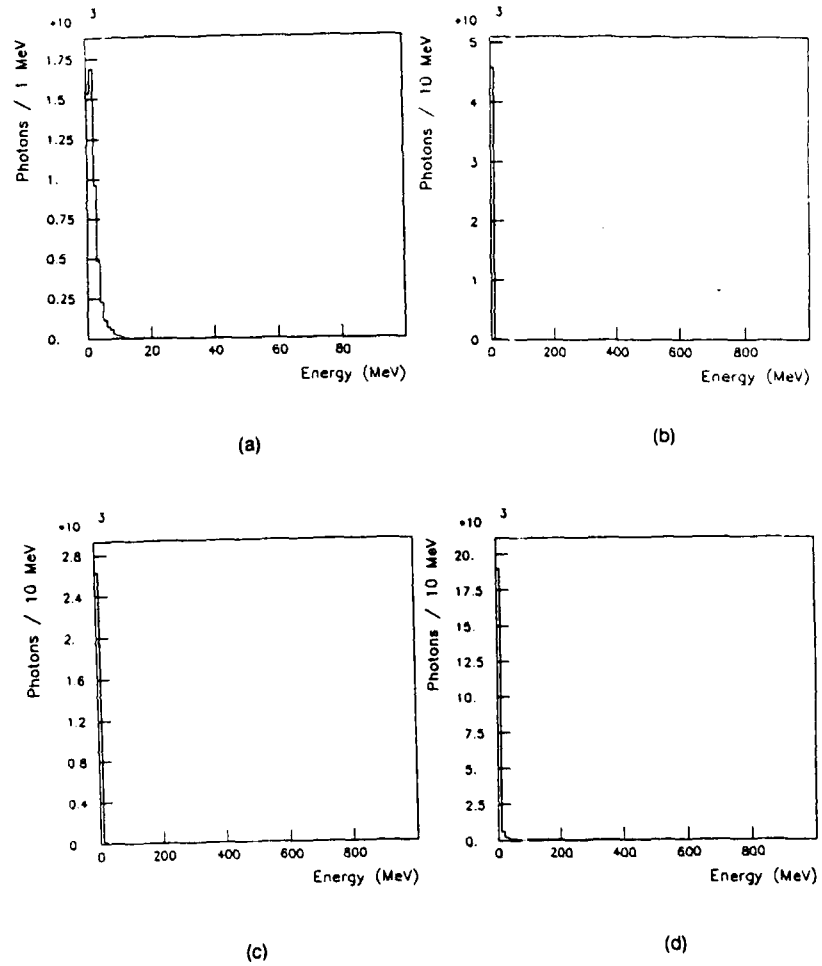

Figure A.5: Photons per MeV vs. Energy [MeV] Exiting the (a) Shell #8, (b) Shield, (c) Plane at z=+120 cm, and (d) the Plane at z=-50 cm, from a Total of 100,000 Annihilation Photons.

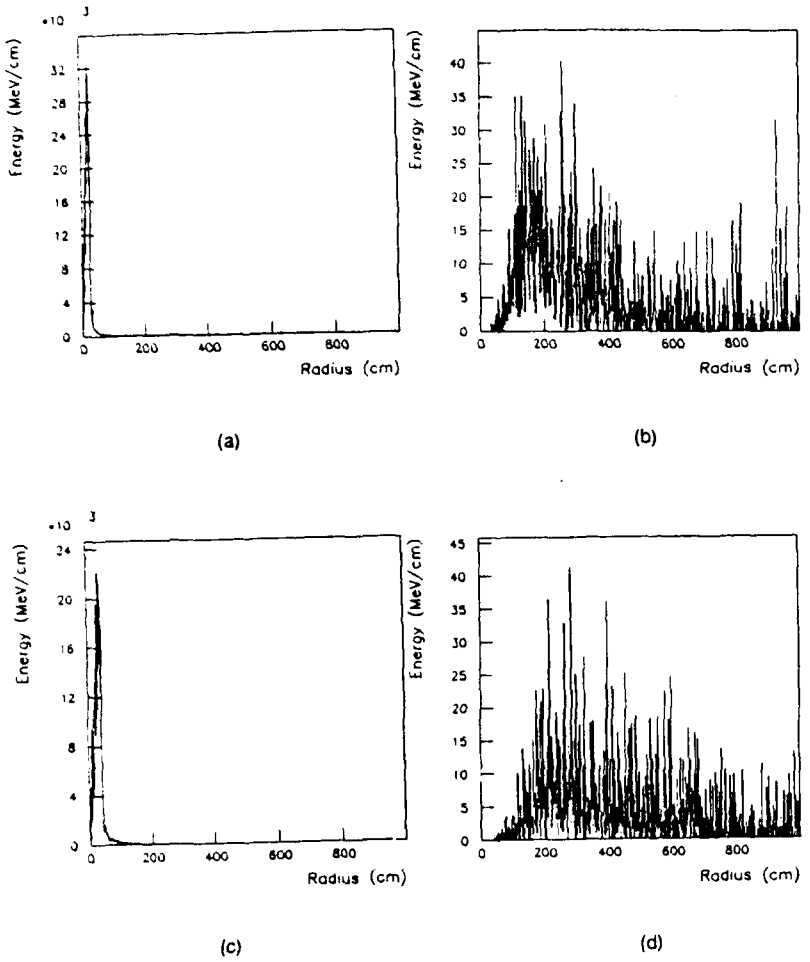

Figure A.6: Energy [MeV/cm] vs. Radius [cm] for (a) z=-50 cm, No Shield, (b) z=-50, Shield, (c) z=-100 cm, No Shield, (d) z=-100 cm, Shield for 100,000 Total Annihilation Photons.

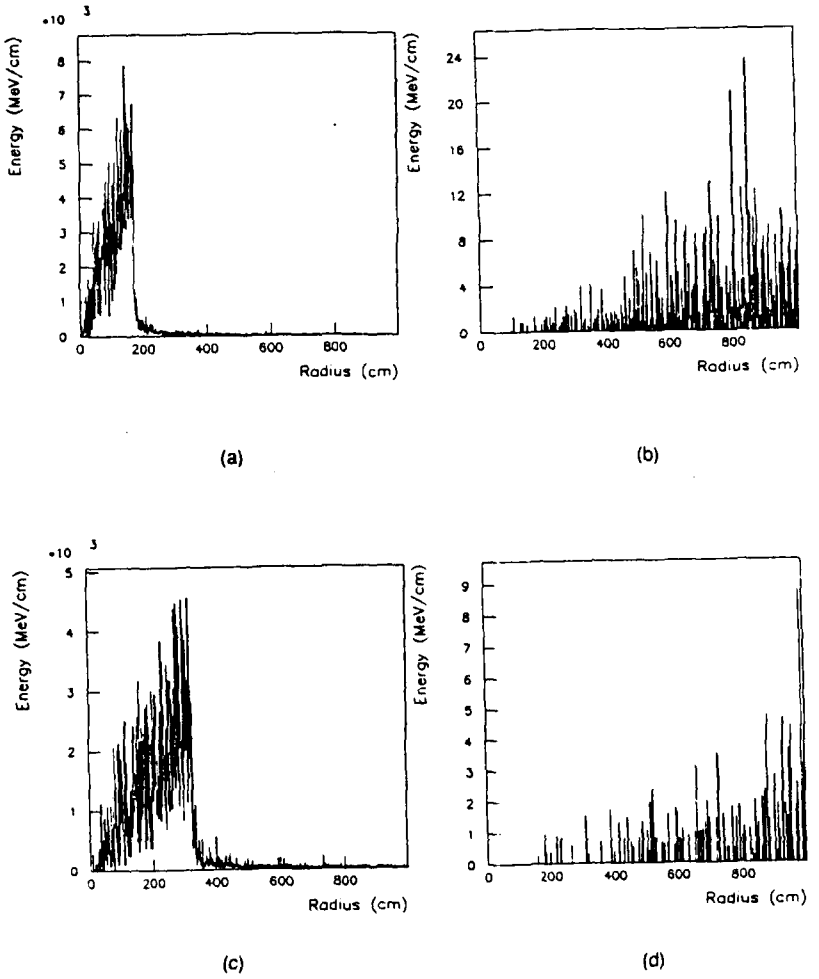

Figure A.7: Energy [MeV/cm] vs. Radius [cm] for (a) z=-500 cm, No Shield, (b) z=-500, Shield, (c) z=-1000 cm, No Shield, (d) z=-1000 cm, Shield for 100,000 Total Annihilation Photons.

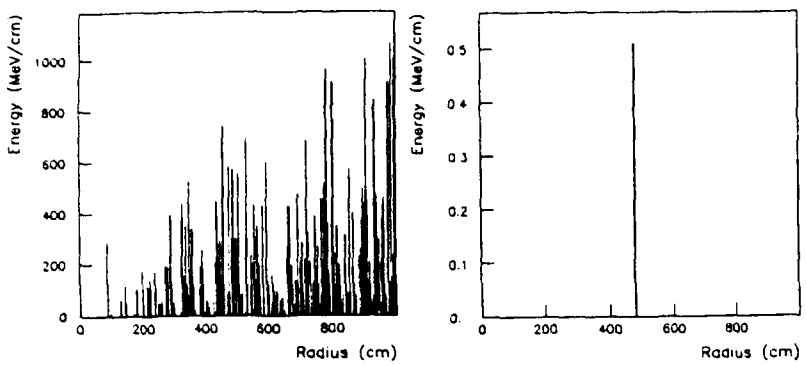

(a)

(b)

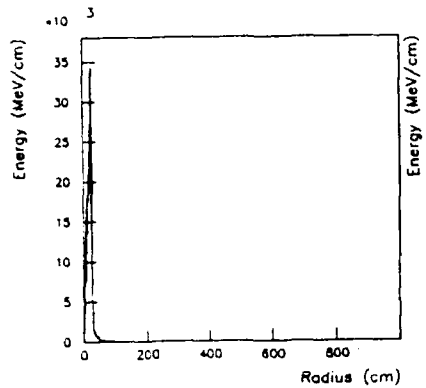

(c)

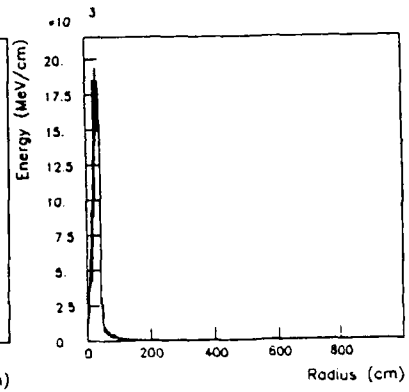

(d)

Figure A.8: Energy [MeV/cm] vs. Radius [cm] for (a) z=-10,000 cm, No Shield, (b) z=-10,000, Shield, (c) z=+120 cm, and (d) z=+170 cm, for 100,000 Total Annihilation Photons.

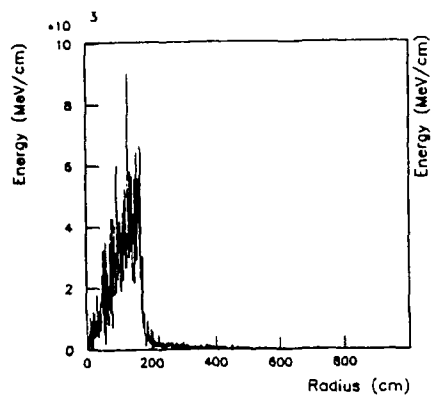

(a)

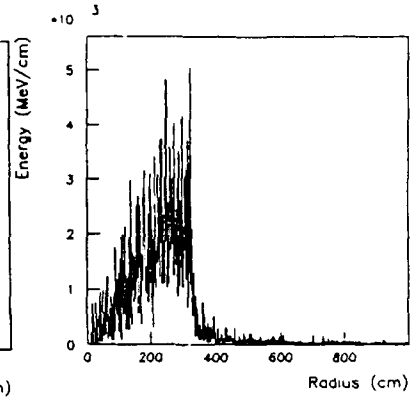

(b)

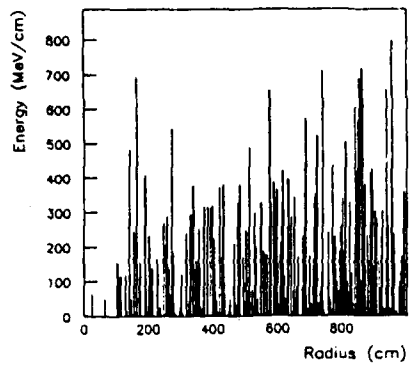

(c)

Figure A.9: Energy [MeV/cm] vs. Radius [cm] for (a) z=+570 cm, (b) z=+1070 cm, and (c) z=+10,070 cm, for 100,000 Total Annihilation Photons.

REFERENCES

[1] Dirac, P.A.M. 1928. Proc. Roy. Soc. London Series A 117: 610.

[2] Anderson, Carl D. 1933. The positive electron. Physical Review 43 (March).

[3] Chamberlain, Owen et al. 1955. Observation of antiprotons. The Physical Review 100 #1 (October).

[4] Forward, R.L. 1982. Antimatter Propulsion. JBIS 35: 391-395.

[5] Massier, Paul, F. 1982. The need for expanded exploration of matter-antimatter annihilation for propulsion application. JBIS 35: 387-390.

[6] Shepherd, L.R. 1952. Interstellar Flight. JBIS 11: 149-167.

[7] Sutton, George P. and Donald M Ross. 1976. Rocket Propulsion Elements: An Introduction to the Engineering of Rockets. 4th ed. New York: John Wiley & Sons.

[8] Augenstein, B. W. 1989. 1987 RAND workshops on antiproton science and technology - implications for antimatter propulsion RDT&E. AIAA Presentation (14 February): 1-16.

[9] Morgan, David L. 1982. Concepts for the design of an antimatter annihilation rocket. JBIS 35: 405-412.

[10] Vulpetti, Giovanni. 1984. A propulsion-oriented synthesis of the antiproton-nucleon annihilation experimental results. JBIS 37: 124-134.

[11] Adiels, L. et al. 1986. Search for narrow signals in the g-spectrum from $p\bar{p}$ annihilations at rest. Physics Letters B 182 #3,4 (25 December): 405-408.

[12] Armstrong, T.A. et al. 1988. Nuclear gamma-ray emission from antiproton annihilation at rest in uranium. Z. Phys. A. - Atomic Nuclei 331: 519-520.

[13] *Armstrong, T.A. et al. 1989. Energy transfer by intranuclear cascade of* pi-zeros produced in antiproton annihilation at rest in nuclear targets. Z. Phys. A. - Atomic Nuclei 332: 467-472.

[14] Angelopoulos, A. et al. 1988. Neutron emission from antiproton annihilation at rest. Physical Letters B 205 #4 (5 May): 590-594.

[15] Messel. H. and D.F. Crawford. 1970. Electron-Photon Shower Distribution Function: Tables for Lead, Copper and Air Absorbers. Oxford: Pergamon Press, Ltd.

[16] Storm, E. and H.I. Israel. 1970. Photon cross sections from 1 keV to 100 MeV for elements z=1 to z=100. Atomic Data and Nucl. Data Tables 7: 566-638.

[17] Anno, J. N. 1984. Notes on Radiation Effects on Materials. Washington: Hemisphere Publishing Corporation.

[18] Messenger, George C. and Milton S. Ash. 1986. The Effects of Radiation on Electronic Systems. New York: Van Nostrand Reinhold Company Inc.

[19] Nelson, Walter R., Hideo Hirayama, and David W.O. Rogers. 1985. The EGS4 Code System. SLAC-265: Stanford Linear Accelerator Center.

[20] Cassenti, Brice N. 1987. Radiation shield analyses for antimatter rockets. AIAA-87-1813: AIAA/SAE/ASME/ASEE 23rd Joint Propulsion Conference (29 June-2 July).

[21] Taylor, Theodore, B. 1987. Third-Generation Nuclear Weapons. Scientific American *256 #4 (April 1987)*: 30-39.

[22] Vulpetti, Giovanni and Enrico Pieragostini. 1986. Matter-antimatter annihilation engine design concept for earth-space missions. IAF-86-178: 37th Congress of the International Astronautical Federation (4-11 October).

[23] *Pecchioli, Mauro and Giovanni Vulpetti. 1988. A multi-megawatt antimatter* engine design concept for earth-space and interplanetary unmanned flights. IAF-88-264: 39th Congress of the International Astronautical Federation (8-15 October).

APPENDIX VIII

WHITE PAPER

**ANTIPROTON RESEARCH
SCIENCE, AND TECHNOLOGY APPLICATIONS:
RELEVANCE TO DOD**

Bruno W. Augenstein,[1] Johndale C. Solem,[2]
Gerald A. Smith,[3] Stephen J. Lukasik[4]

Antiprotons can have many near term applications to validated DoD requirements. A new look suggests that use of antiprotons can provide leapfrogging approaches to DoD problems, going far beyond evolutionary developments using current DoD tools. Antiproton-initiated fusion, giving unique access to a number of energy and power needs and effects simulations, is one possibility. For serious antiproton work in the United States, a new U.S. facility is needed. Such a facility is being proposed to Fermilab by a large scientific collaboration. The DoD could initiate concerted antiproton RDT&E when the new Fermilab facility comes on line. Basic Fermilab facility costs are in the $10-20 million range, with availability in about three years. DoD should support the facility proposed by the *scientific collaboration* and assume a partial share of the costs, to ensure availability of some fraction of the facility's antiproton output for DoD experimental needs. This draft paper should interest audiences planning DoD science and technology programs leading to very significant near term contributions in DoD mission-relevant research.

[1]Senior Scientist, RAND Corporation.
[2]Staff Member/former Associate Division Leader, T-Division, Los Alamos National Laboratory.
[3]Professor, Laboratory for Elementary Particle Science, Department of Physics, Pennsylvania State University.
[4]Vice President - Technology, Northrop Corporation.

WHITE PAPF. - ANTIPROTON RESEARCH - SUMMARY

1. An extensive scientific collaboration - universities, national laboratories, industry - is proposing to Fermilab (FNAL), via a Letter-of-Intent, to conduct three major classes of compelling low-energy antiproton basic research experiments.
2. Required for this research is a new, small dedicated decelerator ring at FNAL, and associated tools for that ring, to permit antiproton research at energies below 400 MeV, down to the KeV range.
3. Capital costs for these new FNAL facilities appear to be about $10-20 million for the ring, plus about $5 million for the three collaboration experiments, to achieve operation in about three years. This cost and schedule are roughly commensurate with average parameters of FNAL fixed-target experiments. Operating costs are also to be considered for experiments.
4. Acceptance by FNAL of this proposal for compelling antiproton experiments is not assured. Cost and the intersection with FNAL missions and priorities are likely to be relevant factors.
5. If these new FNAL facilities are brought on-line, many opportunities for near-term antiproton applications research relevant to DoD will be available.
6. Several contentions re DoD are discussed in this White Paper:
   - Support for the collaboration proposal by DoD is likely to be helpful for acceptance of the collaboration proposal, and as a means for reducing FNAL fiscal loads.
   - There are important classes of applications experiments of interest to DoD, and *within or directly associated with* DoD missions (generally, DoD already has analogous efforts underway, using other means), which the FNAL facility would enable.

- The experiments are *doable in the near term* - that is, when the tools of 3. are on line - and promise uniquely powerful results and techniques.
- The experimental paths include:
  - A table-top tool testing extreme states of matter
  - Antiproton-initiated fusion and applications
  - Imaging (for NDE, medical purposes), and therapy
  - A Laboratory Micro-Fusion Facility for DoD/DOE missions
  - Special missions
  - Small laboratories for hands-on antiproton experimentation

The White Paper proposes that the identifiable relevance to DoD of various experiments warrants DoD cooperation with the collaboration program defined in the text.

7. A few of the ultimate *operational applications implementations* of DoD relevance using antiprotons would require scaleup of the current FNAL capability to produce and accumulate antiprotons. In every case, however, *definitive evaluation* of the opportunities and promise of such DoD-relevant antiproton applications can be done *within the constraints* of the initial FNAL antiproton source. Decisions on scaling up current FNAL capabilities to produce and accumulate antiprotons can then be based on firm knowledge.
8. Acceptance by the appropriate community of the collaboration proposal must rest primarily on the compelling scientific merit of the experiments proposed. However, DoD support would help assuage *pragmatic funding concerns*, and would, under mutually acceptable guidelines, put the DoD in the *least costly position* of having available some share of the FNAL antiproton output dedicatable for DoD use.
9. The DoD is therefore urged to *support the collaboration proposal*, and concurrently to *set up mechanisms* for conduct of antiproton applications RDT&E trials relevant for DoD missions and functions.

CONTENTS

WHITE PAPER - ANTIPROTON RESEARCH - SUMMARY iii

FIGURES vii

Section

WHITE PAPER - FEBRUARY, 1990 ANTIPROTON RESEARCH - CONFLUENCE OF SCIENCE AND TECHNOLOGY APPLICATIONS AND RELEVANCE TO

A. Introduction 1
B. A Recent Proposal 4
C. The Breckenridge Scientific Collaboration Proposed Experiments 5
D. What is needed at FNAL to conduct the Section C experiments? 8
E. If we had these tools (Section D), what are implications for applications-related antiproton work for DoD (and DOE)? 11
F. Two major U.S.-participant experiments at CERN 13
G. Brief discussion of DoD-relevant Near-Term antiproton RDT&E 15
H. DoD Funding Implications 26
I. What should DoD do? 28

FIGURES

1. Small ring, using present FNAL facilities. 10

WHITE PAPER - FEBRUARY, 1990

ANTIPROTON RESEARCH - CONFLUENCE OF SCIENCE AND TECHNOLOGY APPLICATIONS AND RELEVANCE TO DOD

A. INTRODUCTION

In 1987, RAND conducted two large-scale internationally attended conferences on antiproton science and technology, under sponsorship by USAF. The conferences were held to explore in detail three main aspects of antiproton science and technology, with these explorations conducted by three groups, I, II, and III.

Group I was to consider fundamental issues of production and collection of antiprotons. Consideration was first to be given to options, characteristics, and schedules for a near-term North American low-energy antiproton source, to be based in U.S. sites at Brookhaven National Laboratory or Fermi National Accelerator Laboratory, and *capable of delivering of the order of* 10^{14} *low-energy antiprotons per* year, or more, at energies suitable for both fundamental physics and applications experiments. It was recognized that special earlier capabilities might be considered, giving us fewer low-energy antiprotons, but the level noted remains as the important goal. Next, consideration was to be given to the feasibility of small transportable antiproton storage rings, storing antiprotons at typical energies of tens of MeV, for antiproton delivery at any suitable laboratory site. Such rings were to be filled with antiprotons at the low-energy antiproton source.

Finally, issues of scaleup were to be addressed, in two stages: first, the level of scaleup potentially available if one utilizes the advanced hadron/kaon facilities now being proposed, and second, the additional scaleup potentially available by fundamental machine considerations of production, collection, and cooling (in effectively real time). We know that considerable RDT&E is vital to achieve the latter level of scaleup (with which we would achieve the milligrams per year lev speculations on means to achieve ~gram/yr production we.e

also voiced. A first cut at these RDT&E issues was a goal for Group I activities.

Group II was to consider the basic physics programs accessible with the delivery of a near-term North American low-energy antiproton source (i.e., of the order of 10^{14} antiprotons per year).

The science case for a U.S. (North American) low-energy antiproton source is critical for adequate development. We believe that a remarkably broad science program was discussed at the Workshop. Antiproton science and the science experiments will provide major incentives for a U.S. antiproton source, as well as an essential technical infrastructure for rapid closing of information gaps now inhibiting confident assessment of the possibilities and merits of many applications. The science base should be a strong attractor for interesting the scientific community in antiproton research.

The array of experiments feasible with the low-energy antiproton source is impressively large. Group II was accordingly to consider a diverse and multi-disciplinary set of programs, including classes of experiments relevant to:

- Tests of invariance principles
- Antiproton annihilation in nuclei
- Gravity and antiprotons
- Antihydrogen and basic physics tests
- Antimatter cluster ions, and other atomic/molecular issues
- Meson spectroscopy
- Antiprotons and condensed matter (storage in normal matter, etc.)
- Antiproton studies at momenta up to several GeV/c

Group III was to consider a range of applications-related issues for which experiments could be carried out using the number of antiprotons deliverable from an initial North American antiproton source (i.e., again of the order of 10^{14} antiprotons/year).

Accordingly, the topics to be addressed included:

- Design of portable ion traps capable of accepting antiprotons at about 50 KeV. The quantity of antiprotons storable would be scalable to about 10^{13}, commensurate with intended experiment/applications purposes.
- A "table-top" high pressure/high temperature/high particle flux testing tool, using as a source antiprotons stored in small rings or traps.
- A prototype tool for exploration, testing, and development of a new and revolutionary class of medical imaging and therapy procedures.
- A facility for initial testing and screening of a range of interesting design concepts for antiproton propulsion and energy storage, providing for "hands-on" testing of ideas in this area.
- Exploration and development prospects, where useful, of classes of scientific and commercial diagnostic probes, tools, and special techniques, vitally useful for applications such as Non-Destructive Evaluation (NDE).

These considerations for all three groups are discussed in full detail in two publications:

a. "Proceedings of the RAND Workshop on Antiproton Science and Technology" (*World Scientific*, Singapore, New Jersey, and Hong Kong, June 1988; 759 pages).

b. N-2763-AF (October 1988). *RAND Workshop on Antiproton Science and Technology, October 6-7, 1987 - Annotated Executive Summary.*

The purpose of this White Paper is to bring readers up to date on current happenings in this field, as of early 1990.

B. A RECENT PROPOSAL

One ongoing event is the formation of a large scientific collaboration (collaboration correspondent - G. A. Smith), present firm composition as shown, proposing to run a group of major basic physics experiments at the Fermi National Accelerator Laboratory (FNAL), with a Letter-of-Intent submitted to FNAL on February 19, 1990.

LETTER-OF-INTENT

Precision Tests of CPT and Gravity
Using Low Energy Antiprotons at Fermilab

GSI Darmstadt
Manne Siegbahn Institute - Stockholm
Fermilab
University of Iowa
University of California - Irvine
University of Trieste
Integrated Accelerator Technologies
Max Planck Institute for Quantum Optics - Munich
Los Alamos National Laboratory
University of Michigan
University of New Mexico
Penn State University
Rutgers University

The specific experiments to be run were discussed at a Workshop in Breckenridge, Colorado, in August 1989, on "Physics at Fermilab in the 1990's." Several interesting topics emerged. Prominent among these were tests of invariance principles inherent in the theories of gravity and electro-magnetism, specifically the weak equivalence principle and CPT.

Although LEAR at CERN [illegible] principle of achieving significant tests in these areas, it was felt that, considering the extreme degree of difficulty and considerable time required to perfect these experiments, and current decisions bringing uncertainty to the future of LEAR, plans should be made to establish a capability at Fermilab to carry out this work to its deserving conclusion. Furthermore, there is substantial intrinsic merit in having available a U.S. facility.

The planned experiments are discussed more fully in Section C. Note that the facilities at Brookhaven National Laboratory (BNL) could also be proposed as the site for basic physics experiments such as are proposed in Group II in Section A.

C. THE BRECKENRIDGE SCIENTIFIC COLLABORATION PROPOSED EXPERIMENTS

Physics Objectives and Methods

The proposed experiments aim at three principal goals:

1) Test of the CPT theorem with very high precision by comparing the mass and the magnetic moment of the antiproton with that of the proton (CPT test in an elementary system).

The techniques used to measure the mass of trapped ions are highly developed and allow us to apply them to the hadronic constituent of atomic antimatter. They provide the most sensitive test of CPT in the baryon domain. Since there exists no general theory from which a confirmation of the validity of the CPT theorem in one sector can impose bounds on other sectors, we must test the fundamental symmetry with ultimate precision wherever we can obtain ultrahigh sensitivity, in order to detect a possible violation.

The difference of the magnetic moment of the antiproton compared to that of the proton is determined only to two parts in 10^3, this precision should imminently be improved. Similarly, the proton-antiproton mass difference is known to one part in 10^8, whereas the electron-positron mass difference is known to one part in 10^9. We can

show that limits on both the magnetic moment and mass differences can be reduced by many orders of magnitude in the proposed experiments.

2) Comparison of the gravitational interaction between particles and between particles and antiparticles (weak equivalence principle).

Clearly the question of whether antimatter is in compliance with weak equivalence is a fundamental experimental issue, which can best be addressed with low-energy antiprotons. Some thirty years ago, the notion of "antigravity," according to which antimatter would fall up, enjoyed a brief popularity. However, theoretical arguments were raised against this idea, and it was not until the development of supergravity theories that weak equivalence for antimatter was again questioned.

In 1979, Joel Scherk pointed out that certain supergravity theories could allow the antiproton to fall down faster than ordinary matter. This idea, which is in a sense the exact opposite of "antigravity," avoids the old objections, and connects the anomalous gravity for antimatter with both some "fifth-force" concepts and with gravitational redshift experiments. In Scherk's model, the graviton, which provided the conventional infinite range attractive force, has two partners, known as the "graviphoton" and "graviscalar," which are capable of providing additional gravitational strength forces of macroscopic range. The graviphoton is a vector field and so must be coupled to some conserved charge, which could be taken phenomenologically to be a baryon number. This field would then give a repulsive force between "like" charges, so that it would tend to repel normal matter from the Earth. However, the graviscalar, which is a spin zero field, would always be attractive, and would therefore tend to mask the effects of the graviphoton on normal matter.

For antiprotons, on the other hand, both the graviphoton and graviscalar would give attraction in the Earth's field, and so the antiproton would experience a larger gravitational acceleration than normal matter. The strongest constraints on Scherk's model come from gravitational redshift experiments. These currently allow a few percent

larger gravitational acceleration for antiprotons and for antihydrogen than for normal matter.

3) First synthesis of atomic antimatter, study of its confinement, high resolution spectroscopy of antihydrogen and investigation of its gravitational interaction.

This fundamental system has neither been detected in nature nor produced in the laboratory. Its synthesis is of great interest for studying matter-antimatter symmetries and interactions. Its electric neutrality imposes, on one hand, the problem of its storage (methods are known to store such neutrals without wall contact), but on the other hand offers the possibility of accumulating large amounts due to the absence of space-charge effects. In turn, large amounts of antihydrogen increase the sensitivity for detecting specific effects of great physics interest (via improved statistics).

The fact that a lepton is attached to the antiproton permits atomic spectroscopy (in particular, laser and microwave spectroscopy) to be performed, and thus extend the precision of our knowledge of fundamental properties and symmetries. For example, a measurement of the hyperfine splitting in the ground state of antihydrogen, and other QED-related tests, allows, in principle, a test of CPT many orders of magnitude better than the antiproton mass measurement. This is based on the fact that the same measurement in hydrogen has been made with a maser to a precision of one part in 10^{13}. It also follows that this measurement immediately results in a more accurate value of the antiproton magnetic moment.

The neutral antihydrogen atom is not affected by electric fields, and much less than the antiproton by magnetic fields. Therefore, the gravitational interaction can eventually be studied with much greater precision. The possibility of manipulating antihydrogen with laser light and selecting hyperfine states provides a way to polarize antiprotons. Such a source of polarized antiprotons would be of great interest for both low and high energy antiproton-proton strong interaction physics.

To date, three methods for the production of antihydrogen have been proposed: (1) spontaneous or induced radiative capture of a positron by an antiproton in a merged beam arrangement; (2) a three-body reaction using positronium atoms and antiprotons; and (3) a three-body reaction using a dense positron plasma and antiprotons at very low temperature. Processes (2) and (3) exhibit a much larger cross section than the spontaneous radiative capture process (1). The dense positron plasma approach makes it necessary to cool the antiprotons and positrons to temperatures of ~ 1 K or below, but in turn offers the advantage of producing ultra-cooled antihydrogen atoms which subsequently could be trapped in a magnetic bottle, thus permitting further investigations. Also, the induced radiative capture process (1) could be applied to trapped antiprotons and positrons, thereby helping to reduce the need for a dense electron gas. High precision measurements of the mass, magnetic moment, and gravitational interaction of the antiproton require very slow particles. The initial synthesis of antihydrogen can be achieved with weakly relativistic energies with a subsequent in-flight study of its spectroscopy to fair precision. For the ultimate spectroscopy, trapped and very cold particles are required. It is therefore necessary to reduce the kinetic energy of the antiprotons from the FNAL accumulation energy of 8 GeV to energies comparable to room temperature or below.

D. WHAT IS NEEDED AT FNAL TO CONDUCT THE SECTION C EXPERIMENTS?

Certain new tools will be needed at FNAL to conduct these experiments (these tools are also discussed in great detail in the 1987 RAND Conference documentation noted in Section A). These tools are:

a. A method for decelerating the antiprotons generated by the FNAL antiproton target system from their accumulation (storage ring) energy of 8 GeV to the few MeV level.

b. A further deceleration to the tens of KeV level, to allow capture and storage of antiprotons in ion traps (i.e., Penning traps).

Discussion of these tools follows:

a. Dedicated Decelerator Ring (DR)

It is desirable to have antiprotons decelerated to ~ 2 MeV energy with emittances appropriate for injection into a RFQ. As pointed out by Mills, Mohl, MacLachlan, and Marriner at Breckenridge, the DR could be provided antiprotons by extracting in the standard way (11, 52.8 MHz bunches) from the Accumulator, sending the 8 GeV beam backward through the Main Ring (or Main Injector) into the Booster, decelerating to 400 MeV, extracting the bunches at the bottom of the magnetic field cycle, and transporting them to the DR. Here they must be cooled and decelerated to 2 MeV. The lattice design can be patterned after several previous studies at CERN. The ring would have four bands, 16 quads, and four long straight section. A sketch of the ring location is shown in Fig. 1. Injection could be in a single turn via magnetic septum in a medium straight section and a fast kicker in a long straight section. Ejection can be done either in a single turn or slow mode.

Cooling is needed (to compact phase space volume) at several stages: after injection, during deceleration, and at 2 MeV. At injection, stochastic cooling of 1-2 GHz band width will provide a cooling time of 1-2 minutes. Electron cooling would be faster, but also bulkier, at this energy. Space charge effects and instabilities limit the number of stored particles at 2 MeV. A good phase space density is, however, needed for efficient deceleration and trapping. Hence, one needs a good repetition rate with reliable beam intensity when filling the trap. This requires the fast cooling times provided by electron cooling. The DR can be operated as a normal synchrotron and thus need not have the sophistication of a stretcher ring such as LEAR (ultrahigh vacuum, ultraslow extraction, instabilities, ripples, etc.).

The sketch provided in Fig. 1 of the location of the DR, and further details of the ring parameters and design, will naturally need to be refined at the proposal stage. Very preliminary estimates place the capital cost in the $10-20M range, comparable to a major fixed target experiment at Fermilab. Additional tools and experiment-unique

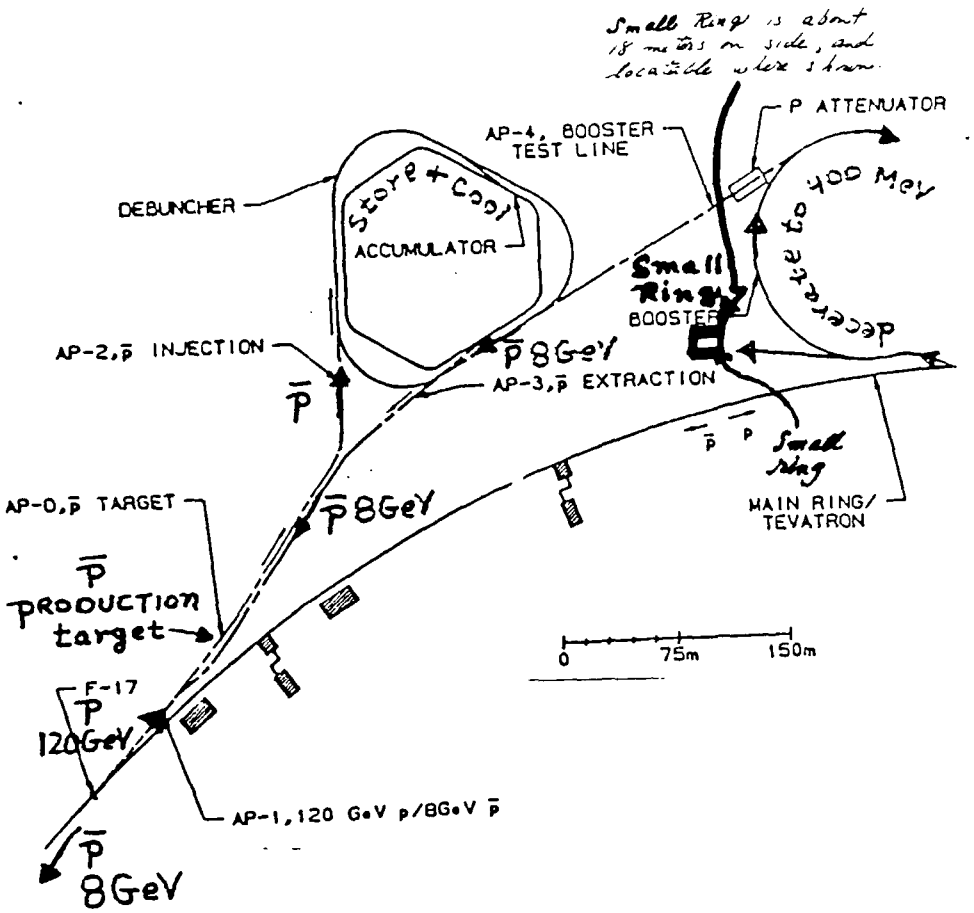

Fig. 1--Small ring, using present FNAL facilities.

facilities for several experiments might increase this cost by up to $5M.

Operating costs are not precisely fixable now. Operation of the DR and specialized experimental tools, and operation of the Tevatron (necessary to produce and collect the antiprotons) will be the main operating cost items, including power costs. Costs will reflect dedicated runs and runs which might share operations. Such costs might run, as a very preliminary estimate, in the range of ~ $100K-250K per week. Total annual operating costs would also depend on the numbers of antiprotons needed, additional to those for the basic FNAL antiproton-proton collider operation. Several FNAL scenarios need review.

Post Deceleration

There are several methods to decelerate antiprotons from MeV energies to energies appropriate for trapping experiments. These include a radio frequency quadrupole (RFQ) decelerator, which is potentially the most efficient and is our preferred option. With proper phase space matching from 2 MeV kinetic energy, one can decelerate 40-50% of the incident particles to about 20 KeV for capture in a Penning trap. A design study for these specific requirements was presented by P. Zhou and Fred Mills of Fermilab at Breckenridge.

E. IF WE HAD THESE TOOLS (SECTION D), WHAT ARE IMPLICATIONS FOR APPLICATIONS-RELATED ANTIPROTON WORK FOR DOD (AND DOE)?

The Breckenridge collaboration is premised on the very exciting science programs (in the three major areas described) *motivating* FNAL construction and operation of the necessary tools (Section D). This outcome is not wholly assured, however. Clearly, money is tight, and the kinds of experiments proposed are not automatically deemed to be in the charter of a high-energy physics laboratory like FNAL (and their priority position has uncertainties).

It is proper that the basic scientific promise of the three major experiments described be the major desideratum for FNAL deciding that the experiments have merit and are worth supporting - within the

abilities of FNAL to accommodate funding (and space allocation). Clearly, however, it might be very helpful if FNAL received funding support for this effort which reduced demands on FNAL laboratory funds per se.

It is the contention of this White Paper that:

- A careful reading of DoD mission and functional capabilities/needs statements suggests a number of areas wherein antiproton technology could have direct relevance, and would provide unique capabilities.
- If the tools of Section D are in place, DoD could utilize those tools to examine the utility of antiprotons to DoD missions.
- If the DoD can justify mission-appropriate antiproton research, it can consider partial funding support to FNAL/DOE to enable provision of the necessary capital facilities/tools and operations.
- If DoD partial funding support is provided, DoD could work out an arrangement whereby it got access to a pro-rated share of the FNAL antiproton production potential for use in DoD mission-relevant research.

Support by DoD in this area of antiproton technology applications would in no way, of course, inhibit DoD participation in the science experiments described and in other kinds of science experiments, at FNAL (or BNL), with the necessary tools in place. Note also that the issues of antihydrogen formation and storage (Sec. C.3) are of direct DoD interest in what follows.

In the remainder of this White Paper, we will raise some of the issues relevant to near-term DoD mission-oriented research in the following areas *(a partial list only)*:

a. A table-top tool for investigating extreme states of matter.
b. Fusion work, using antiproton-initiated fusion.
c. Imaging and Non-Destructive Evaluation (NDE) using antiprotons.

d. A Laboratory Micro-Fusion Facility (LMF) dedicated to: applied research on weapon physics, weapon effects; basic research on various phenomenologies; and fundamental aspects of energy and power technology. These are areas of interest jointly to DoD/DOE.
e. Special applications requiring separate discussion. See, e.g., WD-3826-SDIO, *Defense Applications of Advanced Physics Concepts*, March, 1988, by J. Solem, H. Mayer, B. Augenstein.
f. Applications which integrate in small laboratory facilities the several components of research discussed in areas a, b, c, d, and e.

We emphasize that in all these areas a. through f., the definitive RDT&E can be done using the *present FNAL capabilities* for producing and accumulating antiprotons (~ 10^{14}-10^{15} per year).

Before discussing areas a.-f., we note two major classes of experiments using antiprotons, and having special applications significance, undertaken by U.S.-participant experimental teams at the LEAR facility at CERN (the only facility worldwide currently able to conduct low-energy antiproton experiments).

F. TWO MAJOR U.S.-PARTICIPANT EXPERIMENTS AT CERN

a. Antiproton annihilation phenomena in U^{238}. Two very complex experiments were done at CERN in which antiprotons from LEAR annihilated in U^{238}, with the annihilation phenomenology studied in great detail (CERN experiments PS 183, PS 177). One very remarkable finding, among many, was that there is a 100% probability of fission per annihilation, giving us a very interesting *floor on the energy density* (and power density) possible to create in uranium via impinging antiprotons (G. Smith, Penn State University).

Representative calculations were initially done by S. Polikanov at CERN in 1981, and were very considerably extended by J. Solem of LANL at the 1987 RAND conference, on the creation of hot, dense plasmas by antiproton induced fission. Depending on assumptions on numbers of antiprotons and the space-time compression possible in antiproton bunches, pressures of ~ 4-100 Mbars and temperatures in the 0.1-1.0 KeV or more range seem achievable (using always numbers of antiprotons within current FNAL capabilities). G. Smith, Penn State University, has further extended those calculations. Material environments produced by such pressures and temperatures are comparable to those hitherto available in nuclear weapon testing.

The resultant hot dense plasmas are of interest, both in themselves and as drivers for other materials, for investigations in fusion, astrophysics, planetary physics, equation-of-state, opacity, production of novel beams, energy and space applications, materials evaluation, defect healing in materials, and other areas.

A specific example of conditions in U^{238} is due to G. Smith: A pencil beam of 6.5 MeV antiprotons (10^{10} in the beam) produces an energy density of the order of ~ 1 MJ/cm^3, and, with a 100 nsec dump, a power density of ~ 10 TW/cm^3, based on realistic beam parameters internal to the small U^{238} beam stopper. The calculations consider use of embodiments of current technology which are challenging today. Further development of technologies along lines now considered ready for experimental trial offers grounds for optimism that, for the same particle numbers, the energy and power densities can be increased by, roughly, another order of magnitude.

b. Penning trap capture of antiprotons at CERN. In a recent experiment - Gabrielse, et al. - approximately 6×10^4 antiprotons have been captured into a small trap employing a 3 keV energy bite. Scaleup issues for such traps (capture up to about 10^{13} antiprotons) were fully discussed at the RAND conferences. The technical risk seems reasonably low (and a number of aspects of this risk are amenable to simulations using normal matter). In

this initial trap stage (commonly referred to as the catching trap), the antiprotons can easily be cooled to room temperature by mixing the antiproton cloud with an electron cloud of sufficient density. At this point, the antiprotons can be extracted (and reaccelerated, if necessary) at very low energy spread for collision type experiments, or they can be transported to a next stage trapping experiment better suited for the specific physics case at issue. Both experiments currently under preparation at LEAR with ultra-low-energy antiprotons, namely the comparison of the inertial mass of the antiproton and the proton and the study of the gravitational acceleration of antiprotons in the Earth's gravitational field, require cooling to cryogenic temperatures and extreme vacua, more easily obtained in a specifically designed, small Penning trap.

The importance of both experiments a. and b. is that they provide basic knowledge and tools for a number of the DoD applications-related experiments to be described.

It is also important to comment that partial support for these experiments has been provided by DoD. For example, the Air Force Office of Scientific Research (AFOSR) has supported this research, in part as a response to Air Force Forecast II initiatives. Thus DoD already has a stake in important antimatter research.

Note that the basis for these experiments, and possibilities available therefrom, are described in detailed papers in the RAND references given in Section A.

G. BRIEF DISCUSSION OF DOD-RELEVANT NEAR-TERM ANTIPROTON RDT&E

We contend that the representative near-term antiproton RDT&E (investigations which can be undertaken when the basic tools of Sec. D are operational - i.e., in about three years) described in the following paragraphs directly affects or impacts on missions of the DoD; can be justified for activities the DoD has historically used to support such missions; is warranted to maintain skills and expertise customarily

exercised by DoD to assure in-house competence to satisfy its functional needs; and bolsters DoD goals of advancing the state-of-the-art in areas related to technical problems encountered in developing and maintaining superior DoD forces, and of creating/preventing technological surprise. The antiproton RDT&E to be described is also consistent with points being developed in a current review of the DoD Science and Technology Investment Strategy.

a. The Table-Top Tool

The basic question here is whether antiprotons can be used for experiments in extreme states of matter without the need for large and expensive centralized facilities (very large lasers, underground nuclear test facilities) available to relatively few researchers A "table-top" tool using antiprotons from a portable storage device would open up the research area to a much wider audience. The main areas of interest include high temperature, high pressure, high secondary particle (pions, γs, etc.) flux research, and other work. These areas have many applications ramifications. They translate, for example, into further research in plasma energetics, particle beam technologies and terminal effects of particle beams, and the like, research substantially supported currently.

In the high temperature area, interest centers around opacity or radiation transport measurements. Classical opacity measurements, involving filling a spherical cavity with black body radiation and observing the emergent black body radiation front, can be adapted to an antiproton driver, but the energy requirements for a table-top device are high. On the other hand, non-classical experiments using the heat capacity of the target for energy storage appear more feasible with foreseeable near-term antiproton technology; one such was described in some detail in the Solem paper.

The case for equation-of-state experiments (looking at the interdependence of thermodynamic variables at high pressure) is clear. Using 10^{12} to 10^{14} antiprotons and challenging pulse characteristics, a shock pressure of the order of 100 Mbar could be obtained. This is

fully competitive with the best nuclear-explosive-driven and laser-driven experiments. These results depend on foreseeable antiproton technology, and on details of the pulse characteristics attainable.

Assuming a small storage ring with 10^{10} 100 MeV antiproton capacity, a table-top driver generating ~ 10^{15} pions per cm^2-sec was described. Some specific experiments were discussed, and there is general agreement that this would be a useful capability. Such a driver is scalable, and can serve as an interesting source for a number of external particle flux experiments.

b. Fusion Work Using Antiproton-initiated Fusion

This work incorporates the "table-top" tool of a., above, and the critical experimental results on antiproton-induced fission (Section F.a). Several research directions are possible; these have been the subject of consideration by several groups. Briefly, one path, for example, proposes to use the work on the very hot, dense plasmas produced by antiproton annihilation in Uranium to shock compress mixtures of deuterium (D) and tritium (T) in various geometrical arrangements (the DT assemblies are called targets, from now on).

A variety of target configurations has been considered and subjected to the appropriate hydrodynamic-transport calculations. Sometimes special secondary physical features are proposed to be included (e.g., using timed neutron deliveries on uranium mixture portions of the target).

The targets are millimeters in size or less, and under the circumstances of these calculations (e.g., numbers of antiprotons always $\leq 10^{14}$, and with very short pulse durations for antiproton delivery), highly promising results seem within reach:

- Total thermonuclear burn efficiencies from ~ 0.001 to very high, in the 1-10% or more range.

- Corresponding gains (fusion energy/antiproton energy) up to several orders of magnitude (constrained burn propagation conditions).
- Peak DT pressures of ~ 2×10^3 Mbar

Note that what is really needed here is a *systematic exploration*, by appropriate and uniformly based calculational codes coupled with antiproton experiments, of a variety of target configurations, including configurations subjected to dynamic external environments, potentially capable of thermonuclear ignition or ignition with sustained burn. Definitive critical experiments could be done well within the range of antiproton numbers available from FNAL.

Achieving antiproton-initiated fusion with such characteristics would have many implications of very significant interest, including:

- Possibilities for antiprotons becoming a *net energy source*.
- For comparable energy releases, far fewer antiprotons would be needed, with consequent *great reductions* in antiproton production scaleup requirements.
- Power and energy sources capable of a very broad and controllable range of release rates could become available in small engineering embodiments.

Many of the *applications* of DT burning are very useful at the lower ends of the parameter ranges, in a *variety of RDT&E situations* (where ignition of the DT is desired, but short of the conditions needed for sustained propagation of DT burning). Some of these applications are noted in comments which follow. Item d. specifically lists applications which carry over into many areas of direct and critical concern to DoD.

c. Imaging and NDE Using Antiprotons

The DoD has recognized medical functions to best provide care for its personnel. DoD also currently invests substantially in NDE capabilities. Both concerns are specifically addressable with antiproton technology, using numbers of antiprotons well within FNAL production capabilities. Discussions of these possibilities at the prior RAND Conference specifically stressed portability of these applications of antiproton technology (use of portable storage devices).

Experiments with low-energy antiprotons are important in three general areas of medicine: dE/dx imaging, therapy, and antiproton mesic chemistry. Portable storage devices can be exploited.

Imaging appears to be perhaps one of the most promising single near-term special applications for antiprotons. As an example of the potential of antiprotons, 10^7 antiprotons could give the same quality image as a computer tomography scan, with 1/15 the dose and none of the artifacts that can cluster in a CT image. An entire image requires only 10^9 antiprotons, which is also well within the portable storage capacities envisioned.

For tumor therapy, the doses must be increased one or two orders of magnitude, and at those levels more information is useful concerning the local energy deposition in biological targets. One potential application for antiprotons in therapy is as a tool for testing, monitoring, simulating, and improving current proton and heavy ion therapies. Because antiprotons annihilate at the end of their range and send out products that can be traced back to the annihilation point, they are unique among portable particle beams in their ability to determine accurately where the therapeutic effects are taking place.

The third interesting area for medical experimentation with antiprotons, using x-ray emissions or nuclear gammas, is in the general area of "mesic chemistry" or imaging elemental atoms *in vivo* or *in vitro*. Antiprotons have several advantages over muons used for the same purpose and, with portable storage devices, promise the ability to monitor all elements in the living body. Oxygen, carbon, hydrogen, nitrogen, calcium, and phosphorus - in fact, all elements at once - can

be imaged by events with 10^9 antiprotons (i.e., ~ 1 rad), with images of constituents up to phosphorus made with millions of events.

A highly important counterpart capability for NDE suggests uses of antiprotons for quantitative non-destructive evaluation of materials, measuring local densities and density gradients; new material processing techniques; defect healing in materials; and identification of material compositions. These uses have analogues in the prior biomedical applications. One potentially important industrial use employing amounts of antiprotons available in the near term is illustrated by an example comparing use of computer tomography (CT) and antiprotons, in terms of inspection speed, for inspecting a critical component (a carbon-carbon exit cone). The comparisons suggest that use of antiprotons might speed up this process by a factor of ~ 1000. There is thus very substantial motivation for fuller assessment of such uses of antiprotons as soon as a *low-energy antiproton facility becomes available, for* potential industrial/military benefits. The importance to DoD of NDE capabilities can be judged by the fact that DoD has purchased *individual NDE machines costing more* than the FNAL facility in consideration would cost.

It should be noted that the current size of these applications markets nationally is immense:

- Biomedical applications - up to ~ $100 billion per year (combining imaging and therapy).
- NDE (in aerospace alone) - $1 billion per year for the imaging capabilities.

The size of these markets suggests two considerations. First, even a very small penetration of antiproton techniques into these markets would promptly amortize investments in the basic antiproton tools; and second, there is likely here an excellent opportunity to bring in industrial participation for development of tools and buildup of infrastructure.

d. Laboratory Micro Fusion Facility (LMF)

The DOE has identified a requirement for an LMF to perform a great variety of mission-critical experiments over a 30-year period, as the list to follow shows. The DOE has released a 1989 document on the LMF which forms the basis of many of the following remarks.

The official DOE plan contemplates use of one or another form of inertial confinement fusion (ICF) device, likely candidates being laser or ion beam drivers, impinging on targets wherein thermonuclear burn is initiated, and delivering total energies (including DT burning) of ~ 100 to 1000 Megajoules (a practical constraint for laboratory-scale confinement of the energy release and its consequences).

Specific application experiments are envisioned, including:

- ICF high-gain target development
  - hohlraum physics experiments
  - implosion and symmetry studies
  - ignition experiments
  - propagating burn experiments
  - high target gain
  - high target yield
  - mix and shell break-up experiments
  - reduced drive studies.
- Weapon physics experiments
  - equation of state
  - opacity measurements
  - thermonuclear burn physics
  - mixing studies
  - non-LTE physics
  - radiochemical tracer modeling
  - effects of shock waves on burn
  - radiation flow modeling
  - x-ray laser physics

- hypervelocity fragment development
- other classified experiments

- Weapon effects, vulnerability, and survivability
  - special source development
  - electronic component testing
  - weapon system testing
  - reentry body testing
  - satellite systems testing
  - small satellite testing
  - utilization of total x-ray spectral fidelity
  - concurrent x-ray and neutron effects
  - EMP testing
- Commercial power application
  - high-gain target development
  - materials development
  - data for design of test reactor
- Other application experiments, including long-term applications
  - strategic nuclear material production
  - fissile fuel breeding
  - space propulsion
  - energy/power technologies
  - basic research

Clearly, many of these application experiments are of direct concern for, and of influence on, DoD mission capabilities. Indeed, the DOE document calls for specific participation by DoD in the effects portion of the proposed program. The DoD has, for example, responsibilities in a broad range of effects considerations. The Charter of the Defense Nuclear Agency (DNA) covers a significant portion of the research topics summarized in the previous list of specific applications experiments. Special DoD needs suggest that an active role in this field (in concert with DOE and perhaps other partners) would shorten times to effect responsive modifications to DoD assets, and maintain an indigenous proficiency base to anticipate future needs.

Both DoD and DOE have a need to maintain skills, expertise, and access to experiments, at a time when many of today's experimental tools might become heavily constrained in the future.

Estimates by DOE suggest that, depending on design details, about 5-20 Megajoules of laser or ion beam energy should drive the targets to deliver 100-1000 Megajoules. Thus thermonuclear burn is to produce a "gain" of one to two orders of magnitude over intrinsic driver energy. The technical feasibility of the DOE designs is not assured, and currently estimated facilities costs are ~ $1 to $2 billion.

If the promise of the technical capabilities outlined in a. and b., above, is realized, then a candidate for the LMF could be an antiproton driven device. The potential of such an antiproton driven device warrants high emphasis on experimental trials as soon as practical. Experiments to evaluate these possibilities could be done well within the ~ 10^{14}-10^{15} antiprotons per year yield FNAL allows.

Furthermore, it should be emphasized that the schedule for these evaluation experiments could antedate significantly that for a laser or ion beam driven LMF. That is, the time scale for availability of antiprotons is less than the time to build a new laser or ion beam facility capable of LMF experiments; and one may therefore be able to demonstrate antiproton driven ICF burn in a time scale commensurate with or shorter than that for laser or ion beam drivers, taking into account needs for new target designs for the antiproton driven possibilities. Antiproton-based experiments could be initiated when the FNAL facilities are operative - i.e., in approximately three years.

An operational LMF, capable of many shots per year, would justify an advanced antiproton source (Section A, Group I comments). The technical feasibility of an antiproton source producing and storing ~ 10^{17}-10^{19} antiprotons per year is now possible to evaluate on a sound engineering basis, with progressive reduction of uncertainty as the information base is built up. Costs for such a source, based on past studies, should be a modest fraction of the DOE LMF estimated costs for laser or ion beam drivers.

It is important to repeat that a number of the application tests just described are of *direct mission interest to DoD*, and fall within the mission charter of DoD (or strongly intersect the DOE mission charter). Therefore, DoD can be said to have a vested interest in these mission-related experiments, and thus a potential stake in enabling the development of antiproton applications technology which can bring about such capabilities.

e. Special Applications

A variety of DoD applications warrant separate discussions. Limited documentation is available. It is, perhaps, reasonably apparent where additional implementations of capabilities outlined in a.-d., above, might lead.

f. Integrating Applications - Small Laboratories

In reviewing sections a, b, c, d, and e, it is clear that many diverse experimental areas can be subjected to "hands-on" RDT&E - that is, to RDT&E in which necessary theoretical and engineering calculations can go hand-in-hand with actual antiproton experiments (it will be evident that in certain cases prior normal matter simulations of specific experiments will substantially increase the desired information base).

For example, the applications called "Long-Term" in d, above - specifically *Energy*, and *Space and Other Applications* - are of special interest, because they are, again, directly relevant to DoD missions. Possibilities of antiproton initiated fusion reactions in such applications offer exciting new options to explore. Studies have suggested that with the availability of a basic antiproton source - that is, a source capable of meeting the needs of the Breckenridge collaboration - specialized small laboratory facilities can be set up to conduct the vital preliminary investigations needed to pursue these applications RDT&E objectives. It is easy to describe the many

technology issues and technology embodiments investigatable, and the laboratory engineering outputs available, by testing small model devices of laboratory scale. Experiments along the lines contemplated could be done at *any laboratory location*, using portable antiproton storage devices, as well as having the option of *in situ* experiments at FNAL, say, collocated with the DR facility.

The experiments themselves, in these applications, will in a substantial way intersect basic science RDT&E. For example, the research will involve matter/antimatter collision dynamics (annihilation phenomenology, energy spectrum, energy deposition and coupling). Work can also very likely include antihydrogen in some form suitable for storage in relatively large amounts, and can use many of the techniques employed today in atomic and molecular physics. While basic tests can always employ antiprotons, for actual long-term applications, learning how to use antihydrogen can become a practical necessity (because when charged particles - like antiprotons - are stored in a Penning trap, the energy in the confining electromagnetic fields must always exceed, or at least equal, the rest energy of the stored particles; energetically there is therefore nothing to be gained via such storage).

The information base derivable in principle from such test facilities is detailed and very broad; this is evidenced by the outputs of comparable laboratories already operated by DoD. The base includes insights on those factors which we need to know to proceed with confident designs of larger device embodiments, and which are needed to provide a thorough understanding of performance levels attainable. This information base is also vital for making informed *scaleup decisions* - e.g., is the long-term promise of these kinds of advanced systems such that facilities producing and accumulating much larger amounts of antimatter warrant development?

There accordingly seems to be a compelling case to explore the potential of antiproton techniques to accomplish the goals of the RDT&E outlined thus far. Availability of the basic tools required by the Breckenridge collaboration will enable near-term exploration of this potential, via laboratory facilities of the kind suggested.

H. DOD FUNDING IMPLICATIONS

DoD funding needs to pursue the areas a. through f. of Sec. G can be based on three cost categories:

a. Support of the FNAL capital investments required to pursue the aims of the Breckenridge collaboration (Section D.), plus any DoD-unique capital expenditures.
b. Support of the FNAL annual operating expenses, to allow the DR and other tools to operate (Section D.).
c. Support of DoD experiment-unique facilities implied in Sec. G, areas a. through f., for both laboratory facility and annual operating costs, including possible provision of portable antiproton storage devices.

Categories a. and b. are subject to the same current uncertainties as are reflected in Sec. D. Support by DoD in both categories a. and b. would likely enhance the prospects that the basic antiproton source proposed by the Breckenridge collaboration is acted on favorably. The precise support formula would no doubt be based on some version of a. and b. jointly, or on a specific commitment by DoD to some appropriate level in b.

Category c. support would consist of setting up small special DoD laboratory facilities (capital investment) and annual operating support to enable laboratory RDT&E. This support would likely be expected to come from the same base now supporting the overall DoD laboratory structure. Capital expenditures of a few million dollars and annual operating expenses of very roughly comparable amounts, per laboratory, would seem more than adequate, since current DoD laboratory sites could be utilized.

Category a. and b. DoD funding would necessarily reflect both the importance assigned to the unique antiproton RDT&E possible in areas directly relevant to DoD, and, particularly for category b., the DoD needs for numbers of antiprotons annually. One week's production of antiprotons at FNAL can easily be in the 10^{12}-10^{13} range. A fraction of

a year's production would likely, for the first few years of operation, meet yearly demands for the *executable* DoD-relevant RDT&E experiments, leading to a prorated DoD category b. expenditure of, roughly, not more than one to a few million dollars, annually.

Category a. DoD expenditures for essentially unique DoD needs are again subject to a wide range of uncertainties. A multi-use facility might be desirable at FNAL to permit special experiments (e.g., multi-port antiproton beam arrangements to allow several experiments to proceed, or specific experiments using more than one beam). Such a facility could likely be put in place (assuming space available) for a few (probably ≤ 5) million dollars. The alternative is primary emphasis on portable storage devices, filled by the DR. Such devices could require use of reacceleration (or deceleration) at the laboratory site remote from FNAL.

Finally, the probability of FNAL (or, as an alternative, BNL) going ahead with the commitment to the DR and associated tools is likely to be enhanced by DoD support of the basic low-energy antiproton source, at least to the extent of some prorated share. If that share is based on using one-fourth to one-half of the total source output, a DoD capital investment of up to $2-4 million per year for ~ 3 years might be considered realistic, and would have to be judged against the alternative of a possibly more substantial commitment to supporting FNAL category b. (operating) expenses.

There are therefore a number of variants for total DoD funding expenditures in categories a. and b. Even a *high end* version of these expenditures (say, capital expenditures in the ~ $3-6 million range annually for ~ 3 years, and a roughly comparable subsequent annual operating expense) would buy a very large opportunity for DoD antiproton research in a minimal cost way. More precise sharing formulas and mutually equitable arrangements would come from DoD/DOE coordination.

I. WHAT SHOULD DOD DO?

We are aware that some past reviews of DoD participation in antiproton RDT&E have concluded earlier that the work is of such a far term nature that it warrants little DoD attention in the foreseeable future. The DoD applications RDT&E discussed in this Draft Paper is of high interest to DoD; is doable in the near term, using outputs of FNAL facilities in critical experimental trials; and, very significantly, can result in entirely new approaches and unique possibilities affecting early on major DoD mission areas. These factors, combined with modest costs for DoD pursuit of antiproton RDT&E, suggest that these new considerations and circumstances warrant basic revisions of the earlier conclusions.

There is here an excellent opportunity for the DoD to support experimental proposals such as those spelled out by the Breckenridge collaboration (Section B), and thus create the opportunity to "sequester" for DoD a part of the prospective FNAL antiproton delivery capability for mission-related RDT&E of continuing interest to DoD.

This approach is one option, of several, to enable substantive near-term DoD antiproton research. The option appears to have some desirable features: It leaves basic procedural decisions to the appropriate scientific community; it constrains ingoing DoD costs to a reasonable level; it is unobtrusive, in the sense that it does not unilaterally force the necessary facilities; and it works hand-in-hand with the people and organizations vital to a successful U.S. commitment to this kind of research. It makes DoD a strong participant, without the risk of trying to play a leadership role initially best played by others.

Several near-term aspects of such an arrangement could include:

a. Support preliminary investments (study efforts) in such areas as:
   - Refinement of FNAL machine designs.
   - Support work on antiproton induced fusion reactions.
   - Support design studies of antiproton driven LMF options.

   - Prepare experimental and study plans for imaging/NDE work.
   - Refine appropriate cost studies.

   Such studies might usefully be conducted at an annual 100K-250K level each over the next one or several years.

b. Support construction and operation of the basic FNAL tools, under the proviso that the basic premise of the collaboration is concurred in.

c. On the basis of a. and b., above, initiate arrangements to purchase part of the FNAL antiproton production to support DoD mission-related research, as appropriate.

d. Develop the programs and infrastructure to exploit early antiproton applications, such as are outlined in Sec. G, including contractor associations.

e. Conduct the necessary RDT&E once the FNAL tools are in place.

f. If the DoD mission-related RDT&E results are sufficiently promising, then explore and develop options for possible "next steps" in antiproton RDT&E (scaleup issues, etc.) which build on the near-term results.

We urge the DoD to seize this opportunity to support and get significantly involved in near-term antiproton RDT&E, recognizing that such RDT&E potentially is of importance to a number of its constituent organizations. This form of involvement, under the arguments advanced in this White Paper, would avoid prior concerns that broad antiproton research, while exciting and of intrinsic basic merit, is properly an exclusive domain of other Departments and Agencies, or is of such a long-term nature, before it can be useful in applications, that no immediate interest is warranted by DoD. Pursuing such research in carefully selected areas is consistent with and supports validated DoD missions and functions definitions, as is apparent upon reviewing such definitions and analogous work already pursued by DoD, but employing other means.